Design, Synthesis and Characterisation of CCL2 Constructs: Selective Delivery of Fluorophores to Monocytes

by

Ryan Brown

A thesis submitted to the University of Birmingham for the degree of

DOCTOR OF PHILOSOPHY

PSIBS Doctoral Training Centre

School of Chemistry

University of Birmingham

July 2017

Abstract

Monocytes and macrophages are key mediators of the immune response in the host immune system and are principally responsible for pathogen clearance, inflammatory induction and tissue repair. A pathogenic role for these immune cells has also been identified in a number of diseases including cancer, atherosclerosis, liver fibrosis and rheumatoid arthritis. There is growing evidence that phenotypic variations within monocytes and macrophages have individual, and in some cases, opposing roles in many of these diseases. This presents a need for tools that can selectively target phenotypic subsets of monocytes and macrophages for both research and therapeutic purposes. CCL2 is a chemokine which has been shown to be involved in these diseases in terms of recruitment of pathogenic monocyte subsets and also in the direction of adaptive immune responses. The chemokine is selective for the CCR2 receptor which is expressed on classical and intermediate monocytes, M1 macrophages, MDSCs and some subsets of lymphocytes. CCL2 is a potentially attractive target for use as a targeting vector towards these phenotypes which are implicated in disease and has recently been the utilised in a number of protein conjugates including fluorophores and peptide toxins.

The work herein describes the design of CCL2 constructs to include an alkyne tag for copper-mediated alkyne-azide cycloaddition reactions which do not affect the biological function of the chemokines. Three CCL2 sequences were designed and synthesised: WT-CCL2, P8A-CCL2 and CCL2 Ala^{-1} each containing small modifications at the C-terminus to include a propargyl glycine for CuAAC. These CCL2 variants are known in the literature to have distinct functional activities and behaviours which were selected to identify the optimal sequence for monocyte targeting and fluorophore delivery. A range of azide-containing fluorophores and a FRET pair were synthesised in chapter 3 which differed in lipophilicity and linker stability in intracellular environments. These fluorophores were then conjugated using copper-catalysed azide-alkyne cycloaddition (CuAAC) to the CCL2 variants, including extensive optimisation of reaction conditions for compatibility with poorly soluble and disulfide linked fluorophores in chapter 4. This resulted in the formation of 10 CCL2 conjugates across

the three CCL2 variants. Chapter 5 then extensively characterised the functional activity of alkyl-linked hydrophilic CCL2-fluorophore conjugates using chemotaxis assays. Induction of chemotaxis and internalisation of the fluorescent conjugates was determined, highlighting differences between the variants. CCR2-dependent chemotaxis and internalisation was determined through the use of the CCR2 antagonist INCB 3284, surface depletion of CCR2 using high concentrations of CCL2, and also experiments using $CCR2^{-}$ jurkat cells. The functional activity of the CCL2 alanine addition (CCL2 Ala^{-1}) and P8A-CCL2 conjugates synthesised through the optimised methods was also determined using these assays which revealed an incompatibility of CCL2 with a combination of DMSO and sodium ascorbate. The P8A-CCL2 conjugates were therefore taken forward into primary cell experiments with the alkyl-linked hydrophilic WT-CCL2 and CCL2 Ala^{-1} conjugates. Uptake of five CCL2 conjugates was then measured across peripheral blood mononuclear cells (PBMCs) using flow cytometry, in these experiments neutrophils and the majority of lymphocytes were not labelled by the CCL2 conjugates. Further experiments determined that CCL2 uptake was highly selective for $CCR2^{+}$ cells, these included classical monocytes, intermediate monocytes, NKT cells, subsets of NK cells and minor subsets of T cells. Some uptake was also observed in non-classical monocytes although all CCL2 uptake was dependent on the presence of surface CCR2 and correlated with the magnitude of receptor expression. Evidence for endosomal escape of lipophilic disulfide linked conjugates was observed most likely due to leaching into $CCR2^{-}$ cells. Fluorescence microscopy in THP-1 cells and PBMCs identified that fluorescence from hydrophilic fluorophores was constricted to vesicles and the disulfide-linked lipophilic fluorophore exhibited a diffuse fluorescence profile suggesting this compound was escaping the vesicles. This project successfully developed general methods for forming a diverse array of CCL2 conjugates of varying CCR2 affinities which will aid in the research of monocytes and could potentially translate into targeted therapeutics towards monocyte and lymphocyte subsets.

Acknowledgements

Firstly, I would like to thank all members of the Butterworth group, chatting to you guys when I was actually in the chemistry lab was always a laugh and helped ease the pressure, I've missed 'Burrito Fridays' since you all mercilessly abandoned me to follow Sam's move to Manchester! Edgar, I hope I have had some positive influence in your quest to become 'a lad', though it seems you still have a long way to go. Don't get too stressed out in your final year, I'm sure you've managed to do enough in your 'throw everything and the kitchen sink' approach to organic chemistry. Gary, your help in the lab when I was tying up loose ends was generous and saved me a lot of hassle. Francois and Alejandro, try as you might you will still always get absolutely done by me on the football pitch, that continental flair is overrated! It was great coming to your wedding (Boda?) Alex, and Francois - I look forward to coming to your big day!

I also have to thank the PSIBS CDT firstly for the excellent training which was essential to me completing this project successfully. Special thanks go to Chris 'ginger lightning' Meah and David 'eyesore' Kershaw, it's always a laugh with you guys and we managed to achieve some incredible feats such as organising an international conference with celebrity speakers and how could we top the laser maze?! Chris, I hope the School of Code takes off in the way you want it to (don't forget the little people) and David, good luck in your new dream job of spying on people for the government.

To my Northamptonian friends back home, thank you for keeping me grounded and reminding me there is a world outside academia. Thank you for the endless barrage of encouraging gems including, 'get a real job', 'living on benefits', 'shouldn't you still be in bed?' and the multiple substitutions for the PHD abbreviation. The days out, holidays, Glastonbury, stag do's and just having a few drinks down the pub probably haven't helped my work output but they definitely helped my wellbeing, sort of! I acknowledge the squad for their heroic efforts at feigning some interest on the chat about my research and thesis woes, specifically

Kellyshero6189, marcdngale, PMSMITHY89, Osty1989, jgreeny89 and Dazzlebear69. At the beginning of my PhD many of you were in very different positions to where you are now which has been an inspiration to me to keep pushing for what I want, so thank you!

Thanks to my many supervisors for your support and guidance in this project. Iain, sorry I didn't do more computational science but chemistry/biology was always where my interests lie. Robin, thank you for your encouragement and for purchasing the Attune and Zeiss microscope, I'm not sure where I would have got to without them. I must also thank the analytical staff who were very helpful in getting a good method for detecting the proteins by mass spec and I also thank all the phlebotomists who collected blood for me. Sam, thank you for devising this project in the first place, the level of planning that went into this was essential and your willingness to change gear when things weren't working so well and to then go out of your way to find the best people/companies/equipment was integral. Your enthusiasm for science is infectious, you have also been a great teacher and mentor along the way. I must also thank you for my job: the contacts, advice and desire to help me get experience was essential to making my first step in my career. I know that the move to Manchester wasn't an easy one but I think it has turned out well and I'm sure you will continue to be successful - I'm looking forward to hearing about the next steps in this project, keep me posted! Special thanks must also go to Chris Weston, I don't think we would have got very far without your help which you gave generously. Thank you for helping a chemist get to grips with chemotaxis, monocytes and particularly for your help with the flow cytometry.

I would like to thank my family for nurturing my fascination with science from a young age and for all your love and support along the way. I know it wasn't easy to get me through University during a global financial crisis and so I thank you for the many sacrifices you made. Finally, thank you Sarah for putting up with a stressy, miserable and poor PhD student, I hope that now we can begin to enact the plans we have made for the future. Before I started my PhD I asked your permission if I could go another 4 years being stressed and being a pauper, without hesitation you said yes. Thank you for putting me first so many times, the comfort food, the encouragement, and of course, for marrying me.

I dedicate this thesis to my first niece Selah Christian-Farman, I hope that there continue to be naive but optimistic young people that want to change the world from a fume cupboard, maybe one of us will do just that.

Author's Declaration

This thesis has been written by Ryan Brown and I declare I have performed all experiments unless stated otherwise at the beginning of a chapter. This thesis has not been submitted for any other degree at the University of Birmingham or any other institution.

Contents

List of Figures

List of Tables

Abbreviations

7TM - 7 transmembrane receptor

ACKR - atypical chemokine receptor

ADC - antibody drug conjugates

ALD - alcoholics liver disease

AMC - antibody maytansinoid conjugate

AP-2 - adaptin-2

APC - antigen presenting cell

BHT - butylated hydroxytoluene

(BimH)$_3$ - tris(2-benzimidazolylmethyl)amine

BODIPY - boron dipyrrin

BPDS - bathophenanthroline disulfonate disodium salt

CAD - coronary artery disease

cAMP - cyclic adenosine monophosphate

CCL2 - chemokine (C-C motif) ligand 2

CCL2 Ala^{-1} - CCL2 alanine addition

CCR2 - C-C chemokine receptor type 2

CD - cluster of differentiation

CHO - chinese hamster ovary

CMP - common myeloid progenitor

CSF - colony-stimulating factor

CuAAC - copper-catalysed azide-alkyne cycloaddition

CX_3CL1 - chemokine (C-X3-C motif) ligand 1

CX_3CR1 - CX3C chemokine receptor 1

DAPI - 4',6-diamidino-2-phenylindole

DARC - Duffy antigen receptor for chemokines

DC - dendritic cell

DFT - density functional theory

DTT - dithiothreitol

DW-MRI - diffusion-weighted magnetic resonance imaging

EBFP - enhanced blue fluorescent protein

EC - endothelial cell

ECL - extracellular loop

ECM - extracellular matrix

EDTA - ethylenediaminetetraacetic acid

EGFP - enhanced green fluorescent protein

EMT - epithelial-to-mesenchymal transition

ESI-FTICR - electrospray ionisation fourier transform ion cyclotron resonance mass spectrometry

FLT3 - fms like tyrosine kinase type 3

FMO - fluorescence minus one

fmoc - fluorenylmethyloxycarbamate

FRET - Förster resonance energy transfer

GAG - glycosylaminoglycan

GDP - guanosine-5'-diphosphate

GM-CFU - granulocyte-macrophage colony-forming unit

GM-CSF - granulocyte-macrophage colony-stimulating factor

GMP - granulocyte-macrophage progenitor

GPCR - G protein-coupled receptor

GRK - G protein-coupled receptor kinase

GTP - guanosine-5'-triphosphate

HBTU - *N,N,N',N'*-tetramethyl-O-(1H-benzotriazol-1-yl)uronium

HCV - hepatitis C virus

HDL - high-density lipoprotein

hERG - human ether-a-go-go-related gene

HLA-DR - human leukocyte antigen - antigen D related

HIV - human immunodeficiency virus

HPLC - high performance liquid chromatography

HSA - human serum albumin

HSC - hematopoietic stem cell

IC_{50} - half-maximal inhibitory concentration

ICAM-1 - intercellular adhesion molecule 1

IFN-γ - Interferon-gamma

IgG - immunoglobulin G

IL - interleukin

IMC - immature myeloid cell

iNOS - inducible nitric oxide synthase

JAK - janus kinase

K_a - acid dissociation constant

LAP - latency-associated peptide

LDL - low-density lipoprotein

LFA-1 - lymphocyte functional antigen 1

LMICs - Lower and Middle Income Countries

LPS - lipopolysaccharide

Mϕ - macrophage

M-CSF - macrophage colony-stimulating factor

M-CFU - macrophage colony-forming unit

MALDI - matrix-assisted laser desorption ionisation

MAP2K - mitogen-activated protein kinase kinase

MAPK - mitogen activated protein kinase

MCP-1 - monocyte chemoattractant protein 1

MDP - macrophage-dendritic cell progenitor

MDSC - myeloid-derived suppressor cell

MFI - median fluorescence intensity

MHC - major histocompatibility complex

MMP - matrix metalloprotease

MS - mass spectrometry

MYD - myeloid differentiation primary response

NAFLD - non-alcoholics fatty liver disease

NMR - nuclear magnetic resonance

NSAIDs - non-steroidal anti-inflammatories

ON - oligonucleotide

PBMC - peripheral blood mononuclear cell

PEG - polyethylene glycol

pFA - para-formaldehyde

PI3K - phosphatidylinositol-4,5-bisphosphate 3-kinase

PIP_3 - phosphatidylinositol (3,4,5)-trisphosphate

pK_a - - $\log(K_a)$

PKA - protein kinase A

PKC - protein kinase C

PLC - phosphoinositide phospholipase C

PPTase - phosphopantetheinyl transferase enzyme

RA - rheumatoid arthritis

RBC - red blood cell

R_f - relative front

RNA - ribonucleic acid

RNS - reactive nitrogen species

ROS - reactive oxygen species

SA1 - *Shigella dysenteriae* holotoxin

SAR - structure-activity relationship

SCF - stem cell factor

scFv - single chain variable fragment

siRNA - small interfering RNA

SPPS - solid phase peptide synthesis

STAT - signal transducer and activator of transcription

TAM - tumour associated macrophage

TB - tuberculosis

TBTA - *tris*-(benzyltriazolylmethyl)amine

TCEP - tris(2-carboxyethyl)phosphine

TFA - trifluoroacetic acid

TGF-β - transforming growth factor beta

T_h - T helper cell

T_h1 - type 1 helper cell

T_h2 - type 2 helper cell

THPTA - tris(3-hydroxypropyltriazolylmethyl)amine

TLC - thin-layer chromatography

TLR - toll-like receptor

TNF-α - tumour necrosis factor alpha

T_{reg} - regulatory T cell

UV - ultra-violet

VLA-1 - very late activation antigen-1

VCAM-1 - vascular cell adhesion molecule 1

WT - wild-type

Chapter 1

Introduction

1.1 Background

Many debilitating and life threatening conditions are caused by inflammatory processes both in advanced economies and also in Lower and Middle Income Countries (LMICs). The mechanism of these processes are complex, involving a variety of cell types and as such, broad spectrum therapeutics have been largely ineffective.[1] Successful therapies such as anti-TNF (Tumour Necrosis Factor) treatment in rheumatoid arthritis are highly selective for disease causing cells. Furthermore, understanding the mechanistic process behind inflammatory disease requires *in vivo* experiments using research tools which can interrogate cells selectively. This project aims to develop tools targeted at monocytes, this is a platform technology which could be designed for research and therapeutics. Monocytes are innate immune cells which clear pathogens, repair damaged tissues and also produce pro-inflammatory mediators. The cells are implicated in a number of inflammatory diseases such as cancer, liver fibrosis, rheumatoid arthritis and atherosclerosis.[2] However, monocytes have many phenotypic variations which in some cases have dual or even opposing functions in disease progression meaning targeted therapies are needed.[3,4] This project aims to utilise chemical conjugates of the chemokine, CCL2, to target monocytes. CCL2 is a small protein which is highly specific for the receptor C-C chemokine receptor type 2 (CCR2), a number of conjugates have been reported but a simple method to form a wide variety of conjugates is lacking.[5–7] The use of CCL2 provides subset specificity for monocytes aligned with the pathogenesis of many diseases through differential expression of it's major receptor CCR2. The use of CCL2 conjugates provides selectivity for classical and intermediate monocytes which are high in CCR2, and it is these monocyte subsets which are pro-inflammatory.[8–10] The aims of the project are therefore:

1. To develop a CCL2 construct which contains an alkyne tag for subsequent CuAAC conjugations.

2. To synthesise a range of fluorophores with varying physicochemical properties with an

azide tag for CuAAC conjugation.

3. To form the fluorescent CCL2 conjugates and then assess their biological function with *in vitro* experiments in monocytic cells.

1.2 Monocytes

White blood cells are key mediators of the human immune system and have three major roles in the body: pathogen destruction, tissue repair and phagocytosis of dead cells.[2] Traditionally, these roles are grouped into the innate immune system and the adaptive immune system; innate immunity is a naive system which mainly deals with the non-specific destruction of pathogens, whereas adaptive immunity is a higher-learned process concerned with antibody production towards encountered antigens and antigen presentation.[11] Recently, evidence suggests this classification is over-simplistic and cell-types previously considered part of innate immunity have an intricate and complex role in adaptive immunity as well, with many feedback mechanisms relaying into both systems. Monocytes represent around 2-8% of white blood cells and are classified as part of the innate immune system. Monocytes are mononuclear white blood cells which circulate in the blood, often for extended periods, before differentiating into macrophages, dendritic cells and osteoclasts.[2] The cells are relatively large in diameter (ranging from 16-25 um, depending on phenotype) and possess a distinctive elliptical (or kidney-shaped) nucleus.[12] Monocytes have a complex range of phenotypes and it is this feature which has gained these cells significant research attention due to their unparalleled heterogeneity. These cell types cannot be distinguished by light microscopy or by light scatter in flow cytometric analysis and so the majority of research into these cells has been achieved *via* antibody labelling in flow cytometry. This body of research has been performed on both human and murine cells and much conflicting nomenclature has arisen in the field as a result of heterogeneity in surface markers between the species. The structure of this section on the biology of these cells will therefore cover macrophages first, followed by a broad discussion of diseases related to macrophages and monocytes, before finally reviewing monocyte subsets in more detail and then applying this information to diseases linked to specific monocyte subsets. This structure has been used due to the distinct terminology used surrounding macrophages and monocytes in broad terms (often interchangeably), relative to the description of individual monocyte subsets.

Monocytes circulate in the blood and are the precursor cell for many cell types such as macrophages, specialised antigen presenting cells (APCs) such as dendritic cells (DCs), and osteoclasts.[2] Monocytes originate in the bone marrow from hematopoietic stem cells (HSCs), this lineage is also shared with neutrophils. They are stimulated with growth factors to differentiate towards monocytes before entering the peripheral blood for eventual recruitment into tissues where they may differentiate into tissue macrophages or dendritic cells. Even at early stages in their development monocytes represent a hetergeneous population of cells that differ in size, surface marker expression and their differentiation potency in response to many factors.[13] Monocytes generally have irregular shape and an oval-shaped nuclues, along with a high nucleus:cytoplasm ratio. The development of monocytes from stem cell precursors depends on the growth factor macrophage colony-stimulating factor (M-CSF) as demonstrated by knockout mice studies.[14,15] The developmental pathway (see Figure 1.1) from HSCs to monocytes includes several intermediate progenitors including the common myeloid progenitor (CMP), the granulocyte-macrophage progenitor (GMP), and the macrophage-dendritic cell progenitor (MDP).[13,16] Myeloid progenitor cells are known to respond to CSF-1 by both differentiating and proliferating, monocytes however are not thought to proliferate and differentiated monocytes can sense CSF-1 but do not respond by proliferation, ending in cell-cycle arrest.[17,18]

Until recently, immunologists believed that homeostasis of tissue-resident macrophages is dependent on the recruitment of blood monocytes. Further research has since shown that macrophages do not rely on this recruitment pathway to maintain their population or expand. Indeed, monocytes can differentiate into macrophages (particularly during inflammation), however, it would appear this is not an exclusive, or even necessary, pathway. Adult tissue macrophages are derived from embryonic precursors where tissues are seeded before birth and macrophages can actually self-maintain their population.[19,20] It would appear that monocytes represent a separate, plastic and dynamic cellular system which is complementary to tissue macrophages, rather than being an intermediate cell-type towards the final macrophage.[21] Thus, macrophages which have descended from monocytes are termed monocyte-derived

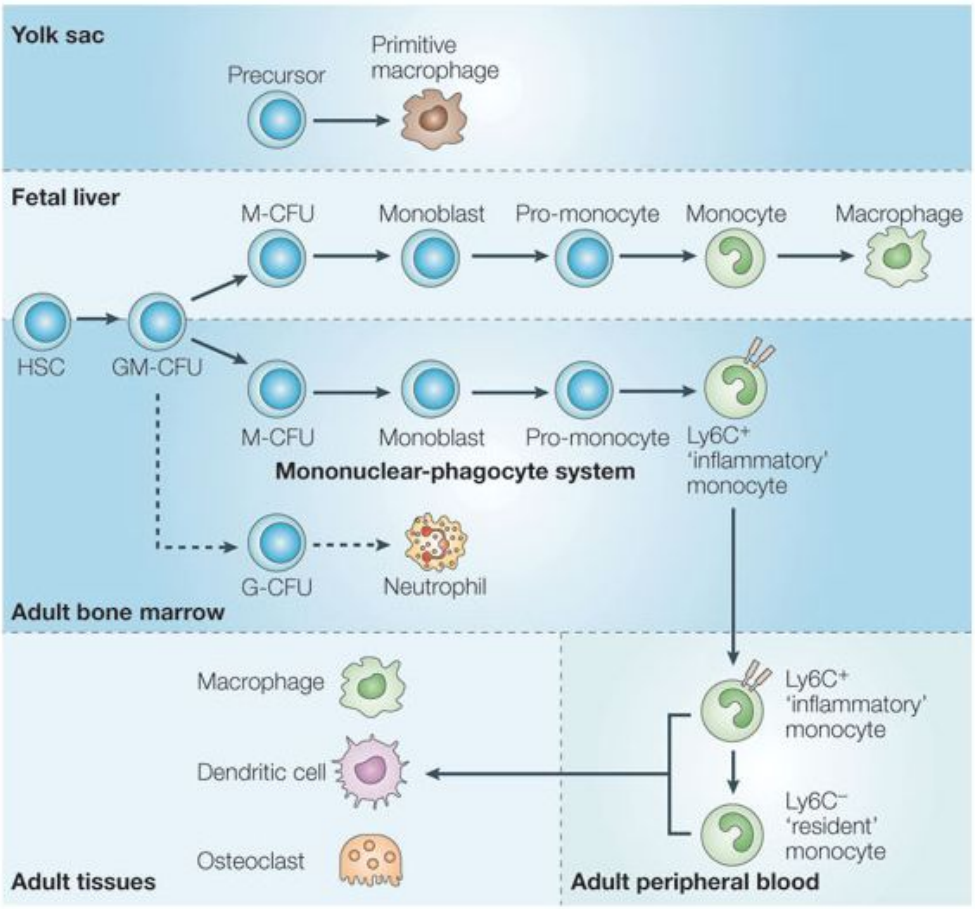

Figure 1.1: The development of adult and fetal monocytes are broadly identical in the early stages. Both begin as HSCs before differentiating into GM-CFUs, followed by M-CFUs, monoblasts and pro-monocytes. Adults and adult bone marrow and fetal lover then diverge, with the latter forming Ly6C 'inflammatory' monocytes (in mice) and entering the peripheral blood. Here the inflammatory monocyte can either invade tissues or differentiate into 'anti-inflammatory' monocytes. Once transmigrated into tissues each subset can differentiate into macrophages, dendritic cells or osteoclasts. At each progressive stage the differntial potential is reduced as can be seen from the highly potent GM-CFU transitioning into the less potent M-CFU. Reproduced with permission from Gordon *et al.*[2]

macrophages and macrophages derived from an organ or tissue are termed tissue-resident macrophages.

Ly6C is a common marker used to identify murine monocytes, Ly6C^{hi} monocytes have a poorly defined function in the blood circulation, however, the mobilisation of this subset could be controlled by circadian rhythms through association with the gene Bmal1; this gene releases Ly6C^{hi} monocytes in diurnal waves in a process termed 'anticipatory inflammation'.[22] This preparatory behaviour is thought to be an evolutionary response to predicted environmental challenges in an effort to boost the innate immune system. The mobilisation of Ly6C^{hi} monocytes into the peripheral blood is CCR2-dependent as demonstrated by parabiosis experiments in mice.[23] In these experiments, bone-marrow grafts of wild-type mice are adoptively transferred into CCR2-deficient mice and the relative genotypically distinct monocytes are tracked through the body.[23] Only ∼30% of circulating blood monocytes were the endogenous CCR2^{-} monocytes, the remaining proportion were the wild-type parabiont. Evidence of the separation of lineages between monocytes and tissue-resident macrophages was exemplified by the lack of chimeric change in the resident-macrophages.[23] The life cycle of monocytes has been shown to include extravasation into tissues without differentiation into macrophages or DCs.[24] Expansion of monocyte-derived macrophages is heavily contextual in the steady state, with the majority of tissues not having any contribution from monocyte-derived macrophages.[21] However, some tissues are dependent on this subset, for example, in the gut; adoptive transfer of monocytes into macrophage ablated mice demonstrated that intestinal M2 macrophages are descended from Ly6C^{hi} monocytes.[25,26] Another study involving chimeric mice (containing both CCR2^{-} and CCR2^{+} monocytes) showed that intestinal macrophages were exclusively descended from the wild-type CCR2^{+} monocytes.[27]

1.2.0.1 Biology of Macrophages

The steady state homeostasis of macrophages is not wholly dependent on replenishment by bone-marrow derived monocytes, except in tissue specific environments. This situation is not

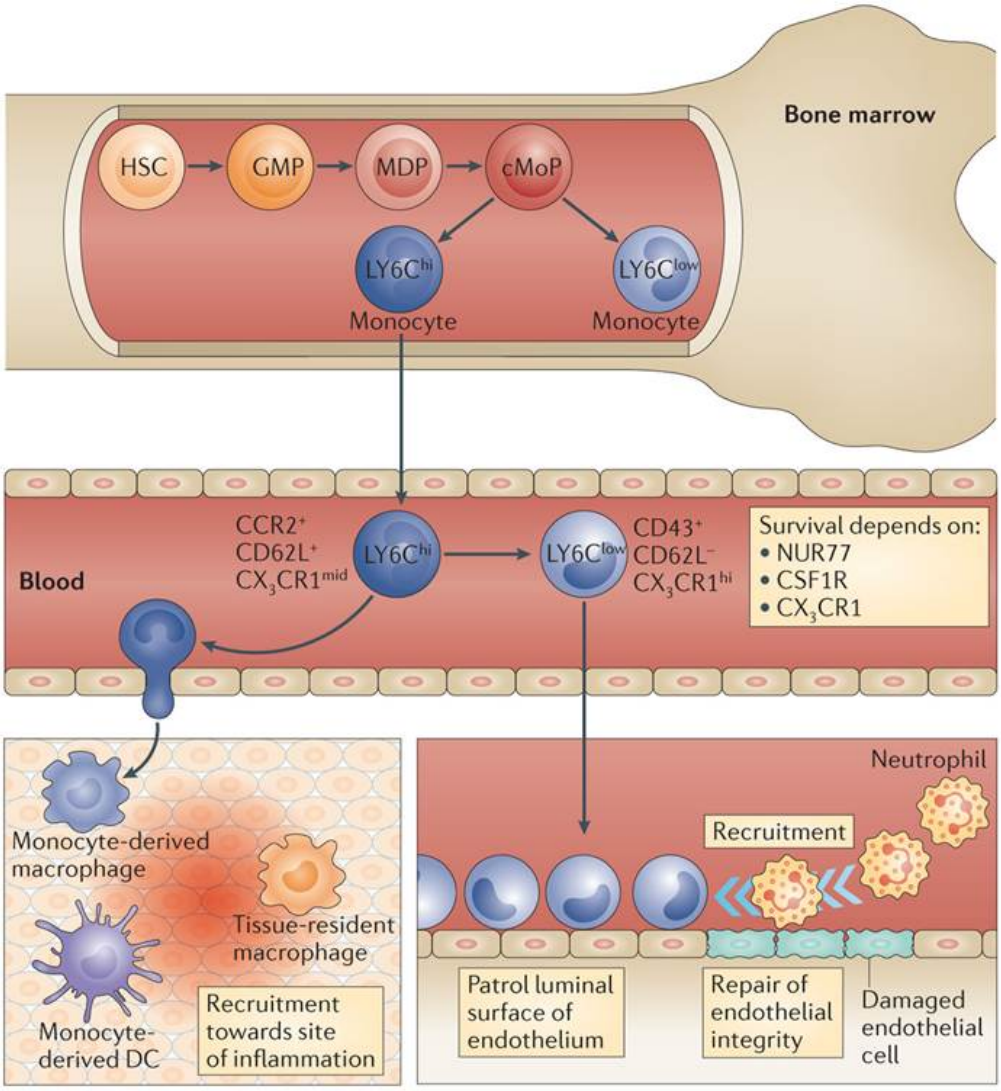

Figure 1.2: Murine monocyte development from HSCs to Ly6C^{hi} monocytes which are recruited from bone marrow into the peripheral blood in a CCR2-dependent manner. These monocytes circulate before transmigrating at inflammation sites to differentiate into monocyte-derived macrophages or DCs, joining the alternately descended tissue-resident macrophages. The Ly6C^{hi} monocytes can also differentiate to Ly6C^{low} monocytes in the blood which proceed to patrol the luminal side of the endothelium in a protective function. Reproduced with permission from Ginhoux *et al.*[21]

reflected in pathological inflammation, where Ly6C^{hi} monocytes form a large part of tissue resident macrophages (Figure 1.2).[21] These monocytes exhibit potency towards differentiating towards M1 or M2 macrophages for increased inflammation or resolution depending on environmental stimuli, and it is suspected these monocytes are sequentially recruited for this purpose.[28] This behaviour is reflected in atherosclerosis where lesions are first identified using Ly6C^{+} (in mice, and the human equivalent) accumulation at the blood vessel wall.[29,30] The monocytes differentiate into macrophages which ingest lipoproteins and contribute to the advancement of the atherosclerotic plaque *via* their development into foam cells (lipid rich macrophages). This relationship has been confirmed through a study in the reduction of monocyte specific chemokines such as, chemokine (C-X3-C motif) ligand 1 (CX_3CL1) or CX3C chemokine receptor 1 (CX_3CR1), leading to a reduction of monocytes and foam cells in atherosclerotic plaques, linked with a reduction in atherogenesis.[31] Monocytes would therefore seem to be responsible for circulating in blood for the anticipation of inflammation and also for transient, short-lived differentiation into macrophages in response to environmental stimuli.

Macrophage development within tissues is generally dependent on embryonic cues which linger into adulthood, whereby the macrophages self-proliferate.[32,33] Initially, it was thought T cells direct adaptive immunity and the innate immune system, however, it is now believed that macrophages are the directors which initiate T cell proliferation and T helper cell (T_h) responses.[34] This led to classification of macrophages as M1 and M2 to reflect this link to T helper cell activation; M1 preferentially express inducible nitric oxide synthase (iNOS) and major histocompatibility complex (MHC) class II, whereas M2 macrophages express arginase and do not express MHC class II.[35] This expression denotes a difference in arginine metabolism where M1 macrophages produce NO using arginine and M2 produce ornithine and polyamines to promote healing and growth.[36] M1 macrophages are generally terminally differentiated cells but M2 have been shown to differentiate to M1 macrophages in response to differentiating stimuli.[35] M1 macrophages display an inflammatory phenotype whereas M2 macrophages display a tissue-repair functional phenotype.[37] A critical aspect of research in

this area is that innate immunity is dynamic, with many cell-cell interactions meaning that *in vitro* studies on one or two subsets can lead to cellular responses that do not occur *in vivo*.[34] As macrophages appear to be at the centre of many immune responses there is a great need for better understanding of these cells and specific targeting of therapeutics to M1/M2 subsets.

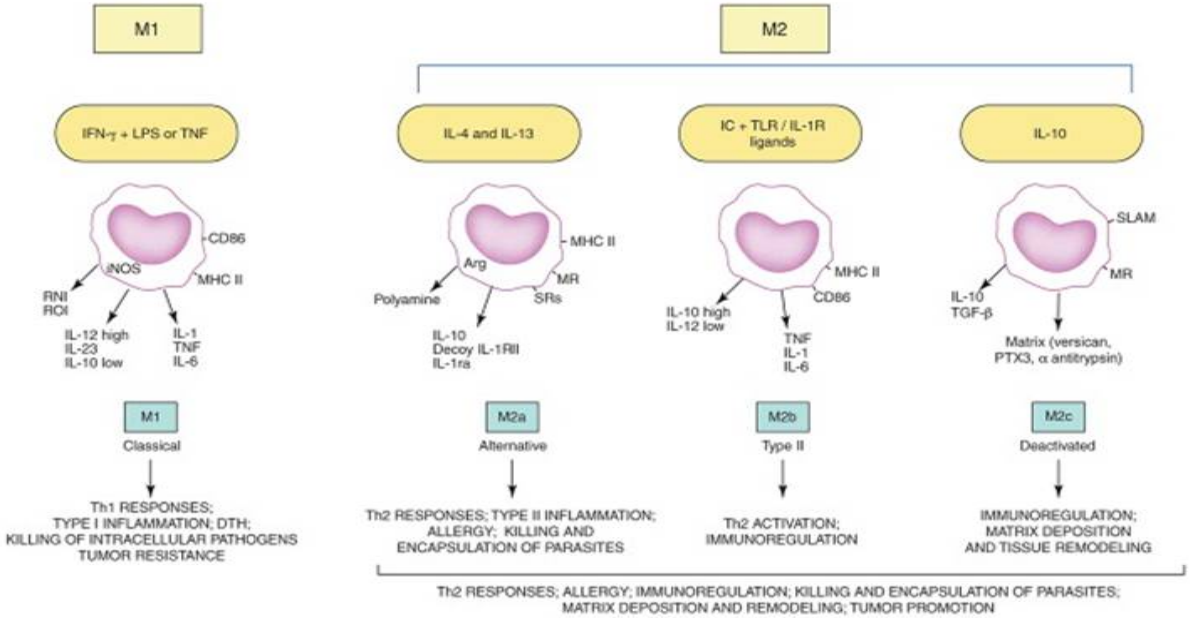

Figure 1.3: The four activation subsets of macrophages and the surface markers which classify them. Initially, iNOS and MHC class II expression was an identifier of M1 macrophages but it has been shown that M2a macrophages also express MHC class II, therefore multiple markers are needed to fully attribute a subset. Both major subsets incite killing of pathogens though through distinct T_h1 and T_h2 immunoregulatory pathways. The receptor expression and functional contexts of macrophages should therefore be considered in this research. Reproduced with permission from Martinez *et al.*[38]

The grouping of macrophages into two subsets is an over-simplification of two extremes of macrophage polarisation.[39] Figure 1.3 shows the four subsets of macrophage activation and the markers involved in classification and activation of these subsets. It is well known that monocytes respond to various environmental stimuli such as Interferon-gamma (IFN-γ) or IL-4 by differentiating into macrophages with distinct functional phenotypes, such as M1 or M2 respectively.[40] Polarisation towards an M1 state is initiated by pro-inflammatory cytokines such as IFN-γ, tumour necrosis factor alpha (TNF-α) and granulocyte-macrophage colony-stimulating factor (GM-CSF) or by bacterial stimuli such as lipopolysaccharide (LPS).

M2 polarisation on the other hand is initiated by IL-4, IL-13 and other T_h2 associated cytokines such as IL-33. Furthermore, macrophages can be polarised towards an M2-like state which partially resemble the M2 phenotype, this is generally caused by stimulation with immune complexes together with LPS, transforming growth factor beta (TGF-β) or interleukin-10 (IL-10) to produce functions such as high expression of angiogenic factors but not all M2-characteristics.[36,40] The function of M1 macrophages is to induce and effect T_h1 responses such as combating intracellular parasites and anti-tumour activity; this is achieved through production of reactive oxygen species (ROS) and reactive nitrogen species (RNS) and increased expression of cytokines such as TNF-α and IL-6.[40] M2 cells have increased expression levels of mannose, scavenger and galactose-type receptors; these cells also differentially regulate the IL-1 system with low IL-1β but high IL-1ra. Polarised M2 cells initiate T_h2 responses, clear parasites, immunosuppression, tissue remodelling and also tumour development.[40–42] Interestingly, chemokines can also drive this polarisation, CCL2 has been linked with cancer progression and has been shown to induce an M2-like phenotype suggesting a link between these systems.[43] Polarised macrophages also differ in glucose metabolism which is likely to reflect the functional roles of these subsets, as M1 macrophages need to act quickly in response to acute infections whereas M2 macrophages patrol tissues over longer periods carrying out tasks such as tissue remodelling and repair. M1 macrophages therefore utilise an anaerobic glycolytic pathway which enables these cells to quickly generate energy in the hypoxic tissue environment.[44] To provide sustained energy, M2 cells use oxidative glucose metabolism to deal with the long term demands of tissue repair.[40] Macrophages also use iron metabolism to contain infections and aid tissue repair, for example, M1 macrophages express higher levels of ferritin in order to remove iron, an essential mineral for bacterial growth, from the microenvironment.[45] Alternatively, M2 cells express high levels of ferroportin which acts to promote cell growth by secreting iron into the microenvironment, aiding the M2-tissue repair paradigm.[45] Interestingly, macrophages play a role in the immune regulation at the fetal-mother interface in the placenta.[46] Here, macrophages exhibit an immunosuppressive role with an M2-like phenotype in order to prevent rejection of the foetus as a foreign body;

M2 cells also interact with NK cells and induce regulatory T cells (T_{reg}s) and so most likely have a role in remodelling the vascular interface.[40,47]

1.2.1 Monocyte and Macrophage Role in Pathology

1.2.1.1 Inflammation and Liver Fibrosis

Inflammation is an immune response to detection of pathogens or to injury. The process involves the innate immune system engulfing pathogens *via* phagocytosis, the release of powerful lytic enzymes and chemical free radicals, such as ROS.[11] This is part of a normal functioning immune system in response to an environment which is constantly presenting a pathogenic threat to the organism.[10] This response can unfortunately result in damage to surrounding cells and tissues as many of the innate immunity's defence mechanisms are non-specific.[10] Many diseases are partially or predominantly caused by chronic inflammation, these include atherosclerosis, rheumatoid arthritis, cancer and organ failure caused by fibrosis. As monocytes and their more advanced progeny, macrophages, have large phenotypical variety, these subsets often have multiple and sometimes opposing roles in inflammatory conditions.[2]

Fibrosis is a result of chronic inflammation leading to the formation of excessive scar tissue, nodule formation and, in the case of liver fibrosis, altered hepatic function (see Figure 1.4).[3] When tissue is damaged by inflammation, fibroblasts secrete extracellular matrix (ECM) proteins (mostly type I and III collagens) and if this area is regularly damaged the ECM develops into scar tissue.[3] Tissues eventually become fibrotic over time, this is life-threatening in the case of liver cirrhosis which is a end-stage outcome of disease such as alcoholics liver disease (ALD) and non-alcoholics fatty liver disease (NAFLD). The liver has a unparalleled ability to regenerate in a short amount of time and there is some evidence that even late-stage fibrosis is reversable; this creates a need to develop novel anti-inflammatories to stop fibrogenesis and anti-fibrotics to aid regression.[4]

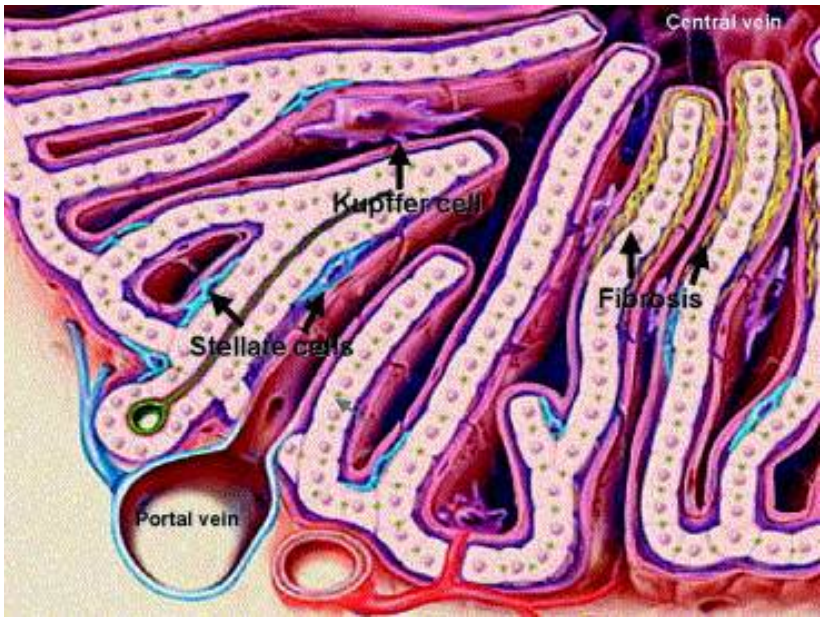

Figure 1.4: Sinusoidal cross-sectional diagram of the liver, showing hepatic stellate cells (blue, responsible for collagen secretion pathologically in fibrosis). Hepatocytes are arranged in cords surrounded by a fenestrated endothelial lining. Macrophages (purple) patrol the intervening space and can activate stellate cells to produce collagen, leading to fibrosis. Reproduced with permission from Piast *et al.*[48]

Monocytes and macrophages have been shown to facilitate an integral role in the progression and also resolution of liver fibrosis. Monocytes and macrophages can non-specifically damage surrounding liver tissue in inflammation, again triggering collagen deposition as part of the wound healing process.[3,49] The 'tissue-repair' M2 macrophages on the other hand can be both fibrogenic, through excessive deposition of collagen and fibrolytic through anti-inflammatory functions.[4] For example, fibrolytic macrophages in murine liver have been shown to be derived from circulating $Ly6C^+$ monocytes (inflammatory murine blood monocytes) transmigrate and differentiate into $Ly6C^-$ macrophages, expressing high amounts of matrix metalloprotease (MMP).[50] Furthermore, evidence of the detrimental effects of M1 polarisation in the liver in the context of NAFLD and protective effects of M2 macrophages provide a strong driving force for subset specific therapeutic development in certain disease states.[51]

1.2.1.2 Tumour-Associated Macrophages

The tumour micro-environment contains many cell types which are involved in the progression and lifecycle of the tumour; tumour associated macrophages (TAMs) are descended from monocytes which have been 'captured' by the tumour to facilitate tumourigenesis.[52] Blood monocytes are more likely to be activated towards an M2 phenotype in the tumour microenvironment due to hypoxic conditions and T_h2 cytokines such as IL-10. Interestingly, the monocytes are recruited to the tumour site by inflammatory cytokines where the cells then experience T_h2 immunoregulatory signals to progress into the TAM phenotype.[52,53] Circulating blood monocytes are recruited *via* CCL2, whereby the monocytes transmigrate across the endothelium into the tumour microenvironment. This has been demonstrated by CCL2 expression levels in tumuors correlating with the increased influx of monocytes to the tumour.[52,54] TAMs support the tumour as they do not present cytotoxic activity towards tumour cells, they produce growth factors towards cancer and endothelial cells (ECs) and also have immunosuppressive functions.[55,56] Further studies have revealed a central role of macrophages in the angiogenic switch of abnormal cells into a malignant tumour, and this effect is reversed in mice lacking the key macrophage growth factor, colony-stimulating factor - 1 (CSF-1).[57] Macrophage heterogeneity also translates into TAMs where considerable TAM phenotypical variety exists, with phenotypical modulations having a role in tumour metastatic progression.[58] This modulation typically ends with TGF-β production by the tumour leading to M2 polarisation in a tumour-promoting direction.[59]

1.2.1.3 Myeloid-Derived Suppressor Cells

Monocytes have further responsibility for pathogenesis through their link to immature myeloid cells which have been identified as having a role in many dieases, although most notably in cancer. In the steady state, these immature myeloid cells (IMCs) quickly develop into mature granulocytes, monocytes or dendritic cells (Figure 1.5). However, in cancer for example, IMCs are expanded *via* blockage of the natural differentiation pathway.[60] These cells have

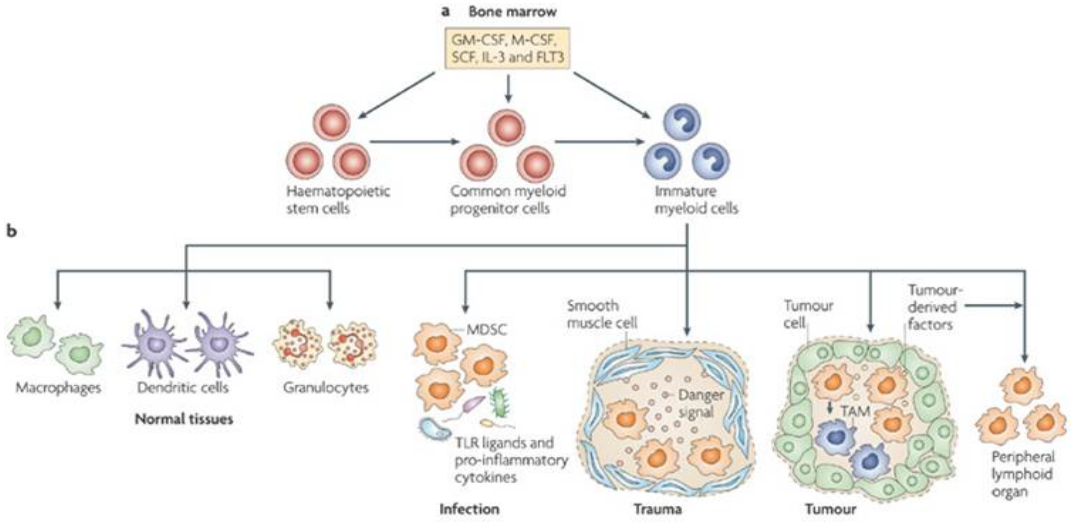

Figure 1.5: Hematopoietic stem cells begin in the bone marrow and upon exposure to differentiating cytokines and growth factors (such as GM-CSF, macrophage colony-stimulating factor (M-CSF), SCF, IL-3 and FLT3), these cells progress into immature myeloid cells (a). The immature myeloid cells enter the peripheral blood as monocytes or granulocytes before transmigrating into normal tissues and differentiating into macrophages, dendritic cells or other granolucytes. In some disease associated microenvironments the immature myeloid cells can differentiate towards disease causing phenotypes such as MDSCs in infection, trauma and cancer, or towards TAMs (b). Reproduced with permission from Gabrilovich *et al.*[60]

immunosuppresive functions and represent a heterogeneous population of myeloid cells, some with granulocytic and some with monocytic morphology.[61] Interestingly, human MDSCs do not express typical monocyte markers such as CD14 which reflects the immaturity of these cells, instead, they are defined as $CD14^{-}CD11b^{+}CD33^{+}$ cells which have also been shown to express CCR2.[60,62–64] MDSC subsets have been identified in various roles, such as in infection, trauma responses, in the tumour environment and in lymphoid tissues; factors produced by inflammation and tumours prevent MDSC differentiation leading to pathogenesis.[60,65,66] The expansion of the MDSC population in response to cancer can be tenfold, as has been demonstrated in murine studies, and these cells have a strong ability to inhibit T cell proliferation, aiding tumour growth.[60,67] The mechanism by which MDSCs suppress T cell activity in disease is thought to be *via* arginine metabolism through both iNOS and arginase 1.[62,68] This leads to an arginine shortage in the MDSC microenvironment which has been linked to a reduction in T cell proliferation and also an increase in T cell apoptosis.[69,70] Therapeutic strategies include initiation of MDSC differentiation into more mature myeloid cells, inhibi-

tion of immunosuppressive pathways and direct elimination of MDSCs.[60,71–73] Development of tools that can help understand MDSCs *in vivo* function are needed, as well as targeted therapeutics.

1.2.2 Classical, Intermediate and Non-classical Monocytes

Monocytes were previously delineated through functional phenotypes such as pro- or anti-inflammatory. This arose due to experiments performed in mice which discovered differential expression of the inflammatory surface marker Ly6C (GR1).[10] Human monocytes, however, have increased heterogeneity from this murine model in the form of relative expression of CD14 and CD16. The inflammatory classifications in mice can be unhelpful as there can be a significant amount of functional crossover of these broad subsets. It was therefore decided in 2008 to refer to only three types of human monocyte based on CD surface receptor expression: classical, intermediate and non-classical monocytes.[8] **??** highlights the CD receptors used for distinguishing these subsets; it is based on relative expression of CD14 and CD16. Murine monocyte subsets are also listed which highlights the homology between the species, however the species have some functional differences which has confused some of the literature. For example, it was previously suggested that classical and intermediate monocytes resemble mouse Ly6C$^+$ inflammatory monocytes and the non-classical monocytes resemble the anti-inflammatory Ly6C$^-$ mouse monocytes.[8] However, much research has revealed the non-classical monocytes can be pro-inflammatory but through distinct mechanisms to both murine and human subsets.[10]

The major function of the CD14 marker is in LPS binding as part of the innate immune system and so any cell that presents this marker is identified as a monocyte. A subset of cells that also express CD16 (an Fc receptor for antibody-dependent cell-mediated cytotoxicity) were later identified as a class of monocytes with distinct functional behaviours from ordinary CD14$^+$ monocytes.[75] Classical monocytes are able to phagocytose erythrocytes and are greatly adherent to surfaces, however, the CD16$^+$ subset was found unable to effectively

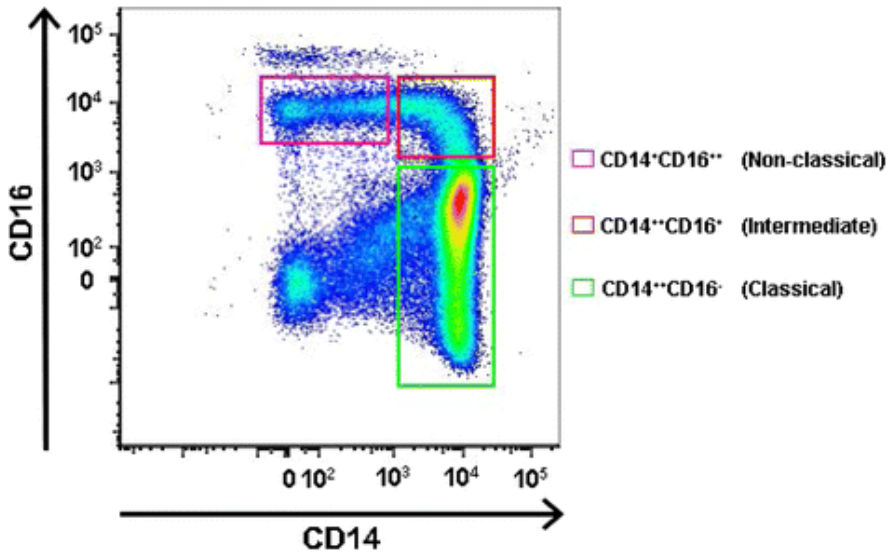

Figure 1.6: Monoclonal antibody labelling of CD14 and CD16 reveals three populations of monocyte displaying a characteristic overall "banana" shape.[74] The $CD14^+$ cells and the $CD14^-$ $CD16^+$ also differ in size, with $CD14^-$ $CD16^+$ monocytes generally being smaller in size (13-18 um) than the larger $CD14^+$ monocytes. Reproduced under a Creative Commons licence from Stansfield *et al.*[74]

phagocytose erythrocytes, were largely non-adherent and express higher levels of MHC class II complex for antigen presentation.

Following on from this research, the $CD16^+$ population was further divided into two subsets which now make up the aforementioned non-classical and intermediate monocytes.[76] In flow cytometric analysis the three monocyte subsets exhibit a "banana" shaped distribution with respect to CD14/CD16 expression; Figure 1.6 shows this labeling strategy and highlights the three subsets. Interestingly, this distinctive distribution may actually show a progression of the classical monocyte differentiating to a non-classical monocyte, with the intermediate subset acting as a bridging population.[77] For example, a phase I clinical trial investigating the effects of M-CSF and interferon on monocytosis found that classical monocytes were present at the beginning, followed by mixtures of classical and intermediate at eight days post-treatment and finally, after fifteen days the population was almost entirely consistent of non-classical monocytes.[78] Transcriptional analysis of $CD16^+$ and $CD16^-$ monocytes established that $CD16^+$ monocytes represent a more advanced stage of immune cell and have more macrophage character, expressing adhesion molecule CL62L and chemokine receptors such as CX_3CR1.[79] $CD16^-$ monocytes possess more similarity to myeloid precursors, for ex-

ample, CCR2 expression and the lack of surface adhesion molecules. Futhermore, $CD16^+$ monocytes were found to be arrested by, and migrate towards, fractalkine (CX_3CL1) as an exclusive mechanism for $CD16^+$ monocyte recruitment.[80] A patient study also demonstrated similar phenotypic chemokine trafficking differences between the subsets; CCR2 expression was observed to be higher in classical and intermediate monocytes and low in non-classical monocytes.[9] This was reversed for CX_3CR1 expression with the classical monocytes expressing low levels and the intermediate and non-classical being high in CX_3CR1; this suggests a phenotypic switching as the monocytes progress through the subsets *via* the intermediate transitional subset. The distinct molecular recruitment mechanisms of monocyte subsets leads to potential for therapeutic development towards context specific disease states.

Further evidence suggestive of phenotypic progression from classical to non-classical monocytes stems from surface marker expression of the intermediate monocytes residing at levels between the extremes of classical and non-classical (See **??**).[10,81] Studies by Geissman et al. have highlighted functional differences between the subsets and also provide more evidence for the transitional nature of the intermediate monocyte.[82] Efforts to draw functional homologs between human and murine monocyte subsets were undertaken in that human classical and intermediate monocytes resembled murine "pro-inflammatory" monocytes. Indeed, like their murine counterparts, classical and intermediate monocytes both were unable to attach to the endothelium of blood vessels nor exhibit any crawling behaviour. The $CD14^-CD16^+$ population however, quickly attached and crawled along the endothelium akin to Ly6Clo monocytes. The classical and intermediate monocytes were also found to differ in inflammatory function; $CD14^+CD16^-$ easily phagocytosed latex beads and released ROS in response to bacterial stimuli, the double positive intermediate cells did not reflect this behaviour. The various behaviours and cytokine/chemokine production of monocyte subsets found in this study are summarised in Table 1.1.[82] This study also highlighted why grouping subsets functionally can be unhelpful, for example, non-classical monocytes did not exhibit pro-inflammatory behaviours in response to bacterial cues (ROS production, phagocytosis) and even exhibited some anti-inflammatory behaviour (IL-1 receptor antagonism). However, in response to vi-

ral nucleic acid detection non-classical monocytes exhibited distinct inflammatory cytokine production. These findings suggest that the multiple subsets have independent roles in the clearance of pathogens rather than a 'pro' or 'anti' inflammatory phenotype.

The trafficking and development of the human monocyte subsets is now widely accepted to originate from the bone marrow as classical $CD14^{++}$ monocytes before differentiating into intermediate, and non-classical monocytes in blood circulation (Figure 1.7).[10,83] The behaviours of the monocyte subsets then become quite different; classical and intermediate monocytes function together by invading tissues through CCL2/CCR2 signalling and/or CCL5/CCR5 signalling *via* a VLA-1/VCAM-1 dependent manner. The non-classical monocytes do not circulate as the other subsets, instead they patrol the vessel wall for long periods and only transmigrate in response to CX_3CR1/CX_3CL1 activation in a lymphocyte functional antigen 1 (LFA-1)/intercellular adhesion molecule 1 (ICAM-1)-dependent manner.[10]

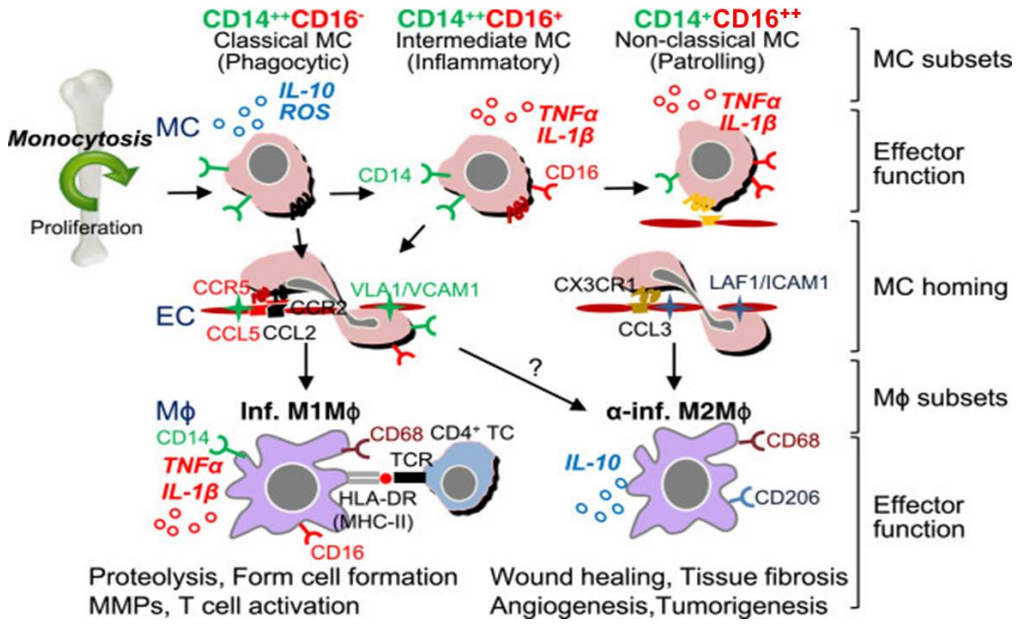

Figure 1.7: Classical monocytes exit the bone marrow in a CCR2 dependent manner and enter the bloodstream. The classical monocytes can be recruited into tissues by CCL2/CCR2 and/or CCL5/CCR5 signalling or this subset transitions to intermediate monocytes; this subset can undergo tissue invasion by the same mechanisms as their classical counterparts. The intermediate monocytes can also transition into non-classical monocytes which proceed to patrol the vessel wall. These cells transmigrate *via* CX_3CL1/CX_3CR1 signalling. Post-transmigration, the classical and intermediate monocytes differentiate into M1 macrophages (inflammatory), non-classical monocytes differentiate into M2 macrophages (anti-inflammatory). It is speculated that the classical and intermediate monocytes can also differentiate into M2 macrophages. MC - monocyte, endothelial cell (EC), TC - T cell, Mϕ. Reproduced with permission from Yang *et al.*[10]

Table 1.1: Comparison of functional behaviour and cytokine/chemokine production across the three monocyte subsets.[82] This research highlights the differing roles the subsets can play, with non-classical monocytes exhibiting both pro-inflammatory (unique TLR7-TLR8-MYD88-MAP2K dependent pathway) and anti-inflammatory IL-1 antagonism. Adapted from Cros *et al.*[82]

	Classical $\mathbf{CD14^{+}CD16^{-}}$	**Intermediate** $\mathbf{CD14^{+}CD16^{+}}$	**Non-classical** $\mathbf{CD14^{dim}CD16^{+}}$
Endothelium patrolling	no	no	yes
Phagocytose beads	high	high	low
ROS production	high	none	none
TNF-α	none	high	low
IL-1β	low	high	high
CCR2	high	med	low
IL-10	high	med	none
IL-8	high	med	low
IL-6	high	high	low
CCL3	high	high	low
IL-1 receptor antagonist	none	low	high

1.2.2.1 Diseases Associated with Monocyte Subsets

Many diseases have been associated with monocytes and their subsets, interestingly, expansion of the CD16$^+$ populations are often observed in response to these diseases or infections.[84] Generally, the intermediate subset is expanded, often with expansion of the non-classical subset as well and diseases include sepsis, tuberculosis (TB), hepatitis B and C, and auto-immune diseases.[84–90] This expansion of the intermediate subset was often accompanied by a reduction in classical populations, suggesting a progression of the classical monocytes towards the intermediate monocytes.[84,90]

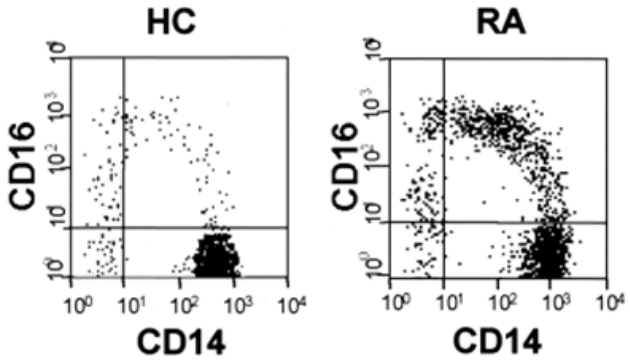

Figure 1.8: Flow cytometric analysis of CD14 and CD16 in RA patients' monocytes compared with healthy control groups. A clear increase in CD16$^+$ monocytes can be seen in RA patients with 32.8% of the dual-positive CD14/CD16 population of RA patients compared to 6.9% of healthy control patients; this suggests a role for CD16$^+$ monocytes in RA. Patients were grouped into rheumatoid arthritis (RA) or healthy control (HC) according to levels of C-reactive protein: active RA corresponding to CRP $\geq 30\ \mathrm{mg\,L^{-1}}$. Reproduced with permission from Kawanaka *et al.*[91]

In rheumatoid arthritis, CD14$^+$CD16$^+$ monocytes were shown to be expanded in patients with the active disease (Figure 1.8).[91,92] Interestingly, this population was depleted in response to RA therapy suggesting that treatment with glucocorticoids can actually selectively deplete this disease associated population.[93,94] A molecular mechanism for recruitment and/or expansion of the CD16$^+$ population has been suggested as a result of TGF-β (expressed in synovial fluid) induction of CD16$^+$ on monocytes.[95] However, it is unclear whether CD16$^+$ monocytes are recruited to the synovium in RA or the classical CD14^{++}CD16$^-$ monocytes migrate towards the inflamed site and differentiate into CD16$^+$ subsets in response to TGF-β.[96]

Atherosclerosis is a disease of the arterial wall where excessive amounts of lipids accumulate on the endothelium leading to coronary heart disease. Monocytes have been identified as contributing to the inflammation present around atherosclerotic plaques.[97] Two broad subsets of $CD16^+$ and $CD16^-$ were defined in this murine study which found that $CD16^-$ monocytes were dependent on CCR2 for recruitment at the introduced plaque but $CD16^+$ monocytes utilised CX_3CR1 for this purpose. Intermediate monocytes have been associated with low levels of the beneficial high-density lipoprotein (HDL) and high levels of the deleterious low-density lipoprotein (LDL).[98] Larger studies into coronary artery disease (CAD) have shown an increase in intermediate monocytes suggesting a broader role for this subset in CAD.[96] Again, whether this intermediate population is recruited to the plaques independently, or arrives as a classical monocyte before transitioning to the disease associated intermediate monocyte, is unclear. This provides an opportunity for further investigation of the phenotypical role in this disease and thus therapeutic development in a subset specific manner

Monocyte subsets have been identified in having diverse roles in liver fibrosis, in this organ, resident macrophages known as Kupffer cells are continually replenished by blood monocytes.[99,100] These populations are also modified to a great extent by infiltrating blood monocytes in response to liver injury.[101] A study into monocyte subset expansion in response to liver injury and the subsequent effect on liver fibrosis demonstrated that $CD14^+CD16^+$ monocytes were expanded in liver sections which were fibrotic.[99] This actually increased in a dose-dependent manner in terms of the progression from healthy, to fibrotic, to cirrhotic which correlated with a gradual increase in the intermediate/non-classical subset. These subsets were also found to exhibit increased production of pro-inflammatory cytokines such as TNF-α which leads to further recruitment of blood monocytes and potentially increased inflammatory cytokine production. Furthermore, $CD14^+CD16^+$ monocytes in patients with chronic liver disease were also found to be in a highly activated phenotype in terms of pro-inflammatory cytokine production relative to the same subset in healthy control patients. A difference in paracrine activity was also observed in the $CD14^+CD16^+$ subset as these cells

were shown to induce activation of hepatic stellate cells towards increased collagen deposition in *ex vivo* experiments, this behaviour was not observed in classical monocytes.[99] This fibrogenesis activation was most likely *via* TGF-β expression by $CD14^{+}CD16^{+}$ monocytes and this pro-inflammatory, pro-fibrogenic phenotype was associated with increased CCR2 expression on this subset.[99] Other murine studies complicate this issue as while liver macrophages are associated with liver fibrosis, these cells also play a key role in fibrosis regression.[102] In human livers, fibrotic diseases have been linked to an expansion of intrahepatic monocytes relative to healthy controls.[103] The authors suggest two mechanisms of intermediate monocyte recruitment in the liver: recruitment from blood, as this subset underwent higher transendothelial migration than classical monocytes, and differentiation in the liver from classical monocytes in response to TGF-β and IL-10. These intermediate monocytes were characterised by many pro-inflammatory and pro-fibrotic markers such as increased phagocytic activity, antigen presentation, and up-regulation of pro-inflammatory and pro-fibrogenic cytokines, such as TNF-α and CCL2. Intermediate monocytes therefore represent a key fibrogenic subset of monocytes which increases inflammation and progression of liver fibrosis.[103]

1.3 Chemokines and CCL2

1.3.1 Chemokine Structure, Function and Families

First identified in 1977, chemokines are small heparin-binding binding proteins which are structurally related to cytokines and are responsible for cell trafficking in a process called chemotaxis.[104,105] There are many different chemokines with around half as many chemokine receptors. Chemokines are generally small proteins with a molecular weight of around 8-12 kDa, containing four cysteine residues which are highly conserved across the chemokine family.[106] There are four classes of chemokine which are grouped according to the number of cysteine residues nearest the N-terminus and their location in the peptide sequence: CXC, CC, CX_3C and C (see Figure 1.9).[106] For example, 'CXC' refers to the two cysteines nearest the N-terminus separated by a single amino acid, whereas 'CC' refers to two adjacent cysteines nearest the N-terminus. Chemokines are secreted by many cell types to recruit monocytes, however, the chemokine receptors are mostly found only on leukocytes. The majority of chemokines are found dissolved in serum, though there are some exceptions such as CX_3CL1 (fractalkine) which is a membrane protein presented on the surface of ECs and is responsible for non-classical monocyte transmigration.[10] While chemokines are structurally related, even within sub-families, they are functionally diverse.

The three-dimensional structure of chemokines has three domains containing a highly flexible N-terminus which is held in place by disulfide bonds, a loop which extends around the molecule before entering three antiparallel β -pleated sheets and finally an α -helix that lies over the sheets; this arrangement is known as a 'Greek key' (Figure 1.10).[107] The sequence homology of chemokines ranges from highly conserved to varied but interestingly the three dimensional structure is relatively similar, regardless of the amino acid sequence differences.[108] Crystallographic and NMR studies have shown that chemokines exist as multimers in solution, with the majority being dimeric. The mode of dimerisation also separates into the subfamilies, for example, CXC chemokines dimerise along the edges of the first β -pleated sheet,

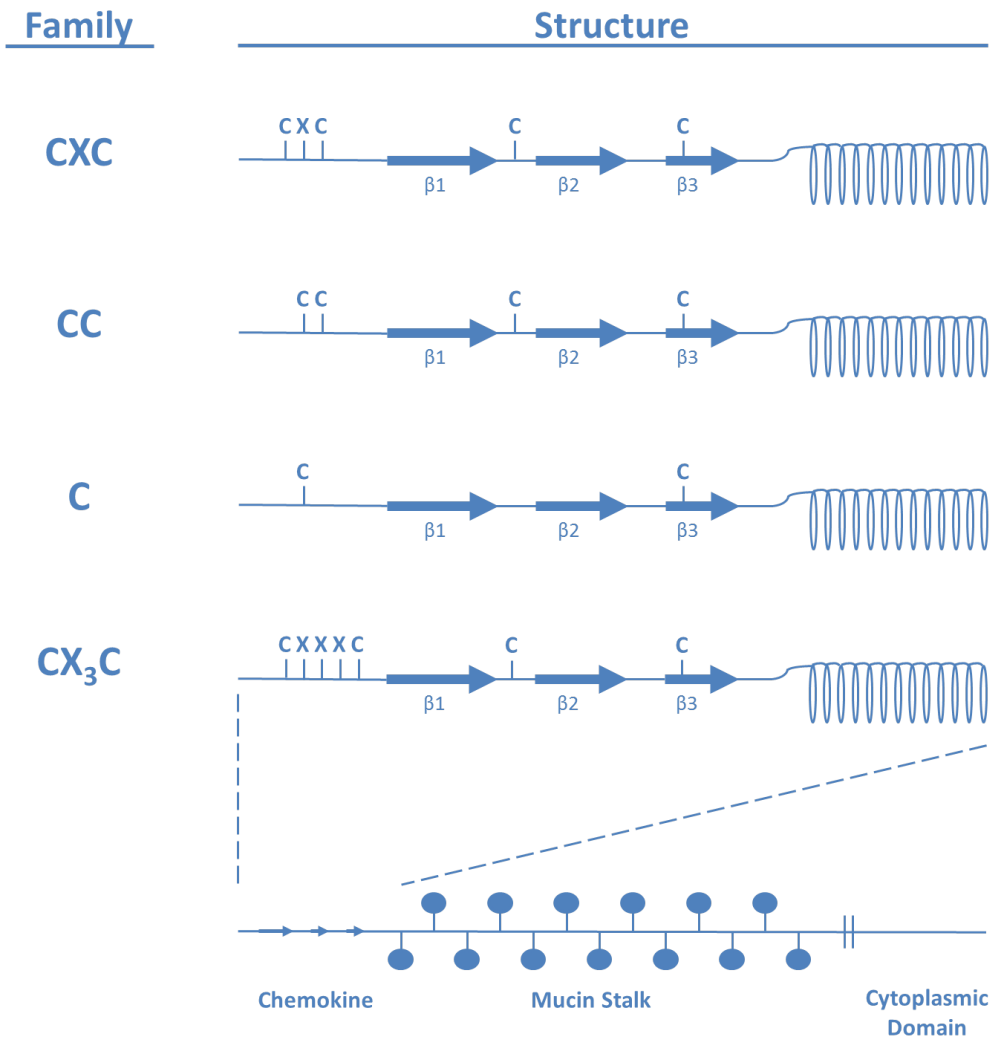

Figure 1.9: The four sub-families of chemokines and their overall defining structures. Each chemokine sub-family contains three β -pleated sheets and an α-helix at the C-terminus. Chemokines are grouped into the number of chemokines found proximally to the N-terminus, CXC, CC, C and CX_3C. The CXC chemokines have two cysteines separated by a single amino acid, CC chemokines have adjacent cysteine residues and the C chemokines have only one cysteine near the N-terminus. The CX_3C chemokines are different in that the cysteines are separated by three amino acids and also have a carbohydrate-rich mucin stalk, as well as a short cytoplasmic domain (being a membrane protein). Adapted from Rollins *et al.*[106]

resulting in a parallel arrangement of the molecules.[109] The CC chemokines, on the other hand, dimerise through interactions between short β sheets near the N-termini which gives a larger cylindrical structure than CXC dimers.[110] The importance of dimerisation for initiation of chemotaxis has been controversial although it would seem this is a prerequisite for signalling, either *in situ* dimerisation or upon interaction with glycosylaminoglycans (GAGs).[111] This dimerisation behaviour is variable across chemokines even from the same sub-family, for example, it was found that CCL2 and CCL8 exhibit strong heterodimerisation in NMR studies with a comparable reduction in homodimerisation. Interestingly, electrospray ionisation fourier transform ion cyclotron resonance mass spectrometry (ESI-FTICR) revealed that the glycosylaminoglycan Arixtra can greatly enhance the heterodimerisation ability of many of the CC chemokines (Figure 1.11).[111] It is speculated that heterodimerisation and GAG-heterodimerisation removes the redundancy of the CCR2 chemokines and is an important regulatory process in signalling.[112]

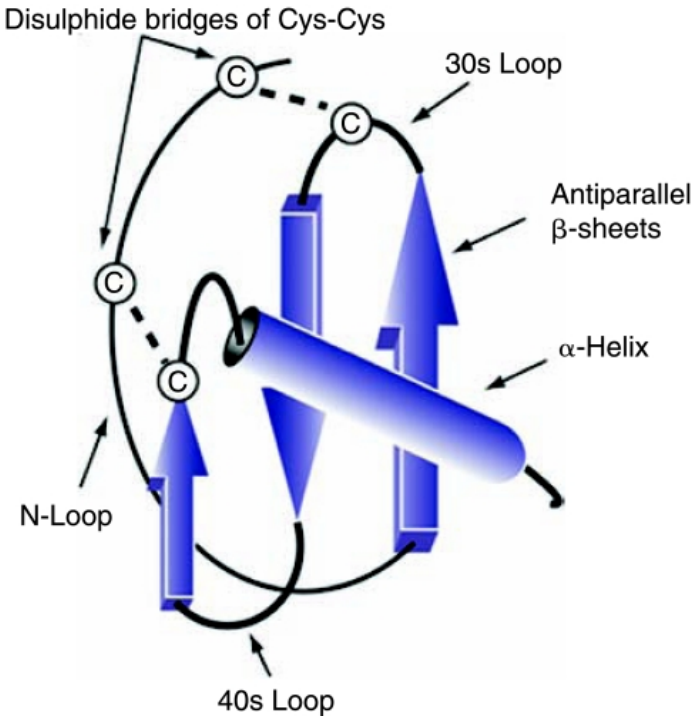

Figure 1.10: Schematic three-dimensional structure of chemokines showing the location of cysteines and the disulfide bridges which anchor the N-terminus to the the β -pleated sheets. Reproduced with permission from Deshmane *et al.*[104]

The N-terminal amino acid sequence has been shown to be crucial for homo and heterodimeri-

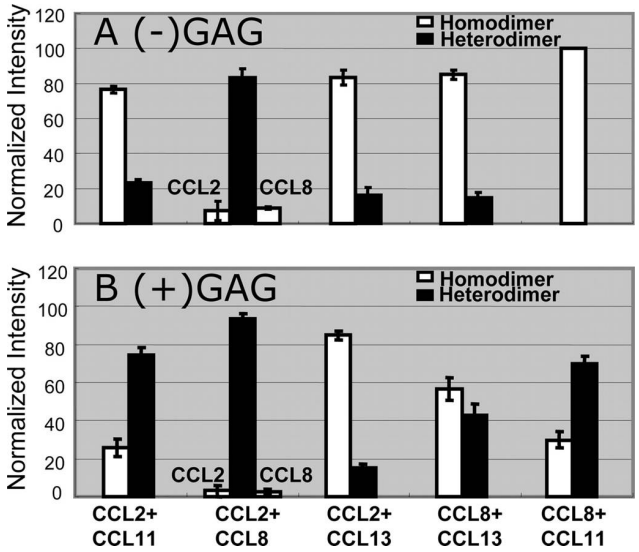

Figure 1.11: Relative abundances of CC chemokine homo- and heterodimers, measured *via* ESI-FTICR MS. Dimers found in the absence of Arixtra GAG are shown in A and dimers formed in the presence of Arixtra are shown in B. Generally, heterodimerisation is enhanced in the presence of GAG except in the case of CCL2-CCL13, of particular note is the effect on CCL8-CCL11 heterodimers where no heterodimers were observed in the absence of GAG but a dramatic increase was observed in teh presence of GAG. Reproduced with permission from Crown *et al.*[111]

sation of chemokines. In the CCR2 chemokines studied by Crown et al., five of the first ten amino acids in the sequence are identical and other studies have demonstrated that a proline at the 8-position is crucial for dimerisation.[111,113] In this study, a group of CCL2 variants were made including: Y13A, V9A, P8A, V9E and T10E; it was found that all constructs were still able to dimerise to varying extents except from P8A which was wholly monomeric. In this study and in others, the P8A construct has been shown to exhibit equimolar chemotactic activity to wild-type CCL2 in chemotaxis assays *in vitro* which provides strong evidence that CCL2 is able to bind and activate CCR2 as a monomer.[112,113] In the vascular space, flow conditions mean that generating a chemotactic gradient for cellular recruitment is impaired, resulting in the need for GAG-heterodimerisation in order to present a monomer of CCL2 for CCR2-binding and subsequent transmigration of the monocyte. In the extravascular space, fixed media allows a chemotactic gradient to be established and so monomeric CCL2 is able to recruit monocytes akin to the behaviour observed from mutant P8A CCL2 *in vitro.*[112] In a broader context, these distinct functional behaviours appear to have evolved to modulate signalling, for example, the CCR2 chemokine, CCL7, has a serine substitution at the proline-

8 position and does not dimerise on GAGs. On the other hand, CX_3CL1 is embedded in EC membranes in the vascular wall which recruits patrolling non-classical monocytes.[10,112]

1.3.2 CCL2-CCR2 Signalling Axis

CCL2 selectively binds the chemokine receptor CCR2 which initiates internalisation and a signalling cascade leading to monocytic cell recruitment *via* chemotaxis. CCR2 is a G protein-coupled receptor (GPCR) comprising of seven-transmembrane domains which are helical and have both intra- and extracellular loops.[114] The N-terminus and three loops are presented extracellularly and three intracellular loops with the C terminus are held in the cytoplasm.[114,115] The intracellular loops couple to heterotrimeric G-proteins which are bound *via* the G-α and G-β subunits, together forming a junction with the G-γ subunit (Figure 1.12).[116] Upon chemokine binding, G protein-coupled receptor kinases (GRKs) phosphorylate Ser and Thr residues on the intracellular loops and the C-terminus. This causes a conformational change in the G-protein subunits, leading to G-α uncoupling from the complex, giving rise to downstream signalling events. The G-$\beta\gamma$ complex also dissociates from the receptor and leads to further signalling. At this stage, continuous stimulation by ligand binding leads to receptor desensitisation and ultimately internalisation *via* β arrestin binding.[117] Endocytosis is initiated by β arrestin binding to the phosphorylated receptor, this then also binds adaptin-2 (AP-2), this complex then links with a clathrin lattice, giving rise to a clathrin-coated pit.[114,118] The receptor is then internalised in a clathrin-coated vesicle through cleavage from the membrane in a dynamin-dependent manner.[114,119] The internalised ligand-receptor complex then progresses into an early endosome which can then be recycled back to the surface for further ligand binding or is trafficked to lysosomes for receptor degradation (Figure 1.12).[114] The signalling pathways that lead to chemotaxis are not wholly understood but a number of molecules have been identified such as: mitogen activated protein kinase (MAPK), phosphatidylinositol-4,5-bisphosphate 3-kinase (PI3K), phosphoinositide phospholipase C (PLC)/protein kinase C (PKC) and gene expression through the JAK/STAT pathway (janus kinase (JAK) and signal transducer and activator of tran-

scription (STAT)).[120] The cell processes that follow these pathways include gene expression, cell polarisation and ultimately chemotaxis.

Clathrin-independent internalisation pathways have also been described, such as through lipid rafts/cavaeloe mechanisms but these are less well characterised than the typical clathrin mediated pathway.[114] Caveolin is a protein which is found in flask-shaped membrane invaginations that are also rich in lipids such as cholesterol and sphingomyelin.[114,116] Research into this internalisation pathway for chemokine receptors is limited, with only CCR5 and CXCR4 being identified in lipid rafts.[114] Post-internalisation, the receptor is held in a caveosome which can then fuse with early endosomes.[121] It has been suggested that caveolae mitigate compartmentalisation of chemokine signalling and may also contribute the rapid recycling of receptors back to the membrane for further agonist binding.[114,116] With respect to CCR2 internalisation, caveolin dependent pathways have been demonstrated in astrocytes, however, further research is needed into the prevalence of these pathways in monocytes.[122]

The chemokine receptors have been shown to amass at the leading edge of the cell during migration, which is thought to occur through receptor dimerisation and movement through the bilayer in lipid rafts.[120] GPCRs can exist as higher order oligomers and it has been reported that chemokine receptors utilise dimerisation to modulate functional responses.[115] The previously mentioned redundancy of chemokines may actually be part of a subtle refinement of response as receptor heterodimers have been shown to influence receptor specificity and subsequent signalling.[115,123] The aggregation state of chemokine receptors has actually been shown to influence the speed of response and the nature of the response itself (see Figure 1.13).[124] For example, calcium mobilisation is almost instantaneous upon ligand binding meaning that this likely occurs as the receptor exists as a monomer because dimerisation of large chemokine receptors is a relatively slow process. Elevation of the response then depends on G-$\beta\gamma$ subunit release, leading to PLC and PI3K activation.[124] Dimerisation does appear to be necessary for activation of the JAK-STAT pathway, which is a slower process.[124,125] Finally, receptor desensitisation and internalisation requires a critical mass of higher order oligomers, this recruitment is a much slower process often taking over 60 seconds. This pro-

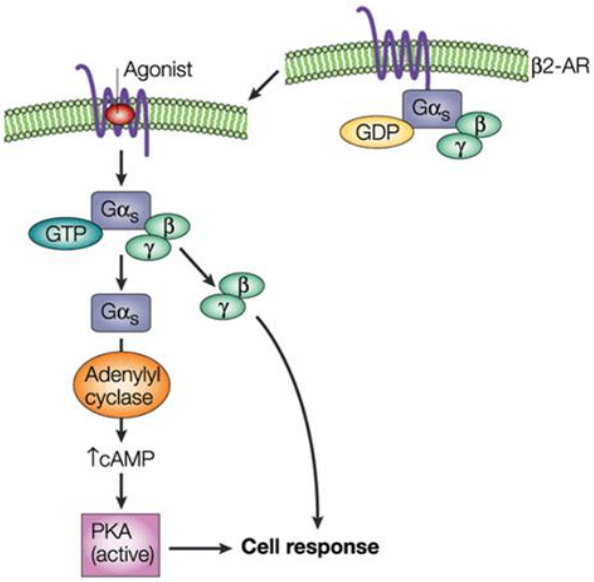

(a) Signalling pathways of 7TM GPCRs such as CCR2.[116]

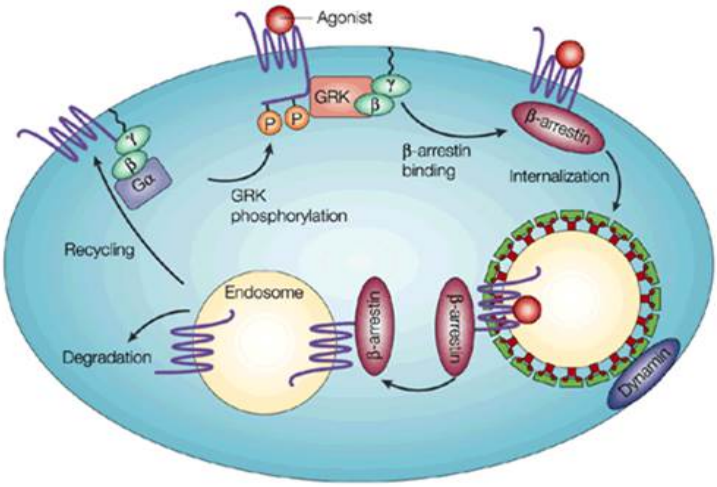

(b) Trafficking of activated 7TM receptors.[116]

Figure 1.12: In the steady state, 7TM receptors have a coupled heterotrimeric G-protein unit at the intracellular C-terminus, with a GDP bound to the α subunit (Figure 1.12a). Upon agonist activation, GTP binds the G-α subunit which dissociates and begins a signalling cascade through cAMP and PKA, leading to chemotaxis. Figure 1.12b shows how the receptor is trafficked post-activation; GRK phosphorylation of the receptor leads to recruitment of β -arrestin for subsequent clathrin-mediated endocytosis. The receptor complex is then either degraded in lysosomes or recycled back to the surface. Reproduced with permission from Pierce *et al.*[116]

cess is mitigated through receptor phosphorylation and subsequent arrestin binding which are both slow processes for which G-protein dissociation is a prerequisite.[124,126] However, much of this research has been performed on an array of chemokine receptors and some on other non-chemokine 7TM receptors meaning the consensus is not complete.

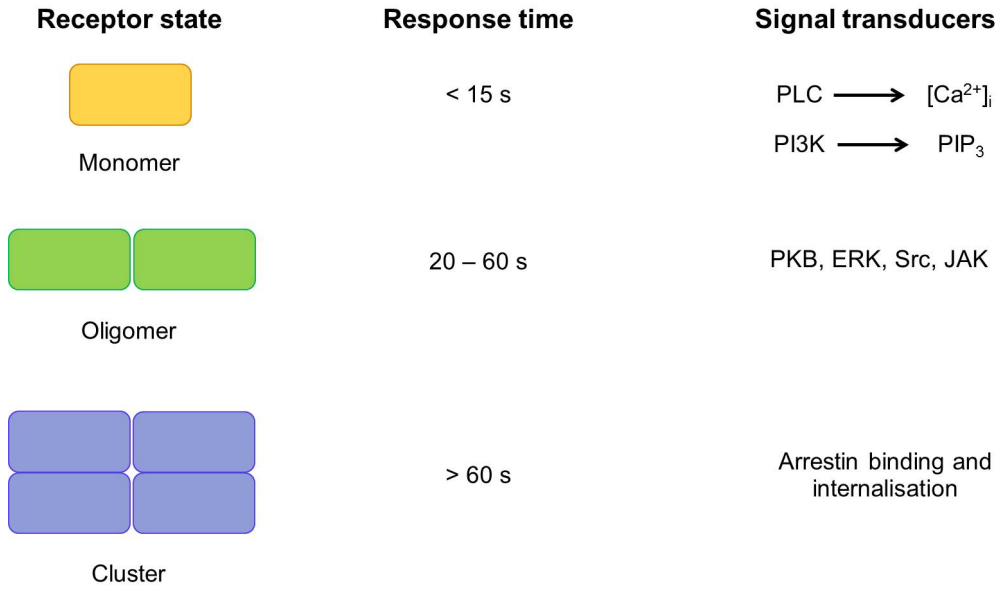

Figure 1.13: Chemokine receptor states and association with response times and signal transduction pathways. Calcium flux and PIP_3 mobilisation are near instantaneous after ligand binding and so occur through monomeric receptors (due to the lag period for receptor orientation for efficient dimerisation). Also, PI3K is directly activated by G-protein subunit release, which is a rapid process. It has also been demonstrated that dimerisation is necessary for JAK-STAT pathways, making this a slower signalling event.[125] Finally, higher order clusters form, with receptor desensitisation through receptor phosphorylation and subsequent arrestin binding; the clusters are then internalised. Adapted from Thelen 2001.[124]

1.3.2.1 Alternative CCL2 Receptors

A number of so-called, atypical chemokine receptors (ACKRs) have been identified which bind and often internalise chemokines but do not initiate the typical G-protein signalling cascade found in conventional chemokine receptors such as CCR2. The Duffy antigen receptor for chemokines (DARC) is an example of an ACKR, which is expressed on erythrocytes and some ECs, this receptor lacks any G-protein coupling motif and so it was initially thought to be a scavenger receptor for chemokines.[127,128] One function of DARC on red blood cells is to hold chemokines on the surface of the cell which acts to regulate chemokine concentrations in

the blood and therefore inflammatory responses.[129] DARC is thought to possess a sink and reservoir function, for example, when chemokines are released into serum they rapidly bind DARC on red blood cells (RBCs), the liver then depletes the concentration of chemokine resulting in release of DARC-bound chemokine back into the serum, equilibrating serum levels.[129] Another role for DARC is in the process of transendocytosis of chemokines to the luminal surface of some ECs.[129] Here, chemokines secreted in tissues are bound by basal DARC which is then migrated through the membrane, likely within lipid rafts, before being presented on the apical surface of the EC.[129,130] Varying chemokine ligands appear to lead to alternative DARC internalisation mechanisms in ECs. DARC has been shown to colocalise with CCL2 within endosomes containing caveolin, presumably this function has evolved to provide greater modulation of chemokines.[131–133]

Another atypical chemokine receptor which binds CCL2 is D6, also known as a scavenger receptor. This receptor is an interesting example due to its similarity to other chemokine receptors, sharing a heptahelical structure and around 60% similarity to the other chemokine receptors.[129,134] Where D6 differs from the typical chemokine receptors is in the C-terminus and a small deviation in the second intracellular loop which contains a DRYLAIV motif but in the case of D6 the motif is DKYLEIV.[129,134] The alterations in the C-terminus and the second intracellular loop render D6 incapable of typical G-protein signalling and therefore calcium flux or chemotactic function which has resulted in this receptor being denoted a silent scavenger.[135] The receptor is present on many cell types including lymphatic endothelial cells, leukocytes and hepatocytes.[129] As opposed to DARC, D6 does not have any transcytosis function in lymphatic endothelial cells, however it is capable of internalising ligand towards endosomal compartments.[136] Furthermore, the receptor has been shown to recycle back to the surface membrane in immortalised cell lines, and undergoes phosphorylation of the C-terminus and subsequent β-arrestin recruitment.[137] *In vitro* studies such as this and also D6 knockdown experiments demonstrate that chemokine ligands are not depleted in media by cells which also lack conventional chemokine receptors.[129] A large number of *in vivo* studies have highlighted an anti-inflammatory role for D6, as mice deificient in the receptor generally

exhibit a pronounced inflammatory response to injury relative to wild-type (WT) mice.[129]

1.3.3 The Function of CCL2 in Homeostasis and Pathology

CCL2 is thought to be largely responsible for recruiting classical monocytes from the bone marrow into the peripheral blood and from there, into tissues (Figure 1.14) *via* CCR2. CCL2 is a ubiquitously secreted protein upon activation by pro-inflammatory cytokines or direct stimulation *via* microbial molecules.[11] The role of CCL2 in influencing the immune response has been shown to also be mitigated through T cell immunity. For example, a number of studies related CCL2 expression with a polarised T_h2 response and also an enhanced production of IL-4.[104,138,139] The levels of CCL2 were highly increased in mouse models of granuloma and this effect was coincident with a switch from T_h1 to T_h2 responses.[138] Upon consideration of this evidence, it would appear that CCL2 is responsible for not only monocyte migration but also has a central role in adaptive immunity and subsequent inflammation.

1.3.3.1 CCL2 Role in Infection

CCL2 expression is associated with infections and inflammation, therefore it is necessary to understand the function of CCL2 is *in vivo*.[140,141] In a study of CCL2 deficient mice, responses to infection were initiated by injecting complete Freund's Adjuvant (CFA) and keyhole limpet hemocyanin (KLH) into the skin.[142] The numbers of circulating monocytes reaching the infection site were reduced on a number of days and this greatly affected monocyte numbers in the lymph nodes. This was due to the monocyte chemoattractant protein 1 (MCP-1) production at the infection site being transferred into the lymphatic system which was thought to aid antigen presentation in the lymph nodes. Therefore, CCL2 is responsible for initial recruitment to the infection site and then subsequent transfer to the lymph node. Intravital microscopy demonstrated that CCL2 deficiency impaired the ability of monocytes to arrest in the inflamed lymph nodes although it did not prevent rolling.[142] Interestingly, the CCL2/CCR2 axis can have positive and negative consequences for infection, for exam-

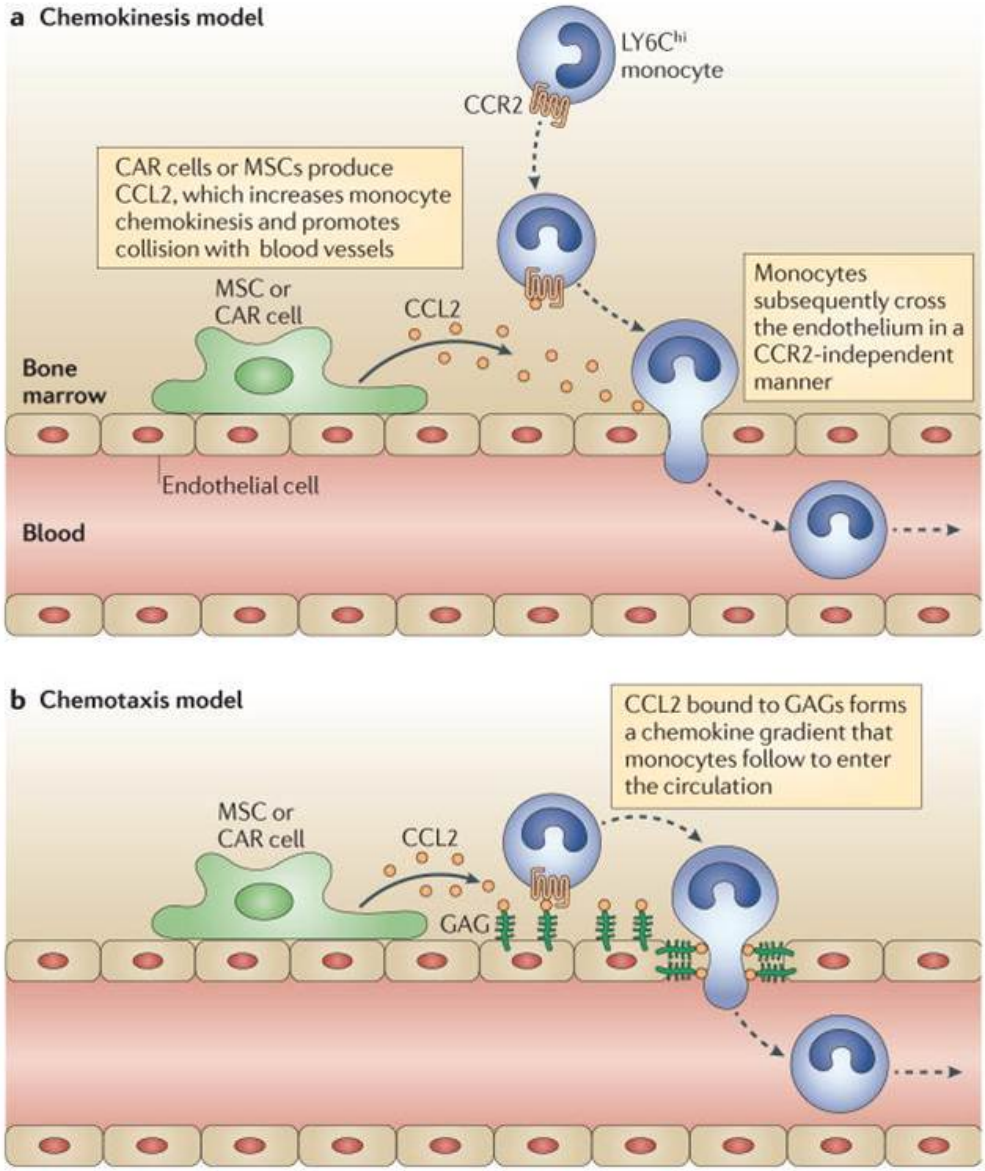

Figure 1.14: Two models of recruitment of monocytes into the peripheral blood from bone marrow: chemokinesis and chemotaxis. In the chemokinesis model, monocytes undergo greater movement which increases the probability of collision with blood vessels, the cells then cross the endothelium in a CCR2 independent manner (a). In the chemotaxis model, CCL2 binds to surface-bound GAGs which then initiates transmigration into the peripheral blood. It is thought that the latter model is particularly important in flow conditions, for example, for circulating monocytes to extravasate into tissues. Reproduced with permission from Shi *et al.*[11]

ple, in many bacterial infections CCR2 is responsible for both recruitment of monocytes to the infection and production of pro-inflammatory cellular responses, such as iNOS.[11] CCL2 has been identified in having a role in the previously discussed 'anticipatory inflammation' whereby monocytes are expanded according to circadian rhythmns; the circadian clock gene, Rev-erbα has been shown to modulate the function of macrophages by down-regulating the expression of CCL2.[143] In the case of *L. monocytogenes*, CCR2 deficiency led to a greater level of infection than wild-type mice; this behaviour was reflected in other studies involving CCL2 and CCL3 mediated recruitment of Ly6C$^+$ mice.[144,145] Other microbials such as influenza complicate the issue as CCR2-deficient mice generally lead to diminished recruitment of monocytes which actually lowered the mortality rate.[146] However, it was also found that CD8 T cell responses were not initiated leading to reduced clearance of the virus; CCL2 production was then partially inhibited leading to both lower mortality rates and an increase in pathogen clearance. This study was further validated by evidence that CCR2 is crucial for the recruitment of antigen-specific IFN-γ producing cells. This would suggest that CCR2-positive monocytes are responsible for linking the innate and adaptive immune responses.[147]

1.3.3.2 CCL2 Role in Inflammation and Liver Fibrosis

The CCL2/CCR2 axis also has a significant role in inflammation and many diseases caused by chronic inflammation. A role for CCL2 has been shown in cardiac fibrosis where CCL2 deficient mice were shown to have reduced numbers of infiltrating monocytes in response to being treated with pro-inflammatory cytokines.[148] Interestingly, not only was the extent of fibrosis lowered in CCL2 deficient mice but the absence of these monocytes led to greater breakdown of collagen in the heart by MMP-9. The effects of the loss of CCL2 were exhibited in a number of ways, including lowered pro-inflammatory cytokine production and the mitigation of T cell responses, suggesting a central role for CCL2 in inflammatory and fibrotic diseases. In other inflammatory diseases such as atherosclerosis, monocytes have been identified as having a central role in both progression and disease resolution through

subset-specific behaviour. In this context, CCL2 and CCR2 are both highly expressed around atherosclerotic plaques and the ligand can induce early atherosclerotic lesion formation.[149]

As discussed in section 1.2.1.1, liver fibrosis and eventual cirrhosis is a condition caused by chronic inflammation which leads to excessive collagen deposition and ultimately scarring. The CCL2/CCR2 axis has been identified as a key mediator of progression and even regression of fibrosis. In non-alcoholics fatty liver disease (NAFLD), serum levels of CCL2 were found to be significantly higher in sufferers of NAFLD, this also positively correlated with disease progression.[150] This complements the previously discussed research which indicated CCL2 is not only responsible for monocyte recruitment but also a potent initiator of inflammation across many cell types. Interestingly, CCR2-deficient obese mice have been shown to exhibit a reduced inflammatory profile and reduction in liver fibrosis compared with WT mice.[151] Mice deficient in CCR2 actually displayed a slightly lower propensity for obesity than WT and this was also reflected by lowered insulin resistance. Promotion of angiogenesis in liver fibrosis has also been linked with CCL2 in mice treated with a CCL2 inhibitor.[152] In this study, liver fibrosis was initiated by CCl_4 injury and surprisingly, inflammation did not seem to be affected, however the formation of new blood vessels was markedly reduced. Similar studies with other CCL2 inhibitors have found a reduction in murine inflammatory monocyte subsets towards injured liver tissues; this has also coincided with a decrease in cytokine production (such as IFN-γ).[153] CCL2 inhibition prevents the accumulation of $Gr1^+$ murine monocytes to the liver which actually enhanced regression of liver fibrosis, relative to uninhibited mice, suggesting potential for monocyte subset selectivity.[154] The authors speculated this was due to a shift in equilibria towards regenerative monocyte-derived macrophages as a result of reduced numbers of inflammatory monocyte-derived macrophages. This area is slightly controversial as restorative macrophages are known to differentiate from $Gr1^+$ monocytes, however, it is possible the restorative macrophages were derived from infiltrating $Gr1^-$ monocytes or expansion of endogenous macrophages.[154]

This complex role of monocytes/macrophages in liver fibrosis and the association with the CCL2/CCR2 axis was demonstrated by Gilgenkrantz et al.[155] The expression levels of many

pro-inflammatory cytokines were found to be significantly reduced in CCR2-deficient mice, such as CCL2, TNF-α IL-6 and IL-1β. Initially, liver fibrosis progressed to a lesser extent in CCR2 deficient mice, most likely due to a reduction in infiltrating inflammatory monocytes. However, resolution of the fibrosis was also reduced in CCR2-deficient mice compared to the wild-type mice which possessed the receptor. This suggests that the CCL2/CCR2 axis is responsible for both recruiting monocytes which lead to fibrosis but these monocytes then later aid in regression. Another interesting aspect of this work is that the initial fibrosis was not wholly reduced in CCR2-deficient mice; this is thought to be a result of the ligand CCL2 having two distinct modes of progressing fibrosis, namely the recruitment of monocytes and also the activation of fibrogenic hepatic stellate cells. This work suggests that a blanket approach on CCR2 inhibition is unlikely to be effective in the treatment of liver disease.

1.3.3.3 CCL2 Role in Cancer

Cancer is primarily a genetic disease in which many cancerous tumours can be traced back to a mutation or mis-regulation of a particular gene.[156] While the gene for CCL2 or the receptor CCR2 have not been directly identified as such, the central role of the CCL2/CCR2 axis in many host immunology activities means CCL2 can have multiple roles in the same tumour setting. This could be activation of anti-tumour responses in T cells, promoting growth or inhibiting growth, depending on the context (for example, CCL2 attracting cytotoxic immune cells whilst also activating angiogenesis). Anti-tumour properties of CCL2 have been described *in vivo*, these properties are a result of monocyte recruitment to the tumour site.[157,158]

The primary role for CCL2 in cancer, however, appears to be that of pro-tumour growth as evidenced by the numerous studies associating CCL2 with progression of many different cancers.[156] For example, breast cancer studies have revealed that high CCL2 levels in tumour biopsies are associated with a poor prognosis and significantly shorter relapse-free survival times.[160] One mechanism elucidated for this behaviour is that tumours express CCL2 in order

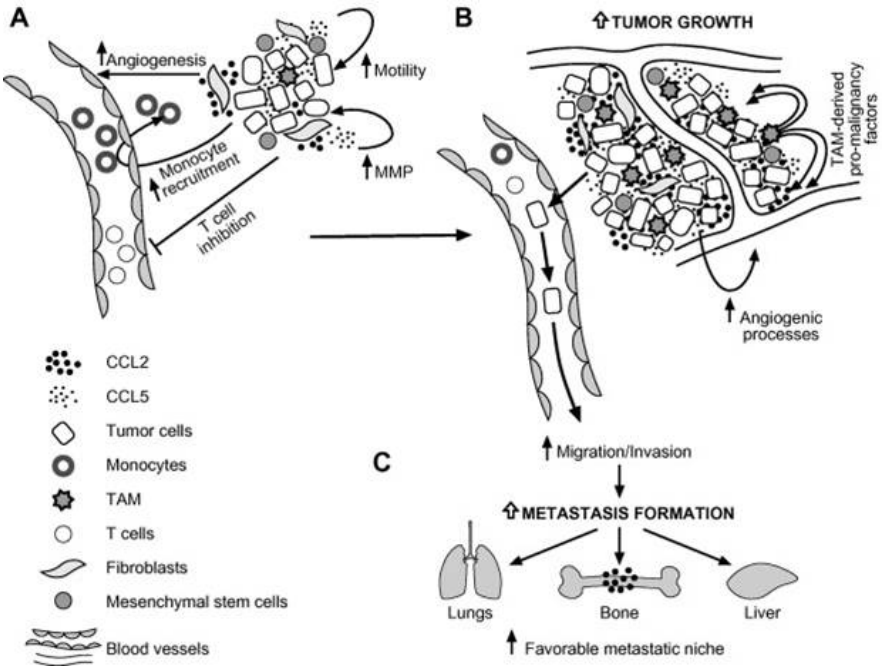

Figure 1.15: Possible pathways for CCL2 mediated malignancy in tumour growth. The tumour microenvironment releases CCL2 which recruits monocyte from the blood which then differentiate to a pro-tumour phenotype, such as a TAM (A). Angiogenesis is also stimulated by CCL2 production and TAMs begin matrix degradation allowing for vessel and tumour growth (B). Finally, CCL2 induce pro-metastatic factor production leading to metastatic cell egress from the tumour to other areas of the body (C). Reproduced with permission from Soria *et al.*[159]

to recruit monocytes to the tumour, this then leads to secretion of growth and angiogenic factors leading to cancer progression (see Figure 1.15).[156,161] TAMs begin as blood monocytes which are recruited to the tumour site and elicit immunosuppressive phenotypes; rises in CCL2 expression has been associated with increases in TAM numbers, which also coincides with poor prognosis in breast cancer.[162] Initially many studies indicated that CCL2 is responsible solely for the recruitment of cancer-progressing cells such as MDSCs, MSCs, and TAMs but more recently CCL2 is beginning to be shown to have a direct role in immunosuppression and tumour progression.[163–166] For example, a key pre-requisite of tumour growth is degradation of the ECM, CCL2 has been shown to promote MMP expression in monocytes, T cells and tumour cells.[159] In cancer metastasis, CCL2 has been shown to have an important role in the epithelial-to-mesenchymal transition (EMT) in which 'Snail' is a transcription factor that allows cancer cells to acquire mobility.[163] The study found that CCL2 is an effector molecule which directly enhances the metastatic potential of $Snail^+$ tumour cells. Stimulation of PBMCs with $Snail^+$ supernatant led to an increase in immunosuppressive T_{reg} cells and MDSC induction and this effect was prevented when the cells were also treated with CCL2-small interfering RNA (siRNA). This study implicitly identifies CCL2 as having multiple roles in tumour progression across a wide spectrum of cell types. Interestingly, another study using CCL2 antibodies in breast cancer also showed a reduction in metastases upon treatment but surprisingly when treatment was withdrawn prematurely, survival rates dramatically decreased relative to untreated mice.[167] This provides a warning of targeting the CCL2/CCR2 axis for cancer therapy as rebound effects can occur due to a boost of infiltrating monocytes which leads to angiogenesis, immunosuppression and metastasis.

1.3.4 CCL2/CCR2 Therapies and CCL2 Conjugates

Evidently the CCL2/CCR2 axis is an attractive target for therapeutic development and many inhibitors of this pathway have been developed. Generally, conventional small molecule antagonists of the receptor, CCR2, have been synthesised and a handful have undergone clinical trials; however, every CCR2 antagonist has either not been approved or is still in clinical tri-

als.[1] There are major and minor binding pockets in the extracellular surface of chemokine receptors (Figure 1.16b), generally chemokines will first be tethered to the receptor by interactions with both the major and minor binding pockets, benefiting from a number of strong supramolecular interactions (Figure 1.16a).[168] With the correct orientation the flexible N-terminus of the chemokine can insert into the helical bundle which initiates the conformational change in the receptor (Figure 1.17).[1,169] The importance of the flexible N-terminus in chemokines has been demonstrated by endogenous antagonists whereby N-terminal truncated chemokines are able to bind the receptor but are unable to activate signalling.[1] The majority of small molecule chemokine receptor antagonists are allosteric modulators which interact with the major/minor binding pockets but do not prevent agonist binding. Instead, these compounds stabilise the inactive receptor allowing the agonist to bind but preventing the agonist from inducing signalling.[1] A more recent strategy is antagonists that bind in the intracellular C-tail which allows agonist binding but prevents the C-tail from initiating signalling.[170]

In total, seven chemokine receptor antagonists have entered clinical trials, the majority are small molecule allosteric modulators but neutralising antibodies have also been reported.[1] A selection of small molecule antagonists are presented in Scheme 1.1, generally the compounds are basic, contain a cyclic amine and a substituted amide. The Merck candidate MK-0812 (**1**) exhibits a low half-maximal inhibitory concentration (IC_{50}) at 5 nM and was entered into phase II clinical trials for rheumatoid athritis and multiple sclerosis.[1,171] Unfortunately the candidate did not exhibit any significant therapeutic benefits relative to placebo and Merck has since ceased referencing the program.[1] Incyte has also generated a number of CCR2 antagonists, the most advanced of which is INCB 3284 (**2**), these compounds share a 3-aminopyrrolidine core and exhibit high potency at IC_{50} = 3.7 nM.[172] This compound progressed to phase II clinical trials for multiple sclerosis and lupus, however, no activity was observed in these trials.[172] Incyte also jointly developed a series with Pfizer, resulting in PF-4254196 (**3**) which is almost structurally identical to the Merck candidate **1**.[1,173]Johnson & Johnson developed a number of CCR antagonists, the leading CCR2 candidate JNJ-17166864

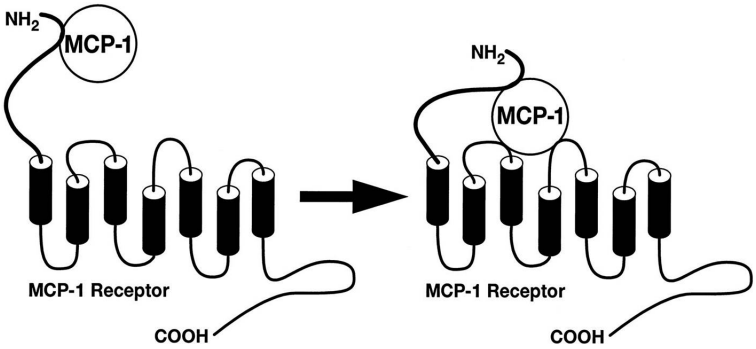

(a) Chemokine ligand tethering before signalling activation.[168]

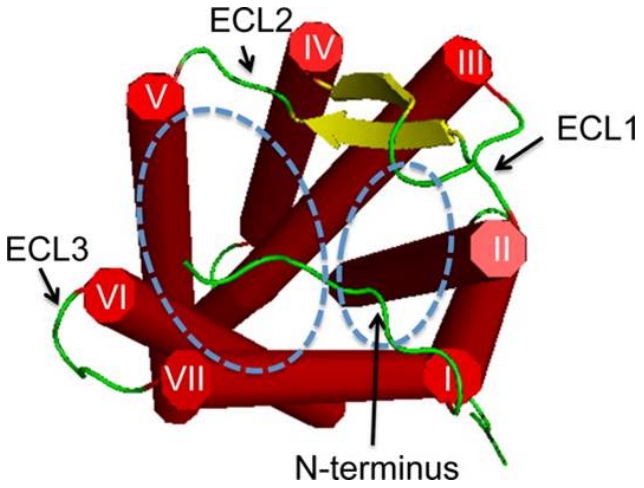

(b) Major and minor binding pockets of chemokine receptors.[1]

Figure 1.16: Receptor chimera and radioligand binding have demonstrated that N-terminal tethering of the receptor to CCL2 occurs through strong binding affinities (Figure 1.16a). The weaker affinity to the extracellular loops is then overcome through this initial tethering step which allows downstream signalling. The tethering step can be avoided with high agonist concentrations.[168] Figure 1.16b shows that chemokine receptors possess a major and minor binding pocket, whereby the flexible N-terminus of the ligand binds the major binding pocket followed by association with the extracellular loops of the receptor surrounding the minor binding pocket. Reproduced with permission from Pease *et al.*[1]

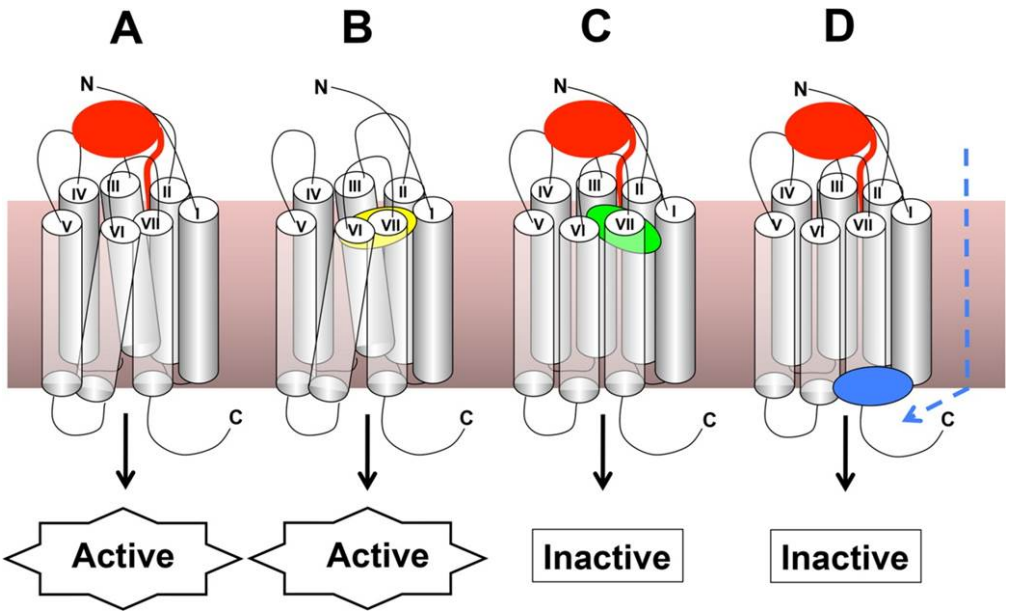

Figure 1.17: The binding states of chemokine receptors in response to varying binding molecules. A - chemokine. B - small mol agonist. C - Small mol. antagonist (allosteric). D - small mol. allosteric antagonist on intracellular loop. Reproduced with permission from Pease *et al.*[1]

(**4**) was modified from a previous CCR2/CCR5 antagonist through structure-activity relationship (SAR) studies to remove its potency for **CCR5!** (**CCR5!**).[174] The quaternary amine confers poor oral bioavailability meaning this candidate was dosed by nasal spray in an allergic rhinitis clinical trial but data was not released following this trial.[175]

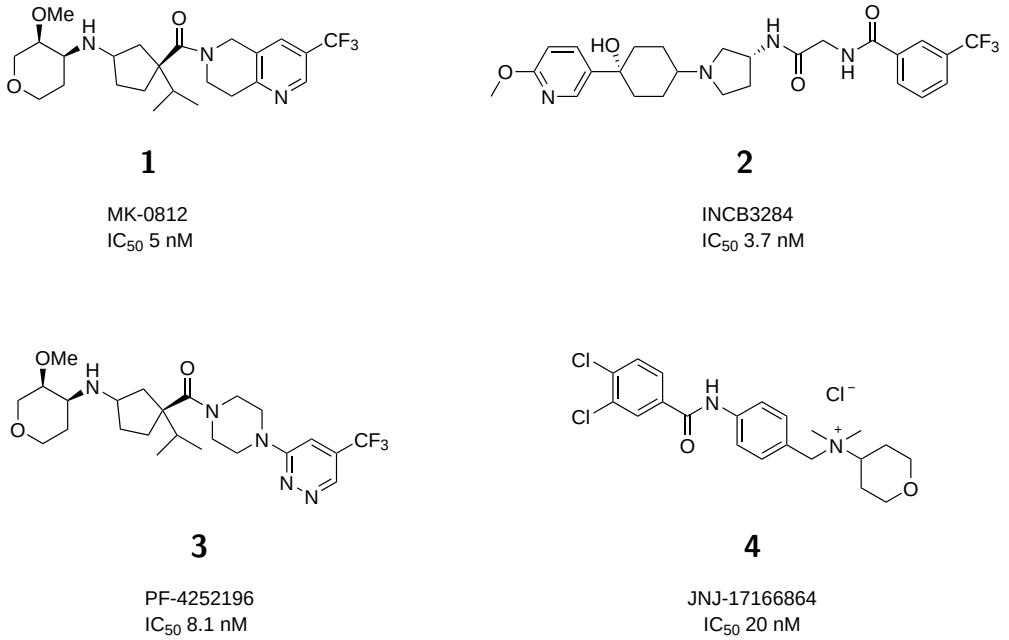

Scheme 1.1: A number of CCR2 antagonists that have entered clinical trials.[1]

A number of CCL2-neutralising antibodies have also been reported in the contexts of rheumatoid arthritis and cancer.[176] For example, in prostate cancer pre-clinical models have shown that anti-CCL2 therapies administered in combination with docetaxel led to reduced tumour burden and also tumour regression.[177] The authors reported previously to this study that bone marrow endothelial cells (BMECs) are a significant source of CCL2 and there is evidence this system encourages metastasis into bone marrow.[178] Therefore, CCL2 neutralising antibodies were administered to mice bearing prostate tumours which led to a 73% reduction in tumour burden after three weeks of treatment. When these agents were administered as a combination therapy the tumour burden was decreased to a greater extent than docetaxel alone and even had lasting effects after treatment was withdrawn.[177] These findings were echoed in another study whereby blockade of CCL2/CCL12 with antibodies was effective at reducing tumour volumes in a number of cancer lines when used in combination with $CD8^+$ T cell immunotherapy *in vivo*.[179] Previously, immunotherapy has been shown to be less effective against cancer than anticipated and a major reason for this is thought to be the immunosuppressive properties of CCL2, either through recruitment of immunosuppressive phenotypes of monocytes or direct polarisation of T cells towards immunosuppressive phenotypes.[179] Interestingly, this study found that combination of CCL2/CCL12 blockade with immunotherapy led to cure of cancer in 50% of subjects, however, whilst the number of activated $CD8^+$ T cells was increased, no effect on MDSCs was observed. It was also found that blockade of CCL2/CCL12 resulted in a proinflammatory tumour microenvironment with $\sim$2-fold greater concentrations of cytokines such as TNF-α and IFN-γ. In the case of glioma, however, a significant effect of MDSC and TAM recruitment has been observed in pre-clinical models of anti-CCL2 therapies, with anti-tumour effects particularly increased in combination with chemotherapies.[180]

Investigations into rheumatoid arthritis have not been as successful when utilising both CCL2 and CCR2 blocking antibodies. A moderately sized clinical study into the therapeutic effects of anti-CCL2 in patients suffering from RA showed that whilst treatment was well tolerated, no significant beneficial effects were observed.[181] Furthermore, another clinical study,

this time on CCR2-blocking antibodies, did show a reduction in recruited monocytes associated with RA but no reduction in synovial biomarkers nor any clinical improvement was observed.[182] Reasons for this have been provided by Tak et al. whereby CCR2 and CCR5 blocking antibodies do prevent CCL2/CCL5 mediated monocyte recruitment, it does not prevent recruitment *via* other pathways into the RA synovium.[183]

1.3.5 Existing CCL2 conjugates

A number of CCL2 conjugates have been prepared to allow either functional behaviour to be evaluated or in the development of novel therapeutics. One example of a fluorescent CCL2 conjugate was developed using protein expression to incorporate a fused mCherry fluorescent protein at the C-terminus of CCL2.[5] The authors demonstrated that the CCL2-mCherry conjugate exhibited similar potency in initiating chemotaxis and calcium mobilisation compared to wild-type (recombinant) CCL2. This is an interesting result as human CCL2 has a mass of ∼8 kDa and mCherry has a much larger mass of ∼30 kDa, meaning CCL2 is able to transport large moelcules with little effect on signalling or uptake. Live cell imaging also demonstrated that CCL2 is concentrated inside the cells and that monocytes are able migrate towards a concentration gradient of the conjugate, as well as being able to rapidly repolarise towards a moving source of chemokine (Figure 1.18). CCL2 is presumably degraded in lysosomes and the receptor is recycled back to the surface for further chemotaxis and ligand internalisation.[5] Further time-lapse experiments found that exposure of monocytes to the G-protein inhibitor pertussis toxin resulted in cessation of chemotaxis towards CCL2-mCherry however, fluorescence did increase over time suggesting coupling to G-proteins is not essential for fluorescence uptake.[5] The authors also showed that uptake was not *via* D6 scavenger receptors or pinocytosis, and continued to show that treatment with a small molecule CCR2 antagonist prevents both chemotaxis and fluorescence uptake. The findings presented in this study highlight the power of utilising functional fluorescent ligands to reveal information about chemokine signalling pathways which is difficult to achieve with conventional antibody methods.

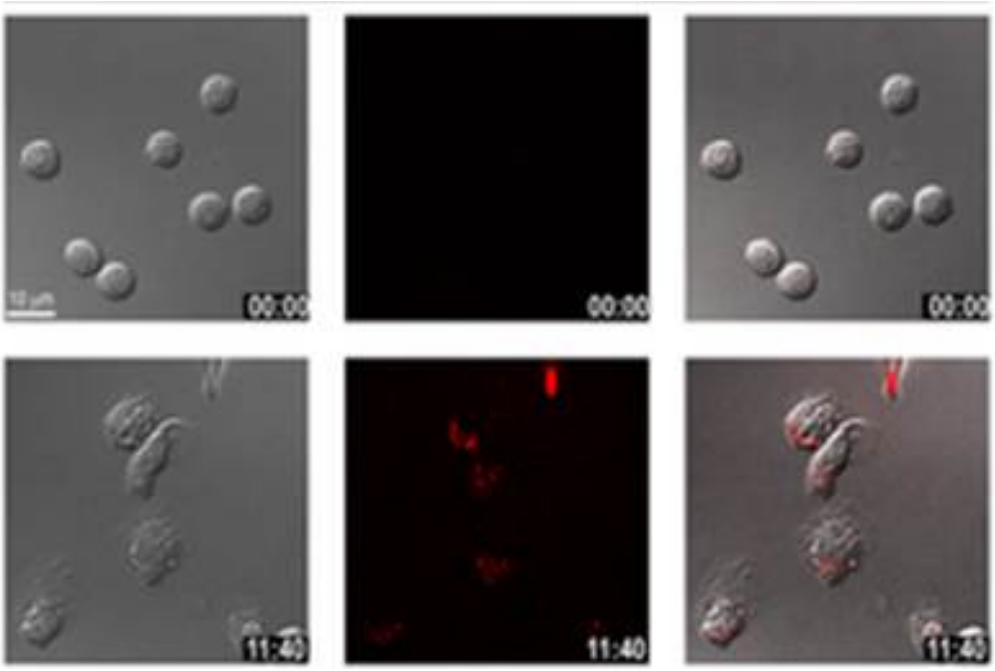

Figure 1.18: Time-lapse images of monocytes responding to CCL2-mCherry conjugates in a chemotactic manner. The chemokine was introduced by micropipette resulting in a dilution into media followed by re-concentration inside the monocytes. Monocytes can be seen projecting towards a concetration gradient of the conjugate and the cells also appear to localise internalised conjugate towards the luminal side of the migrating cell. Reproduced with permission from Volpe *et al.*[5]

An example of using chemokines to deliver therapeutics has been developed by Osprey Pharmaceuticals, whereby a truncated form of the *Shigella dysenteriae* holotoxin (SA1) was conjugated to CCL2 through recombinant protein fusion.[6] The CCL2-SA1 toxin induces cell death in any CCR2-bearing leukocyte, therefore a method for targeting specific subsets of many leukocytes (for example, classical and intermediate monocytes) has been developed. The SA1 toxin enzyme is a ribosome inactivating protein which prevents protein synthesis resulting in cell death; SA1 also depurinates DNA which initiates apoptosis.[6] The group showed that the CCL2-SA1 conjugate was internalised by monocytes bearing CCR2 and this uptake resulted in reduced protein synthesis and subsequent cell death. In a model of kidney nepropathy, this led to significant reductions of infiltrating monocytes/macrophages, reduced glomerular lesions and proteinuria. A non-native CCL2 variant was used (including an alanine addition at the N-terminus) but no chemotactic migration data was reported.[6] This CCL2-variant has been reported elsewhere to have reduced chemotactic potency relative to wild-type CCL2 and so it may have been the case the authors desired to modulate the

effective concentration of CCl2 to match that of the SA1 toxin. A number of conclusions can be drawn from this research: the relatively large SA1 enzyme is able to escape endosomes as the inhibitory function is dependent on cytoplasmic distribution, highly cytotoxic compounds can be safely administered to monocytes selectively *via* CCR2 internalisation.

The previously discussed CCL2 conjugates were both fused recombinantly expressed proteins, the issue with using these methodologies to develop CCL2 conjugates is that a new fusion protein must be engineered from first principles each time a new conjugate is desired; this is time-consuming, expensive and the types of molecules that can be conjugated are also limited to peptides. The peptide synthesis company, Almac Chemokines, synthesise a variety of fluorescently labeled chemokines *via* solid phase peptide synthesis (SPPS). A fluorescent CCL2 conjugate from Almac has been used by Graham *et al.* in the characterisation of atypical chemokine receptors, this study benefited from using a functional analogue of the ligand of interest rather than antibody labeling.[184] In an effort to develop a variety of chemoine conjugates, Handel *et al.* reported a general method for conjugating chemokines.[7] The method uses genetically encoded peptide tags that can be labeled using phosphopantetheinyl transferase enzymes (PPTases) which allows a specific serine to be substituted with a coenzyme A-fluorophore conjugate. This allows a variety of substrates to be used as long as the substrate can be synthesised with the coenzyme A tag. This strategy is shown in Scheme 1.2, including a 12-amino acid peptide as the S6 PPT tag which is then conjugated through a specific serine resulting in a phosphoester linkage to a fluorophore. The chemokine conjugate exhibited a around a ten-fold decrease in potency; the cause of this decrease is unclear and was not discussed.[7] The fluorescent chemokines produced also displayed GAG binding ability and allowed studies to investigate these interactions to be carried out.

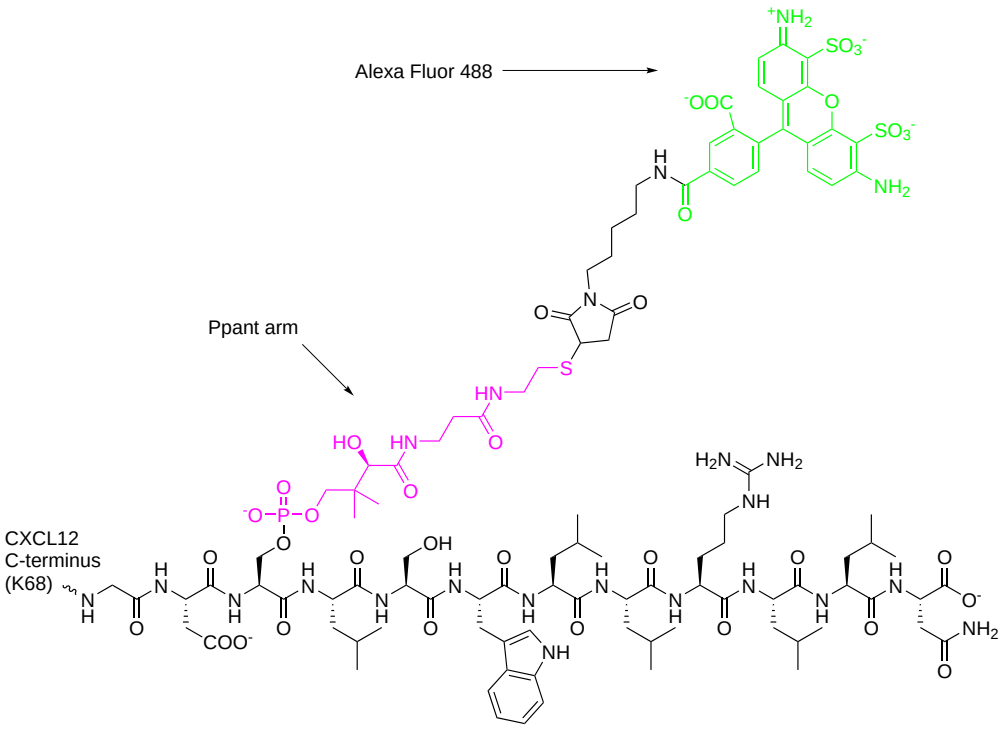

Scheme 1.2: Chemical structure of the PPT tag on the C-terminus of CXCL12 which also shows the conjugated coenzyme A-fluorophore label, which is conjugated through a phosphoester on a specific serine in the S6 PPT tag. Adapted from Kawamura *et al.*[7]

1.4 Peptide Formation and Conjugation Strategies

1.4.1 Fusion Proteins and Linkers

Protein conjugates are important in the development of targeted therapeutics and imaging agents to specific cell-types and one example is the use of recobinant fusion proteins. The proteins are usually separated by a linker peptide sequence which can take three forms: flexible, rigid or cleavable linkers, these act as spacers between the fused proteins and sometimes also provide functionality. The purpose of the linker can be crucial as direct fusion of the two desired proteins can lead to misfolding and poor yields of fused proteins in recombinant expression.[185,186] Flexible linkers allow greater movement and rotation of the fused proteins through the use of small amino acid residues which are stable in aqueous media and therefore do not greatly interact with the fused proteins.[185] Sequences usually employ repeating units of glycine, serine and threonine, the number of repeats allows the separation of the fused proteins to be modulated and the serine or threonine residues provide greater stability in water through hydrogen bonding networks. A common example of a flexible linker of this kind is $(GGGGS)_n$, where the integer n dictates the separation distance of the proteins.[185]

α-helical inducing sequences are used as rigid linkers which contain repeating alanine residues interrupted by glutamic acid or lysine and maintain spatial separation of fused proteins. The ability of rigid linkers which form α-helices to successfully separate fused proteins has been determined by Förster resonance energy transfer (FRET).[187] The sequence $A(EAAAK)_nA$ produced an α-helical structure which was further stabilised by lysine-glutamic acid salt bridges and was used between enhanced blue fluorescent protein (EBFP) and enhanced green fluorescent protein (EGFP). The repeats of the rigid linker sequence were then increased and the FRET signal was measured resulting in an inverse relationship between sequence repeats and FRET efficiency, indicating that fused proteins were separated.[187] Another type of rigid linker uses proline-rich sequences due to the cyclic nature of this amino acid conferring rigidity rather than formation of rigid secondary structures.[185]

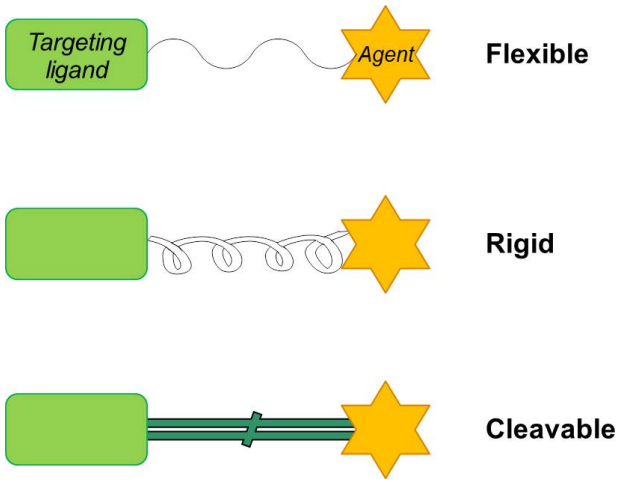

Figure 1.19: Types of fusion protein linkers between a targeting protein and an agent which can include fluorescent proteins or functional proteins. The flexible linkers allow the tethered proteins to freely translate and rotate, this can encourage the fused proteins to interact with each other which can be stabilising or destabilising. Some designs may require prevention of this interaction which can be achieved with rigid linkers, often based on α-helical linkers. Cleavable linkers can be flexible or rigid but are unstable under physiological or intracellular conditions, separating the fusion protein under specific conditions. Adapted from Chen *et al.*[185]

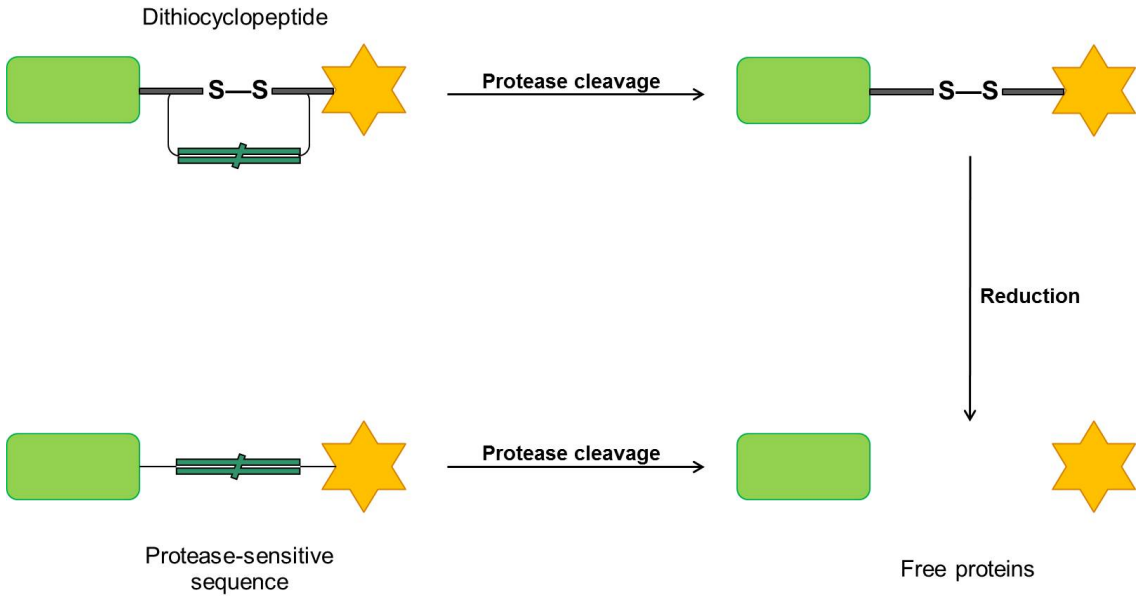

Figure 1.20: Methodology to produce a disulfide cleavable linker using fusion proteins synthesised *via* recombinant protein expression. An initial dithiocyclopeptide is formed with a protease-sensitive sequence, this is cleaved to reveal the disulfide linker which is reduced to finally separate the proteins in biological environments. The protease sensitive sequence is a simpler approach as no initial cleavage step is required before use, although this requires the biological enviornment being used to contain the relevant protease. Adapted from Chen *et al.*[185]

The presence of the fusion protein can affect function and so intracellular cleavable linkers have been developed which possess reasonable stability in plasma but instability inside a cell which allows the targetting protein to separate from the payload.[185] This results in decoupling of the metabolic and distributive fates of the fused proteins leading to enhanced bioactivity and increased cellular dispersion. A common strategy for an intracellular cleavable linker is the disulfide bond, this exploits the reductive environment found within cells which have relatively high concentrations of glutathione (1 mM) and other cysteine proteases, meaning that disulfide bonds are rapidly reduced, liberating the fused proteins.[188] In the case of recombinant fusion proteins, disulfide linkers are reasonably difficult to make as a cyclic peptide is used which contains a disulfide, the backbone of the oligopeptide is then hydrolysed using sequence specific proteases leaving the disulfide linker intact (**??**).[185] Thrombin sensitive dithiocyclopeptides (LEAG**C**KNFFPRSFTS**C**GSLE) are one method of preparing disulfide-linked fusion proteins.[189] The investigators successfully made the fusion protein and the disulfide linker was shown to reduce *in vivo*.

Other peptide cleavable linkers use sequences that help to target the fusion protein towards a specific area of the body or disease state. For example, MMPs are overexpressed in cancer and inflammation, some peptide linkers therefore contain sequences which are hydrolysed by MMPs such that the fusion protein is liberated at the desired disease site.[185] One such method is the use of latency-associated peptide (LAP) to insulate the active fused protein from degradation in the body or acting on sites away from the pathological site.[185] In one study, LAP was fused to IFN-β using an MMP-sensitive PLGLWA sequence flanked by flexible glycine rich oligopeptides, allowing the interferon to associate with LAP.[190] The half-life of the fused interferon was considerably longer than native interferon, dissociation of LAP from the interferon was then promoted at disease sites due to the specific MMP cleavage. Another strategy is to use peptide linkers which are not sensitive to endogenous enzymes but towards pathogen expressed proteases; *E. coli* using the MazE-MazF antitoxin-toxin system have been engineered to create a fusion protein separated by cleavable linker sequences sensitive to either human immunodeficiency virus (HIV) or hepatitis C virus (HCV)

proteases.[191]

1.4.2 Chemical Peptide Conjugation Strategies

Fusion proteins have been a powerful route to generate protein conjugates for imaging, therapeutic and functional applications and by modifying linker nature the *in vivo* activity of these conjugates can be modulated to suit the application. There are numerous drawbacks to this approach, however, the most obvious is that conjugate species are limited to peptides meaning that small molecule therapeutics, small molecule fluorophores, oligonucleotides and polymers are unavailable as conjugates with this strategy. Furthermore, each fusion protein must be *de novo* designed, a plasmid genetically engineered, and a modified organism manufactured which expresses the fusion protein for any slight modification in sequence or conjugate. The nature of the linker, while highly variable, is often designed computationally to have the desired property such as flexibility and there is no guarantee that this will be observed. The methods to produce certain species can also be convoluted such as disulfide linker formation from cyclopeptides. Chemical conjugations allow the linker and fluorophore/therapeutic chemistry to be performed before any need to include the protein.

Protein modification is most useful when a single species is obtained post-conjugation, this means chemo- and regioselectivity is a prerogative. This simplifies purification and allows for greater control over dosing and most likely the reliability of any results obtained. For example, carboxylic acids or reactive derivatives are often used as substrates for conjugation towards lysine side chains or other amines, as is the case in commercially available protein labelling kits. The high abundance of the lysine residue and other amines results in oligo-substitution of the protein with little control over the location of conjugation. This has a number of potentially deleterious effects: loss of bioactivity as substitutions may be in important binding regions and a mixture of difficult to separate products. The conjugation reaction itself therefore requires a number of properties to ensure that as few products are obtained as possible and that the reaction is site-selective. It must also be bio-orthogonal,

this means the reaction must work in aqueous media which is buffered or contains many salts, proceed at ambient temperatures and pH.[192] As proteins in solution are usually at relatively low concentrations, the reaction must be efficient in order to achieve full conversion in reasonable reaction times, otherwise unfavourable kinetics will prevent completion.[192]

Cysteine readily undergoes alkylation with electrophiles and widely used example are α-halocarbonyls and maleimides which produce physiologically stable cnjugates (Scheme 1.3).[192] Examples of this reaction in protein conjugates can be found in mass spectrometry and peptide mapping, biomimetic glycoprotein formation, and glycosylation of dihydrofolate reductase to improve thermal stability.[192–195] Iodoacetamides can undergo side reactions with lysine residues, therefore use of chloroacetamides can avoid this undesired reaction.[192] Due to reactivity issues surrounding haloacetamides, other substitution reactions are used in protein conjugation with cysteines, nominally 1,4-conjugate additions to α,β-unsaturated enone systems (Scheme 1.3).[192] These Michael additions are termed thiol-ene conjugations and are highly chemoselective for thiols meaning cysteine is an ideal target. Substrates for the Michael addition with cysteines are predominantly maleimides and vinyl sulfones.[192] Maleimides have been used to conjugate glycosides to myoglobin through a cysteine to impart greater oxygen affinity.[196] Other bifunctional Michael acceptors have been used to pegylate IFN-α-2b selectively at reduced disulfides as well as on antibody fragments targeting CD4.[197] An inherent issue with using cysteine is the redox reactivity of sulfur (see Scheme 1.4 with protein conjugations usually perfromed under aerobic conditions.[192] In order to carry out cysteine conjugations, the cysteine must first be reduced using common thiol reducing agents such as dithiothreitol (DTT) or tris(2-carboxyethyl)phosphine (TCEP) which can lead to cross-reactivity, the reducing agents must ne removed by dialysis or chromatography.[198] These time-consuming techniques can result in re-oxidation of the cysteine and so poor yields are common. Furthermore, regioselectivity issues of endogenous cysteines can occur resulting in diminished yields and potentially impaired bioactivity.

One of the most widely used cysteine conjugation reaction is the formation of disulfides as conjugation strategy and as a cleavable linker.[188,192,199,200] Activated disulfides can improve

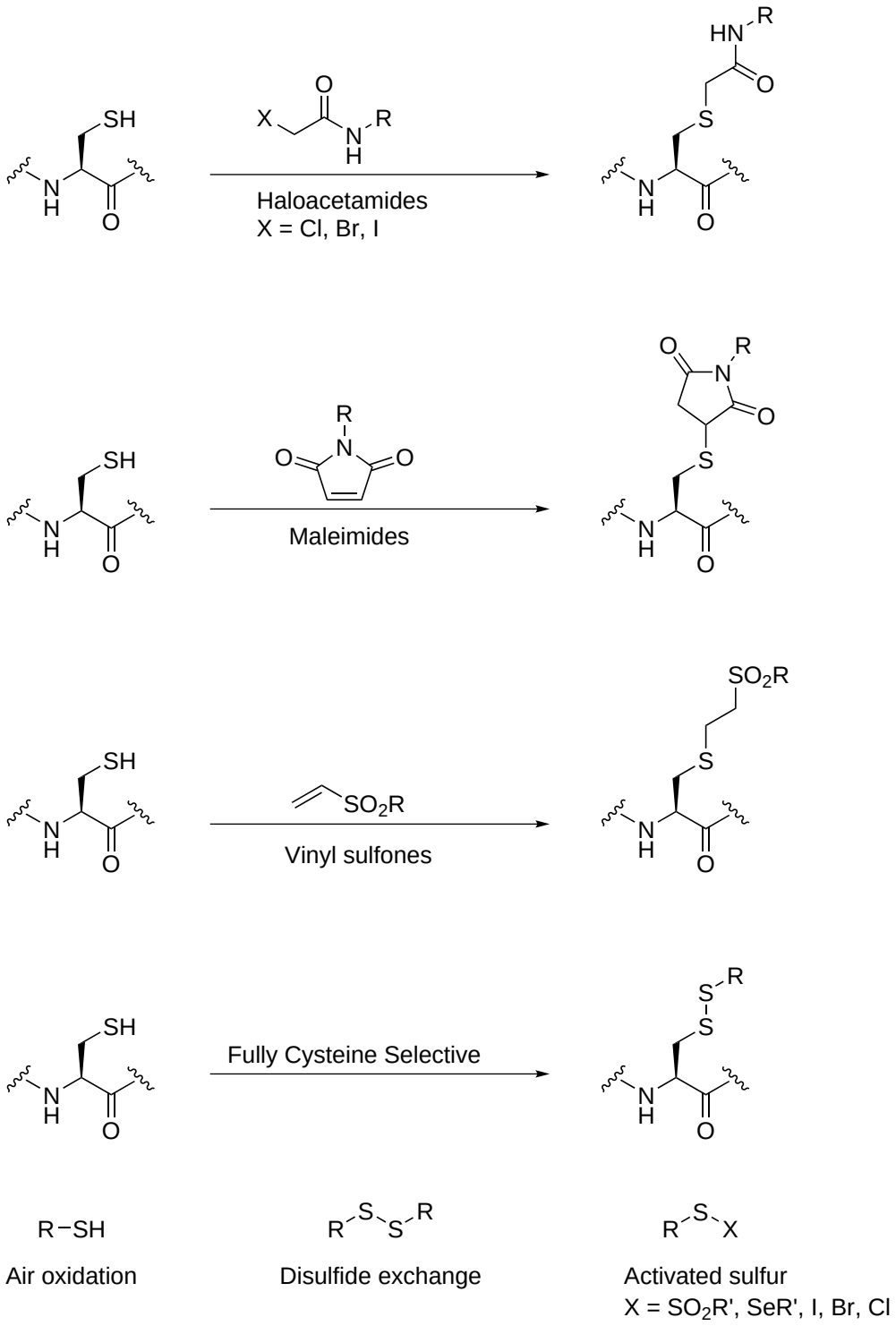

Scheme 1.3: Methods for cysteine conjugation commonly used in protein conjugaton. Adapted from Chalker *et al.*[192]

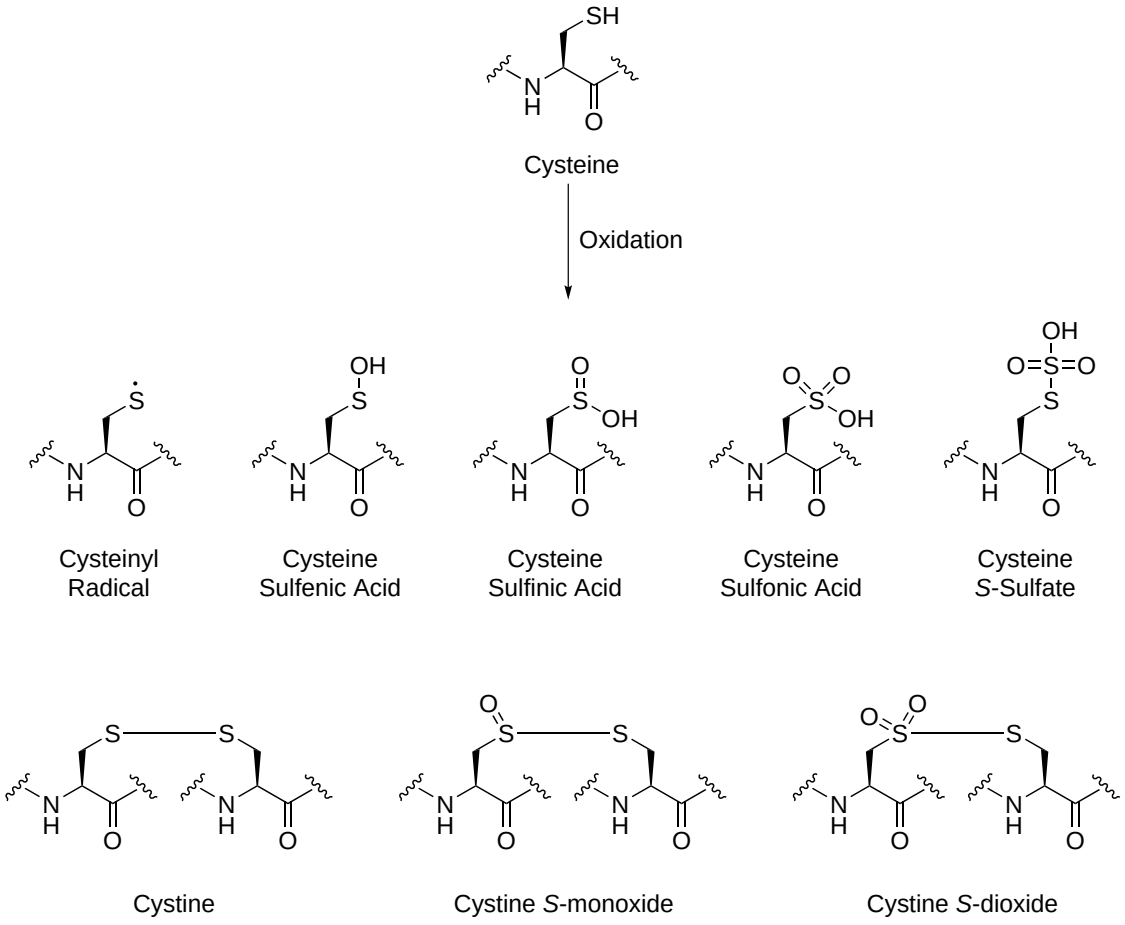

Scheme 1.4: Oxidation states of cysteine. Adapted from Chalker *et al.*[192]

control and reduce reaction times which are associated with this reaction. A well known example of this strategy is Ellman's Reagent, this compound is a disulfide aromatic dimer which reacts with available thiols and is used in colorimetric assays to measure thiol content.[201] Methanethiosulfonate derivatives and other activated thiols follow a similar strategy and have found uses in many applications including post-translational modifications and other biomimetic applications.[192,202] If no endogenous cysteines are available, site-directed mutagenesis can install a cysteine amino acid at an appropriate position in the protein to allow rapid conjugation without affecting bioactivity of the protein.[188]

The use of non-natural amino acids can improve regioselectivity isues inherent with cysteine conjugations if the protein contains more than one cysteine. This also offers the added benefit of introducing many different conjugation strategies with enhanced chemical reactivity and versatility.[203] In chemical peptide synthesis, incorporation of non-natural amino acids is relatively straightforward, however, this technique is limited to shorter chain proteins of around 100 amino acids or less. Synthetic biology advances have allowed the use of non-natural amino acids in recombinant protein expression through several methods such as auxotrophic bacterial strains, stop codon suppressor tRNAs and codon length expansion from natural triplet codons.[203]

These techniques have allowed many non-natural amino acids to be incorporated into proteins with the notable addition of azide or alkyne containing amino acids which has introduced the domain of CuAAC 'Click chemistry' into protein conjugations. The formation of triazoles has been known for decades but it was in 2002 where this copper catalysed reaction between an azide and an alkyne was popularised through independent discoveries by the Meldal and Sharpless groups.[204?] Click chemistry refers to a group of chemical transformations which meet certain criteria including ease of use, no side products, very high yielding, bio-orthogonal and unaffected by substituents.[205] Cu(I) is the active catalytic species, this can present some problems due to the redox chemistry of copper and it's rapid disproportionation in air. The Sharpless group reported *in situ* generation of Cu(I) *via* use of Cu(II) salts such as the cheap copper source, copper (II) sulfate, is the optimal method of gener-

ating copper I. Copper sulfate is reduced *in situ* in the presence of air, this excess reducing agent can then re-reduce any re-oxidised copper as part of a redox cycle. Shortly after this research, the Fokin group, in collaboration with Barry Sharpless, reported the use of polytriazoles as rate-accelerating ligands for the CuAAC reaction.[206] The most successful ligand was *tris*-(benzyltriazolylmethyl)amine (TBTA) which is a tris-triazole capable of tetradentate coordination to Cu(I) which is thought to envelop the metal ion providing a stabilising effect.[206] The high affinity for copper insertion into alkynes is then enough to displace one of the triazole arms and begin the catalytic cycle (Scheme 1.6). This ligand has been superseded by tris(3-hydroxypropyltriazolylmethyl)amine (THPTA), a hydroxylated version of TBTA which is more water soluble than the lipophilic ligand.[207]

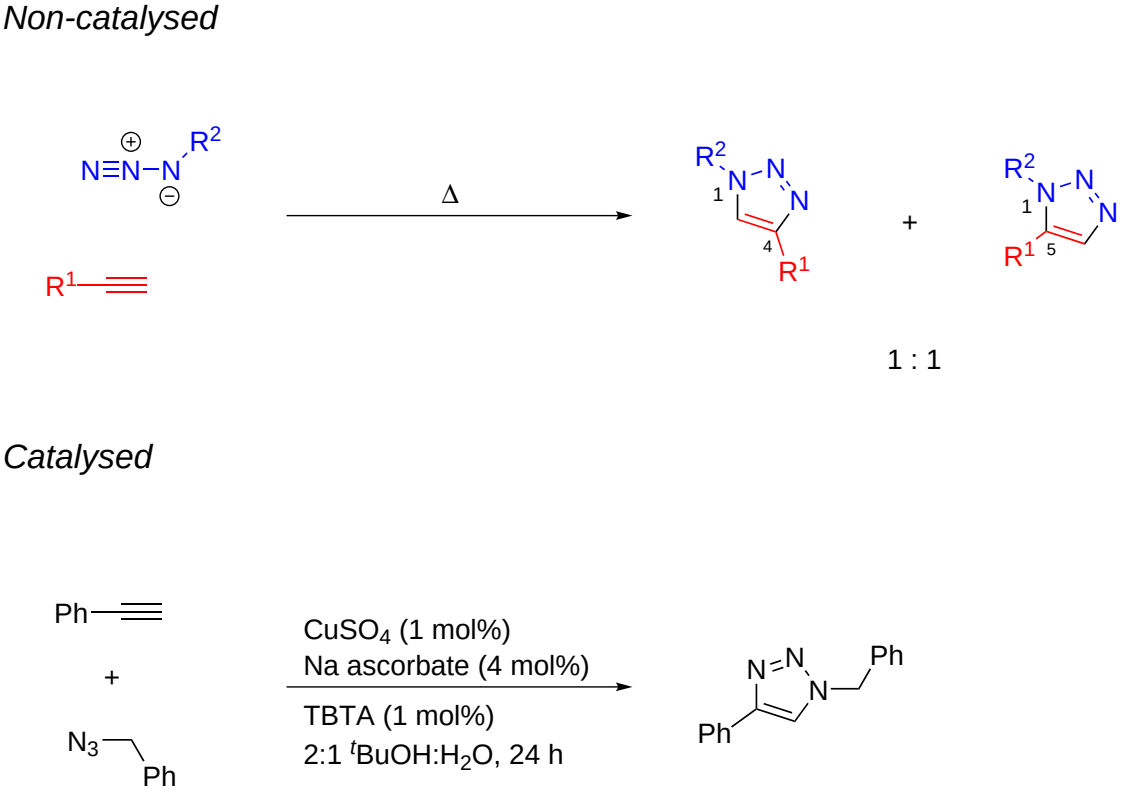

Scheme 1.5: The effects of copper catalysation on the azide-alkyne cycloaddition. Adapted from Sharpless and Fokin *et al.*[204,206]

The mechanism for the CuAAC catalytic cycle has been the subject of some disagreement, initially it was thought to involve formation of a copper-acetylide species akin to the Sonogashira coupling reaction, the azide then coordinates to the copper ion (Scheme 1.6).[205] The azide then attacks the acetylide to form a strained six-membered ring containing a het-

eroatomic allene-type system. This quickly collapses down to the five-membered 1,2,3-triazole ring, selectively forming the 1,4-isomer, before eliminating the product to free the Cu(I) ion to begin the cycle again. Practical and theoretical experiments suggested this was not the correct mechanism, thus density functional theory (DFT) calculations which incorporated a second copper ion demonstrated a marked reduction in the activation energy of the catalytic cycle (Scheme 1.6).[205] These results suggested a second copper ion coordinates to the copper-acetylide species which stabilises this complex and encourages recruitment and attack of the azide. Interestingly, the rate accelerating nature of copper ligands such as THPTA is further rationalised by this second copper ion association with the copper acetylide as these ligands are bidentate meaning one THPTA ligand can coordinate the first copper in the acetylide complex and then aid the recruitment of the second copper ion.[205]

Many practical considerations are necessary to achieve optimal conditions for the cycloaddition to operate successfully. The reaction is highly exothermic with ΔH^0 approximately 250 kJ mol^{-1}, however, this is associated with a high activation energy of around 130 kJ mol^{-1} which gives very low rates of reaction when a catalyst is not used.[205] The reason regioisomers are formed in the absence of copper is that the HOMO and LUMO energy levels for azides and alkynes are very similar meaning there is no preference for one arrangement. The action of the copper ion forces nucleophilic attack of the most-substituted alkyne carbon to the terminal nitrogen in the azide which sets the 1,4-substitution preference. The rate of the CuAAC reaction is increased by a factor of 10^7 relative to the uncatalysed process and is almost unaffected by the electronic or physical nature of azide or alkyne substituents.[205] Formation of a copper-acetylide species activates the alkyne towards nucleophilic attack through π-back donation of the copper into the π^* orbital of the alkyne.[205] Other metals besides copper have been reported in the azide-alkyne cycloaddition, for example, ruthenium-based cyclopentadienyl complexes which resemble the Grubbs catalyst. The main issues with ruthenium catalysis are sensitivity to solvents, the steric nature of azide substituents and most importantly, elevated temperatures which prevent the routine use of this metal in bioconjugations.[205]

The most common source of copper (I) utilised in bioorthogonal reactions is the aforemen-

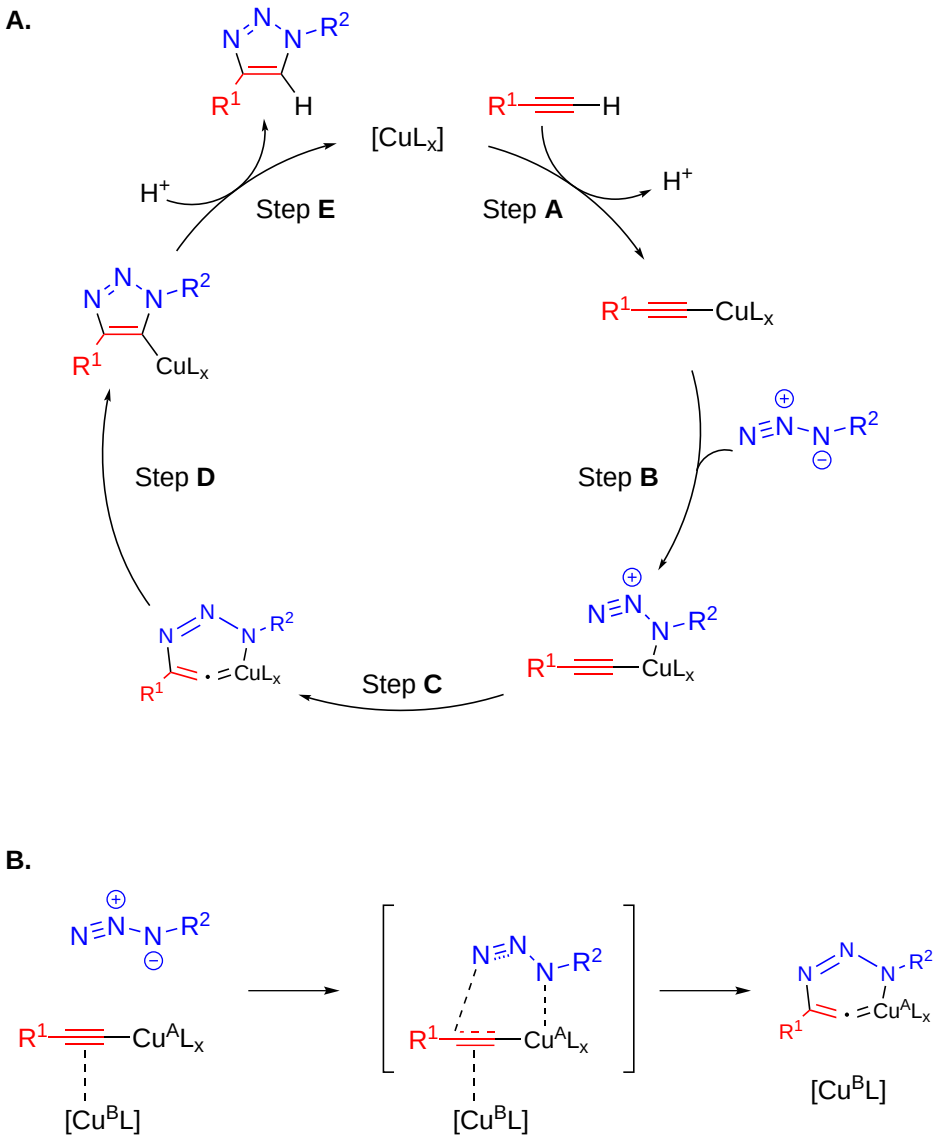

Scheme 1.6: Initial proposed catalytic cycle based on a single copper ion species determined by DFT calculations (A). The copper(I)-acetylide is first formed *via* π-alkyne coordination to copper before deprotonation and an exothermic formation of the acetylide (Step A). The azide then coordinates at the substituted end which enhances the electrophilicity of the terminal nitrogen and also increases nucleophilicty of the alkyne (Step B). A C-N bond is then formed to give a strained copper-mettalacycle, this step is endothermic and in some cases this species can be isolated (Step C).[205] This strained system then collapses to give the 1,2,3-triazole with 1,4-isomerism (Step D) before the triazole leaves the cycle to reform the copper catalyst (Step E). The next scheme (B) shows the revised catalytic cycle based on further DFT modelling and some kinetic observations which indicated a second copper ion likely coordinates to the copper-acetylide. Adapted from Fokin *et al.*[205]

tioned *in situ* reduction of copper (II) sulfate with sodium ascorbate.[205] Copper (I) sources have also been reported which include copper salts such as bromide, iodide, chloride and acetate. Copper iodides should be avoided as copper-iodide-copper bridging has been observed resulting in poly-Cu-acetylide aggregate formation, therefore copper bromide and acetate salts are preferential.[205] Coordination complexes of copper (I) acetonitrile are also used wich are more resistant to oxidation in air.[205] The use of rate-accelerating ligands are also important, not only do these ligands enhance the rate but they have also been shown to stabilise the Cu(I) oxidation state in aerobic conditions.[205,208] The previously mentioned TBTA polytriazole has been successfully used in partially aqueous bioconjugations and this activity has been enhanced through the development of the THPTA ligand.[205,208] The ligand-solvent interactions can be very important, for example, in DMSO mixtures THPTA is not particularly effective whereas tris(2-benzimidazolylmethyl)amine operates efficiently, this is in stark contrast to it's behaviour in water.[205,207] Generally, for conventional chemical synthesis the reaction is very robust and the reaction will proceed efficiently even against some of these factors, however, biological applications are more demanding due to the low concentrations involved and requirement for reaction completion (due to purification difficulty) meaning that greater attention to these issues is required for success.

Biological applications of CuAAC are numerous and varied, not only has this chemistry been used to form conjugates but the triazole ring has been used in many native proteins to improve biological stability.[209] Due to the instability of certain bonds found in peptides, triazoles have found function as replacements for both amide and disulfide bonds which in certain examples has enhanced the drugability of peptides as therapeutics.[209] Triazoles are bioisosteres of the amide bond, for example, both are of a similar size and most importantly each group has a similar dipole moment.[209,210] This dipole moment causes the sp^2 nitrogen atoms in the ring to be weak hydrogen bond acceptors. This is complemented by the C-5 proton being highly polarised and has similar hydrogen bond donating properties as an amide NH-proton.[209,210] The difference between these systems is that the amide bond can be hydrolysed by proteases whereas the triazole is very stable under most conditions found

in biology. For example, triazoles have been successfully used as peptide bond surrogates in the cyclic peptide (PVPY) to inhibit tyrosinase.[211]

To enhance the bioorthogonality of the CuAAC reaction, Finn *et al.* reported modified conditions which enabled live cell surfaces to be successfully labeled with fluorophores.[212] Copper is known to be toxic to cells as free Cu(I) is oxidised by oxygen and produces ROS leading to cell damage and eventually cell death and so copper-free click conditions are usually used instead.[212] This is less convenient though as the alkyne must be under ring strain which is very difficult to incorporate into biological or even chemical species. The successful strategy therefore included use of THPTA and aminoguanidine to allow micromolar concentrations of copper sulfate to be used which did not result in significant cell death. The Cu-ascorbate reduction system produces large amounts of ROS and the THPTA ligand has been shown to intercept ROS as well as accelerate copper-mediated peroxide degradation.[213] The aminoguanidine allows the capture of dehydroascorbate which would otherwise react with protein side chains. Azido-functionalised peracylated mannose was then uptaken by both CHO and jurkat cells and presented on the cell surface, the azide then successfully underwent cycloadditions with rhodamine-alkyne derivatives allowing the progress of the reaction to be monitored by live-cell imaging.[212] The investigators also demonstrated that increasing the copper sulfate concentration resulted in increased toxicity, however, this could be counteracted by THPTA incorporation in a dose-dependent manner.

1.4.3 Cleavable Linkers

The term cleavable linker refers to a chemical species which is covalently bonded between two molecules, of usually different functions, which is stable under ambient conditions but becomes unstable either in the body or inside a cell.[214] The purpose of the cleavable linker is to ensure the two molecules are bonded together until they reach the desired destination in the organism or cell and then covalently separate such that functional responses can then occur which were reduced while the molecules were bonded together. Cleavable linkers must

meet criteria such as cleavage under mild conditions, use of bioorthogonal reagents, highly yielding at biologically relevant concentrations and biocompatibility of waste products.[214] The linker is cleaved only under specific conditions depending on its design, this can be enzymatically, photolytically or chemically cleaved. Due to the versatility of cleavable linkers, uses of these molecules are widespread and include drug delivery, proteomics, imaging and DNA sequencing.[214] For example, in drug delivery some drugs are not particularly water soluble or are unable to cross cell membranes therefore drug delivery uses targeting ligands which deliver the drug across membranes and the linker then cleaves liberating the drug inside the cell. A good example of this are antibody drug conjugatess (ADCs) where an antibody is used to target a particular receptor or cell-type which causes disease resulting in the drug being delivered to the disease causing cell, the cleavable linker is needed as it is unlikely the drug will still be effective with the large antibody still attached.[215] Furthermore, the drug may be highly cytotoxic and so excessive side-effects would persist with the free drug which are avoided through the selective nature of the ADC. Drug delivery ligands are widely varied including antibodies, peptides, proteins, aptamers, liposomes, dendrimers and polymers.[214] In imaging applications, cleavable linkers sensitive to enzymes involved in cancer have been used with MRI contrast agents which allow the presence of tumours to be detected in body.[214,216] Fluorescence imaging allow biological processes to be characterised, for example, through the use of FRET to detect the event or with fluorophore-quencher systems.[214]

Many peptide-based cleavable linkers are known but for the purposes of this review, this section will focus on the disulfide linker. This linker takes advantage of high concentrations of glutathione inside cells which rapidly reduce the disulfide bond leading to separation of the linked molecules; this has led to applications in drug delivery and imaging.[217?,218] For example, campothecin is an anti-cancer drug which is highly lipophilic and also very cytotoxic meaning it exhibits poor pharmacokinetics and side effects.[219] This compound has been conjugated to folic acid *via* a disulfide-containing peptide linker which allowed selective delivery to cancer cells which over-express the folate receptor resulting in uptake *via* endocytosis.

The conjugate exhibited greater solubility than free campothecin due to the presence of the polar peptide and specificity of the targeting folic acid ligand resulted in excellent inhibition of cancer proliferation.[219] The use of disulfides does not always enhance the therapeutic effects of drug conjugates, particularly when the targeting ligand is also therapeutically active is was the case in trastuzumab conjugates.[220] Trastuzumab is a monoclonal antibody therapy for HER-2 positive breast cancers, however, some patients do not respond well to this treatment and so conventional chemotherapies are sometimes co-administered. Conjugates of trastuzumab are therefore desirable as the chemotherapy is targeted toward the HER-2 positive cancer cells which improves efficacy and limits side-effects. Trastuzumab was conjugated to antimitotic agent DM1 through non-cleavable sulfide and cleavable disulfide bonds; interestingly, the sulfide linked conjugate exhibited higher activity than the disulfide linked conjugate.[221] In the case of antibody maytansinoid conjugates (AMCs), disulfide linked conjugates exhibited no significant difference in the cytotoxic activity of the therapy towards antigen positive cells compared to non-cleavable thioether conjugates.[222] This study highlights a useful property of chemically synthesised disulfide linkers which is that the stability in the presence of reducing agents can be improved by introducing steric bulk around the disulfide bond in the form of adjacent methyl or geminal dimethyl groups.[215] In this study, differences in the nature of the disulfide (no methyl, methyl, or dimethyl) resulted in lower reduction rates for more hindered species, however, this had little effect on the efficacy of the conjugate towards antigen-positive cancer cells over the thioether linked conjugate.[215,222] The disulfide linked AMCs was markedly improved in bystander killing assays over thioether acpAMC, where antigen-negative cells were also inhibited. This effect was also exhibited dose-dependency in terms of the number of antigen-positive cells which is beneficial *in vivo* as tumour microenvironment localised cell cytotoxicity will occur. The bystander killing effect was most pronounced in the more hindered disulfide conjugates due to the regioselective reduction which prevents maytansinoid-glutathione species forming allowing egress of the drug out of the cell (**??**).[215,222]

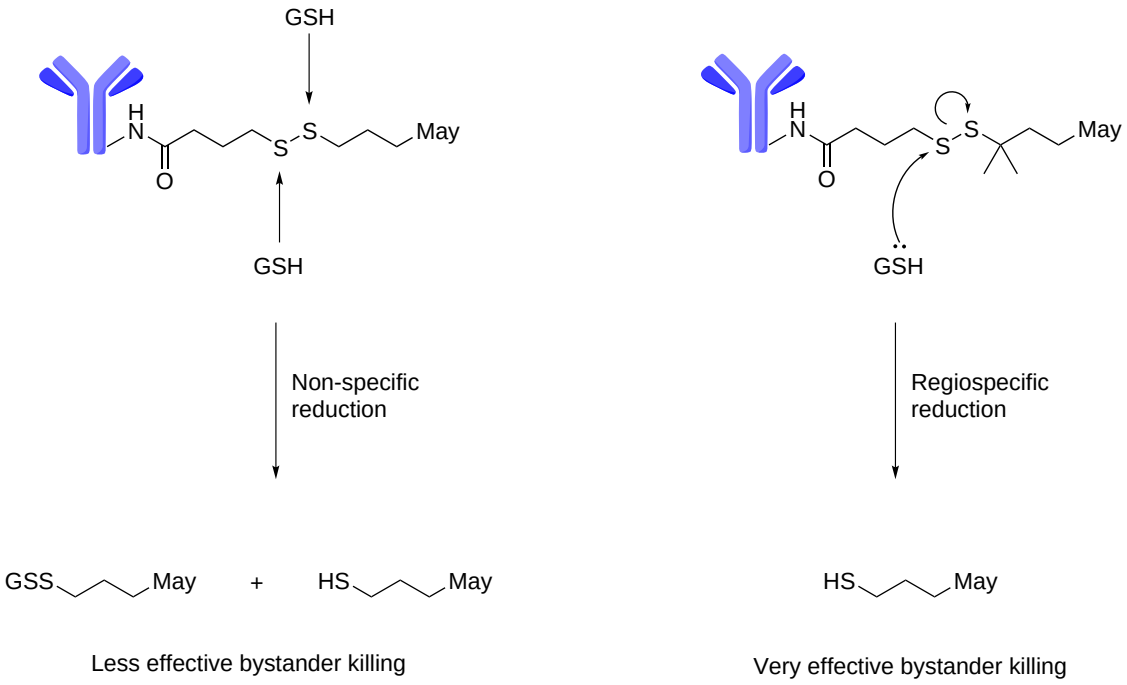

Scheme 1.7: Effects of steric hindrance around the disulfide bond on bystander killing in *in vitro* tumour models containing antigen-positive and antigen-negative cells. When the disulfide reduction is regiospecific towards the antibody side, a small lipophilic maytanisoid compound is liberated which can cross cell membranes allowing entry to antigen-negative cells. When no steric hindrance around the disulfide is present, glutathione-maytanisoid disulfides can be formed which cannot cross cell membranes and therefore do not exhibit as effective bystander killing. May - maytanisoid. Adapted from Widdison *et al.*[215]

1.5 Aims

1.5.1 CCL2 as a Delivery Vehicle to Monocytes

The introduction presents a clear need for tools which are able to selectively target monocytes and also bear subset specificity. This need has been shown in many diseases such as cancer, liver fibrosis and atherosclerosis, with a multitude of monocyte subsets having varying roles in these diseases. The chemokine, CCL2, presents an attractive pathway to utilise for this purpose as it is not only highly selective for monocytes but there is also a spectrum of expression level of the receptor CCR2 across the various monocyte/macrophage subsets. A beneficial aspect of using CCL2 as a delivery vehicle is that this is a natural biological pathway which is even complicit in many of the diseases which are being treated. For example, CCL2 is secreted as part of the inflammatory response which is accompanied by increased CCR2 expression meaning the capacity for delivery may be enhanced towards pathologies related to chronic inflammation. The use of a naturally occurring peptide also renders a reduced chance of an immunogenic reaction compared to non-natural peptide delivery methods. Furthermore, CCL2 is a small protein and so this increases extravasation properties making these conjugates more effective at penetrating disease sites in tissues or tumours compared to larger proteins such as antibodies.[215] The benefit of the CCL2 internalisation pathway is that this area has benefited from a large amount of research and whilst the dynamics are not wholly understood, it is better characterised than the multitude of antibody internalisation pathways. Furthermore, a number of variants of CCL2 have been identified and some of these have altered function, these variants could therefore be evaluated to alter function such as binding affinity, *in vivo* activity, chemokine signalling and half life.

1.5.2 Development of Novel Fluorescent CCL2 Conjugates

The objective of this project is to develop a platform of chemokine conjugates as a proof of concept towards developing successful therapeutic conjugates in the future. Many approaches towards therapeutic peptide conjugates are essentially 'black box' experiments where the success or failure of a peptide conjugate's function is not well understood. Alternatively, developing fluorescent conjugates of CCL2 will provide information into the function and behaviour of the conjugates which can be applied to a therapeutic. The use of fluorophores allows imaging experiments to be performed giving insight into the internalisation and sub-cellular distribution of conjugates. Flow cytometry can also be performed on primary white blood cells to identify the selectivity of the conjugates and demonstrate any modulation of activity resulting from the nature of the CCL2 variant or the conjugate. Fluorescence also provides information in migratory experiments as both the signalling properties of the CCL2 conjugates can be identified as well as internalisation behaviours. This high level of characterisation is important in the development of a biological delivery platform for a variety of applications.

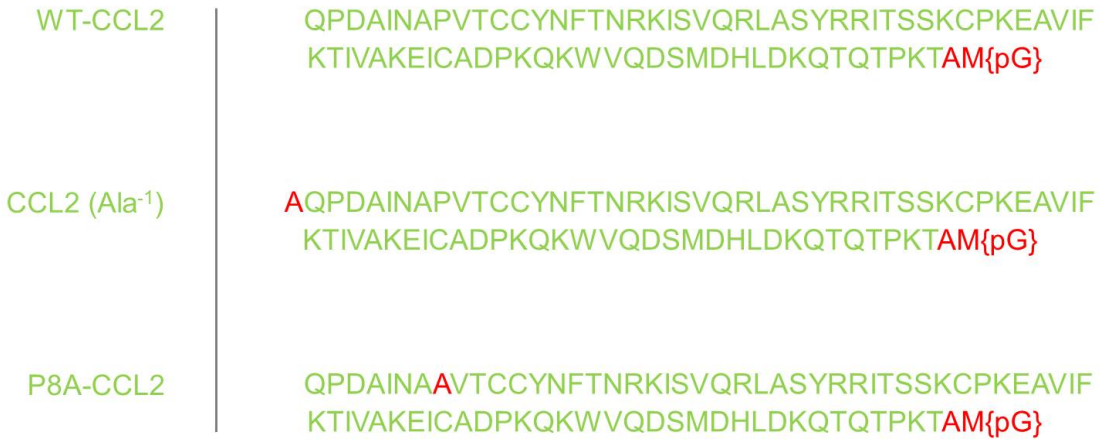

Figure 1.21: The single letter amino acid sequences used for CCL2 variants, red amino acids identify residues not present in the wild-type sequence. nCCL2 refers to a wild-type sequence at the N-terminus, CCL2 (Ala^{-1}) refers to the alanine addition at the N-terminus and P8A-CCL2 refers to the P8A substitution at the N-terminus. All variants bear the AM{pG} sequence at the C-terminus, this includes the AM spacer used in the CCL2-SA1 conjugate and {pG} is a propargyl glycine residue for CuAAC.

Current CCL2 conjugates and the strategies used translate poorly to other applications, for

example, the CCL2-mCherry fusion protein and the CCL2-SA1 fusion protein must be designed for each conjugate and the fusion proteins then developed as a genetic sequence and then expressed. Furthermore, fusion proteins are limited to peptide linkers and conjugates, and the incorporation of the commonly used disulfide linker is a laborious and inefficient process. The fluorescent chemokines developed by Almac Chemokines are a good example of the research that can be performed with functional fluorescent chemokine. The best example in the literature of chemokine conjugation is the S6-PPTase tag developed by Handel *et al.* which allows conjugation of any molecule bearing the Ppant arm, although it does require an oligopeptide sequence to be included at the C-terminus of the chemokine.[7] Issues with these conjugations include some loss of activity and the need for the coenzyme A incorporation which may be difficult in some systems and may also reduce activity of therapeutics. Translating this reaction to larger species, such as oligonucleotides, may also be difficult if these prevent the action of the PPTase enzyme. To avoid these problems and offer an alternative strategy with higher conjugate flexibility this project therefore aims to develop CCL2 constructs which possess an alkyne-containing non-natural amino acid at the C-terminus for use in CuAAC conjugations. This only requires a small modification to the C-terminus of CCL2 which is known to be non-essential for CCR2 binding and is an approach successfully used by the aforementioned conjugates (a schematic representation is shown in Figure 1.22). This alkyne-bearing amino acid can be introduced easily through SPPS chemistry, representing a minor change in structure.

To the best of our knowledge, the nature of the linker between CCL2 conjugates has not previously been varied and so we aim to use non-cleavable and cleavable linkers between CCL2 and the fluorophores. This should allow modulation of the sub-cellular distribution of fluorophores through the use of disulfide cleavable linkers or non-cleavable alkyl-based linkers. Furthermore, this project will investigate the effects of varying the lipophilicity of the fluorophore on behaviour of the conjugates which is an important consideration in developing therapeutic CCL2 conjugates.

A number of CCL2 variants have been reported which have differences in binding affinity due

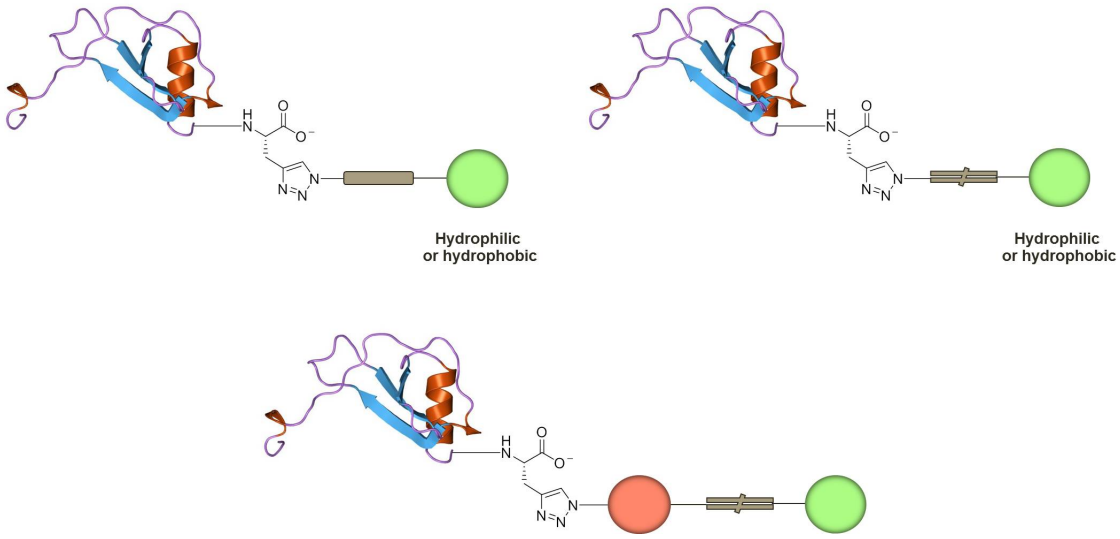

Figure 1.22: Schematic of CCL2 conjugates which will be made in this project, the chemokine will provide monocyte-selective uptake through CCR2-specific endocytosis. The conjugates will be formed using CuAAC giving the 1,4-triazole allowing attachment of various fluorophores and linker species. Non-cleavable linkers will be mainly alkyl based and cleavable linkers will utilise disulfide chemistry which should enhance endosomal escape. The effect of fluorophore polarity will also be examined and so fluorophores will be either hydrophilic of hydrophobic. Finally, a disulfide separated FRET pair will be synthesised allowing disulfide reduction to be detected and both fluorophores to be independently tracked. CCL2 ribbon structure reproduced from PDB, code 1DOL.[223]

to small modifications to the N-terminal sequence. This project will use the wild-type CCL2 sequence (at the N-terminus) as a direct comparison of conjugated CCL2 vs wild-type human CCL2 sourced from Peprotech. The three CCL2 sequences which will be used are shown in Figure 1.21, the C-terminal modification includes a propargyl glycine for the CuAAC and an ala-met dipeptide which was reportedly used in the Osprey CCL2-SA1 patent.[6] As this system was successful this AM spacer will be used between the CCL2 C-terminus and the propargyl glycine. This study was interesting because a CCL2 variant was used which was first reported in 1995 by Clark-Lewis *et al.* called CCL2 Ala^{-1} which exhibited an over 100-fold loss of chemotactic activity relative to wild-type CCL2.[224] Unfortunately, McIntosh *et al.* did not report any migration data for the CCL2-SA1 conjugate and so it is unclear whether this reduced activity was reproduced in this system or why this less active sequence would be selected.[6] This project will therefore investigate fluorescently labeled conjugates of this sequence to ascertain if there is a disconnect between G-protein signalling and ligand internalisation in the CCL2 Ala^{-1} variant which could allow high concentrations of CCL2 to

be internalised without triggering chemotactic activity. The third CCL2 variant used is the alanine substitution of proline at the 8-position (P8A) reported by Handel *et al.*, which is able to induce chemotaxis *in vitro* but loses chemotactic activity *in vivo*.[113,225] This is due to the inability of P8A-CCL2 to dimerise on GAGs which is essential for chemotaxis out of the blood vessel. This P8A-CCL2 is an appealing variant for therapy as it may represent a 'silent' delivery vehicle where affinity for the receptor is retained but chemotactic activity is absent.

The aims of the project are therefore as follows:

1. To synthesise fluorophores which vary in lipophlicity and contain an azide for subsequent CuAAC conjugations.
    (a) Develop disulfide linkers and incorporate these linkers into both hydrophobic and hydrophilic fluorophore azides for comparison with the non-cleavable linker conjugates.
    (b) Synthesise a FRET pair containing a disulfide linker between donor and acceptor allowing the intracellular reduction of the disulfide to be detected and separated fluorophores to be tracked.
2. Design CCL2 sequences amenable to undergo CuAAC reactions with the above azides.
    (a) Form three CCL2 variants including native CCL2 (WT-CCL2), CCL2 Ala^{-1} and P8A-CCL2 each including an alkyne tag for CuAACs.
    (b) Optimise CuAAC reactions to successfully conjugate the above fluorophores and FRET pairs to alkyne-tagged CCL2.
3. Characterise biological activity of fluorescent CCL2 variants.
    (a) Compare chemotactic activity of CCL2 variants with wild-type human CCL2.
    (b) Characterise internalisation efficiency of CCL2 variants in relevant cells.
    (c) Demonstrate that chemotaxis and internalisation is CCR2 specific in each CCL2

variant.

4. Compare properties of the various fluorophore and linker systems in cellular experiments.

   (a) Measure chemotactic activity and internalisation behaviour of the conjugates.

   (b) Perform microscopy to demonstrate sub-cellular distribution differences between different fluorophore and linker systems.

   (c) Determine CCR2-selective uptake of CCL2 variants and the various conjugates in primary mixed cell populations and characterise any subset specificity.

Chapter 2

Experimental

2.1 Biological Methods

2.1.1 Cell Culture

THP-1 (human monocytic cell line derived from the peripheral blood of a male with acute monocytic leukemia) cells and Jurkat cells were cultured in RPMI-1640 (plus 10% FCS, 1% penicilin, streptavidin, glutamate) in T-75 flasks at a density of 0.5 x 10^6 cells per mL. Prior to experiments, live cells were purified with lymphoprep gradient (StemCell Technologies, centrifuged at 800 g, 20 min), then washed with PBS and resuspended into chemotaxis or culture media.

2.1.2 Transwell Migration Assay

Corning HTS Transwell-96 Tissue Culture Systems were used as follows. Lower reservoirs contained chemotaxis buffer (RPMI-1640 plus 0.1 % BSA, 150 µL) with or without the chemoattractant. THP-1 cells (0.3 x 10^6 cells) were seeded onto the membrane in the upper chamber in chemotaxis buffer (75 µL) and incubated for 4 h at 37 °C, 5% CO_2. Cells were then taken directly into flow cytometry.

CCR2 inhibition was carried out as follows: CCL2 pre-incubation was obtained by incubating THP-1's (3.999 x 10^6 per mL) in 250 nM CCL2 (recombinant human CCL2 from Peprotech Ltd.) for 30 min at 37 °C before washing with PBS (1 mL) and resuspending in chemotaxis media at the same density.

Inhibition with INCB 3284 (Tocris Bioscience) was carried out by incubating THP-1 cells in chemotaxis buffer containing either 470, 47 or 4.7 nM, in agreement with a reported IC_{50} = 4.7 nM, for 30 min and taken without washing into the chemotaxis plate.

2.1.3 Timecourse

THP-1 cells (0.1 x 10^6) were incubated in chemotaxis buffer (150 µL RPMI-1640 plus 0.1 % BSA) containing the CCL2 conjugate at the specified concentration for either 0.5, 1, 2, 3 or 4 h before flow cytometry in the AB Biosystems Attune (2.1.4).

2.1.4 Flow Cytometry - Chemotaxis and Timecourse

The Boyden transwell chemotaxis assays were quantified on an AB Biosystems Attune flow cytometer with acoustic focussing and an auto-sampler. Each well was auto-pipetted 3 times before sampling, either 25 x 10^3 events were collected or 75 µL was extracted. The fluorescence was captured using a 488 nm HeNe laser. Data was analysed using Attune 2.1 cytometric software.

2.1.5 Primary Blood Cell Isolation

Human blood was taken from healthy donors into heparin-coated vacuum tubes (10 mL aliquots). The blood was obtained under ethics reference ERN 10_0660.

Peripheral Blood Mononuclear Cells

The blood was layered onto Lymphoprep solution (20 mL, StemCell Technologies) in sterile sterling tubes (50 mL) and centrifuged at 1000 g for 20 min without brakes at ambient temperature. The PBMC layer was extracted and washed with MACS buffer (100 µL, PBS + 2% FCS + 1 mM EDTA) and centrifuged at 1000 g for 5 min and washed again with MACS buffer (500 g, 10 min) before resuspension in MACS buffer at a density of 1 x 10^3 mL^{-1} and kept on ice until treated.

Neutrophil Isolation

Whole blood was treated with 2% w/v dextran (Pharmacosmos, DK) in a 1:6 ratio for 30 min at ambient temperature to sediment erythrocytes. The leukocyte-rich plasma was aspirated

and layered onto a 56/80% w/v Percoll gradient at a ratio of 5:3 and centrifuged at 220 g for 20 min without brakes. The neutrophil layer was extracted and washed in MACS buffer (centrifuged 450 g, 10 min) before resuspension in MACS buffer at a density of 1 x 10^3 mL^{-1} and kept on ice until treated.

2.1.6 Flow Cytometry - PBMC Monoclonal Antibody Labelling

100 x 10^3 PBMCs were transferred to FACS tubes in 100 µL of MACS buffer. The cells were then treated with the chemokine conjugates: CCL2 Ala^{-1}-alk-H (200 nM), WT-alk-H (30 nM), P8A-alk-H (30 nM), P8A-SS-H (30 nM), P8A-SS-L (30 nM) for 1 h at ambient temperature. In initial experiments (Figure 5.24) cells were treated with a live/dead marker (LIVE/DEAD^{TM} dead cell stain kit, ThermoFisher Scientific L10119) for 30 min before washing twice in MACS buffer. In later experiments, the cells were washed twice in MACS buffer, excluding the live/dead labelling step and resuspended in MACS buffer containing the monoclonal antibodies (listed in Table 2.2 and Table 2.3). The cells were labelled for 30 min on ice, washed twice and resuspended in MACS buffer (100 mL) for FC sampling. Flow cytometry was carried out on a Dako CyAn ADP flow cytometer (laser lines: 405 nm, 488 nm and 633 nm) and the data analysed using Summit software (Beckman Coulter, Buckinghamshire, UK).

The tables below summarise the monoclonal antibody panels used to gate the monocyte and lymphocyte subsets in compensation (Table 2.1), monocyte subsets (Table 2.2) and lymphocyte subsets (Table 2.3).

Table 2.1: Antibodies utilised for fluorescence compensation for both monocyte and lymphocyte panels. Suppliers: † - Biolegend, ‡ - BD Biosciences, ⋆ eBioscience.

Antibody	Isotype Control	Source	Clone	Dilution
CD45-BV421†	IgG1 K-BV421	Mouse	H130	1:10
CD45-BV510†	IgG1 K-BV510	Mouse	H130	1:10
CD45-FITC†	IgG1 K-FITC	Mouse	H130	1:10
CD45-PE-CF594‡	IgG1 K-PE-CF594	Mouse	H130	1:10
CD45-PECy7⋆	IgG1 K-PECy7	Mouse	H130	1:10
CD45-APC†	IgG1 K-APC	Mouse	H130	1:10
CD45-APC-eFluor780⋆	IgG1 K-APC-Cy7	Mouse	H130	1:10

Table 2.2: Antibodies utilised for the monocyte subset panel. Suppliers: † - Biolegend, ‡ - BD Biosciences, ⋆ eBioscience.

Antibody	Isotype control	Source	Clone	Dilution
HLA-DR-eFluor450⋆	IgG2a K-eFluor450	Mouse	H130	1:10
CD16-PE-CF594‡	IgG1 K-PE-CF594	Mouse	3G8	1:10
CCR2-APC†	IgG2a K-APC	Mouse	K036C2	1:5
CD14-APC-eFluor780⋆	IgG1 K-APC-eFluor780	Mouse	61D3	1:10

Table 2.3: Antibodies utilised for the lymphocyte subset panel. Suppliers: † - Biolegend, ‡ - BD Biosciences, ⋆ eBioscience.

Antibody	Isotype control	Source	Clone	Dilution
CD3-BV510†	IgG2a K-BV510	Mouse	OKT3	1:10
CD56-PECy7⋆	IgG1 K-PECy7	Mouse	CMSSB	1:10
CCR2-APC†	IgG2a K-APC	Mouse	K036C2	1:5

2.1.7 Fixed Cell Imaging

THP-1 cells or PBMCs (1 x 10^5 in 100 µL) were incubated in either chemoattractant media containing the CCL2 conjugate or chemoattractant media alone for negative controls. Cells were incubated for 2 h before being mounted onto glass slides *via* cytospinning (300 rpm, 3 min), washing with PBS + 0.05% Tween-20 and fixed with para-formaldehyde (4%) for 5 min. Coverslips were then mounted onto microscopy slides with Prolong Gold anti-fade containing DAPI (Life Technologies). Slides were then imaged on a Zeiss Axio Observer-Z1 using LED illumination at 405 and 488 nm with Apotome optical sectioning. The following

filters were used for green fluorescence: excitation (440 - 470 nm), beamsplitter (495 nm) and emission (520 - 550 nm). The following filters were used for DAPI: excitation (G 365 nm), beamsplitter (FT 395 nm) and emission (BP 445 - 450 nm). The image was focused on the centre of the cells and five z-slices were acquired at 0.37 µm intervals, the maximum intensity projection was then averaged through the z-direction.

2.2 Chemical Methods

2.2.1 CCL2 CuAAC Conjugations

CuAAC of Alkyl-linked Fluorophores

Stock solutions of $CuSO_4$, THPTA, Na ascorbate and BODIPY **10** were prepared in PBS. Solid CCL2 was dissolved in PBS and the concentration was determined using UV absorption and the Beer-Lambert law (molar absorption coefficient = 8490 $dm\,mol^{-1}\,cm^{-1}$, calculation performed on www.protcalc.sourceforge.net/ based on number of W and Y residues). The reaction mixture was prepared as follows unless stated otherwise: PBS was added first, followed by $CuSO_4$ (1 eq.), Na ascorbate (25 eq.), THPTA (5 eq.), CCL2 (1 eq.) and finally BODIPY **10** (20 eq.). The reaction was left for the time stated in chapter 4, the CCL2 product was separated from smaller molecules using size exclusion chromatography (PD-25 column, GE Healthcare) eluting in the first 0.7 mL. The concentration of the conjugate was then determined by UV absorption spectroscopy, mass spectrometry determined product mass, and the protein was diluted by a suitable factor with PBS and the solution made up to 0.5% BSA to aid stability. The conjugate was aliquoted and stored at -20 °C.

Lipophilic BODIPY **8** conjugates were prepared using the same method except substituting tris(2-benzimidazolylmethyl)amine ($(BimH)_3$) (0.5 eq.) for THPTA and also being carried out in 30% DMSO in PBS. An extra dialysis step was performed prior to size exclusion chromatography, this utilised Slide-A-Lyzer^{TM} MINI dialysis tubes with a 3.5 kDa MWCO using PBS at 4°C overnight.

CuAAC of Disulfide-linked Fluorophores

An Atmosbag glove bag was perfused with nitrogen according to the user manual and solvents were degassed *via* nitrogen bubbling for 30 min. Stock solutions of CuBr, $(BimH)_3$ and the fluorophore were prepared in DMSO. Solid CCL2 was dissolved in PBS and the concentration was determined using UV absorption and the Beer-Lambert law (molar absorption

coefficient = 8490 $\mathrm{dm\,mol^{-1}\,cm^{-1}}$). The reaction mixture was prepared as follows unless stated otherwise: DMSO was added first, followed by DMSO, CuBr (1 eq.), $(BimH)_3$ (0.5 eq.), CCL2 (1 eq.) and finally the fluorophore (20 eq.). The reaction was left for the time stated in chapter 4 before removal of DMSO *via* dialysis (as above) and size exclusion chromatography (PD-25 column, GE Healthcare) eluting in the first 0.7 mL. The concentration of the conjugate was then determined by UV absorption spectroscopy, mass spectrometry determined product mass, and the protein was diluted by a suitable factor with PBS and the solution made up to 0.5% BSA to aid stability. The conjugate was aliquoted and stored at -20 °C.

2.2.2 MALDI Mass Spectrometry

Samples were desalted using a C-18 ziptip (Millipore) into 1:1 acetonitrile:0.1% TFA. Sinapinic acid (10 $\mathrm{mg\,mL^{-1}}$, 4:6 water:acetone) was used as the matrix in a ratio of 3:1 matrix:sample (v:v). MALDI-TOF-MS was recorded on a Waters Micromass MALDI micro MX mass spectrometer.

2.2.3 UV-Vis Spectroscopy

UV-Vis spectra were recorded on a Shimadzu UV-1800 spectrometer sampling a wavelength range from 220 - 800 nm at 1.0 nm intervals. The concentration of unlabelled CCL2 was calculated using absorption at 280 nm based on tryptophan/tyrosine absorption according to the Beer-Lambert law (molar absorption coefficient = 8490 $\mathrm{dm\,mol^{-1}\,cm^{-1}}$). Post-labelling the concentration was determined using BODIPY absorption at the absorption maxima using the molar absorption coefficient determined in chapter 3.

2.2.4 Fluorimetry

Fluorescence spectra were recorded on a Shimadzu RF-5301 PC spectrofluorimeter with a 5 nm slit width in 1.5 mL quartz cuvettes. Samples were maintained at 15 nM and dissolved in either PBS (pH 7.4, 10 mM, 100 mM NaCl), CH_2Cl_2 or DMSO.

2.2.5 Quantum Yield Calculation

Quantum yields were calculated using the relative quantum yield equation (2.1) using fluorescein as the known standard ($\Phi = 0.95$).[226] The UV-Vis absorbance for both the BODIPY and fluorescein standard were identical at the relevant excitation maxima allowing relative fluorescence intensities to be compared.

$$\Phi = \Phi_{st} \frac{I}{I_{st}} \frac{A_{st}}{A} \frac{\eta^2}{\eta_{st}^2} \tag{2.1}$$

Where Φ = quantum yield, I = integrated emission, A = absorbance, η = solvent refractive index, 'ST' refers to the fluorescein standard.

2.2.6 FRET Efficiency Calculation

The FRET efficiency for the FRET pair **45** was calculated using the methods described by Asunuma *et al.*[227] 2.2 describes the decrease in donor emission using BODIPY azide **8** as the donor-only molecule (I_D) and the donor emission from the FRET pair (I_{DA}).

$$\Phi_{T1} = 1 - \frac{I_{DA,506}}{I_D} \tag{2.2}$$

The second method (2.3)relates to increase in acceptor emission within the FRET pair using BODIPY azide **8** as the donor-only compound and rhodamine **38** as the acceptor-only compound. Where A_A is absorbance of the acceptor-only, A_D is absorbance of the donor-only, I_{DA}

is emission of the FRET pair at the acceptor maxima and I_A is emission of the acceptor-only compound.

$$\Phi_{T2} = \left(\frac{A_A}{A_D}\right)\left(\frac{I_{DA,580}}{I_A - 1}\right) \tag{2.3}$$

2.2.7 Organic Synthesis

General Methods

All reactions were carried out in oven-dried (140 °C) single-necked round bottomed flasks fitted with rubber septa and under positive pressure of argon, unless stated otherwise. Organic solutions were concentrated under reduced pressure at 40°C and 50-500 mbar and residual solvent removed under high vacuum (˜1 mbar). Thin-layer chromatography (TLC) was performed using aluminium plates coated with a 0.25 mm layer of silica gel. Reaction progress was followed by TLC analysis and visualized by UV light and/or submersion in standard TLC stains ($KMnO_4$, anisaldehyde, vanilin) followed by heating with a hot-air gun (˜300°C, 10 s). Flash column chromatography was performed on silica gel (particle size 40-63 µm mesh). All materials were obtained from commercial sources and used without further purification unless stated otherwise. Dichloromethane (CH_2Cl_2), tetrahydrofuran (THF), toluene (PhMe), acetonitrile (CH_3CN), diethyl ether (Et_2O), methanol (CH_3OH) were all purified using a Chromasolv solvent purification system. *N,N*-dimethylformamide was dispensed from a septum-fitted bottle and stored under nitrogen. IR spectra were recorded as neat thin films. Each band is described as s (strong), m (medium), w (weak) in reference to the intensity and with the suffix 'br' (broad), where appropriate. ^1H and ^{13}C NMR were recorded in deuterated solvents at 400 and 100, or 300 and 75 MHz, respectively. Chemical shifts are reported as δ values (measured in ppm) referenced to TMS, δ_H 0.00 ppm. The term 'm' refers to peaks which originate from single or equivalent nuclei but coupling constants could not be assigned. In analysing AB systems where the resonances form well separated groups, these are reported as 'AB'. Peak assignment was analysed from 2D NMR experiments: COSY90, HMBC and

HSQC. Mass spectra were obtained on a liquid-chromatography time-of-flight (LCT) mass spectrometer using electrospray ionisation (ESI) with a methanol mobile phase. HRMS were recorded on an LCT spectrometer utilising a lock-mass incorporated into the mobile phase. Melting points were recorded using open capillary tubes.

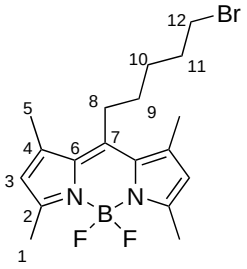

7

10-(5-bromopentyl) -5,5- difluoro -1,3,7,9- tetramethyl -5*H*- dipyrrolo [1,3,2]diazaborinine (7). Bromohexanoyl chloride (0.77 mL, 5.0 mmol) was dissolved in dry CH_2Cl_2 (50 mL) and the mixture was cooled to 0.0 °C. 2,4-dimethylpyrrole (0.95 g, 10 mmol) dissolved in dry CH_2Cl_2 (20 mL), was added dropwise over 30 min before stirring at ambient temperature for 3.5 h. The mixture was then cooled to 0 °C and neutralized by the addition of dry triethylamine (2.8 mL, 20 mmol). After 30 min, boron trifluoride etherate (2.5 mL, 10 mmol) was added slowly and the mixture was stirred at ambient temperature for 1 h. The solvent was evaporated *in vacuo* and the residue was purified on a silica gel column eluting with CH_2Cl_2 : petroleum ether (2:1). The resulting solid was recrystallised from heptane to give **7** as a red-brown solid (0.60 g, 30% yield). MP 134-135 °C, lit. 134-136 °C. IR (thin film)/cm^{-1} ν_{max}; 2928 s, 2868 s, 1546 s, 1438 s, 1305 s, 1195 s, 982 s, 797 s; ^{1}H NMR (300 MHz, chloroform-*d*) δ_H 6.05 (s, 2H, C3), 3.42 (t, J = 6.5 Hz, 2H, C12), 2.93 (dd, J = 10.0, 5.8 Hz, 2H, C8), 2.51 (s, 6H, C1), 2.40 (s, 6H, C5), 2.01 – 1.78 (m, 2H, C11), 1.73 – 1.53 (m, 4H, C9/10); ^{13}C NMR (100 MHz, chloroform-*d*) δ_C 154.0 (C2), 145.9 (C7), 140.2 (C4), 131.4 (C6), 121.7 (C3), 33.4 (C12), 32.2 (C11), 30.9 (C9/10), 28.6 (C9/10), 28.2 (C8), 16.4 (C5), 14.5 (C1); HRMS-ESI; $[M+H]^+$ calc'd for $C_{18}H_{25}BN_2F_2Br$ 397.1262 found; 397.1273. Values consistent with reported data (NMR, MS, MP).[228]

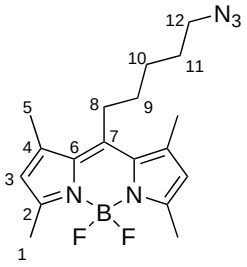

8

10-(5-azidopentyl)-5,5-difluoro -1,3,7,9- tetramethyl-dipyrrolo [1,3,2] diazaborinine 8. Bromo-BODIPY **7** (100 mg, 0.25 mmol) was dissolved in DMF (10 mL) before adding sodium azide (24 mg, 0.38 mmol) and stirring under N_2 at ambient temperature for 16 h. The mixture was then taken into water (20 mL) and extracted with CH_2Cl_2 (20 mL, 3x), dried with $MgSO_4$ and evaporated. The compound was then dissolved in ether (30 mL) and washed with water (20 mL, 2x) and brine (20 mL), dried with $MgSO_4$ and evaporated to give an orange solid (83 mg, 93% yield). MP 175-178 °C. IR (thin film)/cm^{-1} ν_{max} 2928 s, 2870 s, 2093 s, 1547 s, 1472 s, 1197 s, 1074 s, 982 s, 820 w; ^{1}H NMR (300 MHz, chloroform-*d*) δ_H 6.01 (d, J = 19.7 Hz, 2H, C3), 3.25 (dt, J = 12.3, 5.8 Hz, 2H, C12), 2.91 - 2.78 (m, 2H, C8), 2.50 (s, 6H, C1), 2.37 (s, 6H, C5), 1.74 – 1.47 (m, 6H, C9-11); ^{13}C NMR (100 MHz, chloroform-*d*) δ_C 153.9 (C2), 146.1 (C7), 140.2 (C4), 131.4 (C6), 121.7 (C3), 51.2 (C12) 31.4 (C9), 28.7 (C10/11), 28.2 (C8), 27.4 (C10/11), 16.4 (C5), 14.5 (C1); HRMS-ESI; $[M+Na]^+$ calc'd for $C_{18}H_{24}BN_5F_2Na$ 382.1991 found; 382.1998. Values consistent with reported data (NMR, MS).[229]

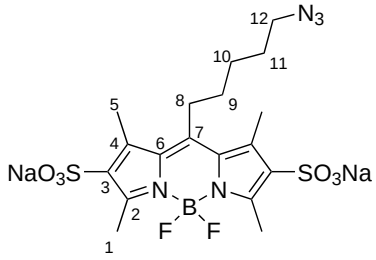

10

Sodium 10-(5-azidopentyl)-5,5-difluoro -1,3,7,9- tetramethyl -5*H*- dipyrrolo [1,3,2]

diazaborinine-2,8-disulfonate (10). AzidoBODIPY **8** (65 mg, 0.18 mmol) was dissolved in dry CH_2Cl_2 (3.0 mL) and was cooled to -25°C with addition of a few crystals of BHT. Chlorosulfonic acid was added dropwise over 15 min and stirred for a further 30 min. The solution was then allowed to warm to ambient temperature and stirred for another hour. Methanol (5.0 mL) was then added followed by sodium bicarbonate (62 mg, 0.73 mmol) and stirred for 20 min. The solvents were removed *in vacuo* and purified *via* column chromatography eluting with CH_2Cl_2:MeOH (80:20) to give the product as an orange solid (60 mg, 59% yield). MP 220-223 °C. IR (thin film)/cm^{-1} ν_{max} 3669 m, 3326 br, 2980 s, 2901 s, 2102 w, 1637 br, 1537 s, 1405 s, 1228 s, 1055 s, 896 s; ^{1}H NMR (300 MHz, methanol-d_4) δ_H 3.41 – 3.35 (m, 2H, C12), 3.30 - 3.22 (m, 2H, C8), 2.82 (s, 6H, C5), 2.77 (s, 6H, C1), 1.79 - 1.58 (m, 6H, C9-11); ^{13}C NMR (100 MHz, methanol-d_4) δ_C 153.6 (C2), 150.5 (C7), 139.6 (C4), 134.4 (C3), 130.6 (C6), 50.8 (C12), 30.9 (C9-11), 28.2 (C9-11), 28.0 (C8), 26.8 (C9-11), 13.4 (C1), 13.0 (C5); HRMS-ESI; $[M+Na]^+$ calc'd for $C_{18}H_{22}BN_5F_2S_2O_6Na_3$ 586.0766 found; 586.0757.

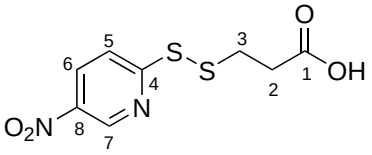

13

Synthesis of 3-((5-nitropyridin-2-yl)disulfanyl)propanoic acid (13). (2,2)'-bis-dithio-5-nitropyridine (0.80 g, 2.7 mmol) was dissolved in 80 mL MeOH:CH_2Cl_2 (1:1). A solution of 3-mercaptopropionic acid (120 µL, 0.88 mmol) in CH_2Cl_2 (1.0 mL) was added drop-wise to the reaction mixture with continuous stirring at ambient temperature, resulting in a bright yellow solution. The formation of a major UV active spot at an R_f identical to that of 3-mercaptopropionic acid (R_f = 0.45) indicated the presence of the desired product. The solvents were removed *in vacuo* and a small portion of CH_2Cl_2 was added, resulting in precipitation of an orange solid (thiolate side-product) which was filtered. The filtrate was concentrated and purified *via* flash column chromatography, eluting with 3.0% MeOH in CH_2Cl_2 giving the product as a pale yellow solid (0.20 g, 87% yield). MP 94-96 °C. IR (thin

film)/cm^{-1} ν_{max}; 3086 s, 2918 s, 1705 s, 1587 s, 1514 s, 1339 s, 1095 s, 854 s, 747 s; ^{1}H NMR (300 MHz, DMSO-d_6) δ_H 9.24 (d, J = 2.5 Hz, 1H, C7), 8.60 - 8.50 (m, 1H, C6), 8.02 (d, J = 8.9 Hz, 1H, C5), 3.07 (t, J = 6.9 Hz, 2H, C2), 2.63 (t, J = 6.9 Hz, 2H, C3); ^{13}C NMR (101 MHz, methanol-d_4) δ_C 176.5 (C1), 167.2 (C8), 144.9 (C7), 142.3 (C4), 132.6 (C6), 119.6 (C5), 33.7 (C3), 33.5 (C2); HRMS-ESI; $[M+H]^+$ calc'd for $C_8H_8N_2O_2S_2$ 261.0004 found; 261.0009.

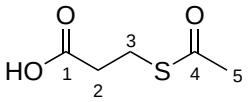

18

3-(acetylthio)propanoic acid (18). 3-iodopropionic acid (100 mg, 0.50 mmol) was dissolved in DMF (10 mL), followed by potassium thioacetate (86 mg, 0.75 mmol). The reaction mixture was stirred at ambient temperature for 6.0 h at which point the starting material was no longer present by thin-layer chromatography (TLC) and formation of a product was observed (R_f = 0.35, 5.0% MeOH in CH_2Cl_2). The mixture was with 1.0 M HCl (20 mL) twice followed by washing with brine (30 mL). The crude reaction mixture was purified *via* column chromatography eluting with 2.0% MeOH in CH_2Cl_2 which gave the product as a colourless oil (42 mg, 47% yield). IR (thin film)/cm^{-1} ν_{max}; 2935 w, 1685 s, 1423 s, 1354 s, 1133 s, 949 s, 685 s; ^{1}H NMR (400 MHz, chloroform-d) δ_H 3.11 (t, J = 6.9 Hz, 2H, C3), 2.70 (t, J = 6.9 Hz, 2H, C2), 2.34 (s, 3H, C5); ^{13}C NMR (100 MHz, chloroform-d) δ_C 195.5 (C4), 177.4 (C1), 34.1 (C2), 30.5 (C5), 23.8 (C3); HRMS-ESI; $[M-H]^+$ calc'd for $C_5H_7O_3S$ 147.0116, found; 147.0109. Values consistent with reported data (NMR, MS).[230]

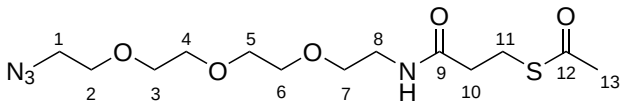

19

S-(1-azido-13- oxo-3,6,9-trioxa -12- azapentadecan-15-yl) ethanethioate (19). 3-thioesterpropionic acid **18** (20 mg, 0.14 mmol) was dissolved in THF (8.0 mL), followed

by triethylamine (33 µL, 0.24 mmol), commercially available 11-azido-3,6,9-trioxaundecan-1-amine (24 µL, 0.12 mmol) and HBTU (51 mg, 0.14 mmol). The reaction mixture was stirred at ambient temperature under an argon atmosphere. Monitoring the reaction by TLC showed consumption of the acidic starting material and formation of a major product (R_f = 0.10, 3.0% MeOH in CH_2Cl_2). The solvents were then removed *in vacuo* and the crude reaction mixture was purified *via* column chromatography eluting with 4.0% MeOH in CH_2Cl_2. This gave the product as a colourless oil (24 mg, 57% yield). IR (thin film)/cm^{-1} ν_{max}; 3359 br, 2935 w, 2108 w, 1687 s, 1649 s, 1549 s, 1294 s, 1130 s, 945 s; ^{1}H NMR (300 MHz, chloroform-*d*) δ_H 6.33 (s, 1H, NH), 3.71 – 3.53 (m, 10H, C2-6), 3.61 – 3.56 (m, 2H, C7), 3.50 - 3.41 (m, 2H, C8), 3.40 - 3.32 (m, 2H, C1), 3.07 (t, J = 7.0 Hz, 2H, C10), 2.42 (t, J = 7.0 Hz, 2H, C11), 2.33 (s, 3H, C13); ^{13}C NMR (100 MHz, chloroform-*d*) δ_C 196.0 (C12), 170.6 (C9), 70.7 (C2/-7), 70.6 (C2/-7), 70.4 (C2/-7), 70.3 (C2/-7), 70.1 (C2/-7), 69.8 (C2/-7), 50.7 (C1) 38.6 (C8), 36.1 (C11), 30.6 (C13), 24.9 (C10); HRMS-ESI; $[M+Na]^+$ calc'd for $C_{13}H_{24}N_4O_5S$ 371.1365 found; 371.1366.

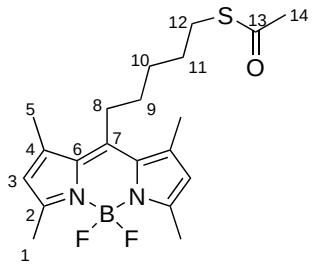

21

***S*-(5-(5,5-difluoro -1,3,7,9- tetramethyl -5*H*- dipyrrolo [1,3,2] diazaborinin-10-yl) pentyl) ethanethioate (21)** 5-bromopentyl-BODIPY **7** (100 mg, 0.25 mmol) was dissolved in acetone (20 mL) then treated with potassium thioacetate (28 mg, 0.25 mmol) and the mixture was stirred under reflux conditions for 3.0 h. The solvent was removed *in vacuo* and resuspended in CH_2Cl_2 before washing with water (3.0 times). The solvent was removed *in vacuo* to give the product as an orange solid (89 mg, 91% yield). MP 146-149 °C, lit. 146-148 °C. IR (thin film)/cm^{-1} ν_{max}; 2927 s, 2865 s, 1687 s, 1545 s, 1472 s, 1307 s, 1194

s, 973 s, 714 s; ^{1}H NMR (300 MHz, chloroform-*d*) δ_{H} 6.04 (s, 2H, C3), 3.43 – 2.76 (m, 4H, C8/12), 2.51 (s, 6H, C1), 2.39 (s, 6H, C5), 2.33 (s, 3H, C14), 1.75 – 1.46 (m, 6H, C9-11); ^{13}C NMR (100 MHz, chloroform-*d*) δ_{C} 195.8 (C13), 153.9 (C2), 146.1 (C7), 140.3 (C4), 131.4 (C6), 121.6 (C3), 31.4 (C9/-11), 30.7 (C14), 29.4 (C9/-11), 29.3 (C9/-11), 28.8 (C8/12), 28.2 (C8/12), 16.4 (C5), 14.4 (C1); HRMS-ESI; $[M+Na]^{+}$ calc'd for $C_{20}H_{27}BN_2F_2SNa$ 415.1803 found; 415.1814. Values consistent with reported data (NMR, MS, MP).[228]

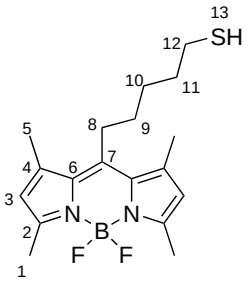

22

(5-(5,5-difluoro-1,3,7,9-tetramethyl -5*H*- dipyrrolo [1,3,2] diazaborinin-10-yl) pentane -1- thiol (22) Pentylthioester-BODIPY **21** (80 mg, 0.20 mmol) was dissolved in EtOH (oxygen removed) followed by addition of potassium carbonate (33 mg, 0.24 mmol) and heated at 30°C for 4.0 h. Product formation was confirmed by TLC (R_f = 0.90, CH_2Cl_2), the mixture was then acidified with sat. NH_4Cl and extracted with CH_2Cl_2. The solvent was removed *in vacuo* and the resulting mixture was purified by column chromatography, eluting with 55:45 CH_2Cl_2:petroleum ether to give the product as an orange solid (54 mg, 77% yield). MP 118-120 °C, lit. 120-121 °C. IR (thin film)/cm^{-1} ν_{max}; 3379 br m, 2927 w, 2853 s, 1547 s, 1408 s, 1224 s, 1158 s, 974 s, 803 s; ^{1}H NMR (300 MHz, chloroform-*d*) δ_{H} 6.05 (s, 2H, C3), 3.08 – 2.84 (m, 2H, C8), 2.61 – 2.53 (m, 2H, C12), 2.51 (s, 6H, C1), 2.41 (s, 6H, C5), 1.75 – 1.55 (m, 6H, C9-11), 1.34 (t, J = 7.8 Hz, 1H, SH); ^{13}C NMR (100 MHz, chloroform-*d*) δ_{C} 153.9 (C2), 146.1 (C7), 140.2 (C4), 131.4 (C6), 121.7 (C3), 33.5 (C12), 31.3 (C9/-11), 28.9 (C9/-11), 28.3 (C8), 24.4 (C9/-11), 16.4 (C5), 14.4 (C1); HRMS-ESI; $[M+Na]^{+}$ calc'd for $C_{18}H_{25}BN_2F_2SNa$ 373.1697 found; 373.1690. Values consistent with reported data (NMR, MS, MP).[228]

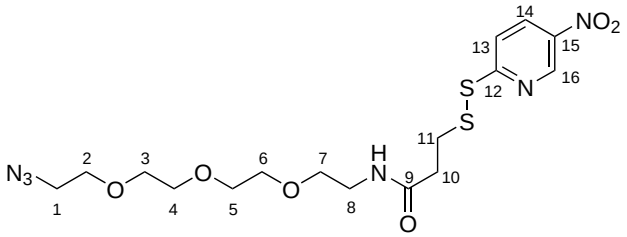

23

N-(2-(2-(2-(2-azidoethoxy) ethoxy) ethoxy) ethyl) -3- ((3-nitropyridin-2-yl) disulfanyl) propanamide 23. Disulfide **13** (110 mg, 0.43 mmol) was dissolved in a solution of dry THF (15 mL) then treated with triethylamine (105 µL, 0.78 mmol), 11-azido-3,6,9-trioxaundecan-1-amine (77 µL, 0.39 mmol) and HBTU (160 mg, 0.43 mmol). The solution was left to stir at ambient temperature for 16 h. Monitoring by TLC revealed formation of a major product (R_f = 0.60, 5.0% MeOH in CH_2Cl_2) and the solvent was then removed *in vacuo*. The reaction mixture was purified *via* column chromatography eluting with 3.0% MeOH in CH_2Cl_2, the gradient was increased to 10% MeOH in CH_2Cl_2 after elution of the first compound. The product was recovered as a yellow oil (146 mg, 81% yield). IR (thin film)/cm^{-1} ν_{max}; 3315 br w, 3064 w, 2882 w, 2194 m s, 1723 s, 1657 s, 1589 s, 1518 s, 1441 s, 1343 s, 1269 s, 1097 s, 855 s, 749 s; ^{1}H NMR (300 MHz, DMSO-d_6) δ_H 9.35 - 9.15 (m, 1H, C16), 8.65 – 8.49 (m, 1H, C14), 8.16 - 7.98 (m, 1H, C13), 3.63 – 3.56 (m, 2H, C2/-7), 3.56 – 3.47 (m, 10H, C2/-7), 3.42 - 3.35 (m, 4H, C1 & C2/-7), 3.20 (q, J = 5.8 Hz, 2H, C8), 3.08 (t, J = 7.0 Hz, 2H, C10), 2.52 - 2.48 (m, 2H, C11); ^{13}C NMR (100 MHz, DMSO-d_6) δ_C 170.2 (C9), 167.9 (C15), 145.4 (C16), 142.8 (C12), 133.1 (C14), 120.0 (C13), 70.2 (C2/-7), 70.2 (C2/-7), 70.0 (C2/-7), 69.7 (C2/-7), 69.5 (C2/-7), 50.5 (C1), 39.1 (C8), 34.9 (C11), 34.8 (C10); HRMS-ESI; $[M+Na]^+$ calc'd for $C_{16}H_{24}N_6O_6S_2$ 483.1096 found; 483.1095.

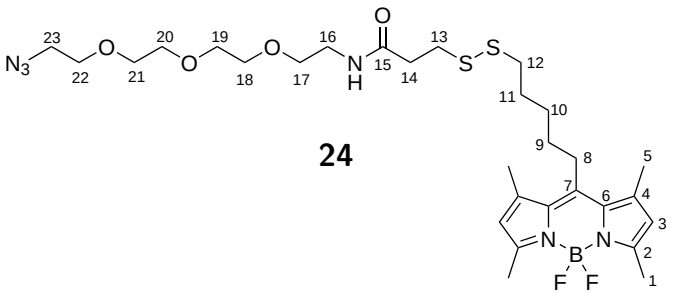

24

1

N-(2-(2-(2-(2-azidoethoxy) ethoxy) ethoxy) ethyl) -3-((5-(5,5- difluoro -1,3,7,9-tetramethyl- 5*H*- 4λ^4,5λ^4- dipyrrolo [1,2-*c*:2', 1'-*f*] [1,3,2] diazaborinin-10-yl) pentyl) disulfanyl) propanamide 24. Azido disulfide **23** (110 mg, 0.24 mmol) was dissolved in a solution of MeOH/CH_2Cl_2 (1:1, 30 mL). BODIPY thiol **22** (61 mg, 0.17 mmol) was then added to the solution and stirred at ambient temperature for 16 h leading to formation of a fluorescent product (R_f = 0.40, 3.0% MeOH in CH_2Cl_2). The solvent was then removed *in vacuo* and the crude mixture was purified *via* column chromatography eluting with 2.0% MeOH in CH_2Cl_2. The product was recovered as a yellow oil, however, some residual azide starting material was present by nuclear magnetic resonance (NMR) and so the mixture was further purified *via* HPLC using an isocratic gradient of 65% MeCN in water, the product eluted after a retention time of 16 min (C18 column, 1.0 mL min^{-1}) to give an orange solid (16 mg, 40% yield). MP 105-107 °C. IR (thin film)/cm^{-1} ν_{max}; 3320 br w, 2912 w, 2104 s, 1663 s, 1545 s, 1488 s, 1341 s, 1245 s, 1149 s, 990 s, 717 s; ^{1}H NMR (300 MHz, chloroform-*d*) δ_H 6.23 (br s, 1H, NH), 6.05 (s, 2H, C3), 3.74 – 3.60 (m, 12H, C16/-22), 3.58 – 3.51 (m, 2H, C16/-22), 3.51 – 3.41 (m, 2H, C16/-22), 3.43 – 3.35 (m, 2H, C23), 2.94 (m, 4H, C8 & C14), 2.70 (t, J = 7.1 Hz, 2H, C12), 2.58 (t, J = 7.3 Hz, 2H, C13), 2.51 (s, 6H, C1), 2.41 (s, 6H, C5), 1.85 – 1.69 (m, 2H, C9/-11), 1.67 – 1.55 (m, 4H, C9/-11); ^{13}C NMR (100 MHz, chloroform-*d*) δ_C 170.8 (C15), 153.9 (C2), 146.1 (C7), 140.3 (C4), 131.4 (C6), 121.7 (C3), 70.7 (C16/-22), 70.6 (C16/-22), 70.6 (C16/-22), 70.3 (C16/-22), 70.1 (C16/-22), 69.8 (C16/-22), 50.7 (C23), 39.2 (C16/-22), 38.2 (C12), 35.9 (C13), 33.7 (C14), 31.5 (C9/-11), 28.9 (C9/-11), 28.7 (C9/-11), 28.3 (C8), 16.5 (C5), 14.5 (C1); HRMS-ESI; $[M+Na]^+$ calc'd for $C_{29}H_{45}BF_2N_6O_4S_2$ 677.2903 found; 677.2903.

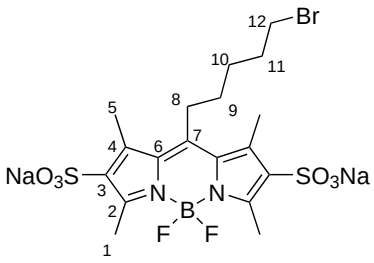

25

sodium 10- (5-bromopentyl)- 5,5-difluoro - 1,3,7,9 - tetramethyl- 5*H*-4λ^4, 5λ^4 - dipyrrolo [1,2-*c*: 2',1'-*f*] [1,3,2] diazaborinine -2,8- disulfonate 46. BODIPY bromide **7** (100 mg, 0.25 mmol) was dissolved in dry CH_2Cl_2 (5.0 mL) and was cooled to -25°C with addition of a few crystals of butylated hydroxytoluene (BHT). Chlorosulfonic acid (35 µL, 0.53 mmol diluted in 1.1 mL CH_2Cl_2) was then added dropwise over 15 min and stirred for a further 30 min. The solution was then allowed to warm to ambient temperature and stirred for 1.0 h. Methanol (5.0 mL) was then added followed by sodium bicarbonate (95 mg, 1.1 mmol) and stirred for 20 min. The solvents were removed *in vacuo* and purified *via* column chromatography eluting with MeOH in CH_2Cl_2 (20:80) to give the product as a brown solid (130 mg, 83% yield). MP 209-212 °C. IR (thin film)/cm^{-1} ν_{max}; 3668 m, 2981 w, 2902 w, 1638 w, 1453 s, 1406 s, 1394 s, 1250 s, 1229 s, 1066 s, 1056 s, 896 s, 793 s; ^{1}H NMR (300 MHz, methanol-d_4) δ_H 3.58 – 3.45 (m, 2H, C12), 3.33 (dt, J = 3.3, 1.6 Hz, 2H, C8), 2.82 (s, 6H, C5), 2.77 (s, 6H, C1), 2.04 – 1.90 (m, 2H, C9/-11), 1.79 - 1.71 (m, 4H, C9/-11); ^{13}C NMR (100 MHz, methanol-d_4)) δ_C 153.6 (C2), 150.5 (C7), 139.7 (C4), 134.4 (C3), 130.6 (C6), 32.7 (C12), 32.0 (C10/11), 30.5 (C9), 28.1 (C8), 28.0 (C10/11) 13.4 (C5), 13.0 (C1); HRMS-ESI; $[M+Na]^+$ calc'd for $C_{18}H_{22}BBrF_2N_2Na_2O_6S_2$ 622.9857 found; 622.9858.

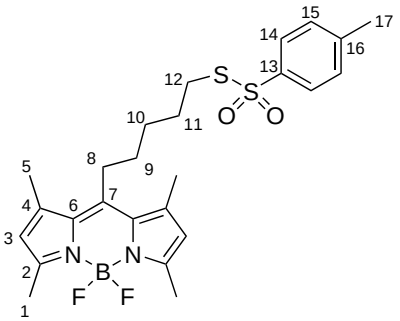

28

S-(5-(5,5-difluoro-1,3,7,9-tetramethyl- 5*H*-4λ^4,5λ^4-dipyrrolo [1,2-*c*:2',1'-*f*] [1,3,2] diazaborinin-10-yl) pentyl) 4-methylbenzenesulfonothioate 28. BODIPY bromide **7** (100 mg, 0.25 mmol) was dissolved in dry acetone (15 mL) followed by the addition of potassium *p*-toluenethiosulfonate (140 mg, 0.60 mmol). The mixture was heated under reflux conditions for 4.0 h resulting in formation of a major product (R_f = 0.70, CH_2Cl_2). The solvent was removed *in vacuo* and purified *via* column chromatography eluting with petroleum ether:CH_2Cl_2 (1:2) to give the product as an orange solid (69 mg, 72% yield). MP 151-153 °C. IR (thin film)/cm^{-1} ν_{max}; 2929 w, 1718 s, 1545 s, 1470 s, 1406 s, 1318 s, 1160 s, 985 s, 813 s; ^{1}H NMR (300 MHz, chloroform-*d*) δ_H 7.90 – 7.74 (m, 1H, C15), 7.32 (d, *J* = 8.1 Hz, 1H, C14), 6.04 (s, 2H, C3), 3.09 – 2.94 (m, 2H, C12), 2.91 – 2.77 (m, 2H, C8), 2.50 (s, 6H, C1), 2.42 (s, 3H, C17), 2.34 (s, 6H, C5), 1.72 – 1.60 (m, 2H, C11), 1.55 – 1.46 (m, 4H, C9-10); ^{13}C NMR (100 MHz, chloroform-*d*) δ_C 153.9 (C2), 145.8 (C7), 144.9 (C16), 142.0 (C13), 140.2 (C4), 131.4 (C6), 129.9 (C15), 127.0 (C14), 121.7 (C3), 35.7 (C12), 31.1 (C9), 28.9 (C10/11), 28.4 (C10/11), 28.0 (C8), 21.6 (C17), 16.4 (C5), 14.5 (C1); HRMS-ESI; $[M+Na]^+$ calc'd for $C_{25}H_{31}BF_2N_2O_2S_2$ 527.1786 found; 527.1788.

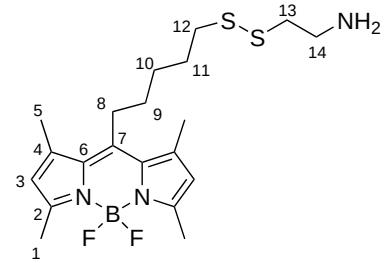

30

2-((5-(5,5-difluoro-1,3,7,9-tetramethyl- 5*H*-4λ^4,5λ^4 -dipyrrolo [1,2-*c*:2',1'-*f*] [1,3,2] diazaborinin-10-yl) pentyl) disulfanyl)ethan-1-amine 30. BODIPY **28** (20 mg, 0.04 mmol) was dissolved in MeOH:CH_2Cl_2 (1:1 5.0 mL) followed by the addition of cysteamine (4.5 mg, 0.04 mmol) and triethylamine (7.0 µL, 0.05 mmol). The solution was stirred at ambient temperature for 15 h leading to formation of a fluorescent product (R_f = 0.1, CH_2Cl_2). The solvents were removed *in vacuo*, resuspended in CH_2Cl_2 and washed with saturated potassium bicarbonate solution (3 times). The organic phase was dried with $MgSO_4$, filtered and the solvent was removed *in vacuo* to give the product as an orange solid (18 mg, 95% yield). MP 133-135 °C. IR (thin film)/cm^{-1} ν_{max}; 2925 w, 2862 w, 1548 s, 1509 s, 1409 s, 1370 s, 1224 s, 1079 s, 985 s, 714 w; ^{1}H NMR (300 MHz, chloroform-*d*) δ_H 6.02 (d, J = 19.3 Hz, 2H, C3), 3.03 – 2.90 (m, 4H, C8& C14), 2.79 – 2.66 (m, 4H, C12& C13), 2.49 (s, 6H, C1), 2.41 (s, 6H, C5), 1.82 – 1.71 (m, 2H, C11), 1.67 – 1.55 (m, 4H, C9-101), 1.45 (br s, 2H, NH_2); ^{13}C NMR (100 MHz, chloroform-*d*) δ_C 153.9 (C2), 146.1 (C7), 140.2 (C4), 131.4 (C6), 121.7 (C3), 42.6 (C13/14), 40.6 (C13/14), 38.5 (C12), 31.5 (C9), 29.8 (C10/-11), 28.7 (C10/-11), 28.3 (C8), 16.5 (C5), 14.5 (C1); HRMS-ESI; $[M+H]^+$ calc'd for $C_{20}H_{30}BF_2N_3S_2$ 426.2021 found; 426.2023

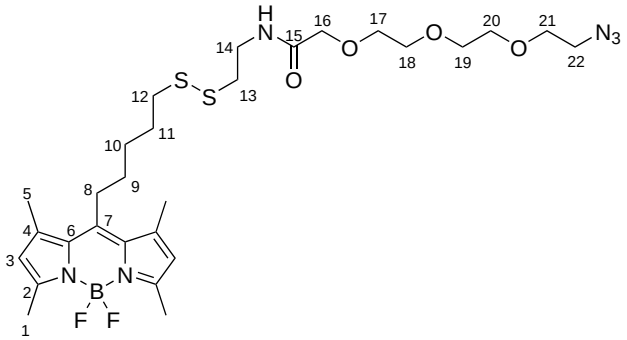

32

2-(2-(2- (2-(2- azidoethoxy) ethoxy) ethoxy) -*N*-(2-((5- (5,5-difluoro -1,3,7,9-tetramethyl- 5*H*- 4λ^4,5λ^4- dipyrrolo [1,2-*c*: 2',1'-*f*] [1,3,2] diazaborinin-10-yl) pentyl) disulfanyl) ethyl) acetamide 32. BODIPY **30** (280 mg, 0.67 mmol) was dissolved in dry THF (25 mL), followed by the addition of 11-azido-3,6,9-trioxaundecanoic acid

(130 µL, 0.61 mmol), triethylamine (160 µL, 1.2 mmol) and HBTU (250 mg, 0.67 mmol). The reaction mixture was stirred at ambient temperature for 16 h and monitoring by TLC revealed formation of a fluorescent product ($R_f = 0.10$, 2.0% MeOH in CH_2Cl_2). The solvent was removed *in vacuo* and the crude product was purified *via* column chromatography eluting with 2.0% MeOH in CH_2Cl_2 which gave the product as an orange solid (280 mg, 71% yield). MP 109-111 °C. IR (thin film)/cm^{-1} ν_{max}; 3332 br, 2922 w, 2880 w, 2106 m, 1720 s, 1660 s, 1544 s, 1442 s, 1407 s, 1344 s, 1197 s, 1097 s, 989 s, 832 w; ^{1}H NMR (300 MHz, chloroform-*d*) δ_H 7.17 (br s, 1H, NH), 5.98 (s, 2H, C3), 3.92 (s, 2H, C16), 3.66 – 3.53 (m, 8H, C14/17-21), 3.49 - 3.42 (m, 2H, C17/-21) 3.37 – 3.24 (m, 2H, C22), 2.91 - 2.80 (m, 2H, C8), 2.74 (dd, J = 8.7, 4.4 Hz, 2H, C13), 2.64 (t, J = 7.1 Hz, 2H, C12), 2.44 (s, 6H, C1), 2.33 (s, 6H, C5), 1.74 – 1.61 (m, 2H, C11), 1.61 – 1.45 (m, 4H, C9-10); ^{13}C NMR (100 MHz, chloroform-*d*) δ_C 170.1 (C15), 153.8 (C2), 146.1 (C7), 140.3 (C4), 131.4 (C6), 121.6 (C3), 71.0 (C14/16/-21), 70.9 (C14/16/-21), 70.7 (C14/16/-21), 70.6 (C14/16/-21), 70.4 (C14/16/-21), 70.0 (C14/16/-21), 50.7 (C22), 38.4 (C12), 37.7 (C13/16/-21), 37.6 (C13/16/-21), 31.4 (C9), 28.9 (C10/11), 28.7 (C10/11), 28.2 (C8), 16.4 (C5), 14.4 (C1); HRMS-ESI; [M-Na]$^-$ calc'd for $C_{28}H_{43}BF_2N_6O_4S_2Na$ 663.2746 found; 663.2744.

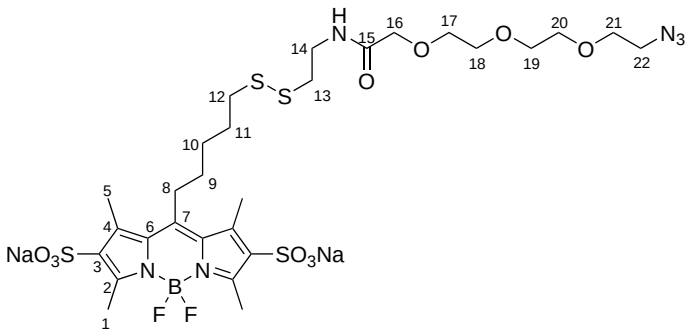

33

sodium 10- (1-azido-11-oxo -3,6,9- trioxa- 15,16-dithia -12- azahenicosan-21-yl) -5,5-difluoro -1,3,7,9- tetramethyl- 5*H*- 4λ^4,5λ^4 -dipyrrolo [1,2-*c*:2',1'-*f*] [1,3,2] diazaborinine -2,8- disulfonate 33. BODIPY **32** (50mg, 0.078 mmol) was dissolved in dry CH_2Cl_2 (3.0 mL) and was cooled to -25°C with addition of a few crystals of BHT.

Chlorosulfonic acid (11 µL, 0.16 mmol, diluted into 0.34 mL of CH_2Cl_2) was then added dropwise over 15 min and stirred for a further 30 min. The solution was then allowed to warm to ambient temperature and stirred for 1.0 h. Methanol (2.0 mL) was then added followed by sodium bicarbonate (33 mg, 1.1 mmol) and stirred for 20 min. The solvents were removed *in vacuo* and purified *via* column chromatography eluting with MeOH in CH_2Cl_2 (20:80) to give the product as an orange solid (35 mg, 53% yield). MP 137-140 °C. IR (thin film)/cm^{-1} ν_{max}; 3317 br, 2927 w, 2865 w, 2104 m, 1662 s, 1548 s, 1472 s, 1370 s, 1307 s, 1200 s, 1081 s, 986 s, 856 s; ^{1}H NMR (300 MHz, DMSO-d_{-6}) δ_H 3.88 (s, 2H, C16), 3.66 - 3.51 (m, 12H, C13/14/17-22), 3.46 – 3.36 (m, 4H, C17/-22 & C23), 3.13 - 2.99 (m, 2H, C8), 2.85 – 2.71 (m, 4H, C12 & C13/14), 2.67 (s, 6H, C5), 2.61 (s, 6H, C1), 1.85 - 1.73 (m, 2H, C11), 1.70 - 1.59 (m, 4H, C9/10); ^{13}C NMR (100 MHz, DMSO-d_{-6}) δ_C 169.8 (C15), 153.0 (C2), 149.1 (C7), 138.1 (C4), 130.2 (C3), 126.7 (C6), 70.7 (C16/-22), 70.4 (C16/-22), 70.2 (C16/-22), 70.1 (C16/-22), 70.0 (C16/-22), 69.7 (C16/-22), 50.4 (C23), 38.0 (C12/-14), 37.9 (C12/-14), 37.4 (C12/-14), 31.3 (C9/10), 28.6 (C9/10), 28.5 (C11), 28.1 (C8), 14.3 (C1), 14.2 (C5); HRMS-ESI; [M-Na]$^-$ calc'd for $C_{28}H_{41}BF_2N_6NaO_{10}S_4$ 821.1726 found; 821.1719.

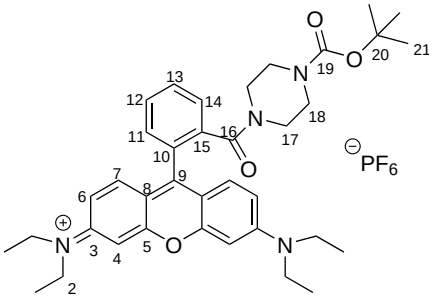

38

Synthesis of (*N*-(9-(2-(4-(*tert*-butoxycarbonyl)piperazine-1-carbonyl)phenyl)-6-(diethylamino)-*3H*-xanthen-3-ylidene)-*N*-ethylethanaminium (38). RhoB base (1.0 g, 2.3 mmol) was dissolved in CH_2Cl_2, under N_2, before adding N-boc piperazine (Sigma, 0.46 g, 2.5 mmol), triethylamine (0.6.0 mL, 4.5 mmol) and HBTU (0.93 g, 2.5 mmol) and stirring for 24 h. This resulted in formation of a major product (9:1 CH_2Cl_2:MeOH, R_f = 0.80) and the solvent was then removed *in vacuo*. This crude mixture was then purified *via*

flash column chromatography eluting with 3.0% MeOH in CH_2Cl_2 to give the product as a dark purple solid (1.3 g, 98% yield). MP = 136-138 °C. IR (thin film)/cm^{-1}; 3661 w, 3356 br, 2988 w, 2901 w, 1636 s, 1595 s, 1465 s, 1337 s, 1259 s, 1127 s, 1066 s, 959 s, 772 s; ^{1}H NMR (400 MHz, chloroform-*d*) δ_H 7.80 - 7.68 (m, 2H, C12-13), 7.62 – 7.49 (m, 1H, C14), 7.39 - 7.28 (m, 1H, C11), 7.25 (d, J = 9.5 Hz, 2H, C7), 6.99 (d, J = 9.5 Hz, 2H, C6), 6.79 (s, 2H, C4), 3.78 – 3.53 (m, 8H, C2), 3.39 -3.25 (m, 8H, C17-18), 1.46 (s, 9H, C21), 1.39 – 1.23 (m, 12H, C1); ^{13}C NMR (100 MHz, chloroform-*d*) δ_C 167.8 (C16), 157.8 (C5/8), 156.0 (C9), 155.7 (C8), 154.6 (C19), 135.2 (C10), 132.1 (C7), 130.8 (C15), 130.4 (C11/-13), 130.2 (C11/-13), 130.2 (C11/-13), 127.6 (C14), 114.1 (C6), 113.8 (C5/8), 96.4 (C4), 80.5 (C20), 47.4 (C17/18), 46.1 (C2), 41.9 (C17/18), 28.3 (C21), 12.6 (C1); HRMS-ESI; M^+ calc'd for $C_{37}H_{47}N_4O_4$ 611.3597 found; 611.3592. Values consistent with reported data (NMR, MS).[231]

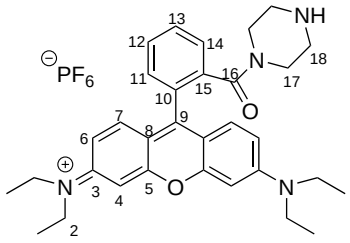

37

Synthesis of *N*-(6-(diethylamino) -9- (2-(piperazine-1-carbonyl) phenyl)- *3H*-xanthen -3- ylidene)- *N*-ethylethanaminium (37). RhoB N-boc piperazine (**38**, 200 mg, 0.33 mmol) was suspended in water (10 mL) and transferred to a microwave vial. The suspension was heated to 170 °C for 30 min (150 W). The suspension had dissolved an exhibited formation of a major product (R_f = 0.30, 9:1 CH_2Cl_2:MeOH) and consumption of **37**. The solution was acidified with addition of HCl (0.10 M, 10 mL) and washed with CH_2Cl_2 (20 mL, 3.0x) to remove any residual starting material. The aqueous phase was then basified *via* addition of potassium carbonate to reach pH 10. The aqueous phase was then extracted with CH_2Cl_2 (30 mL, 3.0x) until a faint pink colour persisted in the aquoues phase. The CH_2Cl_2 extractions were combined, dried with $MgSO_4$ and concentrated *in vacuo* to give **37** as a viscous purple oil which was used without further purification (107 mg, 64%) MP =

165-169 °C, lit. 218-220 °C. IR (thin film)/cm^{-1}; 3374 br, 2978 w, 2934 w, 2877 w, 1645 s, 1589 s, 1530 s, 1468 s, 1414 s, 1395 s, 1339 s, 1275 s, 1248 s, 1161 s, 1074 s, 1009 s, 963 s, 923 s, 840 s, 740 s, 684 s; ^{1}H NMR (300 MHz, methanol-d_4) δ_{H} 7.70 - 7.62 (m, 2H, C12-13), 7.59 – 7.53 (m, 1H, C14), 7.37 – 7.30 (m, 1H, C11), 7.25 (d, J = 9.4 Hz, 2H, C7), 6.97 (dd, J = 9.4, 2.3 Hz, 2H, C6), 6.78 (d, J = 2.3 Hz, 2H, C4), 3.73 – 3.54 (m, 8H, C2), 3.41 - 3.21 (m, 4H, C17/18), 2.55 – 2.46 (m, 4H, C17/18), 1.27 - 1.16 (m, 12H, C1); ^{13}C NMR (100 MHz, methanol-d_4) δ_{C} 169.4 (C16), 159.3 (C8), 157.2 (C3), 157.0 (C9), 136.8 (C10), 133.3 (C7), 132.0 (C15), 131.7 (C11/-13), 131.3 (C11/-13), 131.1 (C11/-13), 128.8 (C14), 115.4 (C6), 114.8 (C5), 97.3 (C4), 46.9 (C2), 45.9 (C17/18), 43.4 (C17/18), 12.8 (C1); HRMS-ESI; M^+ calc'd for $C_{32}H_{39}N_4O_2$ 511.3073 found; 511.3073. Values consistent with reported data (NMR, MS).[232]

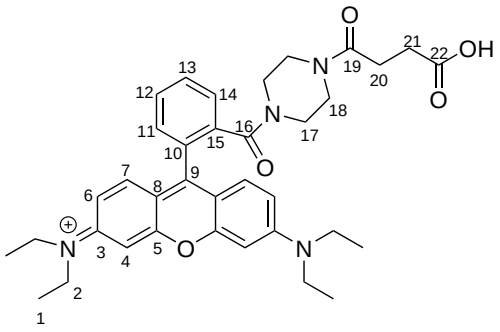

40

***N*-(9-(2-(4-(3- carboxypropanoyl) piperazine-1-carbonyl) phenyl) -6- (diethyl-amino) -*3H*- xanthen -3- ylidene)- *N*-ethylethanaminium 40.** RhoB **37** (109 mg, 0.21 mmol) was dissolved in dry THF (20 mL) before adding triethylamine (57 µL, 0.42 mmol) and succinic anhydride (53 mg, 0.53 mmol). The reaction mixture was left to stir overnight and monitored by TLC to show formation of a product (R_f = 0.10, 8.0% MeOH in CH_2Cl_2). The solvent was removed *in vacuo* and purified *via* column chromatography, eluting with CH_2Cl_2:MeOH (90:10) to give the product as a dark purple solid (26 mg, 20% yield). MP 167-169 °C, lit. 166-168 °C. IR (thin film)/cm $^{-1}$ ν_{max} 3325 br, 2944 w, 1641 s, 1636 s, 1456 s, 1017 s, 903 s, 781 s; ^{1}H NMR (300 MHz, methanol-d_4) δ_{H} 7.80 - 7.74 (m, 2H, C12-13), 7.72 – 7.67 (m, 1H, C14), 7.57 – 7.49 (m, 1H, C11), 7.28 (d, J = 2.9 Hz, 2H, C7),

7.15 - 7.05 (m, 2H, C6), 6.96 (s, 2H, C4), 3.74 – 3.62 (m, 8H, C2), 3.47 - 3.35 (m, 8H, C17/18), 2.56 (t, J = 7.0 Hz, 2H, C20/21), 2.43 (t, J = 7.0 Hz, 2H, C20/21), 1.31 (t, J = 7.1 Hz, 12H, C1); ^{13}C NMR (100 MHz, methanol-d_4) δ_C 179.8 (C22), 173.7 (C19), 169.6 (C16), 159.3 (C8), 157.2 (C3), 157.0 (C9), 136.6 (C10), 133.2 (C7), 132.2 (C15), 131.7 (C11), 131.2 (C12/13) 129.0 (C14), 115.4 (C6), 114.9 (C5), 97.4 (C4), 46.9 (C2), 45.7 (C17/18), 45.4 (C17/18), 33.4 (C20/21), 30.2 (C20/21), 12.8 (C1); HRMS-ESI; $[M+H]^+$ calc'd for $C_{36}H_{43}N_4O_5$ 611.3233 found; 611.3224. Values consistent with reported data (NMR, MS, MP).[232]

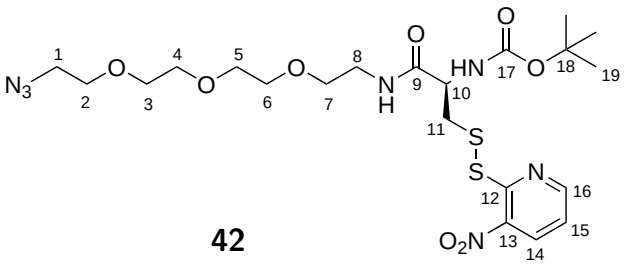

42

***tert*-butyl (1-azido-15- ((3-nitropyridin-2-yl)disulfanyl) -13- oxo -3,6,9- trioxa-12- azapentadecan-14-yl) carbamate 42.** Commercially Npys-Boc-Cys-OH (Sigma, 150 mg, 0.4 mmol) and azide-PEG-amine **47** (96 mg, 0.44 mmol) were dissolved in dry THF (15 mL) followed by triethylamine (110 µL, 0.80 mmol) and HBTU (170 mg, 0.44 mmol) and stirred at ambient temperature for 16 h. The solvent was evaporated and the resulting yellow oil was purified *via* column chromatography eluting with CH_2Cl_2:MeOH (95:5.0) to give the product as a yellow oil (220 mg, 96%). IR (thin film)/cm $^{-1}$ ν_{max} 3301 br, 2977 w, 2870 w, 2103 s, 1711 s, 1667 s, 1582 s, 1517 s, 1342 s, 1120 s, 958 w, 856 s; ^{1}H NMR (300 MHz, DMSO-d_{-6}) δ_H 8.92 (dd, J = 4.5, 1.4 Hz, 1H, C16), 8.61 (dd, J = 8.2, 1.4 Hz, 1H, C14), 7.57 (dd, J = 8.2, 4.5 Hz, 1H, C15), 6.52 (d, J = 7.3 Hz, 1H, NH), 4.16 – 3.91 (m, 1H, C10), 3.63 – 3.57 (m, 4H, C2/-8), 3.56 – 3.49 (m, 8H, C2/-8), 3.38 (dd, J = 6.5, 3.4 Hz, 2H, C1), 3.27 (dd, J = 13.1, 4.4 Hz, 1H, C11H$_{A/B}$), 3.13 (dd, J = 13.1, 7.7 Hz, 1H, H$_{A/B}$), 1.31 (s, 9H, C19); ^{13}C NMR (100 MHz, DMSO-d_6) δ_C 173.5 (C9), 155.6 (C17), 155.0 (C12), 154.2 (C16), 142.5 (C13), 134.5 (C14), 121.9 (C15), 77.8 (C18), 69.8 (C2/-8), 69.7 (C2/-8), 69.3 (C2/-8), 66.8 (C2/-8), 54.7 (C10), 50.0 (C1), 45.5 (C10), 42.0 (C11), 28.2 (C19); HRMS-ESI;

$[M+H]^+$ calc'd for $C_{21}H_{33}N_7O_8S_2$ 576.1910 found; 576.1927.

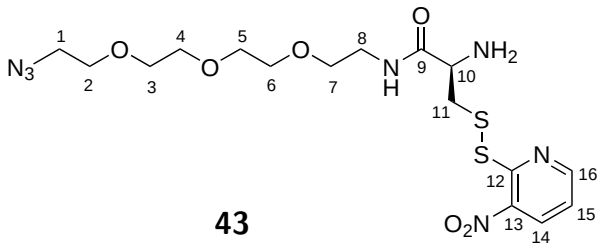

43

2-amino-*N*-(2-(2-(2-(2-azidoethoxy) ethoxy)ethoxy)ethyl) -3- ((3-nitropyridin-2-yl) disulfanyl) propanamide 43. N-boc cysteine-azide **42** (370 mg, 0.62 mmol) was treated with 1:1 TFA:CH_2Cl_2 (6.0 mL) and stirred in air for 1.0 h. Complete consumption of the starting material was observed by TLC (95:5 CH_2Cl_2:MeOH, $R_f = 0.20$). The solution was treated with toluene (10 mL) and evaporated. The resulting oil was used without further purification (290 mg, quant.). IR (thin film)cm $^{-1}$ ν_{max} 3365 br, 3230 br, 2926 w, 2885 w, 2110 m, 1668 s, 1583 s, 1337 s, 1194 s, 1131 s, 801 s; ^{1}H NMR (300 MHz, DMSO-d_6) δ_H 8.99 – 8.90 (m, 1H, C16), 8.67 – 8.61 (m, 1H, C14), 7.99 - 7.89 (br m, 1H, NH), 7.60 (dd, J = 8.2, 4.6 Hz, 1H, C15), 4.49 (tt, J = 15.3, 7.7 Hz, 1H, C10), 3.93 (d, J = 2.2 Hz, 2H, C1/-8), 3.70 – 3.49 (m, 10H, C1/-8), 3.43 – 3.33 (m, 4H, C1/-8), 3.24 (dd, J = 13.5, 8.1 Hz, 4H, C11); ^{13}C NMR (100 MHz, DMSO-d_6) δ_C 169.1 (C9), 155.1 (C12), 154.3 (C16), 142.6 (C13), 134.5 (C14), 122.0 (C15), 70.2 (C2/-8), 69.8 (C2/-8), 69.7 (C2/-8), 69.7 (C2/-8), 69.6 (C2/-8), 69.2 (C2/-8), 51.7 (C10), 50.0 (C1), 38.9 (C11); HRMS-ESI; $[M+H]^+$ calc'd for $C_{16}H_{25}N_7O_6S_2Na$ 498.1205 found; 498.1211.

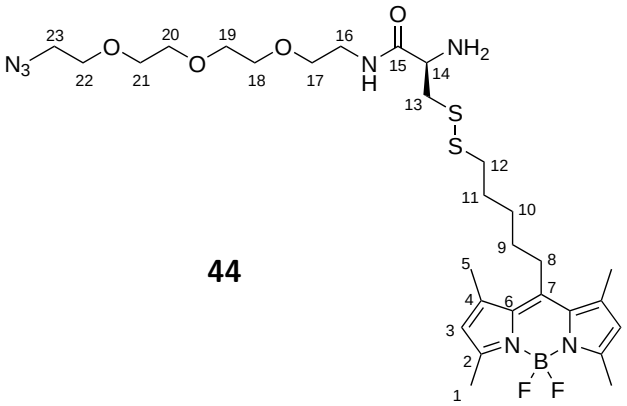

44

2-amino-*N*-(2- (2-(2-(2- azidoethoxy) ethoxy) ethoxy)ethyl) -3- ((5-(5,5-difluoro -1,3,7,9- tetramethyl -5*H*- dipyrrolo [1,3,2] diazaborinin -10- yl) pentyl) disulfanyl) propanamide 44. PEG-azide **43** (170 mg, 0.360 mmol) was dissolved in a 1:1 mixture of CH_2Cl_2:MeOH (30 mL) containing potassium carbonate (50 mg, 0.360 mmol). BODIPY-thiol **22** (63 mg, 0.18 mmol) was dissolved in 1:1 CH_2Cl_2:MeOH (3.0 mL) and added dropwise to the reaction mixture. The solution was then stirred overnight, resulting in a major fluorescent product (R_f = 0.35, 97:3 CH_2Cl_2:MeOH). The solution was evaporated and the resulting orange oil was purified *via* column chromatography eluting with 1.0% MeOH in CH_2Cl_2 before increasing to 2.0% MeOH giving the product as a orange glassy solid (61 mg, 51%). MP 98-100 °C. IR (thin film) cm^{-1} ν_{max} 3677 br w, 2918 m, 2105 m, 1663 s, 1549 s, 1473 s, 1307 s, 1200 s, 1075 s, 802 s; ^{1}H NMR (300 MHz, chloroform-*d*) δ_H 7.72 - 7.64 (m, 1H, NH), 6.02 (s, 2H, C3), 3.73 – 3.61 (m, 14H, C13/17/-23), 3.57 (t, J = 5.2 Hz, 2H, C17/-23), 3.52 – 3.42 (m, 2H, C16), 3.39 - 3.30 (m, 2H, C17/-23), 3.21 (dd, J = 13.7, 3.6 Hz, 1H, C14), 2.95 - 2.88 (m, 2H, C8), 2.78 – 2.68 (m, 2H, C12), 2.50 (s, 6H, C1), 2.41 (s, 6H, C5), 1.84 (br s, 2H, NH_2), 1.76 - 1.70 (m, 2H, C11), 1.66 - 1.54 (m, 4H, C9-10); ^{13}C NMR (100 MHz, chloroform-*d*) δ_C 173.2 (C15), 153.9 (C2), 146.1 (C7), 140.3 (C4), 131.4 (C6), 121.7 (C3), 70.7 (C13/16/-23), 70.6 (C13/16/-23), 70.3 (C13/16/-23), 70.2 (C13/16/-23) 70.1 (C13/16/-23), 69.7 (C13/16/-23), 53.9 (C14), 50.7 (C13/16/-23), 43.3 (C13/16/-23), 39.0 (C13/16/-23), 38.0 (C12), 31.4 (C9), 29.0 (C8/10/11), 28.6 (C8/10/11) 28.3 (C8/10/11), 16.5 (C5), 14.4 (C1); HRMS-ESI; $[M+Na]^+$ calc'd for $C_{29}H_{46}N_7O_4S_2Na$ 692.3012 found; 692.3008.

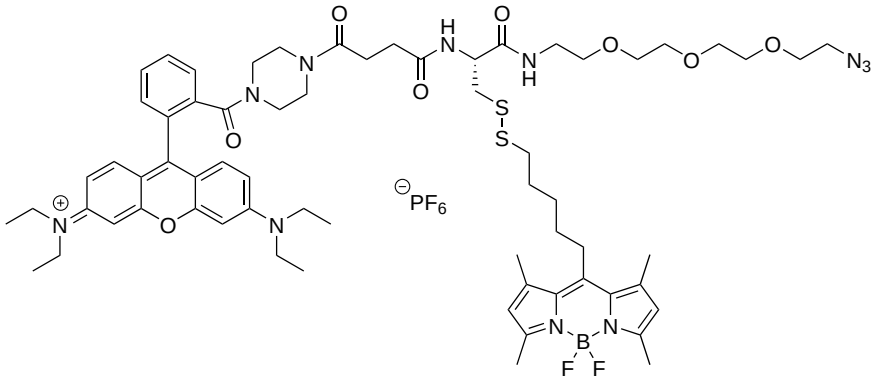

45

***N*-(9- (2-(4-(1-azido-14- (((5- (5,5-difluoro -1,3,7,9- tetramethyl -5*H*- dipyrrolo [1,3,2] diazaborinin-10-yl) pentyl) disulfanyl) methyl) -13,16- dioxo -3,6,9- trioxa -12,15- diaza nonadecan -19- oyl) piperazine -1- carbonyl)phenyl) -6- (diethylamino) -3*H*- xanthen-3-ylidene) -*N*- ethylethanaminium 45.** RhoB acid **40** (16 mg, 0.026 mmol) and BODIPY azide **44** (15 mg, 0.022 mmol) were dissolved in CH_2Cl_2 (4.0 mL) under argon. Triethylamine (7.0 µL, 0.052 mmol) was added to this solution followed by HBTU (11 mg, 0.026 mmol) before stirring at ambient temperature for 20 h. A major red fluorescent spot was observed by TLC (R_f = 0.50, 9:1 CH_2Cl_2:MeOH) and the solvent was removed *in vacuo*. The product was purified *via* column chromatography eluting with 3.0% MeOH in CH_2Cl_2 to give the product as a pink glassy solid (7.5 mg, 27%). IR (thin film)/cm^{-1} ν_{max} 3674 w, 2980 m, 2902 w, 1990 w, 1633 s, 1564 s, 1408 s, 1378 s, 1260 s, 1059 s, 912 s, 793 s; ^{1}H NMR (300 MHz, chloroform-*d*) δ_H 7.67 – 7.54 (m, 2H, CH_{arom}), 7.47 (d, J = 7.0 Hz, 1H, CH_{arom}), 7.35 - 7.20 (m, 5H, CH_{arom}), 7.04 – 6.82 (m, 1H, NH), 6.71 - 6.63 (m, 2H, CH_{arom}), 5.98 (s, 2H, CH_{arom}), 4.60 (br s, 1H, NH), 3.71 – 3.50 (m, 20H, CH_2), 3.49 - 3.32 (m, 16H, CH_2), 3.22 - 3.10 (m, 2H, CH_2), 2.93 - 2.86 (m, 2H, CH_2), 2.65 (t, J = 7.0 Hz, 2H, CH_2), 2.43 (s, 6H, CH_3), 2.34 (s, 6H, CH_2), 1.69 - 1.60 (m, 4H, CH_2), 1.59 - 1.51 (m, 4H, CH_2), 1.41 – 1.14 (m, 12H, CH_3); ^{13}C NMR (100 MHz, chloroform-*d*) δ_C 173.2, 170.4, 157.7, 156.2, 155.7, 153.8, 146.3, 140.4, 135.2, 132.2, 131.4, 130.2, 130.1, 130.0, 127.6, 121.6, 114.2, 113.8, 95.9, 70.5, 69.9, 69.4, 53.0, 50.6, 47.6, 47.1, 46.1, 45.3, 41.6, 41.1, 39.6, 39.2, 38.2, 31.4, 28.9, 28.5, 28.3, 16.4, 14.4, 12.6; MALDI (matrix: 2,5-dihydroxy benzoic acid);

$[M]^+$ for $C_{65}H_{87}BF_2N_{11}O_8S_2$ 1262.

Chapter 3

Development of Fluorophores for Conjugation to CCL2

3.1 Introduction

The work described in this chapter produces a range of fluorophores which contain an azide functional group for use in CuAAC conjugations with alkyne-bearing CCL2. The requirements for these fluorophores are they must be suitable for use as FRET pairs and either the donor or acceptor must exhibit a high degree of synthetic flexibility. This is because both lipophilic and hydrophilic fluorophores are needed and so ideally this would be a single fluorophore core which can include lipophilic functional groups and hydrophilic functional groups. An obvious choice for the fluorophores would be the cyanine dyes which are widely used FRET pairs and also can be synthesised as both polar and non-polar molecules through sulfonation of the aromatic rings. Unfortunately, there is very little literature on the synthesis of these fluorophores and so after extensive literature searching, boron dipyrrin (BODIPY) was selected as the donor fluorophore (which would also be used for all single fluorophore work) and rhodamine B was selected as the acceptor fluorophore.

BODIPY represents a class of fluorophores with excellent quantum yields, neutral overall charge, narrow emission peaks, strong molar absorptivity and forms the basis of many synthetic papers which highlight the scope of reactivity of these molecules.[228,233,234] Scheme 3.1 shows the general core structure for BODIPY dyes and highlights the α-, β- and meso-positions commonly used for substitution of the core. Unsubstituted BODIPYs are not known in the literature, presumably due to further electrophilic attack on the pyrrolo-ring from pyrrole starting materials or intermediates.[233] The boron-free dipyrromethene intermediate is not stable at room temperature in most systems and is not generally observed or isolated. Some regioisomers of BODIPY-dimethyl compounds have not been reported which highlights the difficulty in synthesis of some BODIPYs, indicating planning is needed to ensure synthetic success. The higher degree of substitution on the BODIPY core translates into greater stability and so many tetra-, hexa- and heptaalkyl-substituted BODIPYs have been reported in the literature.[233] A trend can be observed in that increased substitution correlates with a red-shift in absorption and emission maxima. Interestingly, phenyl substituents

at the meso position do not greatly affect absorption or emission maxima but in some cases a significant impact on quantum yield has been observed.[233] This can be rationalised through the rotational freedom of the aromatic ring, if vicinal methyl groups are present, rotation of the aromatic ring is limited and therefore fewer relaxation pathways are available, increasing quantum yield. When the ring can freely rotate, the quantum yield is lowered due to the increase in non-fluorescent relaxation pathways, these findings highlight the sometimes large effects relatively small modifications to BODIPY can have on photophysical properties.

BODIPYs with substituents at the meso-position have been widely reported and are usually prepared from acyl chloride condensation with the relevant pyrrole.[228,233] Alternatively activated carboxylic acids can also be used in this reaction such as anhydrides which result in formation of a carboxylic acid for further reactivity.[233] Pyrroles or aromatic substituents which are particularly reactive may require softer BODIPY formation conditions, these include formation from aromatic aldehydes and pyrroles. This process results in a dipyrrole separated by an sp^3 centre which requires a further oxidation step to generate the dipyrrolo species before boron complexation.[233] This method has allowed the synthesis of α,β-unsubstituted BODIPYs from an aromatic aldehyde, the corresponding acyl chloride would likely be too reactive to successfully form the product.[233,235]

BODIPY has found extensive applications in imaging, chemosensing and light-harvesting systems which highlights the large range of spectral properties available with modifications to the fluorescent rings.[233,234,236] In cellular imaging, neutral BODIPYs offer cytosolic distribution, whereas BODIPYs based on esters (which likely unmask to anionic acids due to esterase-mediated hydrolysis) will localise around the endoplasmic reticulum and positively charged BODIPYs have been used to label mitochondria.[234,237–239] For FRET applications, increased substitution of the BODIPY core would lead to a red-shifted fluorophore which would be suitable for spectral overlap with a typical 'green' BODIPY. However, these compounds usually require aliphatic ring fusion to the aromatic core making these compounds very lipophilic (and thus not water soluble).[233] Furthermore, these compounds are often asymmetric which complicates the synthesis and the extended systems can stabilise the free dipyrrin species

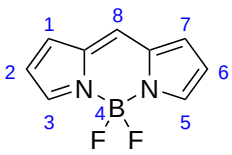

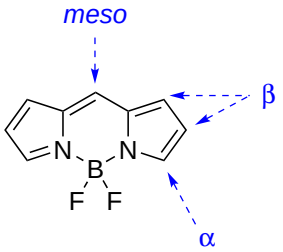

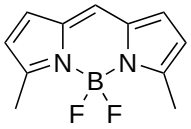

EtOH, φ 0.81
λ_{max} abs 507 nm
λ_{max} em 520 nm

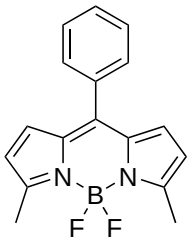

MeOH, φ 0.19
λ_{max} abs 508 nm
λ_{max} em 521 nm

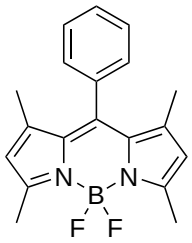

MeOH, φ 0.65
λ_{max} abs 498 nm
λ_{max} em 508 nm

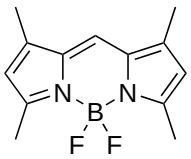

EtOH, φ 0.80
λ_{max} abs 505 nm
λ_{max} em 516 nm

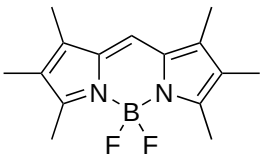

EtOH, φ 0.56
λ_{max} abs 528 nm
λ_{max} em 535 nm

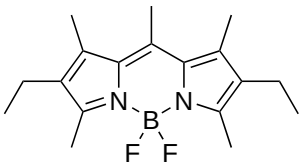

EtOH, φ 0.70
λ_{max} abs 517 nm
λ_{max} em 546 nm

Scheme 3.1: Properties of simple BODIPY fluorophores. Numbering system of BODIPY positions and the α, β and meso positions (Top). Phenyl substituents have little effect on absorption and emission maxima but free rotation of the phenyl ring has a deleterious effect on quantum yield (Middle). Increasing substitution on the BODIPY rings generally leads to a red-shift in emission (Bottom). Adapted from Burgess *et al.*[233]

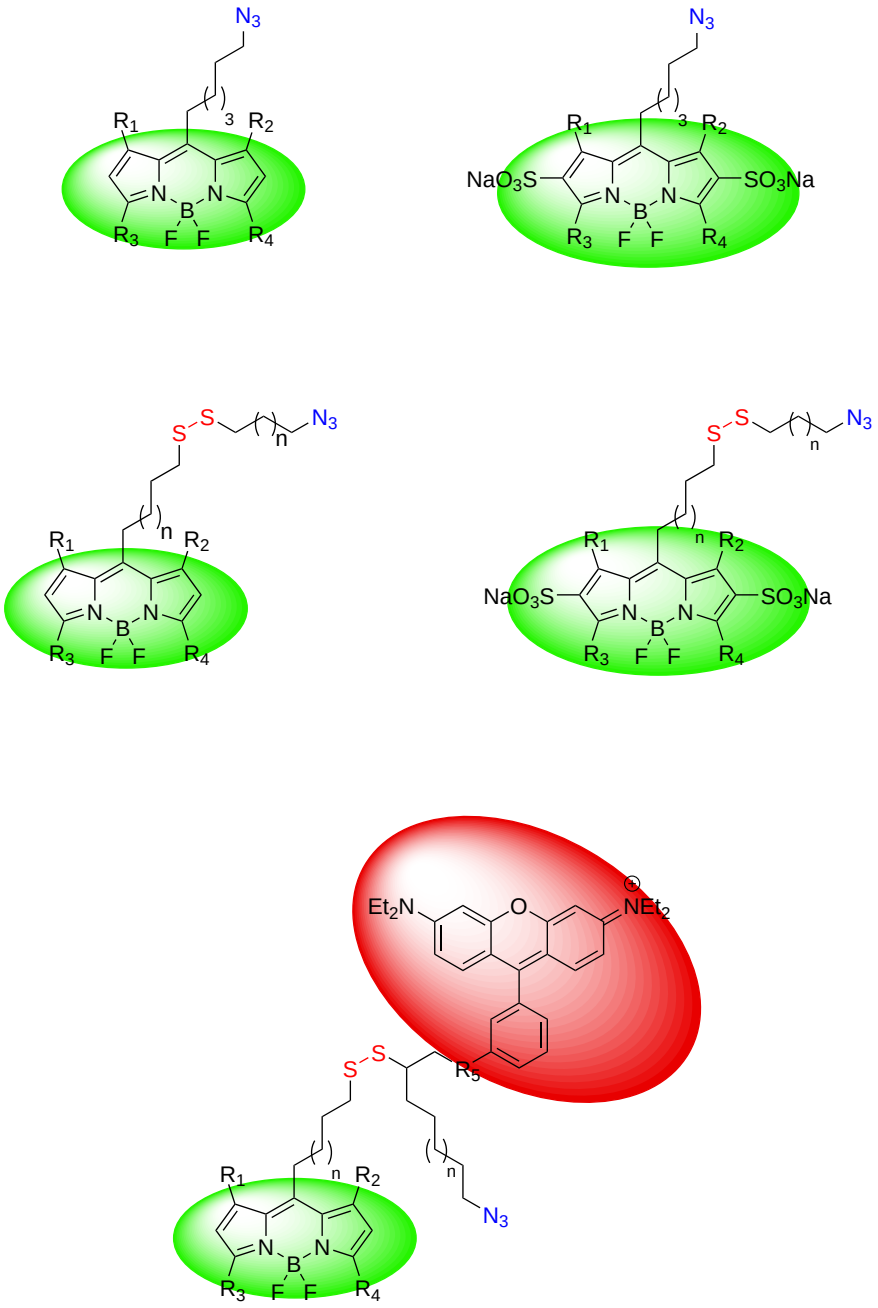

Scheme 3.2: General structures of polar and non-polar fluorophores synthesised in this chapter, including azide groups and disulfide bonds in cleavably-linked compounds.

meaning the boron species is not held in the complex as tightly (Butterworth group unpublished observations). The acceptor fluorophore therefore utilised rhodamine, derivatives of which have been used in FRET pairs with BODIPY.[240] Rhodamine is cationic which results in increased water solubility over BODIPY and the complete fluorophore is commercially available at a relatively low price, unlike the BODIPYs which are only available for specific applications not for further synthesis. Furthermore, a number of derivatisation strategies

exist for rhodamine and so functionalisation of the rhodamine towards a FRET pair would be simpler than generating a red/orange BODIPY from pyrrole starting materials.[241] Due to the cationic nature of rhodamine, this compound may not be able to escape endosomes and any rhodamines that localised in the cytosol would likely traffic to mitochondria; BODIPY will therefore be used as the fluorophore which will be reductively detached from CCL2. The general schematic structures for the fluorophores and FRET pair are displayed in Scheme 3.2.

3.2 Synthesis of Conjugating Substrates

3.2.1 Synthesis of BODIPY Azides

BODIPY was selected as the first fluorophore to be synthesised due to the fluorochrome's favourable spectral properties such as good quantum yield, excellent photostability and chemical stability. We followed the work of Mueller *et al.* to generate a pentasubstituted BODIPY core with a pentyl alkyl chain as a spacer.[228] The highly substituted core increases the stability of the core towards downstream reactions and also limits the number of isomers that can be formed in the reaction. Furthermore, the five-carbon spacer gives the linker flexibility and reduces steric hindrance between the fluorophore and the propargyl glycine residue on the CCL2 derivative, which should increase the probability of obtaining complete conversion to the conjugate. This length of spacer also generally gave the best reaction yields in later synthetic steps reported in the study.[228] The first stage of the synthesis is a two-step, one-pot procedure using 2,4-dimethylpyrrole (**5**), this undergoes an S_NAr reaction with 6-bromo

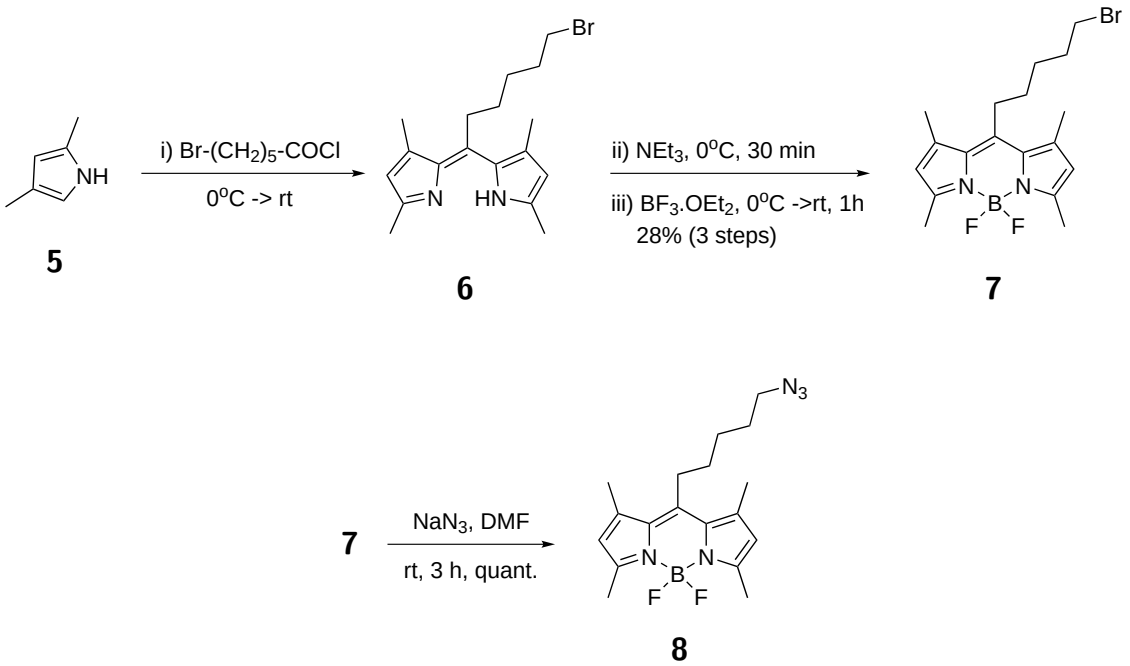

Scheme 3.3: Synthesis of a lipophilic BODIPY azide (**8**) from 2,4-dimethylpyrrole using one-pot conditions. The resulting BODIPY bromide (**7**) was then treated with sodium azide resulting in **8**.

hexanoyl chloride twice, eliminating HCl and producing the dipyrrin core **6** (Scheme 3.3). The next step quenches the HCl and also deprotonates the nitrogen of the dipyrrin core using an excess of cold triethylamine, the deprotonated nitrogen can then coordinate to the lewis acid boron trifluoride, this results in completion of the boron dipyrrin core (**7**) with a fluoride leaving group. The experimental procedure was modified to include a recrystallisation step using heptane as the compound was not pure after column chromatography. Heptane allows heating to elevated temperatures over shorter chain solvents which can aid the recrystallisation process, resulting in pure BODIPY bromide **7**. A reason for typically low yields of BODIPYs is the stability of the dipyrrin core (without the complexed boron species), if this core is not particularly stable, the first step in the one-pot procedure can be limiting. A tenuous trend exists in that the greater the extent of π-conjugation (an extended ring system), the greater the stability of the uncomplexed dipyrrin species. However, this can favour release of any complexed boron making downstream synthesis and subsequent biological experiments more difficult (unpublished observations in the group). The yields reported in this work ranged from 9 - 45% with an average yield of 28%, this is compared with the 33% yield reported by Mueller *et al.*.[228] The authors reported the importance of limiting the boron trifluoride etherate reaction time to 1 h as side products can form after this time but which substrate this was performed on was not discussed. One attempt was therefore made to increase the reaction time of the boron trifluoride etherate step from 1 h to 16 h. A moderate increase in yield to 45% was observed suggesting a longer reaction time can be beneficial for this substrate, however, these conditions were not attempted again. A number of factors were observed to improve yields: fresh distillation of dry triethylamine, replacing pyrrole **5** and boron trifluoride etherate after three months. Whilst this initial step did limit the amount of material needed for subsequent steps (scale up resulted in lower yields), 250-500 mg was consistently obtained and so we proceeded with the synthesis without further optimisation; subsequent steps were therefore performed on relatively small scales ($\tilde{1}$00 mg). The bromide **7** was then substituted with sodium azide to give the azide **8** in excellent yield.

In order to modulate the endosomal escape capabilities of the fluorophore, the lipophilic

BODIPY core was substituted with chlorosulfonic acid. This extremely polar bis-substituent should considerably diminish the ability of the fluorophore to escape endosomes and would also provide a direct comparison with the aforementioned lipophilic azide. BODIPYs are known to be acid sensitive: strong acids lead to dissociation of the boron from the fluorochrome resulting in loss of fluorescence and so the chlorosulfonic acid step was initially performed on BODIPY bromide **7**. The first attempt used chlorosulfonic acid at low temperature in an electrophilic substitution reaction (Scheme 3.4). A high polarity fluorescent spot was observed by TLC suggesting the reaction was successful, however, this was accompanied

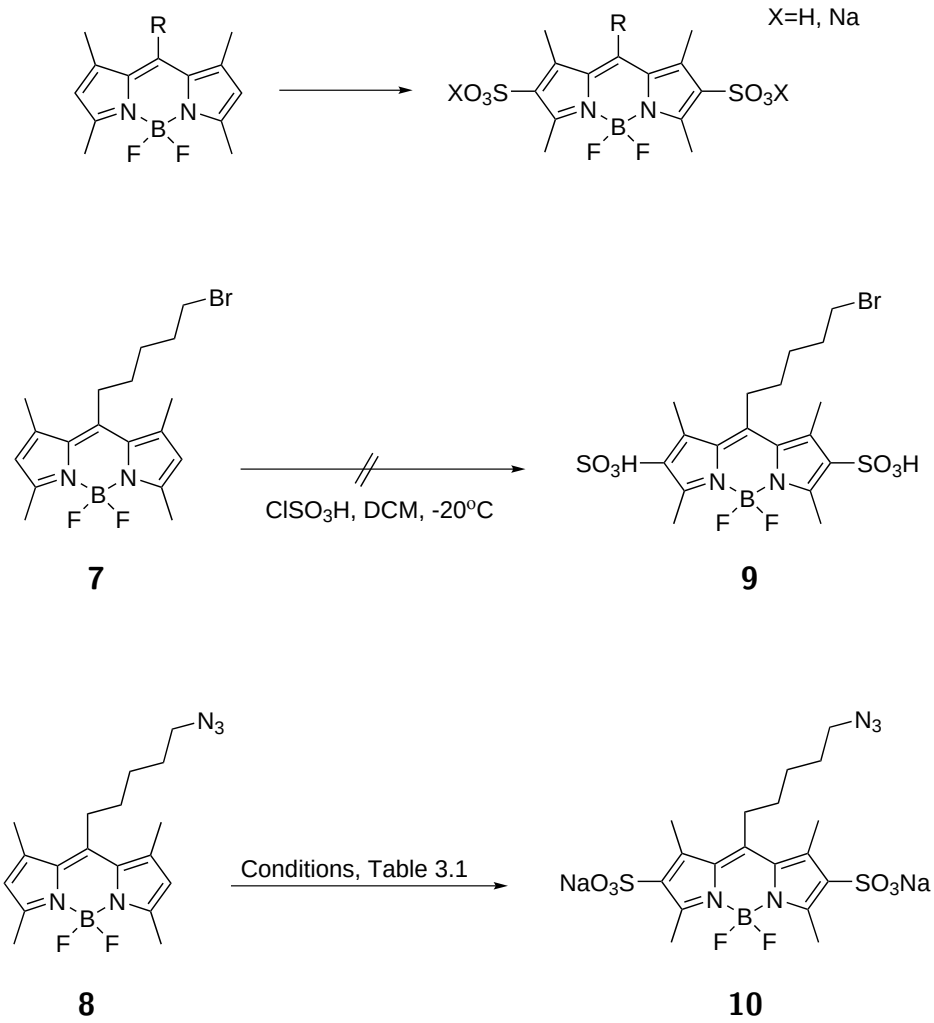

Scheme 3.4: Optimisation of disulfonation of the BODIPY core using chlorosulfonic acid. Initial attempts on BODIPY-bromide (**7**) were not successful, most likely as a result of acid sensitivity of the boron centre. Efforts towards salt formation of disulfonate species on the BODIPY azide were successful, conditions used are summarised in Table 3.1.

by a non-fluorescent red spot suggesting some dissociation of the boron center in response

Table 3.1: Conditions attempted in sodium disulfonate substitution reaction, displayed in Scheme 3.4, B

Reaction	Conditions		Yield
	i)	ii)	
1	$ClSO_3H$, DCM, -40°C, 20 min	$NaHCO_3$, H_2O	0%
2	$ClSO_3H$, DCM, BHT, -25°C, 1 h	$NaHCO_3$, MeOH	59%

to the acidic product and/or conditions (known in the literature[242]). Encouraged by this result, the azide (**8**) was taken forward and the conditions modified such that the sulfonate salt (**10**) was formed, removing the acidic product. Two conditions were attempted, the initial biphasic strategy reported by Burgess *et al.* did not work leading to the successful strategy of Landfester *et al.*.[236,243] This included a dropwise addition of chlorosulfonic acid and the use of BHT as a radical scavenger, followed by addition of sodium bicarbonate in methanol to give a homogeneous, monophasic solution. This method resulted in good yields of 59% giving copious amounts of water soluble, highly polar BODIPY for later conjugations to CCL2.

3.2.1.1 Synthesis of Disulfide Linkers and Fluorescent Disulfide Azides

The potential for endosomal escape of the fluorophores are likely to be enhanced by incorporation of a disulfide linker species which would be reduced by high intracellular concentrations of glutathione. The next stage of the project was therefore to develop methods to prepare mixed disulfide species, which is known to be a difficult and often inefficient process.[244] This was initially carried out on non-fluorescent systems due to the poor scale up capabilities of the BODIPY synthesis, as well as the acid sensitivity which had been problematic. One method of generating mixed disulfides is to form mixed disulfides from an aromatic disulfide homodimer and an alkyl thiol, the aromatic ring acts as a good leaving group to aid in subsequent regioselective thiol substitutions. The homodimer is usually used in excess to prevent the alkyl thiol from forming homodimers through attack on the newly formed product. These

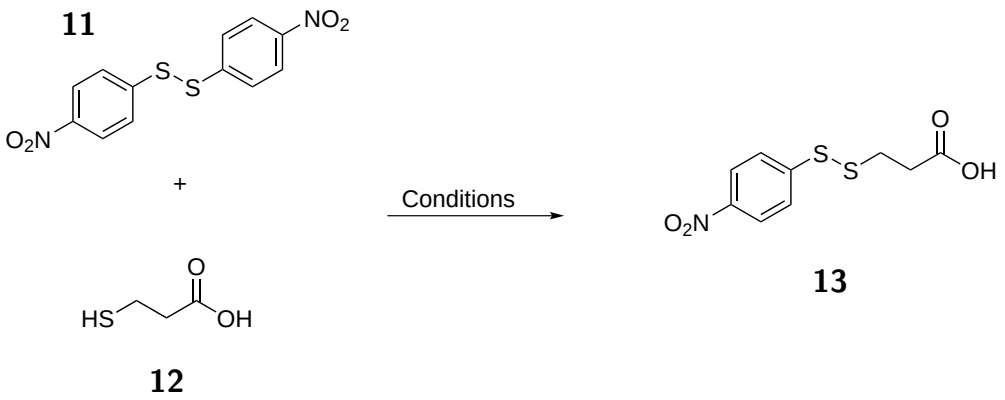

Scheme 3.5: Formation of the mixed disulfide (**13**) from the homodimer disulfide, 2,2'-Dithiobis(5-nitropyridine), **11**. The optimised conditions are reported in Table 3.2

Table 3.2: Optimised conditions of disulfide formation described in Scheme 3.5.

Eq. 11:12	Addition of 12	Base	Solvent	Time / h	Yield / %
2:1	bulk	1 M NaOH	MeOH	16	0
2:1	bulk	1 M NaOH	MeOH	48	0
2:1	bulk	1 M NaOH	$CHCl_3$	16	0
2:1	dropwise	none	MeOH/DCM	1	18
2:1	dropwise	none	MeOH/DCM	24	32
3:1	dropwise	none	MeOH/DCM	16	76
3:1	dropwise	none	MeOH/DCM	16	90
2.5:1	dropwise	none	MeOH/DCM	16	65
2:1	dropwise	none	MeOH/DCM	16	66

considerations led to the selection of 2,2'-Dithiobis(5-nitropyridine) (**11**) as the homodimer, this is shown in Scheme 3.5 and results are summarised in Table 3.2; in spite of this preparation the reaction required extensive optimisation to attain a good yield in moderate scale. The activated aromatic disulfide was relatively labile to nucleophiles and so we tested the stability of this compound in the presence of alanine. Any thiolate aromatic leaving group was easily identifiable by TLC as a strong chromophore, fortunately the disulfide remained intact.

Efforts were then made towards formation of a disulfide-linked azide from the activated disulfide using alkyl thiols. Commercially available polyethylene glycol (PEG) azide derivatives are a useful starting material for this purpose and so an amide coupling with 3-mercaptopropionic acid was attempted (Scheme 3.6). Unfortunately, this attempt was not

successful, most likely due to cross-reactivity of the thiol with HBTU-acid intermediates. Another strategy was therefore pursued which formed a protected thiol (**18**) on a simple iodo-acid substrate (Scheme 3.6, **17**) for subsequent coupling to the aformentioned PEG azide. This was successful which allowed HBTU coupling of the thioester to PEG azide **15** to give the protected thiol azide **19**. Hydrolysis of this ester to the resulting thiol unfortunately resulted in oxidation and therefore dimer formation which could not be avoided by lowering the temperature or dilution. Attempts at reducing the disulfide were also undertaken using dithiobutylamine and TCEP but neither were successful.

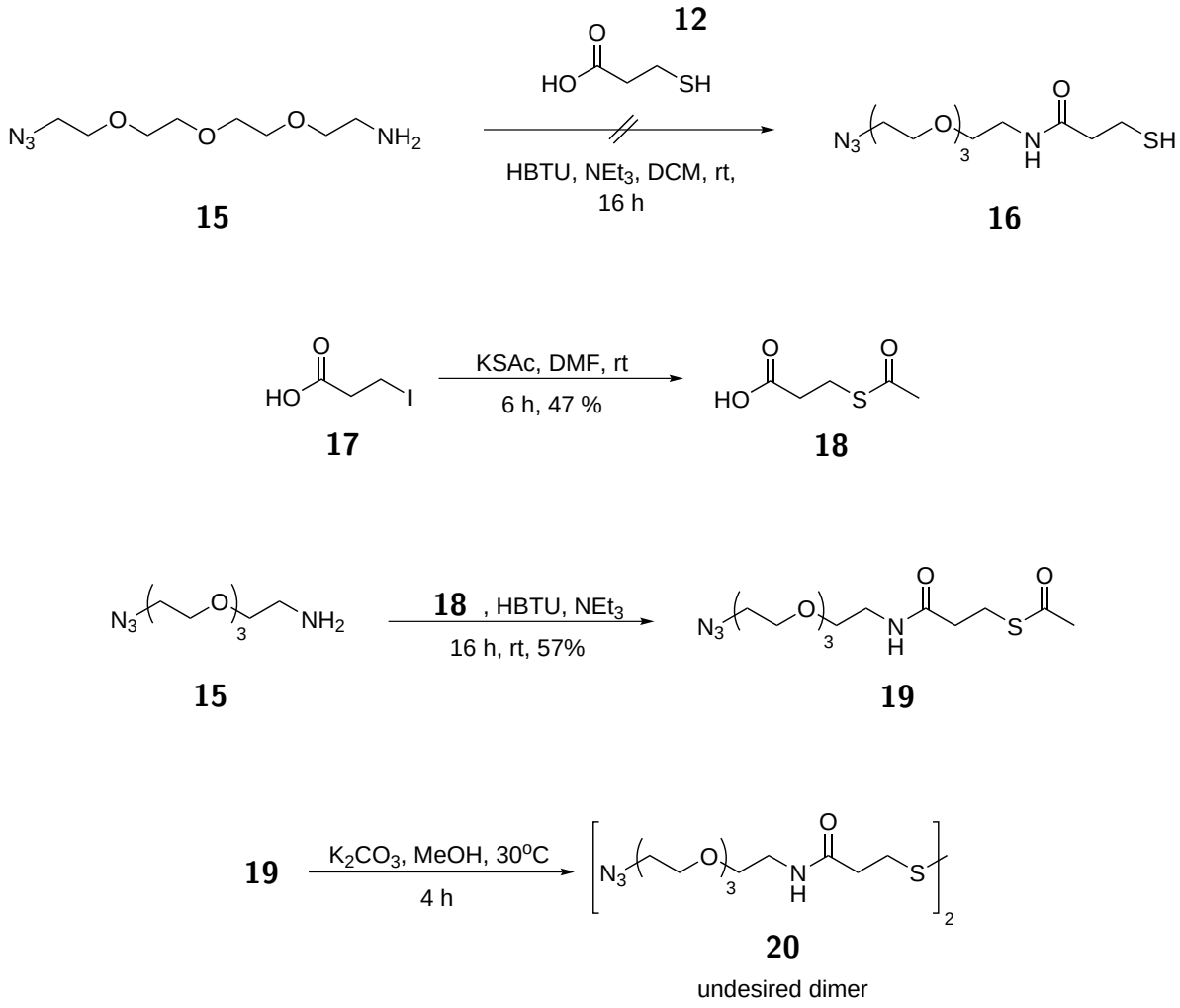

Scheme 3.6: Direct coupling of 3-mercaptopropionic acid to PEG azide **15** was not successful, presumably due to thiol nucleophilicity. Building the thioester (**18**) from 3-iodopropionic acid failed at a late stage when the thioester (**19**) was hydrolysed which resulted in disulfide homodimer formation (**20**).

The strategy was thus revised such that an activated aromatic disulfide was formed on the

PEG azide before substitution with a BODIPY thiol (Scheme 3.7). The previously synthesised acidic disulfide, **13**, was coupled to the commercially available PEG azide, **15**, to give activated disulfide **23**. The BODIPY bromide (**7**) was then treated with potassium thioacetate giving the thioester (**21**) in good yields, following the work of Mueller *et al.*.[228] Subsequent ester hydrolysis using potassium carbonate gave the thiol, **22**, with careful heating to only 30°C which was important to minimise the formation of disulfide homodimers.

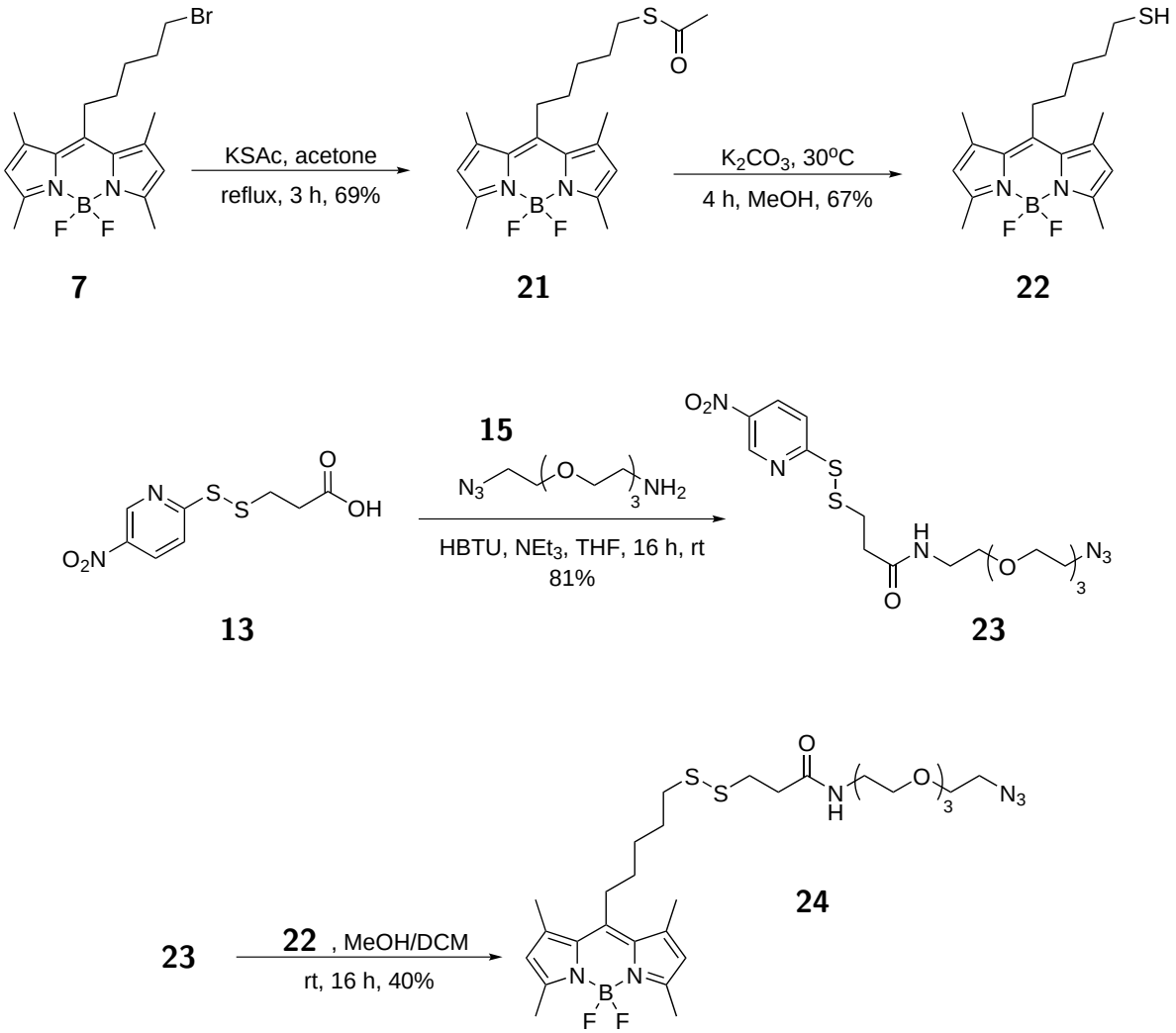

Scheme 3.7: Successful route towards a BODIPY disulfide azide ready for conjugation to CCL2. BODIPY thiol (**22**) was prepared from initial thioester formation (**21**) from BODIPY bromide (**7**), akin to the previous route using iodopropionic acid. Coupling of the activated disulfide **13** to the commercially available PEG azide **15** was achieved using HBTU. The BODIPY thiol **22** then underwent nucleophilic substitution with **23** to give the desired product **24**.

Substitution of the activated disulfide (**23**) with BODIPY thiol was performed using the same

conditions the mixed disulfide synthesis discussed earlier with 3-mercaptopropionic acid. As the disulfide must be used in excess this step resulted in large losses of compound which is difficult to recover due the similarity in polarity of the disulfide starting material and the reduced aryl thiol anion. Furthermore, this reaction did provide the product, **24**, but this product was inseparable by column chromatography from the starting material **23**. Reverse phase high performance liquid chromatography (HPLC) was therefore carried out to separate the two compounds.

With a lipophilic BODIPY azide separated by a cleavable linker synthesised, a hydrophilic version of this system was now needed as a direct comparison in future experiments. As a result of the difficulty in forming lipophilic BODIPY **24**, we decided to synthesise a disulfonated BODIPY thiol and substitute this with the activated disulfide (**23**). Beginning with BODIPY bromide, treatment with the successful chlorosulfonic acid conditions generated the disulfonated product **25** in excellent yield (Scheme 3.8). Production of the thioester **26** from bromide **25** was not successful, the reasons for this were not clear but one issue with synthesising disulfonates is that the high polarity renders any conventional chemical purifications methods very difficult. This meant that the similarity in polarity between these compounds made separation difficult. A final attempt to form the desired thiol product was performed though disulfonation of the liophilic thioester **21** to give **26**. It was difficult to determine the success of this reaction by NMR as the spectra was noisy suggesting the presence of contaminants or side-products, it was decided to take this crude mixture forward into the next thioester hydrolysis step. Unfortunately, formation of the thiol **27** was not observed, possibly because the thiol nucleophile could react with the chlorosulfonic acid.

The successful method to synthesise the lipophilic BODIPY disulfide clearly had some inherent issues such as separation difficulties with the final product and the wasteful nature of installing the activated disulfides on two occasions. Another strategy to form mixed disulfides was therefore explored to provide better polarity separation of reactants and products, as well as improved yields. This method used potassium toluenethiosulfonate which can be used as a nucleophile to attack alkyl halides such as the BODIPY bromide to give an

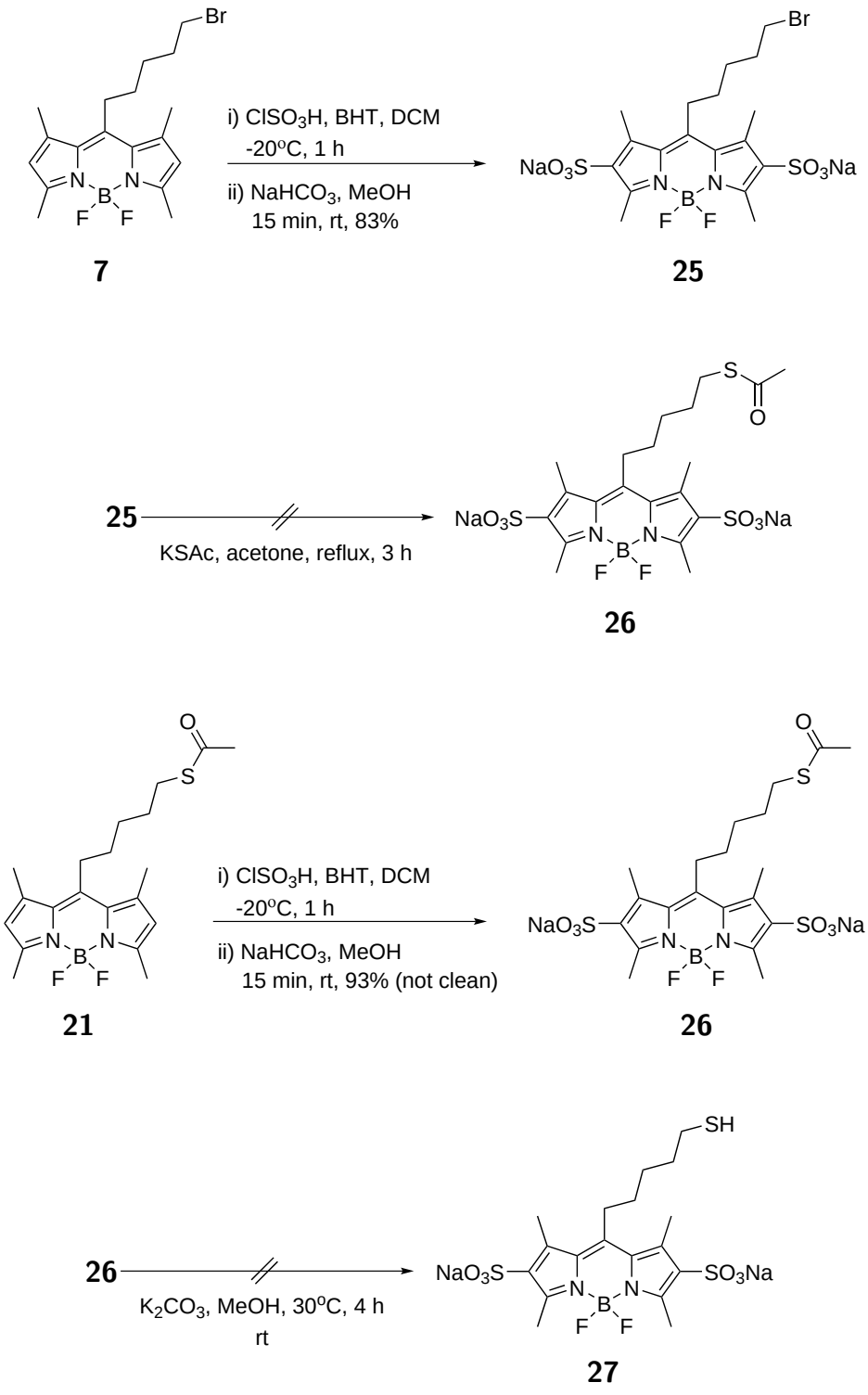

Scheme 3.8: Efforts towards synthesis of a disulfonated BODIPY thiol from BODIPY bromide (**7**) and the thioester **21**.

activated disulfide.[244] This proceeded efficiently to give **28** in good yield, meaning an activated disulfide could be generated in a single step, avoiding the inefficient pathway used previously (Scheme 3.9). This compound was then treated with cysteamine which regiose-

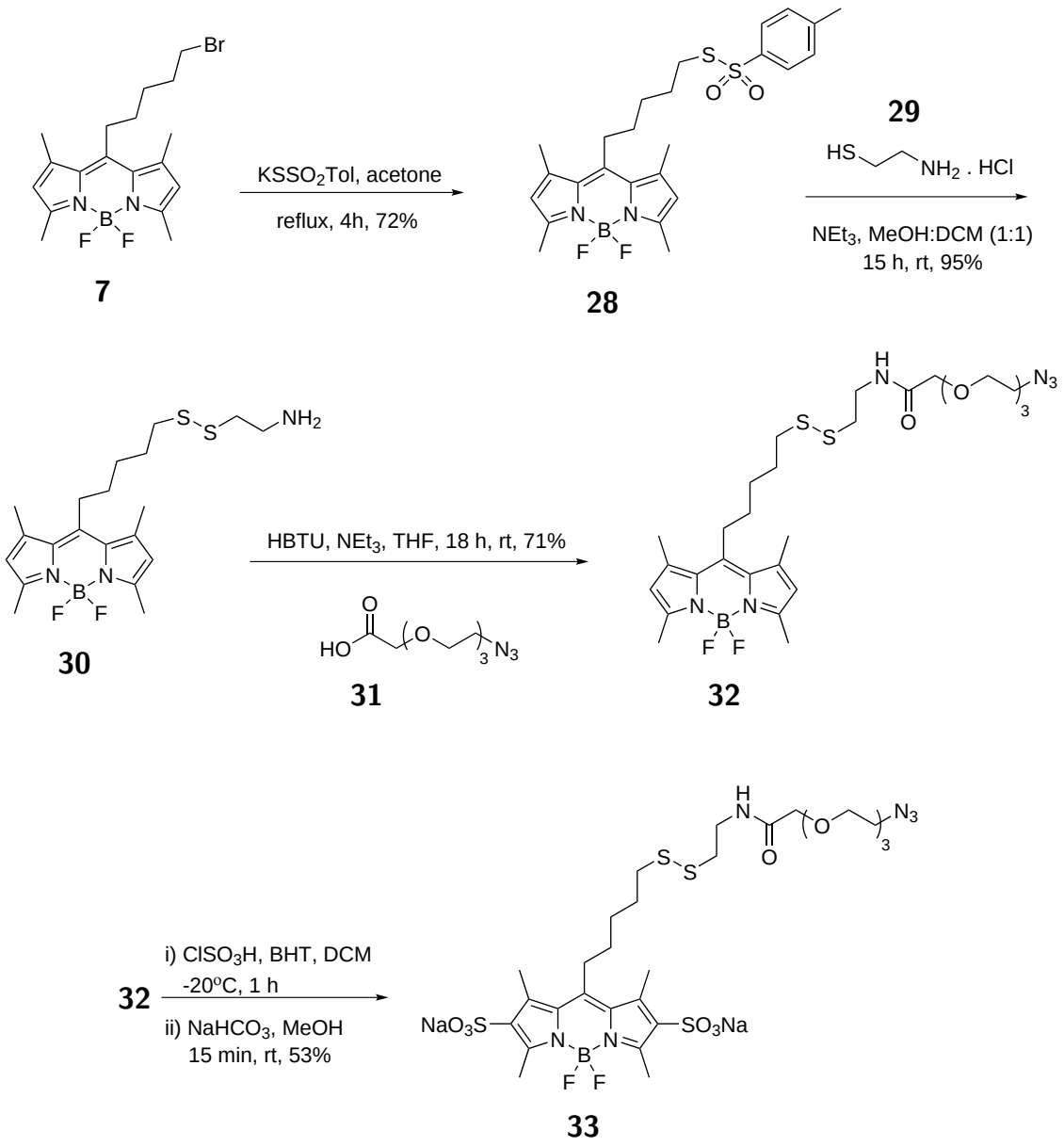

Scheme 3.9: Alternate route to give a disulfide-linked BODIPY azide with a late stage successful disulfonation of the BODIPY core. BODIPY bromide **7** was heated in the presence of potassium toluenethiosulfonate which installs an activated disulfide (**28**) in one step. This disulfide was substituted with cysteamine giving the disulfide amine **30** ready for HBTU coupling a pegylated azide acid giving another BODIPY disulfide-linked azide (**32**) in better yields than the previous route, this enabled the core to be disulfonated giving **33**.

lectively attacks the alkyl sulfur liberating the aforementioned leaving group. Furthermore, this reactant was also chemoselective as the amine was not observed to react, even in the presence of base, this is likely due to the size of the sulfur atom and the the hybridisation of reactive orbitals meaning better orbital overlap is present between sulfur atoms than the smaller sulfur-nitrogen analogue. With the disulfide amine **30** prepared, a HBTU coupling with PEG azido acid **31** gave BODIPY azide **32** in good yield, with a high similarity to the previous BODIPY disulfide **24**. This efficient sequence allowed a final disulfonation reaction with the same chlorosulfonic acid method to give the highly polar BODIPY disulfide **33**.

3.2.2 Synthesis of Rhodamines Derivatives and FRET pair

The use of a FRET pair separated by a disulfide linker allows sensing of intracellular glutathione reduction and subsequent tracking of both fluorophores independently. One fluorophore will be able to freely move according to its own physical properties and the other would remain covalently attached to CCL2 and therefore subject to the processing the cell applies to the chemokine. Upon analysis of the literature, common FRET pairs such as the cyanine class of fluorophore were not selected for use due to the difficulty in synthesis of these compounds. We therefore decided to use BODIPY as the donor species due to our knowledge of the chemistry of this class of compounds and the aforementioned spectral properties of BODIPYs. Rhodamine was selected as the acceptor due to the breadth of scope for synthesis described by Martinho *et al.*, and the excellent spectral properties of these fluorophores.[241]

To synthesise the rhodamine derivatives, we followed a strategy developed by Francis *et al.* to perform amide couplings on a carboxylic acid positioned away from the xanthene ring.[232] It is important to use cyclic amines as less hindered amines lead to spiro-lactam formation which is non-fluorescent (Scheme 3.10). The spiro-lactone rhoadmine B base is activated towards nucleophilic attack using trimethyl aluminium as a Lewis acid and piperazine as the nucleophile.[232] Attempts to reproduce this reaction were unsuccessful (Scheme 3.10), consumption of starting material was observed by TLC but it was difficult to track formation

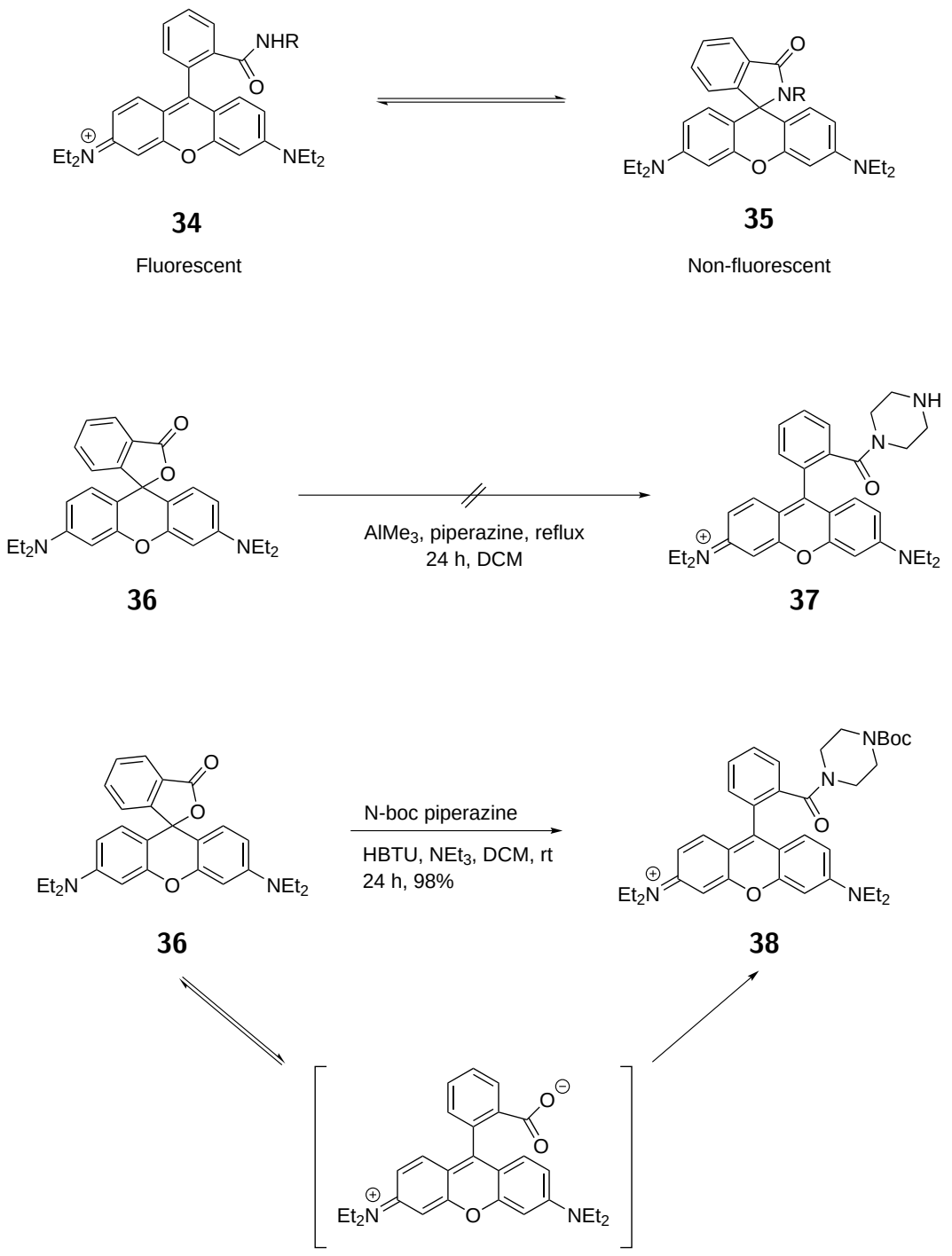

Scheme 3.10: Secondary amides of rhodamines lead to lactam formation which results in loss of fluorescence due to the spiro-ring system removing planarity and π-conjugation (**34** to **35**).[232] Initial attempts at directly forming the cyclic piperazine amide **37** from rhodamine B base **36** were not successful. Amide coupling using N-boc piperazine and HBTU gave the protected cyclic amide **37** in excellent yield, this reaction likely proceeds *via* the open zwitterionic form of rhodamine B base.

of products and purification by chromatography generated many compounds which could not be identified by NMR. Presumably, the presence of trimethyl aluminium led to the formation

of numerous aluminium salts, the result of which gave very polar compounds which were difficult to separate, there could also have been cross-reactivity issues with the unprotected piperazine amine. To circumvent these issues we used a mono-boc-protected piperazine in a HBTU coupling (Scheme 3.10). We hypothesised that the spiro-lactone starting material is actually in an equilibrium with the open carboxylic form, allowing the acid to undergo amide couplings, relying on this equilibrium to drive the reaction through to completion. This resulted in complete consumption of the starting material giving the cationic cyclic amide **38** in excellent yields.

Table 3.3: Optimised conditions of boc deprotection (**38** to **37**) to avoid salt formation. MW heating in water gave a single product in 64% yield, simplifying the synthesis.

Conditions	**Salt Formation**
TFA (50% v/v), DCM	PF_6, halide
HCl (4M) in dioxane	PF_6, halide
MW 165°C, water	PF_6

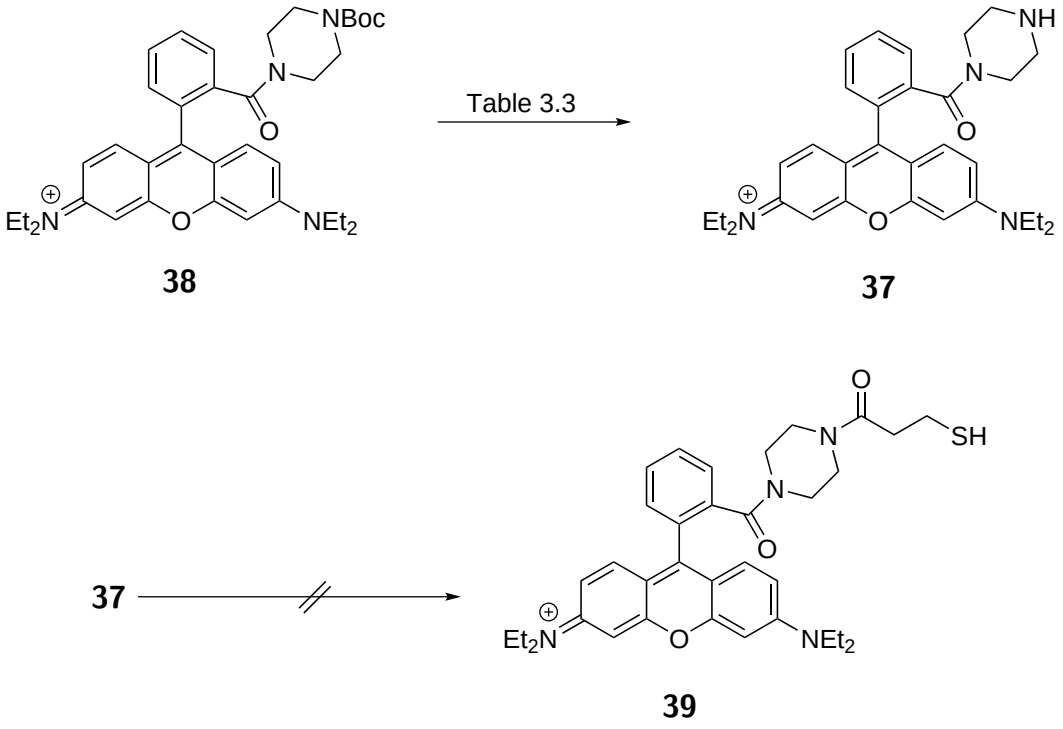

Scheme 3.11: Boc deprotection with optimised conditions listed in Table 3.3. Efforts towards coupling to 3-mercaptopropionic acid were not successful (**39**) likely due to cross-reactivity of the thiol with activated acids.

The next step was to deprotect the amine, however, this step was problematic due to the cationic nature of the compound leading to various salt formations when removing the boc group (Scheme 3.11). Standard conditions, such as treatment of **38** with trifluoroacetic acid (TFA), resulted in complete consumption of starting material and the formation of two polar compounds which could be separated by chromatography. The NMR spectra of these compounds both corresponded to the product as indicated by loss of the tert-butyl singlet and downfield shift of the ethylene piperazine protons. Differences in the peak shapes and chemical shifts of the piperazine protons suggested different environments for these protons, however, mass spectrometry presented a single ion to the correct mass of 510 Da for both compounds. We suspected this was due to different salt formations in the two compounds which resulted in the distinct NMR patterns on the piperazine ring. To verify this, mass spectrometry was performed in negative mode to identify the nature of any salts which resulted in a PF_6 anion associated with one rhodamine and no peak was observed in the other compound. This was likely due a low mass anion such as a chloride which is not able to be detected by mass spectrometry (MS), this 'harder' salt would confer higher polarity to the compound and indeed this compound exhibited a lower relative front (R_f) by TLC. Similar results were also observed with HCl (4M) in dioxane, presumably due to the presence of chloride ions.

To circumvent this issue, salt formation was avoided *via* the use of reagent free deprotection conditions in the form of heating in solvent. Boc groups decompose under heating and so this compound was heated by microwave to 165°C in water resulting in thermal decomposition of the boc group and only single product formation (Table 3.3). In order to install a thiol onto the rhodamine portion of the FRET pair, we attempted to couple rhodamine **37** to 3-mercaptopropionic acid (Scheme 3.11). We envisaged this coupling would proceed with greater efficiency than the PEG-amine attempts because rhodamine **37** is a secondary amine with higher basicity than primary amines meaning this compound should out-compete any thiol nucleophilicity. Unfortunately, this was not the case and any clean product was not recovered. To develop an azide-functionalised FRET pair, the synthetic sequence was again

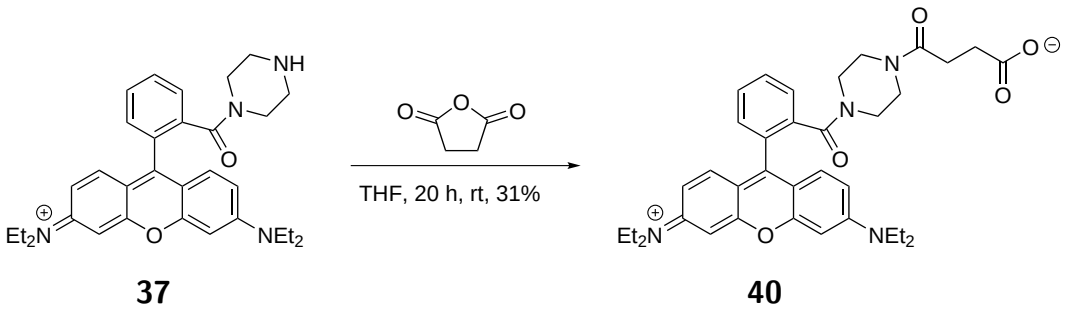

37 **40**

Scheme 3.12: Formation of zwitterionic rhodamine acid for subsequent amide couplings in FRET pair synthesis.

modified to include initial linker synthesis, substitution of the BODIPY thiol giving the disulfide before final coupling of the rhodamine B to limit the use of this compound which had previously diminished yields or been unwieldy. Another reason for this was that we found the BODIPYs were sensitive to acidic pH resulting in loss of fluorescence (likely due to boron dissociation) and so performing a boc-deprotection in the absence of BODIPY was beneficial. The modular synthesis therefore began with preparing a carboxylic acid derivative of the rhodamine **37** *via* reaction with succinic anhydride to form the rhodamine acid **40** (Scheme 3.12). Formation of the zwitterion removes any need for counterions and so this avoided the salt issue meaning a single product was obtained in good yield. A second synthetic sequence was then pursued to disulfide-link this rhodamine to a BODIPY, beginning with an amide coupling of the commercially available Boc-Cys-(Npys)-OH to pegylated azido amine **15** which proceeded *via* HBTU activation in excellent yield (Scheme 3.13). The boc group was removed at this stage to reveal the primary amine **43** in quantitative yields under standard TFA conditions, this avoided deprotection in the presence of BODIPY. Some efficiency was sacrificed in the next step as the initial activated disulfide conditions were used in the formation of **44** meaning that 2 equivalents of **43** were used relative to BODIPY thiol **21**, although this step represents another modular stage of the FRET pair synthesis. Unfortunately, initial attempts under neutral pH conditions resulted in no observable reaction and so potassium carbonate was utilised as a base. This resulted in product formation but was again accompanied by BODIPY disulfide homodimer formation by as much as 30%.

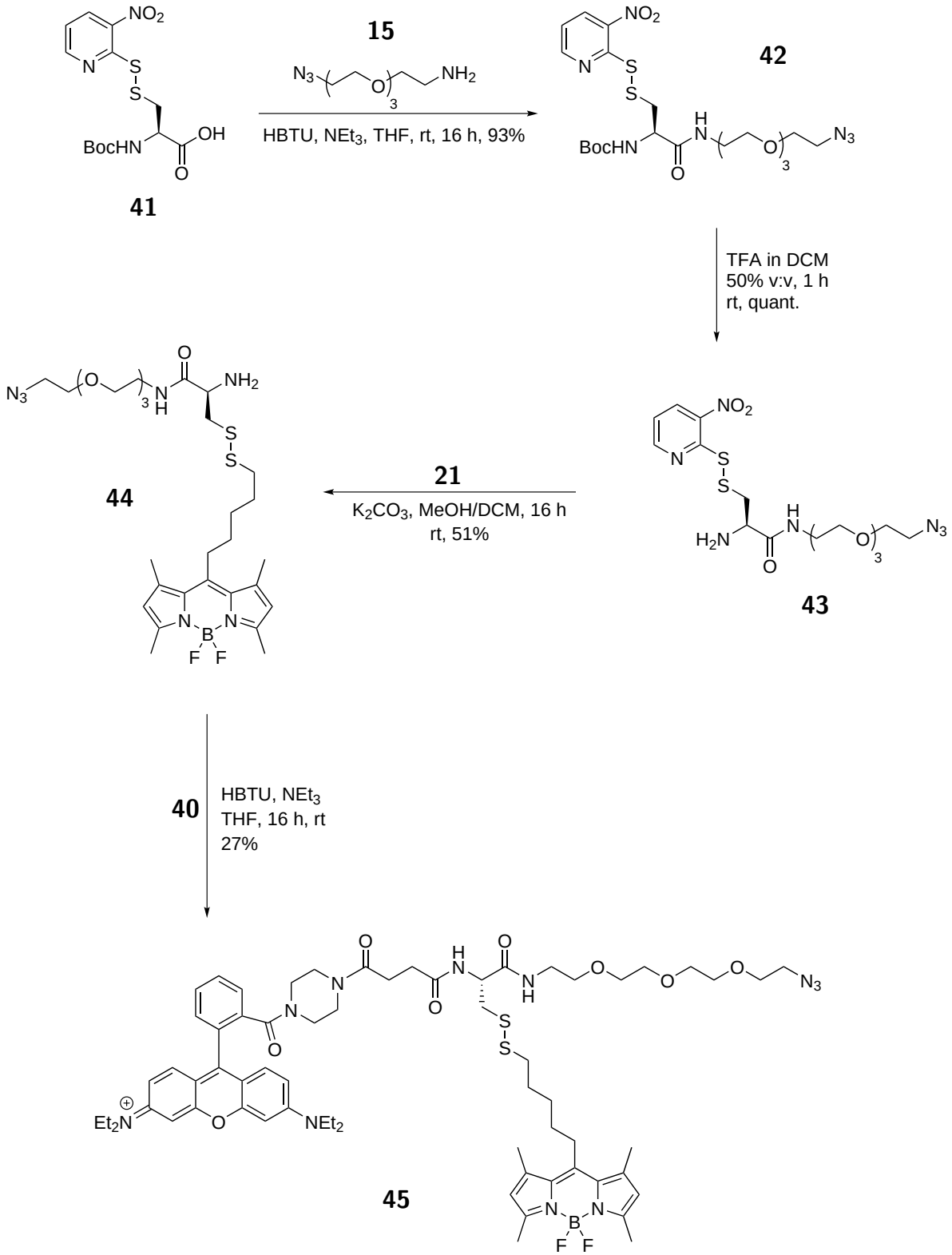

Scheme 3.13: Successful formation of the BODIPY-rhodamine FRET pair with a highly modular synthesis. Commercially available Boc-Cys-(Npys)-OH **41** was coupled to PEG azido amine **48** *via* HBTU in 93% yield. Deprotection of the boc group under standard TFA conditions resulted in quantitative yields of the amine **43**. Substitution of the activated disulfide with BODIPY thiol was successful but substantial losses in yield were incurred as a result of BODIPY dimer formation. Coupling of this compound to rhodamine acid **40** (Scheme 3.12) resulted in completion of the FRET pair synthesis in moderate yields.

The FRET pair synthesis was then completed through amide coupling of the RhoB acid **40** to BODIPY disulfide **44** *via* HBTU to give FRET pair **45** in 27% yield.

3.2.3 Fluorescence Spectra and Data

The final stage of fluorophore development was to measure the spectroscopic properties of the synthesised molecules. Initially, both the BODIPY bromide (**7**) and rhodamine amine (**37**) were measured in a fluorimeter to ensure these compounds exhibited fluorescence spectra similar to literature reports (Figure 3.1).[228] Indeed, BODIPY bromide exhibited fluorescence excitation and emission maxima around 500 nm which is typical for this class of fluorophore. Similarly, the rhodamine exhibited spectroscopic properties almost identical to literature values with maxima centring around 570 nm.[232] Furthermore, the fluorescent spectra are plotted on the same graph which highlights the overlap between BODIPY donor emission and rhodamine acceptor excitation, which is essential for FRET applications. Although the overlap is not donor maxima to acceptor maxima, the benefit of having this level of overlap is the donor and acceptor excitation spectra are wholly distinct and therefore false-positive FRET signals resulting from crossover should be minimised. The fluorescence spectra of single fluorophore compounds were measured, disulfonate BODIPY **10** excitation and emission spectra are displayed in Figure 3.2. This highlights the compound is fluorescent and has a very similar spectral profile to the bromo-BODIPY **7**, fluorescence spectra for the other single fluorophore compounds are displayed in Figure 3.2 and Figure 3.3.

Determination of FRET was then pursued, this was achieved using a number of methods, the first of which encompassed exciting the molecule at the donor's excitation maxima and measuring emission across the donor and acceptor emission wavelength range. If the compound is capable of FRET, a reduction in donor emission should be observed, which would be accompanied by an increase in acceptor emission(Figure 3.4). The spectral properties in DCM exhibited a FRET signal in the emission profile when excited at the donor excitation maxima, both a reduction in donor emission was observed as well as an increase in acceptor

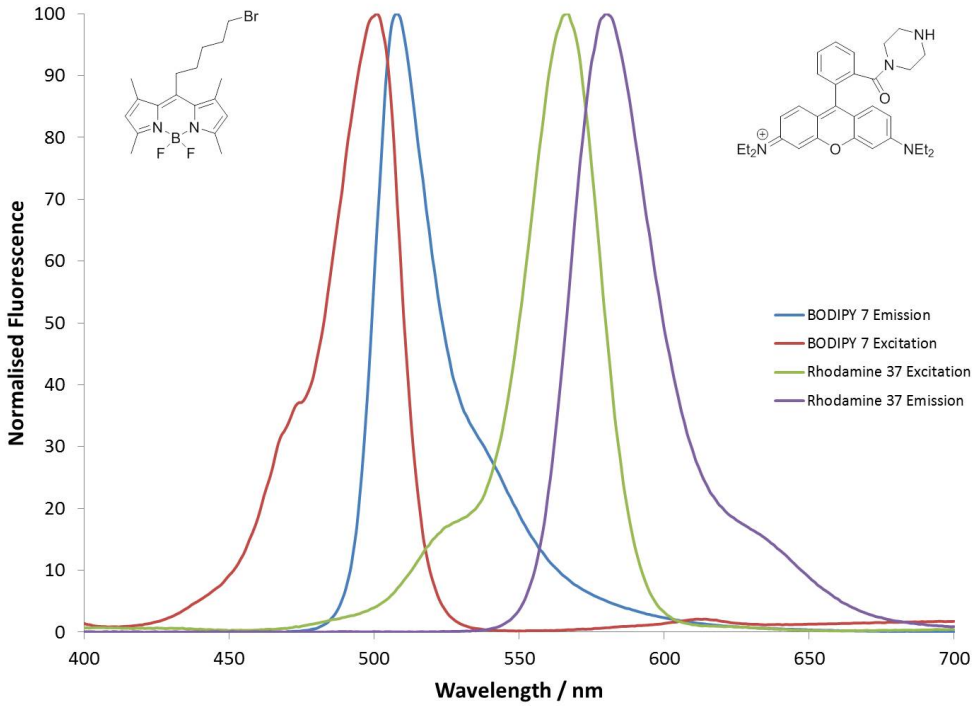

Figure 3.1: Fluorescence spectra of BODIPY bromide **7** measured in DCM and rhodamine **37** measured in MeOH. The excitation maxima of both the BODIPY bromide and rhodamine piperazine match literature values and so the fluorophores are behaving as expected.[228,232]

emission, suggesting energy transfer from donor BODIPY to acceptor rhodamine. The excitation spectrum (monitoring emission at 589 nm) for this compound showed an expected major peak in the acceptor region and a minor contribution from the donor region. This likely indicates some loss of energy through other relaxation pathways, for example, a significant reduction in donor emission suggests a strong transfer of energy to the rhodamine acceptor but this energy may not wholly relax through a fluorescence pathway but could decay thermally. Furthermore, the energy transfer is an indirect excitation and there are energy losses associated with the donor BODIPY excitation, the contribution to the FRET pair excitation spectrum is also dependent on relative molar absorptivities of donor/acceptor and also quantum yields. It was apparent that solvents were having a pronounced effect on the FRET signal whereby the signal was stronger in DCM than in methanol as shown by examination of the decrease in donor emission in DCM relative to methanol.

TCEP treatment could only be carried out in methanol as the reducing agent is stored in aqueous media and so the lack of miscibility of DCM and TCEP would have affected the

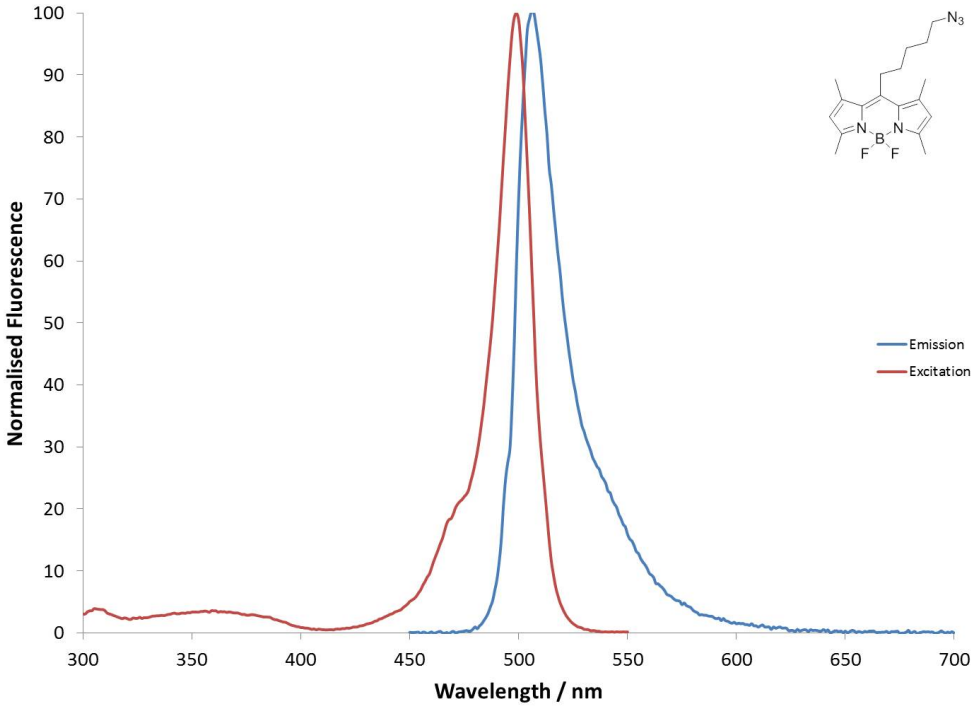

(a) Fluorescence spectra of non-cleavably linked BODIPY azide **8** in DCM. $\lambda_{\text{max, ex}} = 495$ nm, $\lambda_{\text{max, em}} = 506$ nm, $\phi = 0.63$.

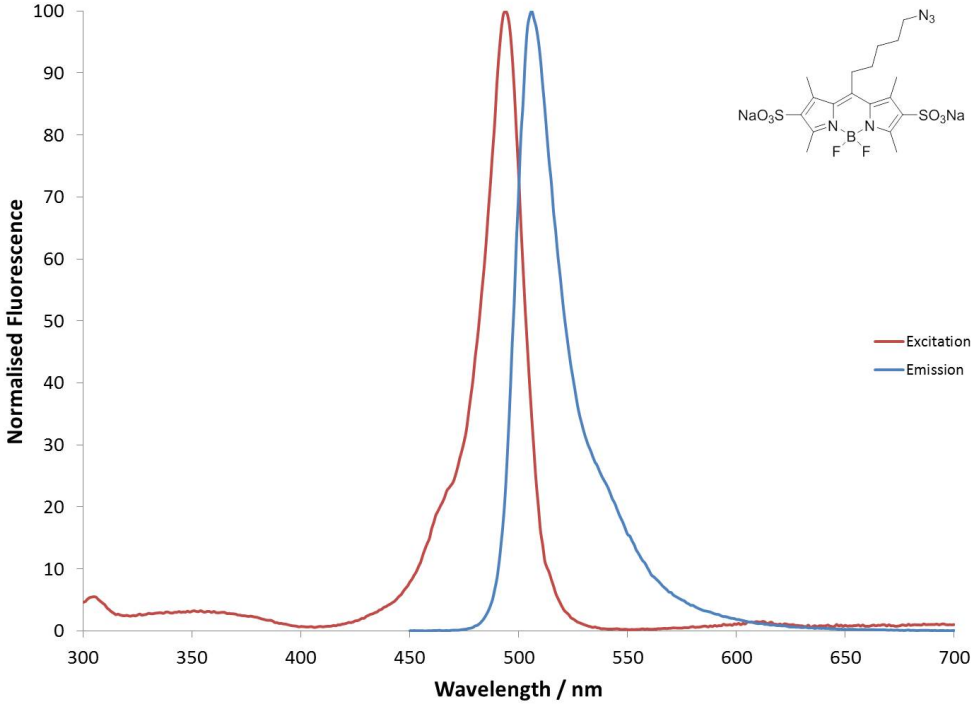

(b) Fluorescence spectra of the disulfonate BODIPY azide **10** in water. $\lambda_{\text{max, ex}} = 494$ nm. $\lambda_{\text{max, em}} = 506$ nm, $\phi = 0.25$.

Figure 3.2: Fluorescence spectra of the alkyl-linked BODIPY azides showing differences in peak width likely due to ring electronics.

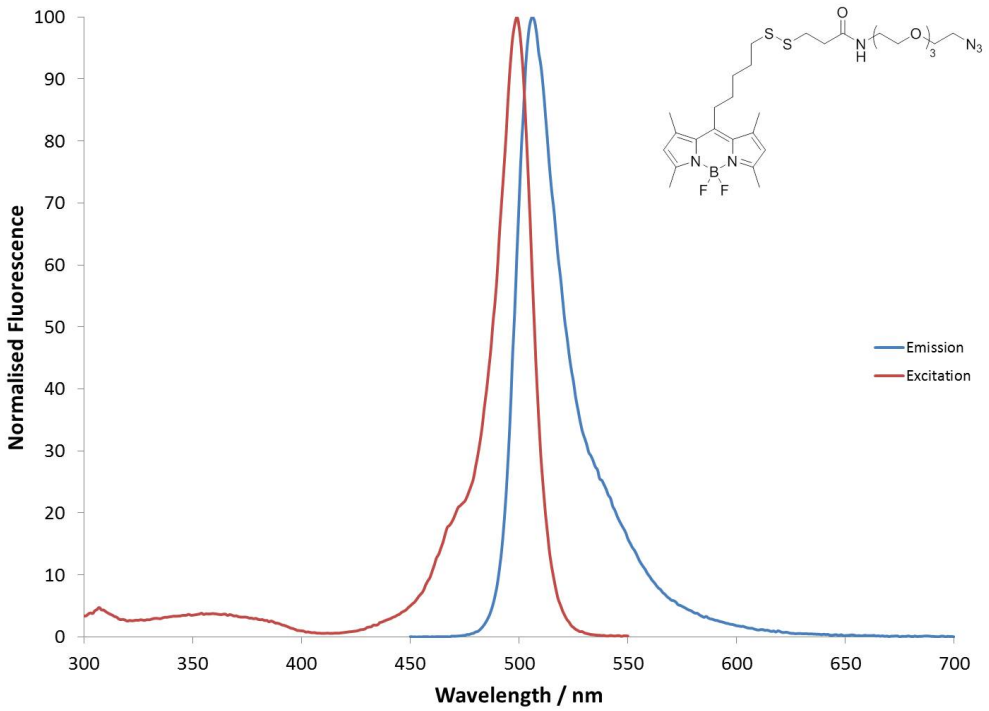

(a) Fluorescence spectra of BODIPY disulfide azide **24** in DMSO. $\lambda_{\text{max, ex}} = 499$ nm. $\lambda_{\text{max, em}} = 506$ nm, $\phi = 0.61$.

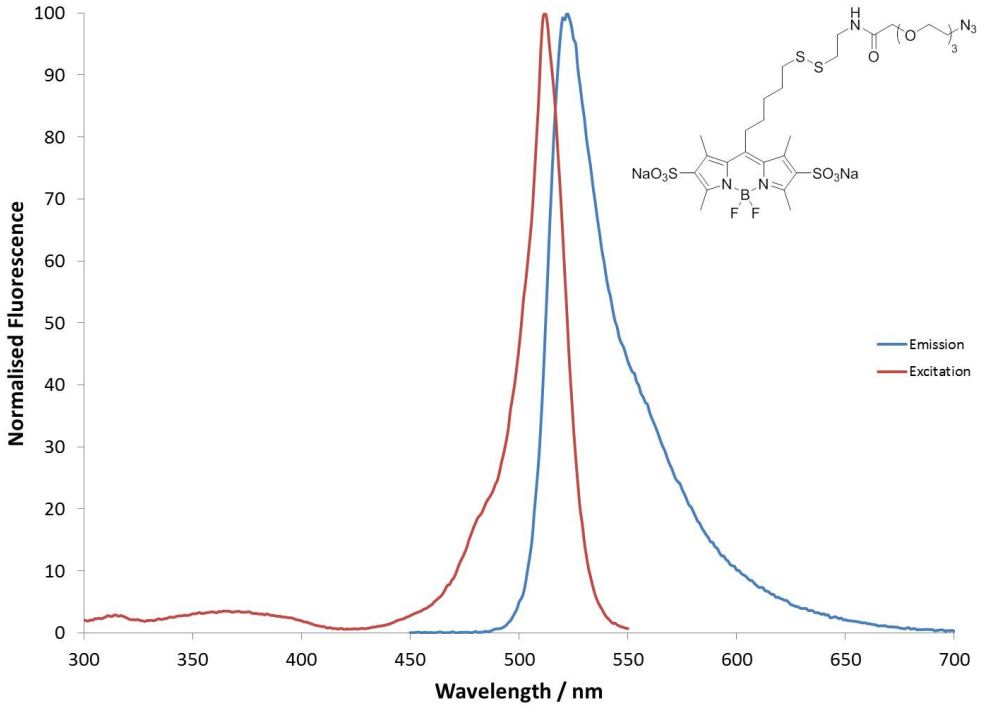

(b) Fluorescence spectra of BODIPY disulfonate disulfide azide **33** in DMSO. $\lambda_{\text{max, ex}} = 512$ nm. $\lambda_{\text{max, em}} = 522$ nm, $\phi = 0.21$.

Figure 3.3: Fluorescence spectra of both cleavably linked BODIPY azides **24** and **49**. The lipophilic BODIPY disulfide exhibited a similar spectra to the non-cleavably linked BODIPYs, however, the hydrophilic BODIPY disulfide exhibited a bathychromic shift of around 15 nm.

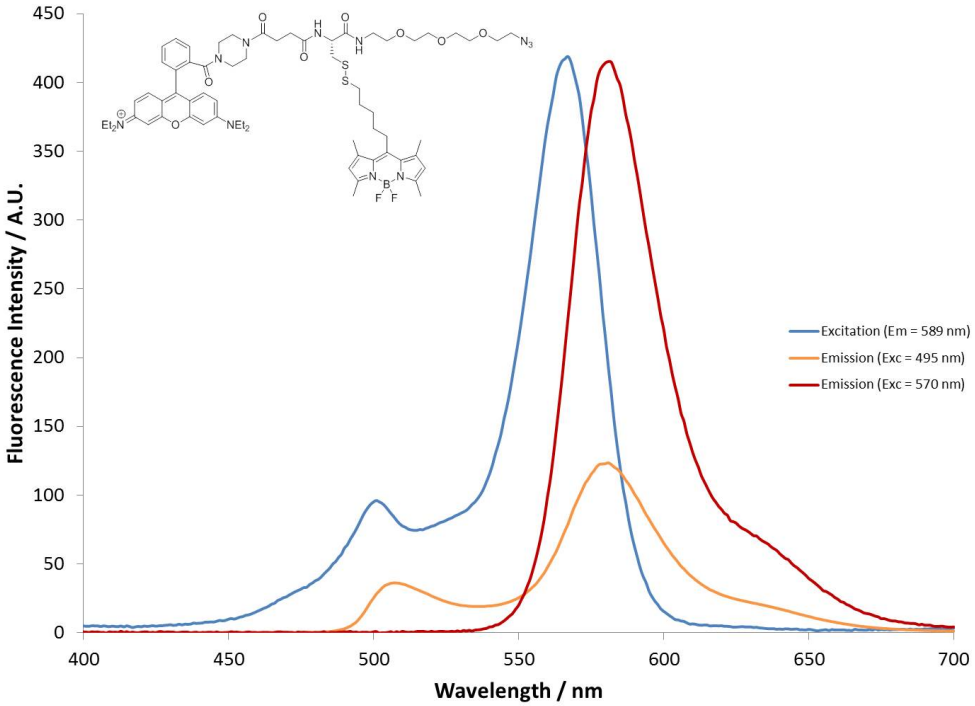

(a) Fluorescence spectra of FRET pair **45** in DCM

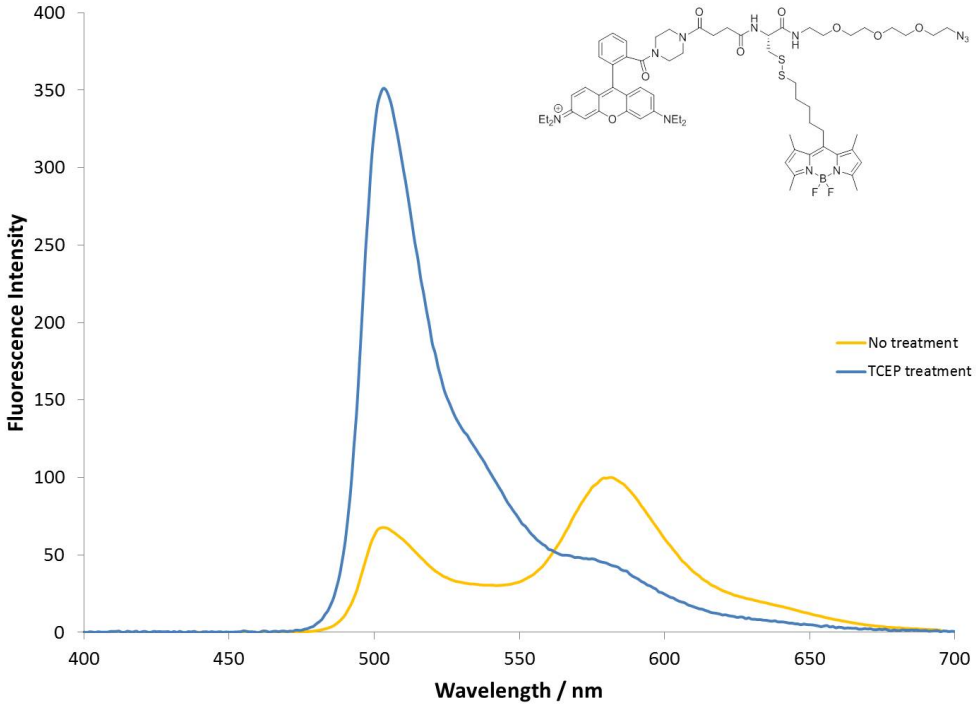

(b) Fluorescence spectra of FRET pair **45** in MeOH. $\lambda_{ex} = 495$ nm.

Figure 3.4: Fluorescence spectra of the FRET pair in DCM and MeOH. A clear FRET signal can be seen through excitation at the donor and a diminished donor emission paired with an increased acceptor emission. The acceptor emission was reduced upon treatment of the disulfide reducing agent TCEP which was also accompanied by an increase in donor emission, indicative of loss of FRET through spatial separation of fluorophores. $\lambda_{\text{max, donor em}} = 506$ nm, $\lambda_{\text{max, acceptor em}} = 589$ nm

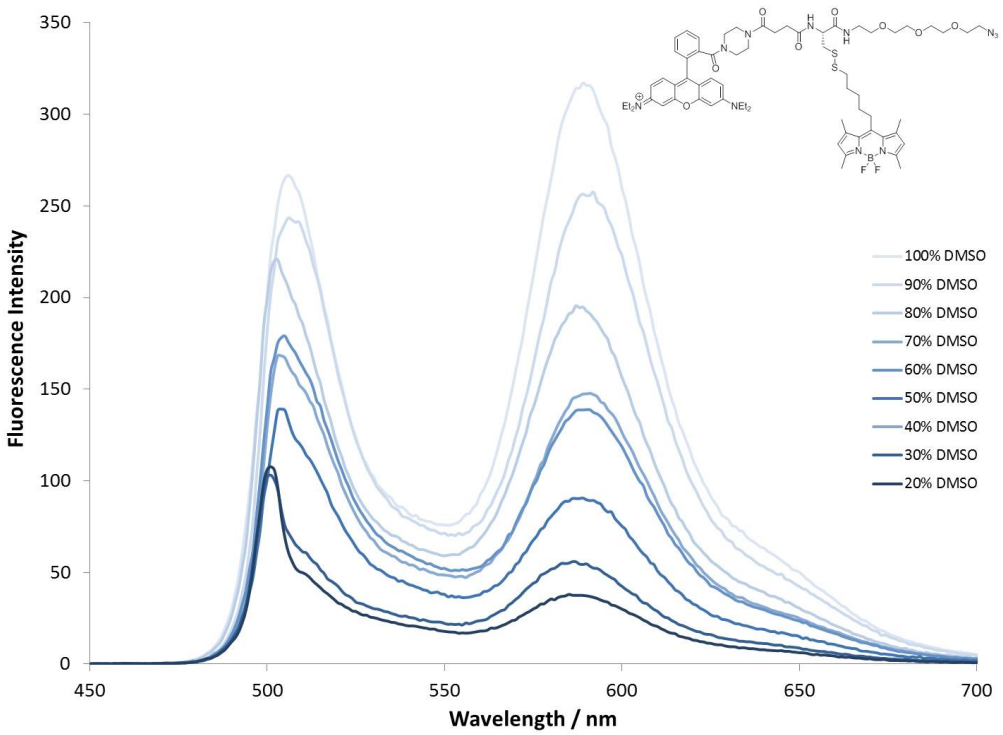

Figure 3.5: The effects of increasing concentrations of DMSO in aqueous media on the fluorescence spectrum of FRET pair **45**. The general trend is decreased fluorescence in high water concentrations, suggesting a solubility effect on fluorescence. $\lambda_{ex} = 495$ nm.

fluorescence spectrum. Interestingly, reduction of the disulfide by TCEP wholly reduced acceptor emission providing further evidence of FRET due to the loss of energy transfer when the fluorophores are spatially separated. However, this loss of acceptor emission was only accompanied by a modest increase in donor emission, this result, and the difference in spectra between DCM and methanol solvents, suggested that solubility of the relatively lipophilic FRET pair **45** has a significant effect on fluorescence. This effect was investigated through measuring the emission spectrum of the FRET pair whilst titrating increasing concentrations of DMSO into water (Figure 3.5). At low concentrations of DMSO, both the donor and acceptor emission is decreased, as the FRET pair is relatively lipophilic this is possibly due to solubility issues in high water concentrations. The behaviour is likely due to aggregation of this compound as the water content increases, as molecules move to minimise unfavourable interactions with water, possibly forming small micellar structures. This reduces fluorescence through auto-quenching of fluorophores in close proximity and as the solubilising DMSO concentration increases the fluorescence quickly returns. While these physicochemical properties

are affecting fluorimetry, it is unlikely to have a significant effect on fluorescent behaviours in imaging experiments in cells due to the complex media that occupies a cell

The presence of CCL2 will prevent aggregation due to sterics and after disulfide reduction in the cell, the liberated BODIPY donor will satisfy hydrophobicity needs through localisation with lipid membranes or other hydrophobic compartments. Studies were then undertaken into loss of FRET in response to TCEP reduction, altering both the concentration of TCEP and the reaction time (Figure 3.6). With a high concentration of 1 mM TCEP, even after 1 minute the BODIPY donor emission had increased with a compensatory decrease n rhodamine acceptor emission. This strongly increased until 60 minutes which suggested that complete reduction of the FRET pair had occurred. The lower concentration of 0.1 mM TCEP did not display as rapid a loss of FRET which provides further evidence that this loss of a FRET signal over time is a result of the TCEP reduction of the disulfide. After 120 minutes the donor emission had not reached the levels of fluorescence observed with 1 mM TCEP treatement. Stratifying this to how the FRET pair may behave inside a cell, it is more likely to reflect the 1 mM TCEP treatment as glutathione concentrations are generally over 1 mM, however, it is unclear what the intracellular concentration of the CCL2 conjugate will be.

Single fluorophore spectroscopic properties are listed in Table 3.4 and these results are generally typical for this class of fluorophore. Molar extinction coefficients at the absorption maxima for the BODIPY fluorophores were around 80000 $dm^3\,mol^{-1}\,cm^{-1}$ which represents a strong absorption at these wavelengths which is good for fluorescence microscopy. The absorption and emission maxima are at wavelengths amenable to overlap with the rhodamine acceptor and also complement common laser lines used in flow cytometry and imaging. The Stokes shifts are quite small, however, which may be a slight issue for imaging due to scattering but the benefit of a small Stokes shift with sharp excitation and emission peaks is reduced crossover and bleedthrough, which is of benefit in flow cytometry and imaging. Lastly, the quantum yields for BODIPYs with unmodified cores were excellent at around 60%, however, disulfonation of the core had a detrimental effect on quantum yield. While this is not ideal,

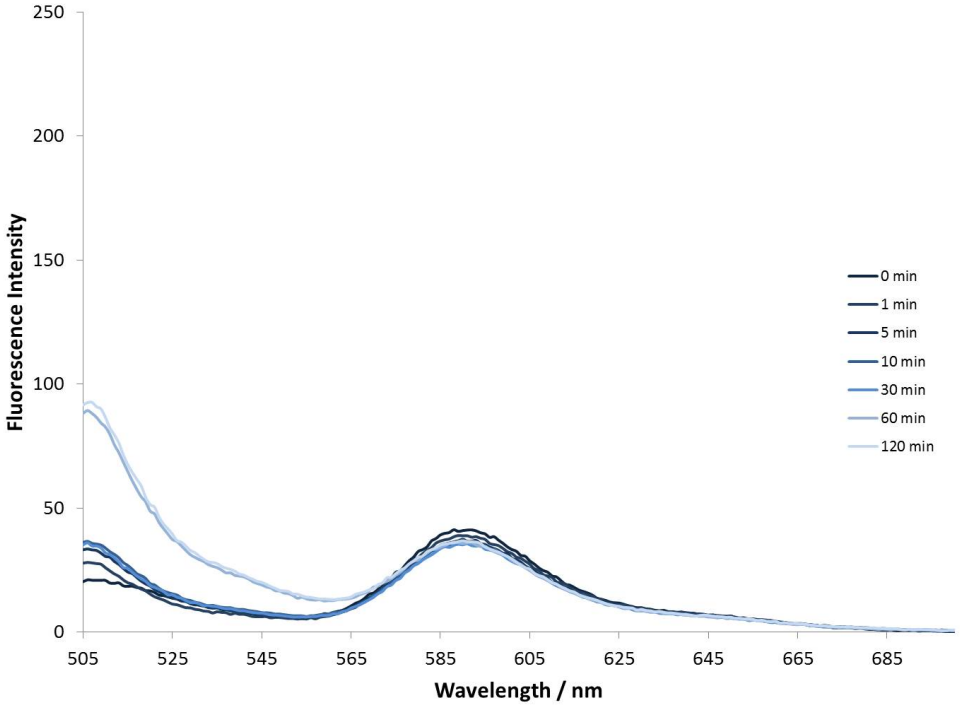

(a) Timecourse treatment of **45** with 0.1 mM TCEP.

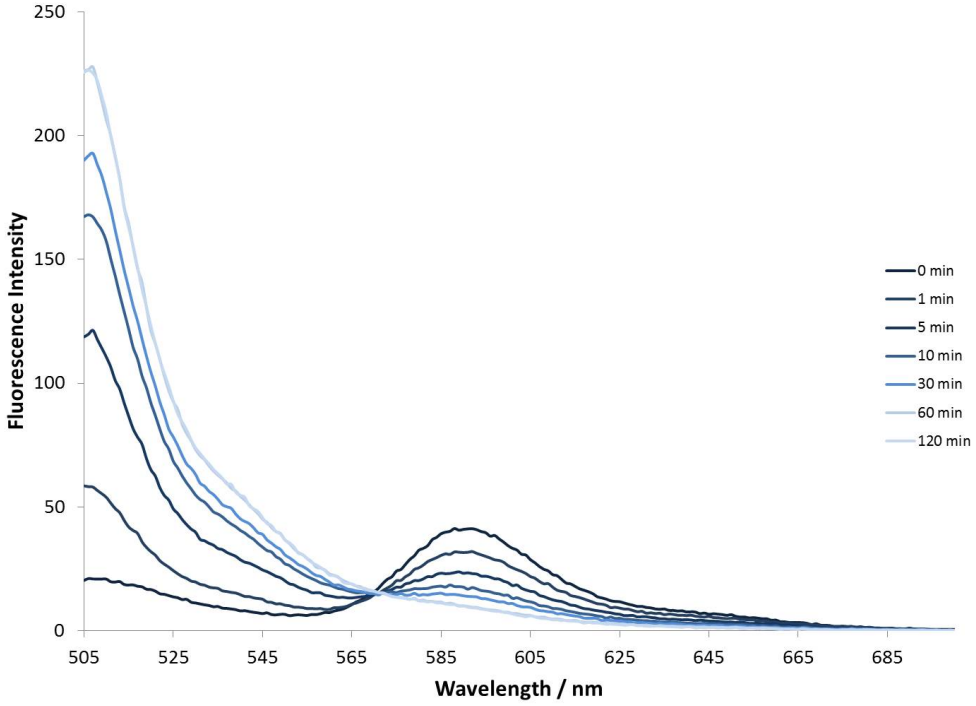

(b) Timecourse treatment of **45** with 1 mM TCEP.

Figure 3.6: Fluorescence spectra of FRET pair **45** measuring the effects of TCEP treatment over time. Gradual loss of FRET over time indicates that disulfide reduction is responsible for loss of FRET. The clear concentration dependency of this loss can also be seen as very little loss of FRET was apparent with the 0.1 mM TCEP treatment compared to the 1 mM treatment. FRET pair was at 15 nM. $\lambda_{ex} = 495$ nm.

the quantum yields are still high enough to be visible in microscopy and the excellent photostability of BODIPYs should ensure the fluorophores with lower quantum yields will remain emissive. This effect of disulfonation on quantum yield has been shown in some BODIPY examples in the literature but not in others. The FRET pair **45** was quantified through two mathematical methods described in the literature which include decrease in donor emission and increase in acceptor emission.[227] The first method Φ_{T1} measures the emission of the donor-alone fluorophore relative to the donor-FRET pair emission, as described in 3.1. The decrease in emission was over 90% showing almost total quenching of the donor emission which correlates well with the TCEP reduction experiments described previously. The second method measures the change in acceptor emission in the FRET pair compared to acceptor alone, relative to a ratio of the absorbance of the individual acceptor and donor fluorophores, giving Φ_{T2} (3.2).

$$\Phi_{T1} = 1 - \frac{I_{DA,506}}{I_D} = 0.96 \tag{3.1}$$

$$\Phi_{T2} = \left(\frac{A_A}{A_D}\right)\left(\frac{I_{DA,589}}{I_A - 1}\right) = 0.57 \tag{3.2}$$

Table 3.4: Spectroscopic properties determined for BODIPY conjugates. ϵ - molar extinction coefficient. λ_{max} abs - absorption maxima. λ_{max} - emission maxima. ϕ - quantum yield. Solvents: †DCM, $^{\star}H_2O$, ‡DMSO.

Compound	ϵ / $dm^3\,mol^{-1}\,cm^{-1}$	λ_{max} **abs** nm	λ_{max} **em** / nm	ϕ
8 †	82468	495	506	0.63
10 *	77160	494	506	0.25
24 ‡	79198	499	506	0.61
33 ‡	86351	512	522	0.21

3.3 Conclusion

The aim of this chapter was to synthesise a range of fluorophore azides for subsequent CuAAC conjugation to an alkyne bearing CCL2 peptide. Successful synthesis of a non-cleavably linked BODIPY azide has been achieved, this fluorophore has been further functionalised with disulfonate groups on the fluorescent rings giving both a lipohilic and a very hydrophilic BODIPY azide for direct comparison. Crucially, these compounds are neutral and so intracellular localisation should be less biased towards any particular organelle such as mitochondria than charged species. The optimised potassium thiosulfonate method reduced the number of steps to form the lipophilic BODIPY disulfide from six to five steps and did not need HPLC purification due to the alternation of non-polar and polar products. These strategies resulted in formation of a lipophilic and hydrophilic BODIPY azide separated by a disulfide bond which can act as direct comparisons in terms of intracellular localisation behaviour and retention times.

A FRET pair based on rhodamine B piperazine and BODIPY was also successfully synthesised after extensive optimisation. The synthetic route had to be revised a number of times due to handling difficulties and salt formation with the rhodamines and the acid sensitivity of BODIPY. Fortunately, a highly modular synthetic strategy allowed the linker and azide regions of the FRET pair to be formed from a derivatised cysteine which were then joined by BODIPY thiol substitutions at a late stage, and finally amide coupling of rhodamine B as the final step.

The spectroscopic properties of the fluorophores and FRET pairs have also been determined which reveal a suite of fluorophores which are suitable for cellular experiments. The BODIPY and rhodamine fluorophores have spectral overlap between the donor emission and acceptor absorption peaks, the overlap is partial but this at least separates the donor/acceptor spectra enough to minimise crossover and/or bleedthrough issues. The synthesised FRET pair is capable of FRET and the FRET efficiency ratios were calculated in terms of decrease of

donor emission and increase of acceptor emission. The acceptor emission increase is reasonable which may be difficult to detect in fluorescence microscopy, however, the almost total quenching of BODIPY donor emission resembles an on-off switch system pre- and post-disulfide reduction. It is unclear whether the fluorophore aggregation observed in fluorimetry experiments will be detected as the large CCL2 conjugated to the FRET pair and any fluorophores will prevent the fluorophores aggregating together. Cleaved lipophilic fluorophores will likely localise in hydrophobic environments in the complex media found inside cells, this may be other proteins, lipid membranes or organelles and so fluorescence should be maintained irrespective of aqueous solubility.

Chapter 4

Optimisation of Copper-mediated Azide-Alkyne Cycloaddition Towards CCL2

4.1 Introduction

The previous chapter described the successful synthesis of azido-bearing fluorophores for the subsequent conjugation towards CCL2 variants through CuAAC; this chapter concerns the optimisation of the CuAAC reaction for CCL2 conjugation to these fluorophores. The incorporation of a C-terminal propargyl glycine provides the alkyne required for CuAAC and this placement of the glycine follows literature precedent of related CCL2 conjugates.[5,104] Two reports of chemically synthesised CCL2 described alternate methods for synthesising CCL2 using SPPS which provided functional CCL2 in good yield.[245,246] The first report involved a linear fmoc solid phase synthesis, followed by oxidation using both oxidised and reduced glutathione, and a final affinity purification using a CCL2 antibody.[245] The N-terminus included a cyclised pyroglutamate residue due to the glutamine of wild-type CCL2 spontaneously cyclising to the pyroglutamate. The second study involved a native chemical ligation between two smaller peptides: residues 1-35 and 36-76, where the N-terminus of amino acid 36 attacked a thioester at the C-terminus of amino acid 35 to form the ligated CCL2 protein.[246] The cysteine oxidation conditions were of a similar nature to the previous CCL2 synthesis which resulted in successful folding of the protein as confirmed by x-ray crystallography. From this literature precedent, outsourcing of the CCL2 synthesis to a specialist protein synthesis company, called Peptide Protein Research Ltd., was selected as the optimal strategy. The three CCL2 sequences included the wild-type sequence, P8A-CCL2 which includes a substitution of alanine at proline-8, and CCL2 Ala^{-1} which includes a N-terminal alanine addition. Each protein sequence included an addition at the C-terminus of CCL2 which is displayed in Scheme 4.1.

An investigation into biocompatible conjugations by Bode *et al.* highlighted the need for stoichiometric equivalents of reagents in CuAAC reactions due to low concentrations.[247] Using catalytic quantities of copper in CuAAC involving low concentration biological molecules would result in nanomolar concentrations of copper which would render the rate of reaction negligible. As described by Bode *et al.*, the second order reaction requires rate constants

R= QPDAINAPVTCCYNFTNRKISVQRLASYRRITSSKCP
KEAVIFKTIVAKEICADPKQKWVQDSMDHLDKQTQTPKT

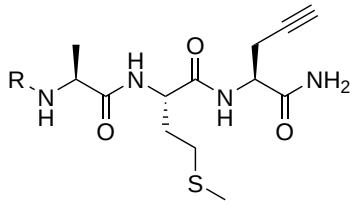

Ala-Met-Propargyl glycine

Scheme 4.1: Peptide sequence of the C-terminal addition of CCL2 for subsequent CuAAC conjugations.

above 10 $mol^{-1}\,dm^{-3}\,s^{-1}$ for 90% yield in an acceptable reaction time.[207] The investigators proceeded to report general conditions for peptide-based CuAAC: $CuSO_4$ (1.0 eq.), Na ascorbate (25 eq.) and TBTA (5.0 eq.) relative to peptide. The large excess of sodium ascorbate ensures continuous reduction of copper (II) in air and also mitigates the production of ROS species which would oxidise amino acids. Mechanistic investigations were reported by Finn *et al.*, particularly into the role of solvents in the Click reaction and how the effects could be influenced by the choice of rate accelerating ligand.[207] The authors evidenced that tris(3-hydroxypropyltriazolylmethyl)amine (THPTA) was better suited to aqueous reactions compared to TBTA due to solubility, aqueous CuAAC reactions in this chapter would therefore use $CuSO_4$ (1.0 eq.), Na ascorbate (25 eq.) and THPTA (5.0 eq.). Finn *et al.* also reported that three classes of ligand exist in the CuAAC reaction dependent on behaviour in DMSO rich or aqueous rich media. Class I ligands (including THPTA and poly-triazole molecules) exhibited highest reaction rates at 5-fold excess in aqueous media, when utilised in high concentrations of DMSO the rate decreased significantly. Conversely, class II ligands (including mixed pyridine/benzimidazole arms) operated most efficiently at 0.5 equivalents and only in DMSO-rich media. Class III ligands (mostly benzimidazole arms) were not active in aqueous media. This behaviour was rationalised by the relative copper-binding affinities whereby benzimidazole is the strongest binder, followed by pyridine and triazole. Therefore, higher equivalents of triazole ligands are needed to bind the copper efficiently, relative to the benzimidazole ligands. This copper binding must be balanced in that the ion is not bound

Table 4.1: Description of the CCL2 conjugate naming system, chemical structures of conjugates are displayed in Figure 4.1. Three CCL2 variants will be used: WT-CCL2, CCL2 Ala^{-1} and P8A-CCL2. Examples of the nomenclature of these conjugates are P8A-alk-H and CCL2 Ala^{-1}-alk-H.

Code	Compound	Meaning
WT-alk-H	**10**	alkyl-linked, hydrophillic
WT-alk-L	**8**	alkyl-linked, lipophillic
WT-SS-H	**33**	disulfide-linked, hydrophillic
WT-SS-L	**24**, **32**	disulfide-linked, lipophillic

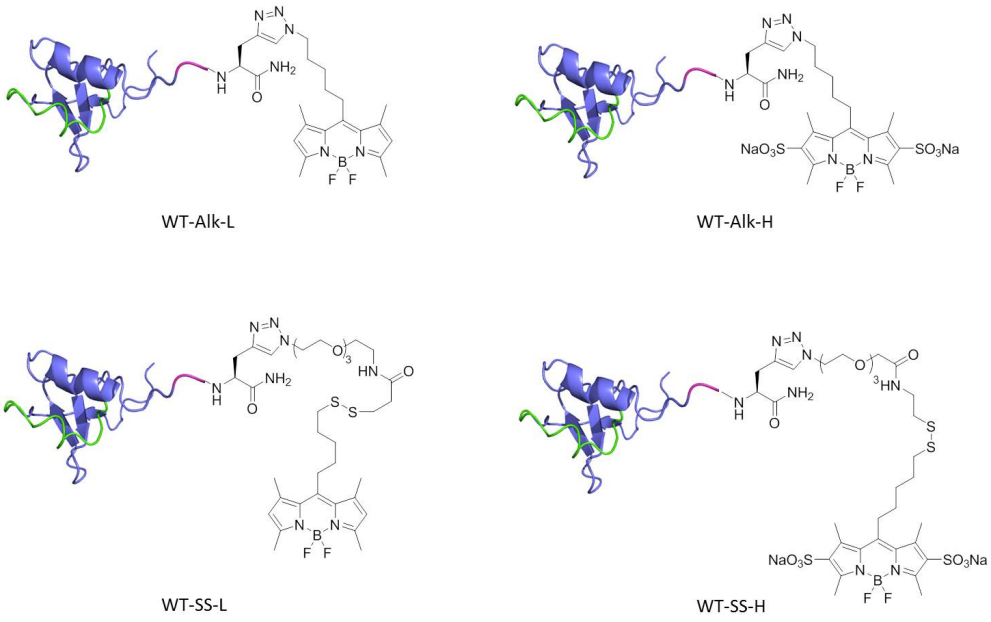

Figure 4.1: Ribbon structures of CCL2 highlighting the chemical structure of the conjugates and naming system below the structure. The naming convention is summarised in more detail in Table 4.1.

too strongly such that the reaction azide/alkyne can displace a ligand arm. The solvent DMSO, is a strong π donating compound which strongly binds copper, class I ligands cannot displace DMSO from the copper centre and so ligands such as THPTA are not suitable, instead strong copper binding ligands such as the class III benzimidazole ligands exhibit excellent rates in high DMSO concentrations. This chapter will therefore utilise THPTA in aqueous rich conjugations in the 1:25:5 molar ratio described above and $(BimH)_3$ in DMSO-rich conjugations (for lipophilic reagents) in a 1:25:0.5 molar ratio as recommended by Finn *et al.*[207] Table 4.1 and Figure 4.1 outlines the CCL2 conjugate targets and terminology.

4.2 Results and Discussion

4.2.1 Conjugation of Fluorophores to CCL2 Ala^{-1}

A specialist protein synthesis company, Peptide Protein Research Ltd. (PPR), was contracted to synthesise three CCL2 variants. As per our instructions, PPR trialled both the native chemical ligation strategy described by Gilliland *et al.*, and the linear step-wise synthesis reported by Kruszynski *et al.*, using Fmoc-SPPS techniques as well as the oxidation conditions described therein.[245,246] The linear step-wise synthesis was successful and the three desired peptides were obtained, CCL2 Ala^{-1} was completed first giving 10 mg at 90% purity. The other peptides were not as efficient as this, only 4 mg of 90% pure P8A-CCL2 was synthesised and three samples of WT-CCL2 (1.0, 2.3 and 5.1 mg) were obtained at lower purities of 74, 76 and 82%, respectively. The declared reasons for the difficulties in synthesis were cyclisation issues of the N-terminal pyroglutamate in both WT-CCL2 and P8A-CCL2. The lowered purities of the WT-CCL2 variant could not be improved upon, however, the major contaminant was an oxidised methionine residue at position 78. The two methionines are located towards the C-terminus and so it is unlikely these impurities would affect the biological function of the chemokine. The difference in lead times, quantity and purity of the three peptides resulted in much of the initial work being performed on CCL2 Ala^{-1}.

The first conjugation attempted was the formation of CCL2 Ala^{-1}-alk-H from BODIPY **10**, this was selected due to the excellent aqueous solubility of the fluorophore and the chemically inert linker. The solubility of the compound ensured that this would not affect the conjugation and the unreactive alkyl spacer would also not complicate any issues found with the reaction. The reaction scheme is displayed in Scheme 4.2 which highlights the equivalents used and bears a slight modification to reported conditions in that the azide is used in large excess of the alkyne to drive the reaction through to total conversion.[247] Obtaining one product was important as any unlabeled peptide would be difficult to separate from labeled peptide and the small amount of material used adds practical issues with HPLC.

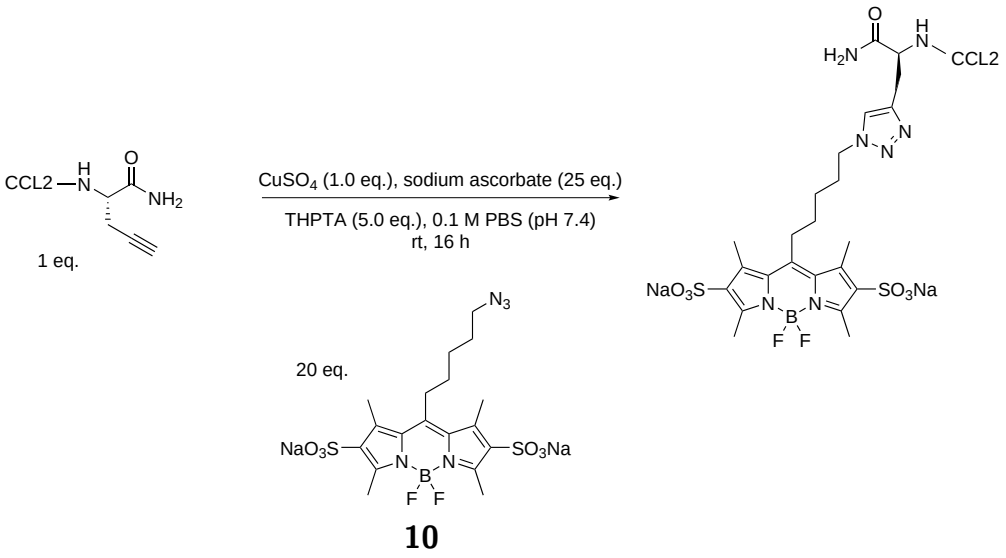

10

Scheme 4.2: Conjugation conditions for CuAAC between CCL2 Ala^{-1} and BODIPY **10** giving the desired triazole as a single product (Expected mass 9611 Da). The equivalents are listed showing the stoichiometric quantity of copper sulfate and the excess of both sodium ascorbate and azide. The concentration of CCL2 was 100 µM.

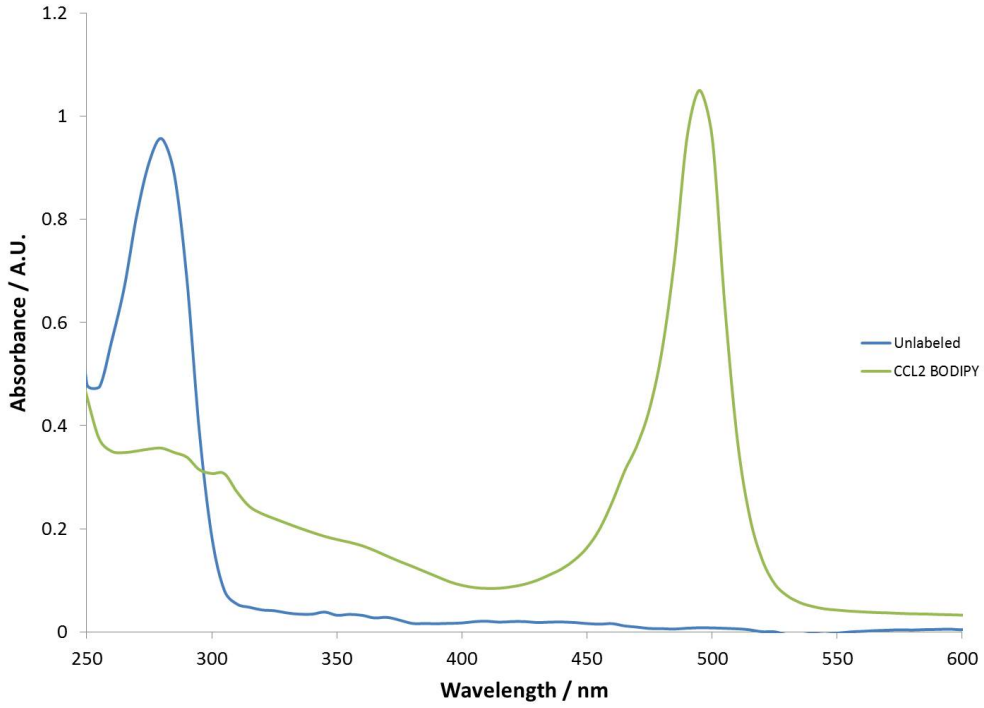

Figure 4.2: UV absorbance spectrum of CCL2 Ala^{-1} before and after the CuAAC reaction. A peak at 280 nm in the unlabelled spectrum corresponds to tryptophan absorbance, this peak broadens after the reaction due to a small contribution from BODIPY absorbance and from dilution effects. A major peak was observed at the BODIPY absorption maxima suggesting that the conjugation was successful as any free BODIPY would be removed *via* size exclusion chromatography.

As discussed in chapter 3, the order of addition of reagents is important in the CuAAC reaction to avoid poly-alkyne-copper aggregates and so the ligand, copper sulfate and ascorbate were mixed first, followed by the CCL2-alkyne and fluorophore azide. The reason for not adding the alkyne last was due to this reagent usually representing the largest volume (and therefore a major dilution) of the reaction mixture. The concentrations used by Bode *et al.* ranged between 50 and 100 µM and so this reaction was performed at 100 µM of CCL2-alkyne. After 4 h the reaction mixture was taken and the protein was separated from small molecule reagents *via* size exclusion chromatography. The concentration of the labeled protein was then determined *via* UV absorbance and the extent of conjugation was assessed using matrix-assisted laser desorption ionisation (MALDI) mass spectrometry (Figure 4.2 and Figure 4.3). The UV spectrum before and after conjugation suggested the BODIPY had indeed conjugated to CCL2 due to the presence of both a tryptophan and BODIPY absorbance peak. The labelled protein was aliquoted and stored at -30 °C in 0.1 M PBS and 0.5% BSA (v/v, a carrier protein). These conditions were used for all subsequent conjugations unless stated otherwise.

The samples were desalted and concentrated using ZipTips for MALDI-MS compatibility which consistently yielded strong MS signals even with dilute samples. The MALDI MS is accurate to 5-10 Da with large molecules and agrees well with the stated mass of 9048 Da, with the 2+M adduct observable at 4531 Da. A clear mass shift can be observed between starting material and product which corresponds to the molecular mass of the BODIPY azide (563 Da). The mass difference between starting material and product, while subject to instrumental error, may not exactly equal the molecular mass of **10** and this may reflect loss of sodium ions in the disulfonate salt as other adducts are formed. A small non-annotated peak adjacent to the parent ion is a sinapinic acid adduct which originates from the MALDI matrix. The origin of the small shoulder peak centring around 10060 Da was not clear but is again similar to the BODIPY molecular mass. However, this double-BODIPY ion was not present in ESI-MS (not shown) which suggests the second peak is a MALDI artifact or a non-covalent adduct. Whilst the MS does not provide direct evidence that the BODIPY

is conjugated to CCL2 through a 1,2,3-triazole, the large body of literature in CuAAC conjugations showing no significant non-selectivity issues suggests the BODIPY is conjugated through a triazole. CCL2-dimer peaks were only observed at high concentrations suggesting Glaser homo-coupling of alkynes did not occur and these peaks are due to supramolecular dimers.

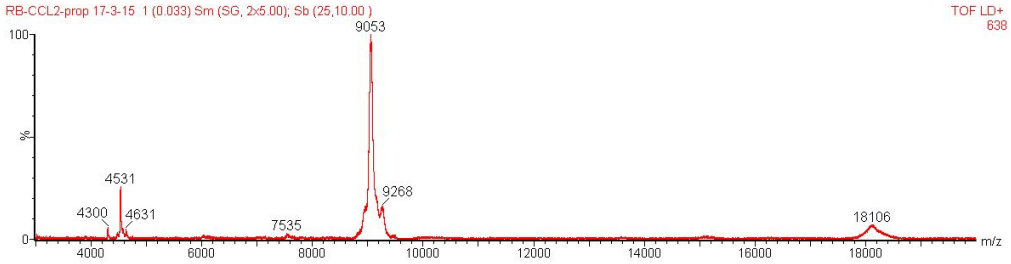

(a) MALDI MS of CCL2 Ala^{-1}.

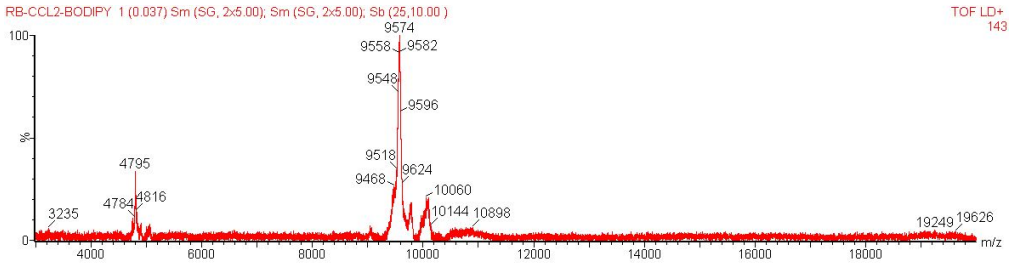

(b) MALDI MS of BODIPY labeled CCL2 Ala^{-1}.

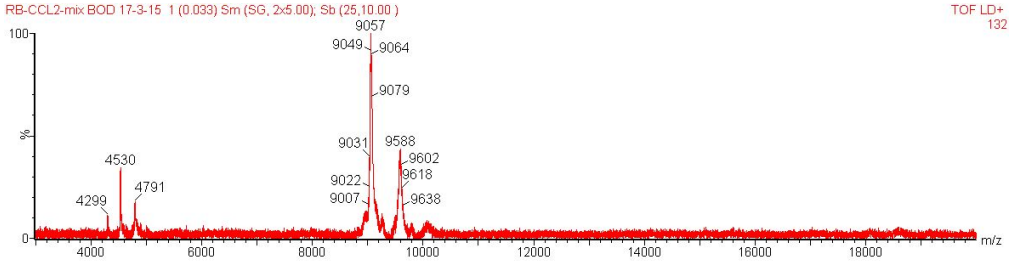

(c) MALDI MS of a mixture of unlabeled and BODIPY labeled CCL2 Ala^{-1}.

Figure 4.3: The MALDI-MS highlights close agreement of the unlabeled CCL2 molecular mass with the theoretical mass of 9048 Da and also exhibits a dimer peak at 18106 Da. A clear mass shift is present post-conjugation which resembles the BODIPY disulfonate mass of 563 Da (expected mass 9611 Da). The mixture of unlabeled and labeled CCL2 provides evidence the mass shift is real and both species give strong MS signals.

The initial attempt with CuAAC was successful and subsequent repeats behaved in a similar manner which highlighted the robust nature of CuAAC. The next step was to perform

CuAAC conjugations using the other four fluorescent systems described in Chapter 3. The lipophilic BODIPY azide **8** was selected for the next reaction as again this compound contained an alkyl linker which should not complicate the reaction if any issues arose. Unfortunately, the lipophilic nature of this compound rendered total insolubility in aqueous media. An attempt at this reaction in water was not successful, even with a potential solubilising equilibrium which could drive the reaction to completion, only unlabeled CCL2 was recovered (not shown). Other reaction conditions were therefore investigated and the most promising system was described by Finn *et al.* which involved using DMSO in aqueous media as a co-solvent.[207] Clearly DMSO is not ideal in protein conjugations as this is known to denature proteins resulting in loss of functional activity. However, the detailed analysis provided by Finn into these reactions gave confidence that the reaction could work and that we could optimise conditions such that permanent denaturation could be avoided. The reasons CCL2 may be resistant to permanent denaturation are described below:

- CCL2 is a small protein with a highly conserved structure, containing two internal disulfide bridges which confer rigidity in the structure. Therefore any unfolding due to interaction with DMSO may be reversible, as the disulfide bonds hold the overall structure in place.

- The literature reported CCL2 syntheses suggested spontaneous folding of linear peptides which ensured correct disulfide linkages in the protein, this suggests that few other possible structures are available when the disulfide bridges are intact.[245,246]

- Any unfolding due to DMSO interaction should only be temporary while DMSO is present, dialysis ensures a slow transition from high to low concentrations of DMSO.

With these considerations in mind, the conditions for a DMSO/water mixture were devised following the excellent work of Finn *et al.* and these conditions are displayed in Scheme 4.3.[207] To minimise permanent denaturation of CCL2, only a 30% solution of DMSO:PBS was used (compared to 90% DMSO described by Finn *et al.*), this was a good comprimise between solubility of **8** and high DMSO concentrations. The work up involved a dialysis step to remove

DMSO before size exclusion chromatography (to prevent sephadex gel dissolution). The reaction was first attempted on the hydrophilic BODIPY **10** used previously for comparitive reasons.

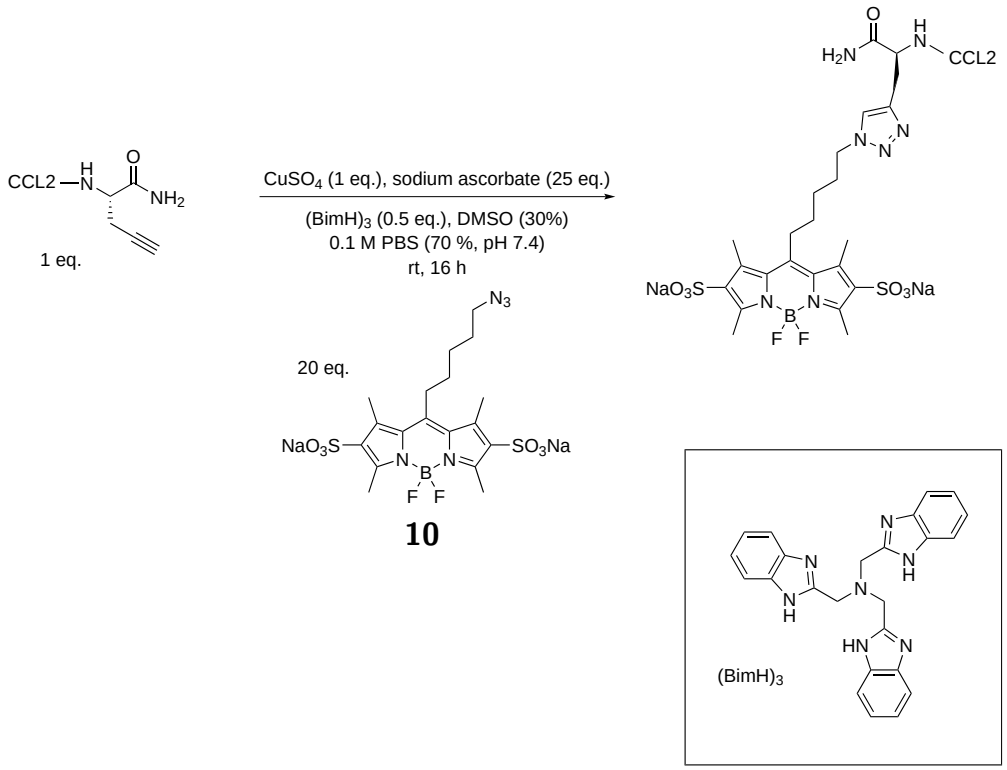

Scheme 4.3: Modified CuAAC conditions for use with DMSO as a co-solvent. The concentration of CCL2 was 100 µM.

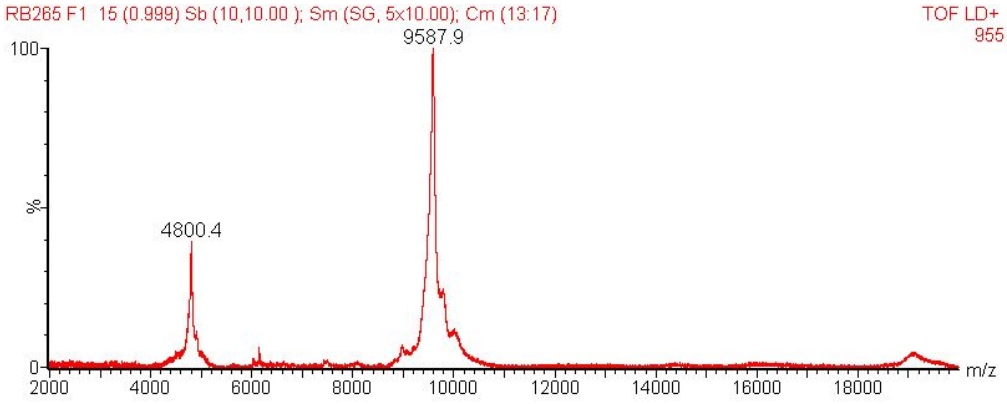

Figure 4.4: MALDI MS of the product of CuAAC between CCL2 Ala^{-1} and BODIPY azide **10** using conditions described in Scheme 4.3. The reaction appears to have gone to completion and a supramolecular dimer peak can also be observed at around 19 kDa.

The conjugation was successful (see Figure 4.4) which demonstrated that the DMSO did not significantly alter the reaction and so if the lipophilic fluorophores are able to dissolve in 30% DMSO, the reaction should occur successfully. These conditions were then repeated on both the lipophilic azide **8**, the lipophilic disulfide-linked BODIPY **24** and the FRET pair **45** (this compound was also reasonably lipophilic). Mass spectra are displayed in Figure 4.5 which highlights an issue consistently encountered in these conjugation; the reactions do not always proceed to completion and the compounds may not be stable. The simple lipophilic azide **8** (Figure 4.5a) appeared to have fully conjugated to CCL2, however, the peak was broad compared to the hydrophilic BODIPY **10** which may overshadow any unconjugated CCL2 due to the small mass shift of 359 Da. More concerningly, the multiple peaks observed in Figures 4.5b and 4.5c appear to originate from cleavage of the disulfide bond in the fluorophore **24**. In Figure 4.5b, CCL2 has fully conjugated as no starting material is present but a mixture of intact CCL2 Ala^{-1}-SS-L and CCL2-SR can be observed corresponding to the 9664.5 and 9397.6 Da peaks respectively. The triazoles have been formed in both cases indicating the reaction is proceeding but a proportion of the disulfide bonds were cleaved at a point during the reaction or work up. The fluorophore starting materials were both analysed by ESI-MS to ensure the compounds had not degraded in the stock solutions; both the FRET pair **45** and BODIPY disulfide **24** were intact (not shown). The cleavage was more pronounced in Figure 4.5c as the desired conjugate was not observed (the mass would be approximately 10310 Da), only unconjugated starting material and the peak at 9872.3 Da; this indicated loss of a BODIPY thiol species.

A literature search found one example of disulfide cleavage in CuAAC reactions was reported in the context of small molecule drug discovery.[248] The authors reported some negative results due to ascorbic acid-mediated reduction of disulfide bonds, the resulting thiol then poisons the copper catalyst preventing the reaction proceeding. Further evidence of the disulfide-reductive ability of ascorbic acid has also been sparingly reported.[249] It is likely the disulfide reduction observed was due to the action of the excess sodium ascorbate, this is supported by the incomplete reaction observed with the FRET pair **45**, suggesting the resulting thiol

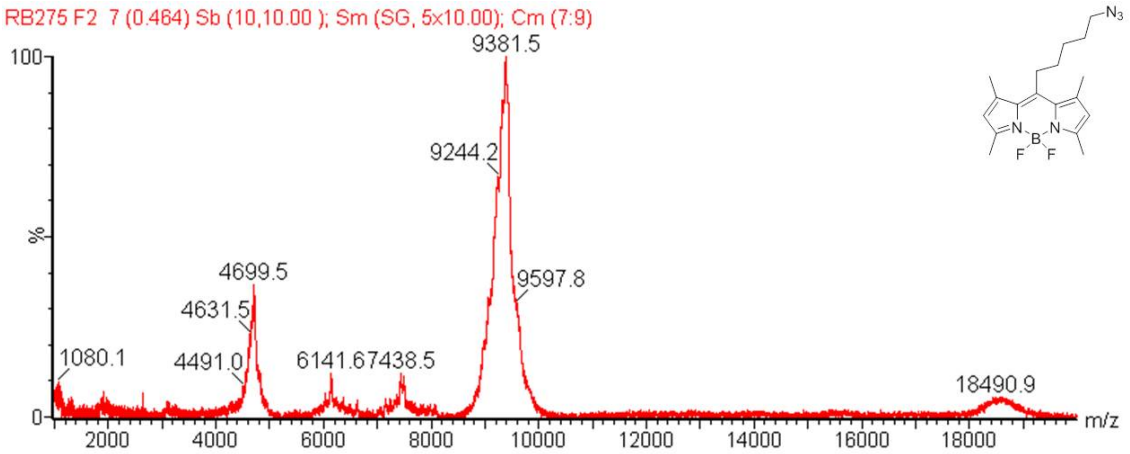

(a) MALDI MS of CuAAC between CCL2 and lipophilic azide **8** (expected mass 9430 Da).

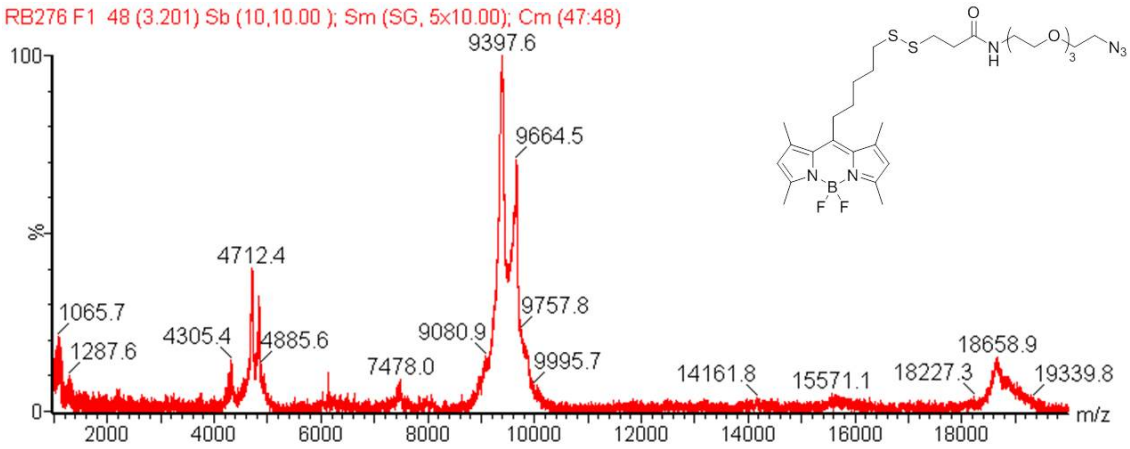

(b) MALDI MS of CuAAC between CCL2 and lipophilic disulfide **24** (expected mass 9725 Da).

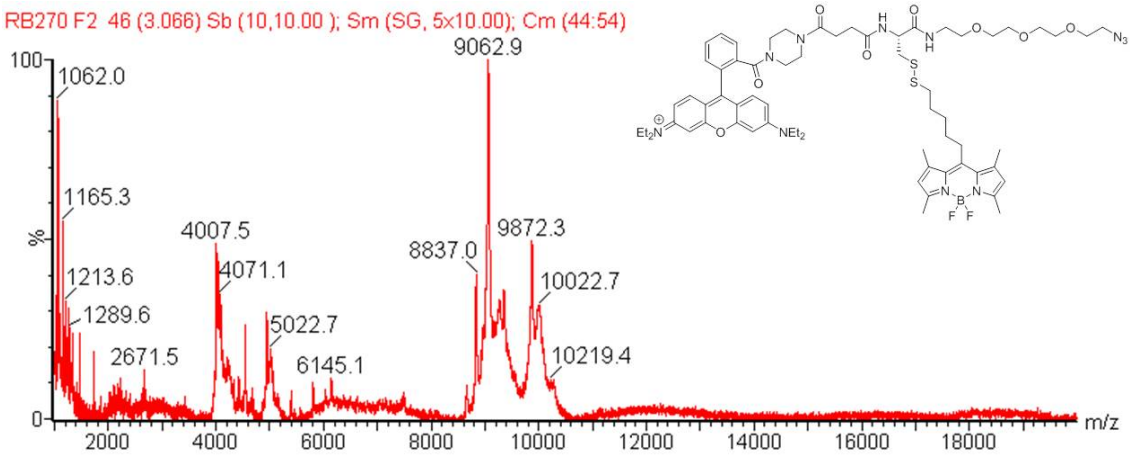

(c) MALDI MS of CuAAC between CCL2 and FRET pair **45** (expected mass 10310 Da).

Figure 4.5: The MALDI-MS of the lipophilic azide **8** demonstrates the conjugation was successful in DMSO. The disulfide-linked fluorophores, however, have multiple peaks which likely correspond to disulfide cleavage and in the case of FRET pair **45**, incomplete reaction. All conjugations were performed on CCL2 Ala^{-1}, UV-Vis spectra in Appendix, Figure 8.16.

poisoned the copper catalyst. Renslo *et al.* avoided this disulfide reduction through the use of copper (I) salts and air free techniques, this avoids the need for *in situ* reduction of copper (II) with ascorbate, indeed other reports of this strategy have been successful in CuAAC involving disulfides.[248,250,251] Many of the reports were on larger scale reactions on small molecules where reactions are practically easier to maintain oxygen-free or high temperatures were used to drive the cycloaddition to completion. The reaction conditions were modified again to include the use of copper (I) sources in DMSO under nitrogen to prevent oxidation of Cu (I) (see Scheme 4.4).

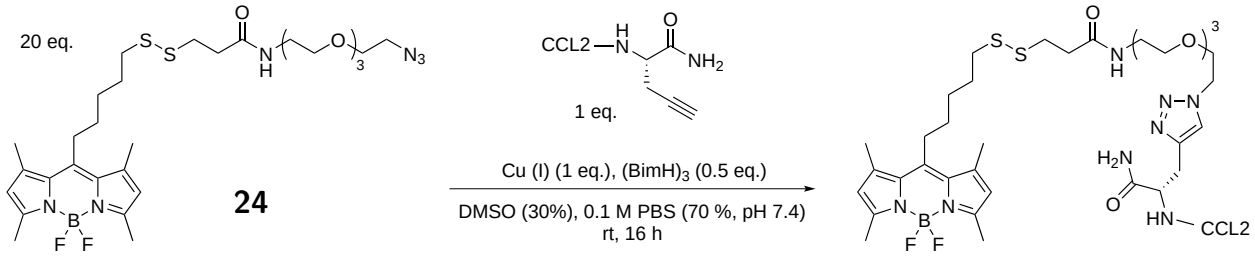

Scheme 4.4: Modified CuAAC conditions for use with Cu (I) sources in prevention of disulfide reduction. Both $Cu(MeCN)_4.PF_6$ and CuBr were used as copper sources and manual attempts at maintaining oxygen-free atmospheres were unsuccessful (MALDI-MS spectrum displayed in Appendix, Figure 8.15).

The initial Cu (I) source was the copper complex $Cu(MeCN)_4.PF_6$ which is thought to be less prone to oxidation, although the use of acetonitrile as a solvent is known to comprimise CuAAC.[207] Attempts at manually maintaining oxygen-free conditions were unsuccessful due to practical reasons as reaction solutions were usually between 100-300 µL. This meant Schlenk-techniques were not available and nitrogen flushing of centrifuge tubes was not able to maintain a nitrogen atmosphere leading to oxidation of the copper source. To circumvent this issue the commercially available Atmosbag^{TM} glove bag was utilised to form a nitrogen atmosphere which could be used to handle the low volume reactions. The experimental set-up is described in Chapter 2, DMSO and PBS were purged with nitrogen before use *via* bubbling nitrogen gas through the liquid such that all solvents and reagents were oxygen-free. The previous conjugations had used a significant amount of the expensive CCL2 Ala^{-1} alkyne and so trial CuAAC conjugations were performed in the Atmosbag^{TM} using an oligonucleotide-alkyne to preserve the protein. This ON was selected for a number of reasons including the

similar molecular mass to CCL2, the rapid availability of relatively large quantities and it's intended use as a therapeutic in parallel running projects in the group.

The trial reactions were performed on the robust disulfonate BODIPY **10** and the disulfide-linked lipophilic BODIPY **24** such that issues with disulfide sensitivity could be detected through comparison. The copper sources used were CuBr and $Cu(MeCN)_4.PF_6$, conditions are listed in Table 4.2 and Table 4.3, and all reactions were carried out in the Atmosbag^{TM} under a nitrogen atmosphere. An excess of copper catalyst was used due to any sequestration of copper by ON base pairs and possible oxidation of Cu(I) *via* oxygen contamination. The success of the reaction was determined by ESI-MS where deconvoluted parent ion peaks would be around 7350 Da and 7450 Da for **10** and **24** respectively. For conjugations on alkyl-linked BODIPY **10**, the CuBr catalyst was most effective and generally performed better with the addition of sodium ascorbate. This is not surprising as the reducing agent would reduce any oxidised copper resulting from preparatory exposure to oxygen, however, this would not be suitable for disulfide-linked fluorophores. The addition of triethylamine has been suggested to enhance Cu-acetylide formation through alkyne deprotonation; the most successful reaction included both triethylamine and sodium ascorbate which suggests this deprotonation may be important. The most surprising result was the relatively poor performance of $Cu(MeCN)_4.PF_6$ which is thought to be less prone to oxidation, this could

Table 4.2: Reaction conditions tested with BODIPY **10** and oligomer-alkyne (molecular mass 6793 Da). All reactions were carried out in the Atmosbag^{TM} under nitrogen with a 30% DMSO in PBS solvent mixture for 24 h at rt, using $(BimH)_3$ (5 eq.) as the ligand. The ON was at 25 µM and corresponded to one equivalent. Reactions were assessed using ESI-MS of dialysed samples post-size exclusion column. SM = starting material, P = product, Asc = sodium ascorbate.

Catalyst	**Base**	**Red. agent**	**Result**	**Notes**
CuBr (10 eq.)	-	-	40:60 SM:P	-
CuBr (10 eq.)	-	Asc (1 eq.)	>90% P	-
CuBr (10 eq.)	-	Asc (10 eq.)	>90% P	Peak at 8 kDa
CuBr (10 eq.)	NEt_3 (10 eq.)	-	>90% P	-
CuBr (10 eq.)	NEt_3 (10 eq.)	Asc (1 eq.)	100% P	Peak at 8 kDa, noisy spectrum
$Cu(MeCN)_4.PF_6$ (10 eq.)	-	-	>80% SM 10% P	-
$Cu(MeCN)_4.PF_6$ (10 eq.)	NEt_3 (10 eq.)	-	4:6 SM:P	-

Table 4.3: Reaction conditions tested with BODIPY **24** and the oligonucleotide-alkyne (molecular mass 6793 Da). All reactions were carried out in the Atmosbag^{TM} under nitrogen with a 30% DMSO in PBS solvent mixture for 24 h at rt, using $(BimH)_3$ (5 eq.) as the ligand. The ON was at 25 µM and corresponded to one equivalent. Reactions were assessed using ESI-MS of dialysed samples post-size exclusion column. SM = starting material, P = product, Asc = sodium ascorbate.

Catalyst	**Base**	**Red. agent**	**Result**	**Notes**
CuBr (10 eq.)	-	-	loss of ON	-
CuBr (10 eq.)	-	Asc (1 eq.)	>90% P	Some SS cleavage, noisy spectrum
CuBr (10 eq.)	NEt_3 (10 eq.)	-	>90% P	Some SS cleavage
CuBr (10 eq.)	NEt_3 (10 eq.)	Asc (1 eq.)	3:7 SM:P	Some SS cleavage
$Cu(MeCN)_4.PF_6$ (10 eq.)	-	-	100% P	-
$Cu(MeCN)_4.PF_6$ (10 eq.)	NEt_3 (10 eq.)	-	>90% P	Some SS cleavage

be a result of strong binding of the acetonitrile ligands which cannot be easily displaced by $(BimH)_3$, this has been shown in studies involving acetonitrile co-solvents.[207] Another point of interest is the nature of an unexpected peak at around 8 kDa, however, this minor peak does not relate to any identifiable molecular mass or adduct.

These results were promising as until this point, the use of copper (I) sources had resulted in no successful CuAAC conjugations and so the use of an Atmosbag^{TM} allowed the reaction to work, in principle. Similar conditions were then performed on the disulfide-linked **24** and the ON (Table 4.3). However, the possible candidates for CCL2 conjugations may not be compatible with the disulfide-linked fluorophores due to disulfide reduction and even nucleophilic attack from triethylamine. The first entry was a surprising result as no ON was observed in the mass spectrum suggesting this molecule had been lost during purification, this was occasionally observed in the project and was likely anomalous. In general, the reactions were successful, very little starting material remained and the desired product was the major component. The action of triethylamine led to some disulfide cleavage where a very minor peak corresponding to triazole formation but loss of a BODIPY-thiolate species was present, suggesting the disulfide underwent nucleophilic substitution with the amine. A similar occurrence was found with the use of a low equivalence of sodium ascorbate, fortunately this reducing agent was not necessary to maintain catalytic copper. The best

performing reaction was the $Cu(MeCN)_4.PF_6$ complex with no base or reducing agent present, in this case the desired product was the only signal present by MS. It is unclear why this complex would perform better with the disulfide **24** than the alkyl-linked **10**, though the azides are chemically very different in terms of polarity and the length of the linker between azide and fluorophore. For example, disulfide **24** contains a PEG chain, the oxygen atoms within may be able to coordinate metal ions such as the copper and this may influence the catalytic cycle between CuBr and $Cu(MeCN)_4.PF_6$.

Table 4.4: Conditions attempted on CCL2 Ala^{-1} to conjugate disulfide-linked BODIPYs using the Atmosbag^{TM} conditions trialled on the ON. Reduced P: triazole formed but disulfide reduced.

Reaction	Compound	Conditions	Result	Notes
A	**10**	$Cu(MeCN)_4.PF_6$ (10 eq.), DMSO (30%)	3:7 SM:P	-
B	**24**	$Cu(MeCN)_4.PF_6$ (10 eq.), DMSO (30%)	No protein	-
C	**33**	$Cu(MeCN)_4.PF_6$ (10 eq.), DMSO (30%)	No protein	-
D	**32**	CuBr (10 eq.), DMSO (30%)	Reduced P	All product reduced
E	**24**	CuBr (10 eq.), DMSO (30%)	>80% P	Some cleavage
F	**33**	CuBr (10 eq.), DMSO (30%)	>80% P	Many side products
G	**33**	CuBr (10 eq.), DMSO (30%)	>90% P	EDTA in work-up

In summary, copper bromide combined with triethylamine and a low equivalence of sodium ascorbate performed best with the ON-alk-H conjugate and the simplest conditions with $Cu(MeCN)_4.PF_6$ was the most successful conditions with disulfide-linked BODIPY **24**. A number of variations on these conditions were also effective and so the next step was to attempt these conditions on CCL2. Attempts are forming a disulfide-linked BODIPY conjugate are summarised in Table 4.4 and offer varying levels of success. The alkyl-linked BODIPY **10** was used in a CuAAC as a control (Table 4.4, A) with the $Cu(MeCN)_4.PF_6$ complex which was more successful in the disulfide trial reactions. This reaction worked relatively efficiently and so the same conditions were repeated on disulfide BODIPY **24** (B), unfortunately protein was not recovered from this reaction, presumably due to work up losses. Precipitates originating from the lipophilic fluorophore, particularly after dialysis, were observed but how

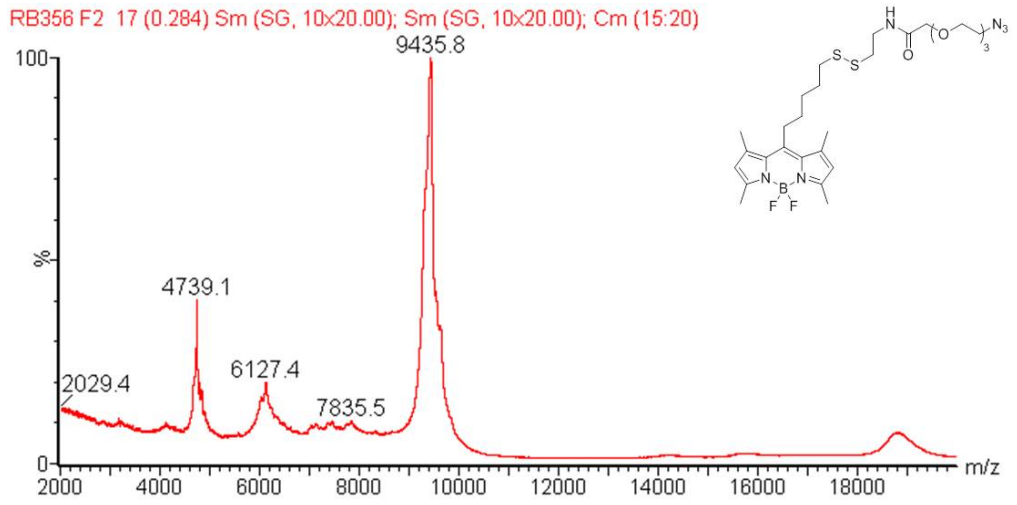

(a) MALDI MS of CuAAC between CCL2 Ala^{-1} and disulfide **32** to form CCL2 Ala^{-1}-SS-L (Expected mass 9711 Da, Table 4.4, D).

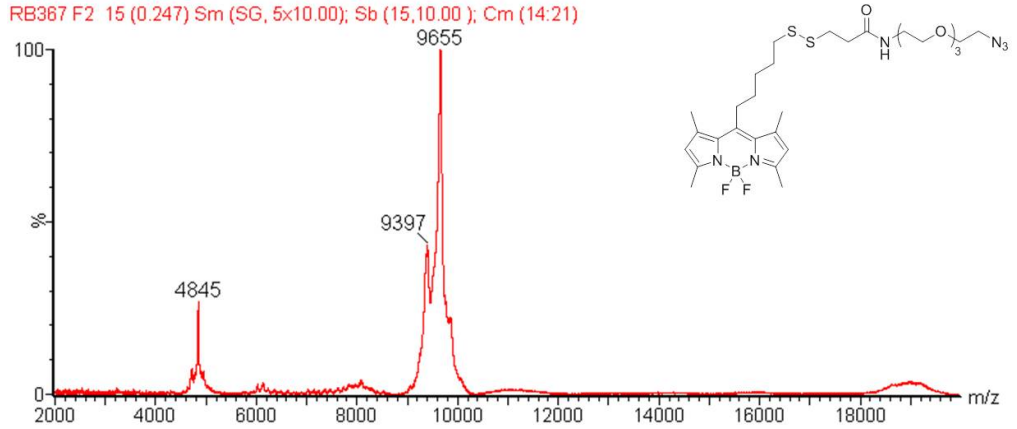

(b) Successful MALDI MS of CuAAC between CCL2 Ala^{-1} and disulfide **24** to form CCL2 Ala^{-1}-SS-L (Expected mass 9725 Da, Table 4.4, E).

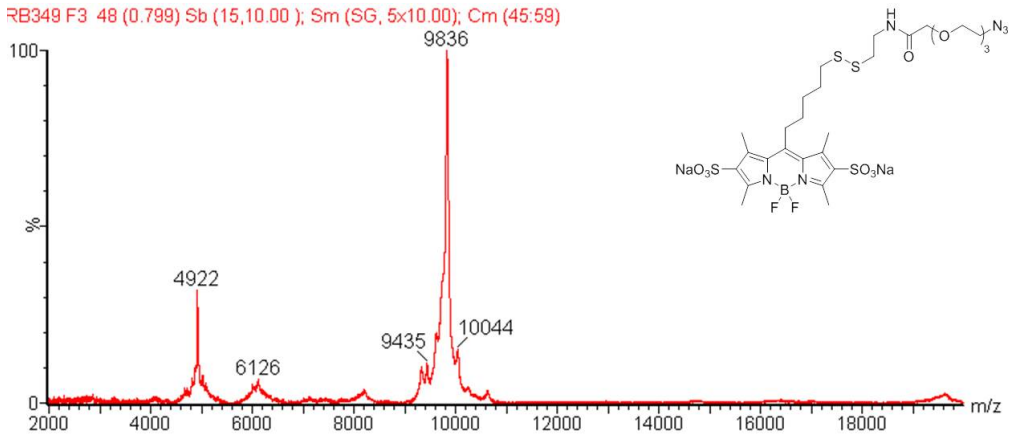

(c) Successful MALDI MS of CuAAC between CCL2 Ala^{-1} and disulfide **33** to form CCL2 Ala^{-1}-SS-H (Expected mass 9892 Da, Table 4.4, G).

Figure 4.6: MALDI MS of reactions described in Table 4.4 highlighting the improvement from initial fully conjugated but reduced products to fully conjugated with almost no disulfide reduction.

this would lead to protein losses is not clear. The polar disulfide BODIPY **33** (C) was then attempted under the same conditions to test this hypothesis, however, this also led to protein losses. At this stage, it was suspected that the combination of disulfide or the PEG chain with the $Cu(MeCN)_4.PF_6$ was involved in the loss of CCL2 and so the copper source was substituted for CuBr. Reaction D therefore utilised CuBr and a slight variation of the fluorophore to lipophilic disulfide **32**. This reaction did fully conjugate although it was associated with complete cleavage of the disulfide (see the MALDI-MS in Figure 4.6), there were no obvious reasons for this cleavage and re-characterisation of the stock fluorophore confirmed the compound was intact. The alternative lipophilic disulfide BODIPY **24** was used and this conjugation was successful, with complete conjugation and only minimal disulfide cleavage. Encouraged by this result, CuAAC on the hydrophilic BODIPY **33** (F) was then attempted under the same conditions, fortunately this reaction was successful with the desired conjugate constituting the major product (Figure 4.6b), although a number of unwanted side products were also present. This reaction was repeated with inclusion of ethylenediaminetetraacetic acid (EDTA) in the work-up in an effort to sequester any copper ions which may be associating with the PEG chain and affecting purification (G). This reaction was successful, producing a clean MALDI MS spectrum and almost no disulfide cleavage.

The next fluorophore to be conjugated to CCL2 Ala^{-1} was the FRET pair **45**; this compound is also relatively lipophilic but of a distinct structure to the problematic fluorophores. As previous attempts at CuAAC with this compound had not been successful, possibly due to solubility of the large molecule, a range of DMSO concentrations in PBS were tested on the ON and **45** (Table 4.5). Only one concentration generated any conjugated product which was the relatively high DMSO concentration of 70%. Interestingly, 90% DMSO did not work possibly due to DNA-mitigated copper sequestration which lowered the effective Cu(I) concentration such that very high DMSO concentrations (90%) are sufficient to trap the copper ion. The successful conditions were then repeated on CCL2 Ala^{-1} which resulted in conjugation of the intact FRET pair, accompanied by some disulfide cleavage and residual starting material (Figure 4.7). Whilst the presence of a mixture of FRET pair, red-fluorescent and

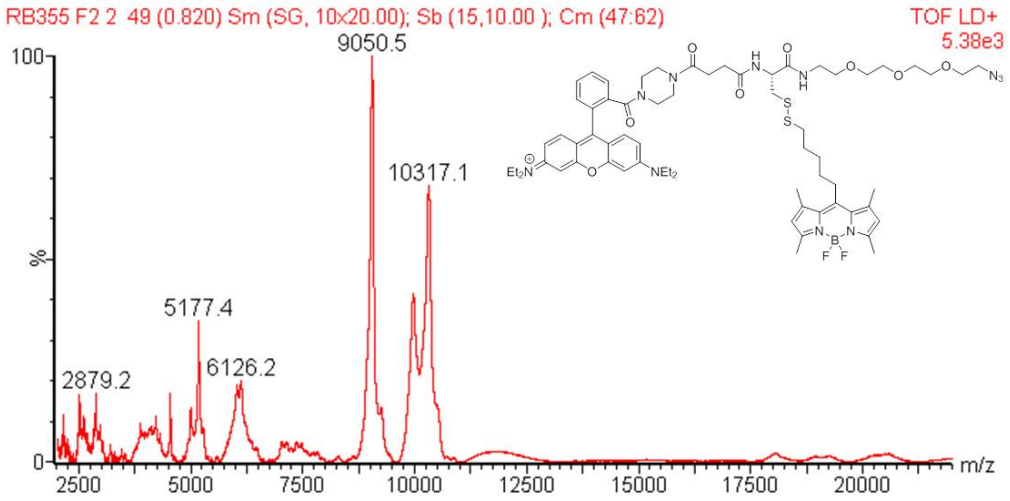

(a) Full spectrum MALDI MS of FRET-pair-CCL2.

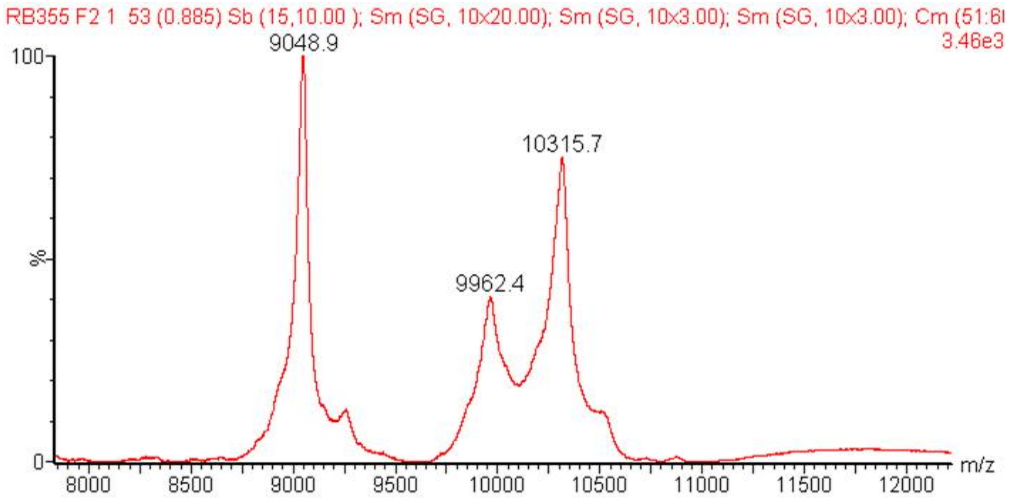

(b) Magnified spectrum MALDI MS of FRET-pair-CCL2.

Figure 4.7: MALDI-MS of successful conjugation of **45** to CCL2 Ala^{-1}, showing a mixture of unlabeled starting material (9051 Da), cleaved disulfide (9962 Da) and desired product (10317 Da). UV-Vis Spectra in Appendix, Figure 8.18.

non-fluorescent CCL2 is not ideal, the lack of remaining CCL2 Ala^{-1} meant this compromise was accepted for imaging applications in view of the conjugation difficulties encountered.

Table 4.5: Reaction conditions tested with FRET pair **45** on ON (A-D) and on CCL2 Ala^{-1} (E). Reagents were identical in each and included CuBr (10 eq.) and $(BimH)_3$ (5 eq.). SM = starting material, P = product.

Reaction	Substrate	DMSO concentration	Result	Notes
A	ON	30%	SM	-
B	ON	50%	SM	-
C	ON	70%	60:30 SM:P	Some cleavage
D	ON	90%	SM	-
E	CCL2 Ala^{-1}	70%	50:40 SM:P	Some cleavage

4.2.2 Conjugation of Fluorophores to WT- and P8A-CCL2

With a range of conjugates successfully synthesised on the CCL2 Ala^{-1} protein, residual stocks of this peptide were low and so the project moved on to conjugations with WT- and P8A-CCL2. Beginning with WT-CCL2, BODIPY **10** was first conjugated using the conventional $CuSO_4$ and sodium ascorbate conditions in air. This CCL2 variant was not as versatile in the CuAAC conjugations as it was often difficult to drive the reaction to completion (see Figure 4.8). A number of attempts were undertaken using the same conditions as conjugations on CCL2 Ala^{-1}, however, the same small starting material peak persisted in the mass spectrum and even a small scale reaction in DMSO did not aid the conjugation. The oxidised methionine present as an impurity in WT-CCL2 could have been adjacent to the propargyl glycine residue, this may have been affecting the availability of copper or the catalytic cycle and so the equivalence of $CuSO_4$ was increased to five equivalents, with matching ratios of sodium ascorbate and THPTA. The reaction profile as assessed by MS improved (Figure 4.8) but the starting material peak could not be completely removed, as this represented a minor impurity, the conjugate was taken forward for functional studies described in chapter 5. Subsequent efforts to form WT-alk-L were not successful, this fluorophore was also more

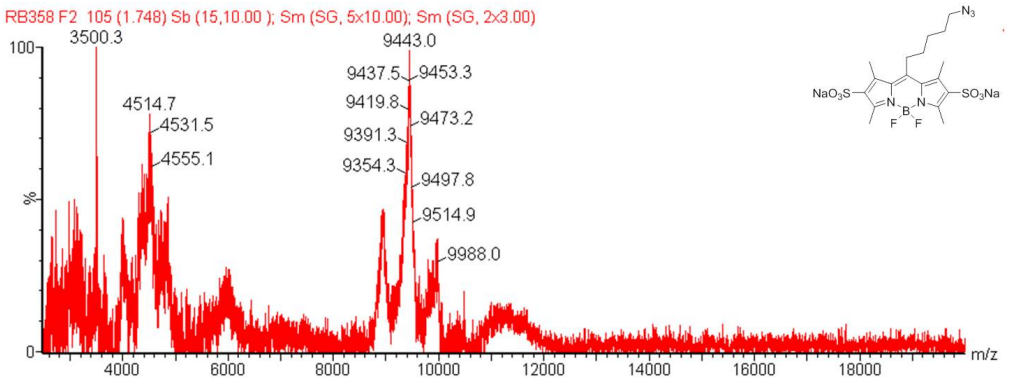

(a) MALDI-MS of CuAAC between WT-CCL2 and **10** (Expected mass 9523 Da).

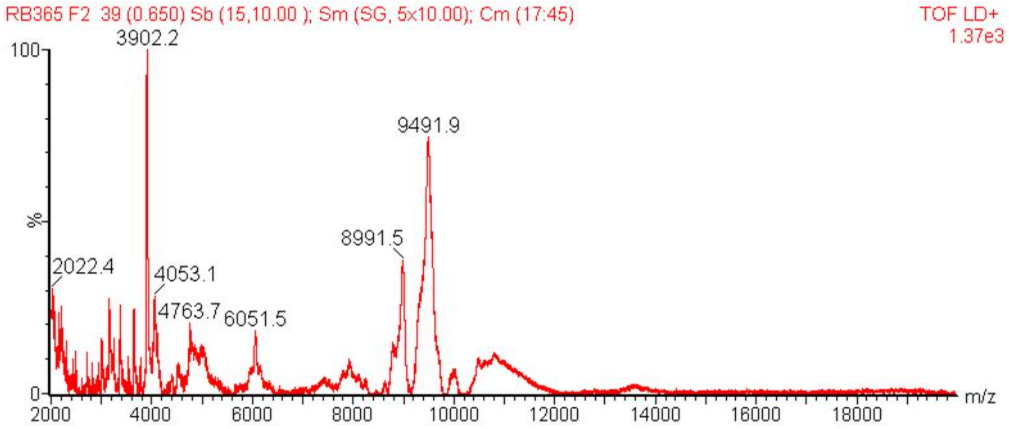

(b) Improved MALDI-MS of CuAAC between WT-CCL2 and **10**.

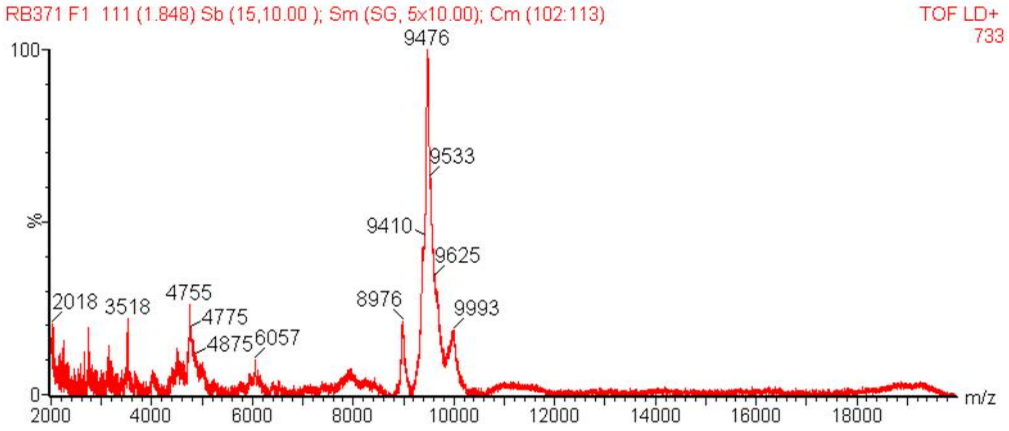

(c) Successful formation of WT-alk-H.

Figure 4.8: MALDI-MS of optimisation of CuAAC between alkyl-linked BODIPY **10** and WT-CCL2, beginning with equimolar $CuSO_4$ stoichiometry (4.8a). This MALDI-MS profile of the reaction products was noisy with some starting material present. A further attempt led to an improved mass spectrum but still had a relatively high percentage of starting material (4.8b). Finally, excess $CuSO_4$ (5 eq.) was able to minimise the presence of starting material, as assessed by MALDI-MS (4.8c), this product was therefore taken forward into functional experiments.

problematic with the previous CCL2 Ala^{-1}, possibly due to self-aggregation.

Due to the difficulties encountered with WT-CCL2 conjugations, which after multiple repeats were consistently performing poorly with a range of fluorophores, it was decided to move onto CuAAC conjugations with the final CCL2 variant, P8A-CCL2. Fortunately this protein was supplied at 90% purity (equivalent to CCL2 Ala^{-1}) and generally conjugated successfully. P8A-alk-H was formed first using BODIPY **10** and the copper (II) sulfate, sodium ascorbate conditions used with CCL2 Ala^{-1} (Table 4.6). This reaction went to completion as indicated by the lack of starting material present in the MALDI-MS spectrum (Figure 4.9), which also showed the double BODIPY peak observed in the CCL2 Ala^{-1} conjugations, again this was not present by ESI-MS (not shown). The next fluorophore to be conjugated was the lipophilic alkyl azide **8**, this was performed in 30% DMSO with *in situ* copper reduction using sodium ascorbate in air. This reaction also proceeded efficiently with the MALDI-MS presenting mostly conjugated protein, with similar double BODIPY shoulder peaks to the previous reaction. Starting material was still present in the mass spectrum although this was a minor peak. Formation of P8A-SS-H using BODIPY **33** was achieved using the previously

Table 4.6: Reaction conditions tested with with fluorophores and the CCL2 variant P8A, the conjugates taken forward are highlighted. Equivalents of reagents were identical to those previously used: fluorophore (20 eq.), CuBr (10 eq.), $CuSO_4$ (1 eq.), $(BimH)_3$ (5 eq.), THPTA (5 eq.) and Na ascorbate (25 eq.). SM = starting material, P = product. Blue highlight: successful reaction.

Reaction	Conjugate & Fluorophore	Conditions	Result	Notes
F	P8A-alk-H **10**	PBS, $CuSO_4$, Na ascorbate and THPTA	>90% P	-
G	P8A-alk-L **8**	30% DMSO, $CuSO_4$, Na ascorbate and THPTA	>80% P	Residual SM
H	P8A-SS-H **33**	30% DMSO, CuBr, $(BimH)_3$	>80% P	Some cleavage
I	P8A-SS-L **32**	30% DMSO, CuBr, $(BimH)_3$	6:4 SM:cleaved SS	-
J	P8A-SS-L **24**	30% DMSO, CuBr, $(BimH)_3$	3:7 SS Cleaved:P	Weak UV-VIS signal
K	P8A-SS-L **24**	60% DMSO, CuBr, $(BimH)_3$	3:7 SS Cleaved:P	-

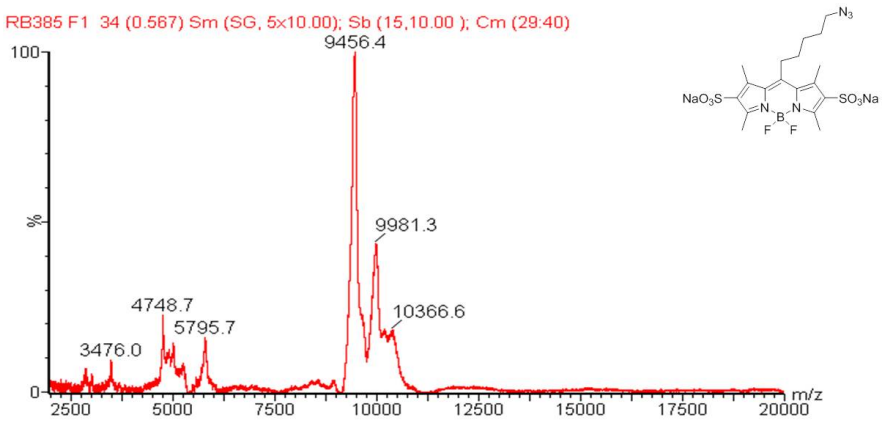

(a) Formation of P8A-alk-H (Expected mass 9497 Da, Reaction F).

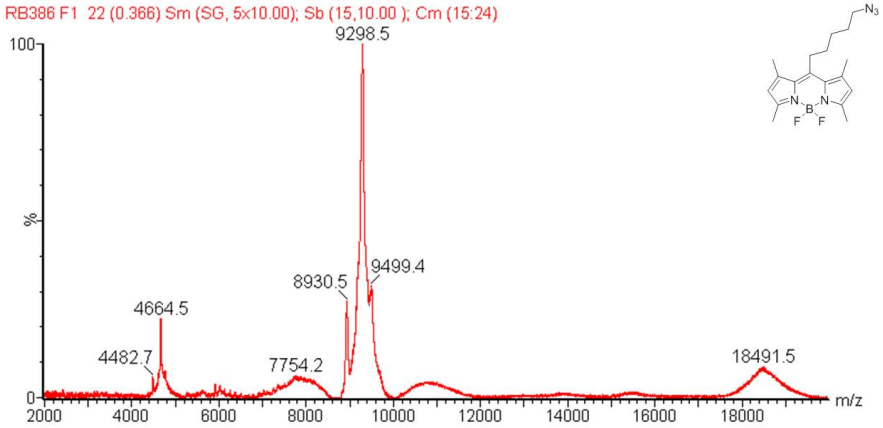

(b) Formation of P8A-alk-L (Expected mass 9316 Da, Reaction G).

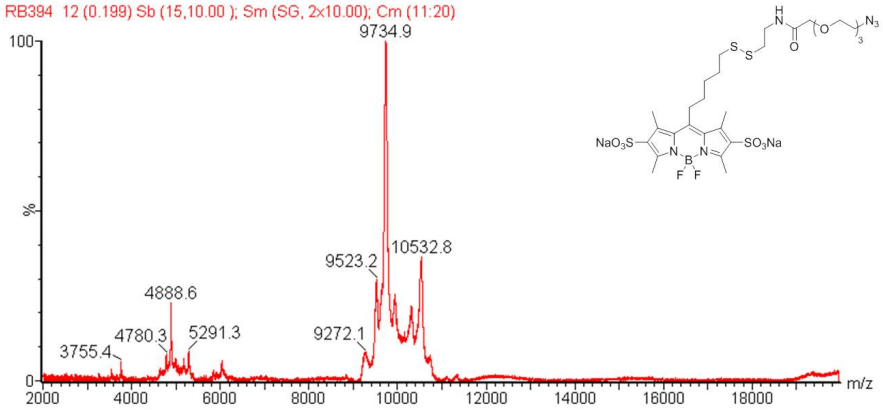

(c) Formation of P8A-SS-H (Expected mass 9778 Da, Reaction H).

Figure 4.9: MALDI-MS of successful conjugations of P8A and BODIPYs **10**, **8** and **33**. The reaction using hydrophilic BODIPY **10** gave complete conjugation and also exhibited similar double-BODIPY peaks found with CCL2 Ala^{-1}. Some residual starting material was observed with the lipophilic azide **8** with the desired product in the majority. Conjugations with the disulfonate disulfide **33** resulted in complete conjugation with small amounts of disulfide cleavage. UV-Vis spectra in Appendix, Figure 8.17

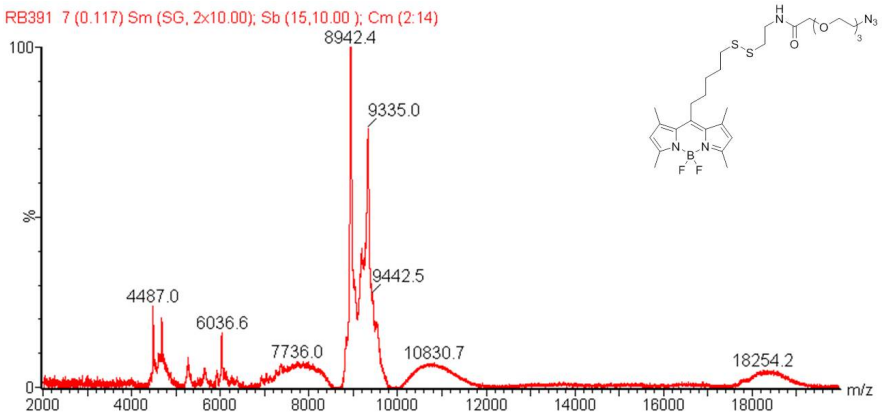

(a) MALDI-MS of CuAAC between P8A and **32** (Expected mass 9597 Da, Reaction I).

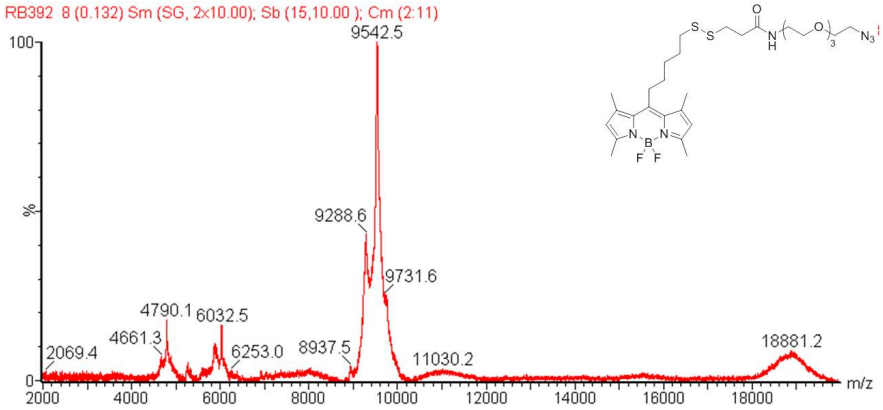

(b) MALDI-MS of CuAAC between P8A and **24** (Expected mass 9611 Da, Reaction J).

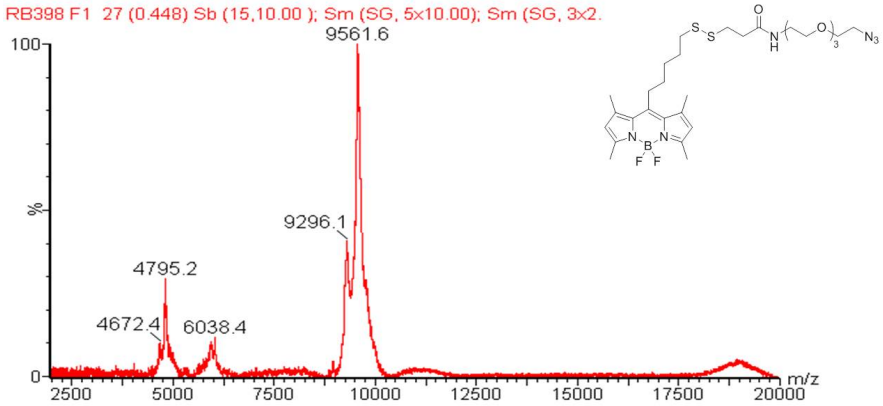

(c) Successful formation of P8A-SS-L using BODIPY **24** (Reaction K).

Figure 4.10: MALDI-MS of optimisation of CuAAC between P8A and a lipophilic disulfide-linked BODIPYs **24** and **32**. At 30% DMSO concentrations, a mixture of starting material and cleaved disulfide conugate was observed with **32** (4.10a). A greater level of complete conjugation was observed with the alternative disulfide **24** (4.10b), however, this was not reflected in the UV-Vis spectrum (Appendix, Figure 8.19). Increasing the DMSO concentration to 60% resulted in a similar MALDI-MS spectrum (4.10c) but an increased level of labelling as determined by UV.

successful CuBr conditions in the Atmosbag^{TM}, this resulted in complete conjugation with only minimal disulfide cleavage. Initial attempts at conjugating the lipophilic disulfide were not successful using either BODIPY **24** or **32**, both using the same CuBr conditions, this resulted in either poor labeling or excessive disulfide cleavage for unclear reasons (Figure 4.10). It was found that increasing the DMSO concentration to 60% and also increasing the P8A-CCL2 concentration to 170 µM (from 100 µM) gave fully conjugated protein with only minimal cleavage of the disulfide. The fluorescence spectra of the CCL2 conjugates generally resembled the unconjugated azide fluorescence spectra, however, some peak broadening relative to the free fluorophore was observed in the disulfonated BODIPYs (Appendix, Figure 8.20).

4.3 Conclusion

A number of CCL2 conjugates have been prepared utilising CuAAC and fluorescent properties have been maintained throughout. The copper (II) sulfate conditions recommended by Bode *et al.* operated as expected in the case of hydrophilic alkyl-linked BODIPY **10** which utilised sodium ascorbate for *in situ* copper reduction.[247] Following this, extensive optimisation was required to successfully conjugate lipophilic azides such as alkyl-linked BODIPY **8**. In this case, a rare example of DMSO as a co-solvent in protein conjugations is reported, following the work of Finn *et al.*, which enabled complete conjugation of simple lipophilic azides in 30% DMSO mixtures.[207] The DMSO was removed *via* dialysis and we reasoned that the small size of CCL2 allows dynamic re-folding to the correct orientation.

Further difficulties were then encountered when CuAAC reactions were performed on disulfide-linked substrates which raised an infrequently mentioned issue which is that conventional CuAAC conditions using sodium ascorbate can lead to disulfide reduction and catalyst poisoning. Evidently this was problematic in the cleavage of the fluorophores from CCL2 but also any effect this may have had on the internal disulfides found in CCL2. Three scenarios are possible from this perspective: the internal disulfides are inaccessible thus remaining oxidised correctly, the internal disulfides are reduced but the tertiary structure of CCL2 ensures rapid re-oxidation in the correct orientation, or the internal disulfides are reduced and do not then oxidise correctly. The reduction of disulfides was largely avoided through the use of copper (I) salts under oxygen-free conditions in an Atmosbag^{TM}. Fortunately, this strategy was successful and enabled the completion of the array of conjugates which were intended to be synthesised. To the best of our knowledge, this is the first report of a cleavably-linked conjugate of CCL2. Furthermore, this is achieved through CuAAC meaning that only a small modification to the C-terminus of CCL2 is required and only needs incorporation of azide functionality into the conjugating species. Finally, fluorescent conjugates of three CCL2 variants are also reported, CCL2 Ala^{-1} and P8A-CCL2 conjugates represent novel examples of fluorescent CCL2 mutants.

Chapter 5

Characterisation of Fluorescent Chemokines

5.1 Introduction

A range of CCL2 conjugates were prepared in the previous chapter on three CCL2 sequences which have been shown to be functionally distinct in the literature.[224,225] The focus of this chapter is to characterise the functional behaviour of the synthesised CCL2 conjugates in terms of chemotactic activity, specificity of the conjugates for CCR2 and assess any uptake of the fluorescent chemokines across primary human immune cells. The binding of CCL2 to CCR2 has been characterised extensively using radioligand binding assays, however, this assay does not provide any functional information. Chemotaxis assays provide functional information whereby cells migrate towards a concentration gradient of a chemokine. A common assay utilised in chemotaxis is the Boyden chamber chemotaxis assay; this assay involves two chambers separated by a porous membrane whereby the chemoattractant is located in the lower chamber and the cells are placed in the upper chamber.[252] If a chemoattractant is present the cells in the upper chamber will invade the lower chamber using the pores in the membrane to migrate across. There are many benefits to using this assay which has established the Boyden chamber assay as the gold standard in identifying new chemokines, for example, it is simple to use and the experiment takes a relatively short amount of time (1-6 hours). The short experiment times prevent cell proliferation having any effect on the migration towards the lower chamber.[252] The physical separation of the cells from the chemoattractant allows multiple factors to be included in the upper chamber, such as chemotaxis inhibitors, to assess selectivity of the chemoattractant.[252] This is generally more difficult or not possible in other assays such as 3D chemotaxis assays where cells are hosted in a collagen matrix. The results are reliable and the assay tends to be successful whereas in more complex chemotaxis assays collagen matrix preparation is difficult and often has a high failure rate. A number of investigations into chemokines have utilised the Boyden chemotaxis assay such as the CCL2-mCherry conjugate, CCL2/CCR2 selectivity, CCR2 antagonism and CCR2 antagonist identification.[5,113,253] Following the chemotactic characterisation of the CCL2 conjugates, the monocyte subset selectivity will be determined using monoclonal an-

tibody labelling in flow cytometry. Finally, the CCL2 conjugates will be used in fluorescence microscopy to determine subcellular localisation in cells, including any differences in localisation across the CCL2 conjugates as a result of differences in fluorophore hydrophilicity or linker chemistry.

The experiments involving monoclonal antibody labelling of PBMCs were performed in collaboration by Ryan Brown (RB) and Dr Christopher Weston (CW). Both RB and CW designed the experiments, RB isolated the primary cells and prepared the labelling experiments, CW operated the flow cytometer, both RB and CW designed the strategy to analyse the data.

5.2 Results and Discussion

5.2.1 Assay Development to Characterise CCL2 Conjugates

The first step towards characterising the chemotactic function of the synthesised CCL2 conjugates was to perform chemotaxis assays using Boyden 96-well transwell plates. Initial experiments counted the migrated cells using a hemocytometer, however, this approach was particularly time-consuming and contained some variation in cell numbers. The plates are intended for high-throughput experiments and so this strategy was modified to include quantification of the experiment *via* the use of the Attune Flow Cytometer; this allowed both cell counts and fluorescence to be rapidly measured in a 96-well auto-sampler. The flow cytometer measures events per microlitre for gated events in a population and this number is an indirect measure of the number of cells. This indirect measurement of cell numbers was therefore validated through seeding a fixed number of cells into a well and comparing this to the number of events (Figure 5.1). The number of events was consistently slightly lower than the number of seeded cells and the accuracy was greater around the number of cells which usually migrate in the transwell experiment and so this showed using this quantification method was reliable.

These experiments suggested that flow cytometry could be effectively coupled to the Boyden transwell chemotaxis assay to allow both cell counting and fluorescence measurements. The experiments were designed as follows: 300 $\times 10^3$ cells were seeded in the top chamber and left to incubate for either 24 or 4 hours. The cells were then fixed in the 96-well plate before sampling in the flow cytometer. Figure 5.2 shows that PBMCs and THP-1 cells exhibited very different chemotactic responses towards recombinant human CCL2 (purchased from Peprotech, used as a positive control). The PBMCs do not exhibit an obvious chemotactic response and also have a number of outliers, for example, at 20 nM. The THP-1 cells on the other hand offer a more obvious response with a maxima at 10 nM which lies inside the 1-10 nM range reported by Peprotech. One possible reason for this difference is the tendency for

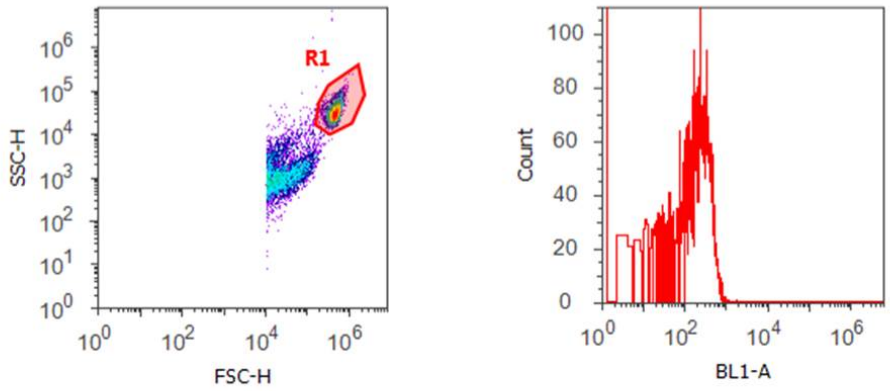

(a) THP-1 population on Attune flow cytometer

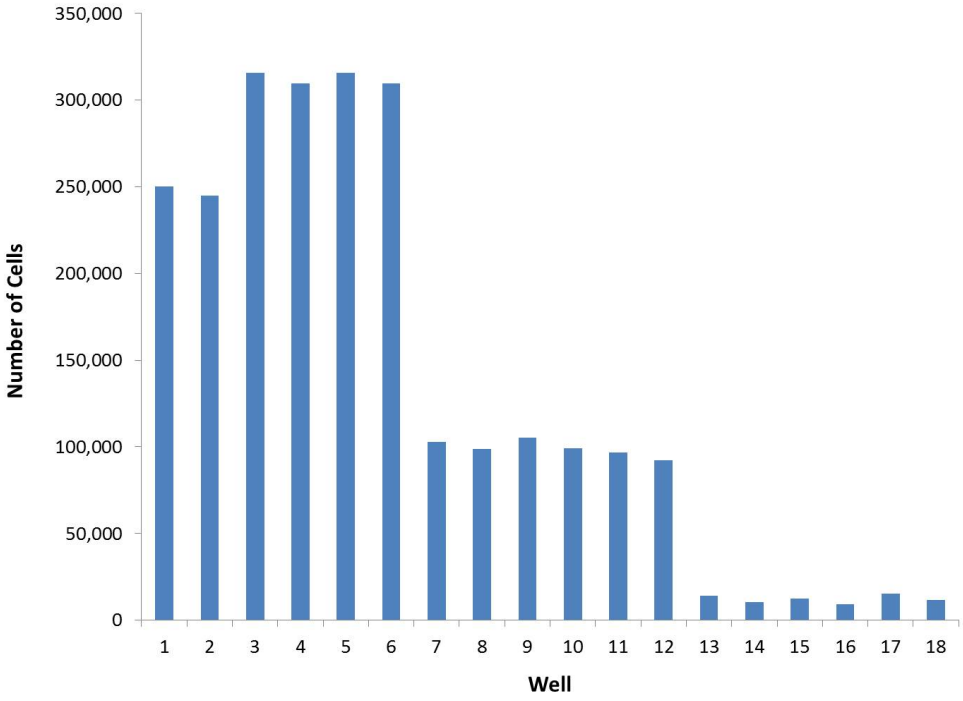

(b) Validation of flow cytometric cell counting

Figure 5.1: Gating strategy using forward and side scatter to isolate the population of cells at R1 (FSC thresholding at 1000). The fluorescence (BL1) was measured using a 488 nm laser for BODIPY excitation which also allows the fluorescence median per event to be determined. Figure 5.1b displays the validation of cell counting in a 96-well plate with using THP-1 cells. 500,000 cells seeded in wells 1-6, 125,000 cells seeded in wells 7-12 and 10,000 cells seeded in wells 13-18. The average cell counts are 290,933 for wells 1-6, 99,202 for wells 7-12 and 12,204 for wells 13-18.

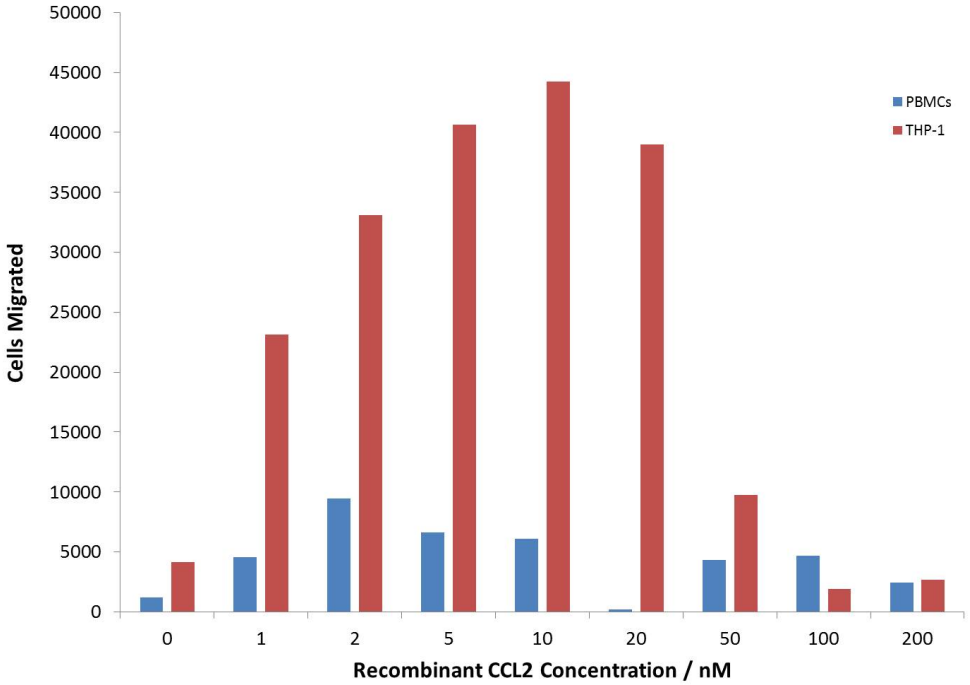

(a) Migrated PBMCs and THP-1 cells in Boyden chemotaxis assay.

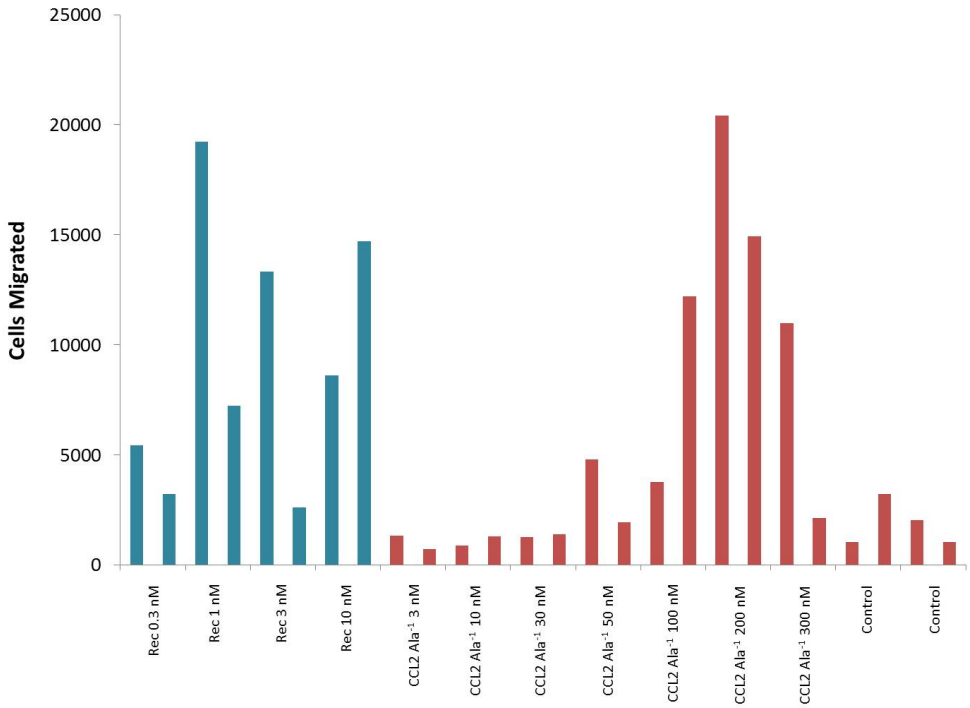

(b) Recombinant CCL2 and CCL2 Ala^{-1}-alk-H chemotactic response.

Figure 5.2: The bar chart highlights the poor and inconsistent response of PBMCs towards recombinant CCL2 in the transwell chemotaxis assay (5.2a). The THP-1 cells gave a strong response which correlated with the 1-10 nM chemotactic maxima range reported by Peprotech. The difference in chemotactic maxima between recombinant CCL2 and the CCL2 Ala^{-1} conjugate is similar to the reduced affinity reported in the literature (5.2b). Duplicate wells exhibit a large amount of variation which was likely due to the fixation step. Cells in 5.2a were incubated in the transwell for 24 h and in 5.2b for 4 h.

human monocytes to adhere to the wells and thus a reliable measure of the number of migrated cells is difficult to establish. Another issue with PBMCs is donor variability leading to inconsistent chemotactic responses. It was therefore decided to use THP-1 cells for migration experiments as these cells were more consistent and were also practically more preferable for the large number of experiments to be completed. The length of the transwell incubation was also reduced to 4 h from 24 h because it was apparent the longer incubation time was not necessary. Figure 5.2b shows the migratory response of THP-1 cells to the recombinant CCL2 and the CCL2 Ala^{-1}-alk-H conjugate, this was an encouraging result as the fluorescent conjugate would appear to be chemotactic and even exhibited a reduced affinity relative to the wild-type sequence which was reported in the literature. However, considerable variation was observed between duplicate wells and upon further investigation this was found to be due to the fixation of the cells in the 96-well plate; subsequent migration experiments were therefore not fixed and flow cytometry was performed on live cells.

5.2.2 CCL2 Variants on Alkyl Linker System

The optimised transwell assay described in the previous section was then used to quantify the three CCL2 variants on the hydrophilic-alkyl-BODIPY conjugates. The chemotactic responses of the variants WT-alk-H, P8A-alk-H and CCL2 Ala^{-1}-alk-H are displayed in Figure 5.3 which highlights clear differences between the peptides. The percentage of migration maxima was used as a normalisation technique between experiments due to the variation of maximal migrational responses of the THP-1 cells between experiments. This accounted for differences in the THP-1 population over time, cell confluence, time for experimental set up, cell counting error and pipetting error; this was deemed acceptable as the maximal responses of the chemokines were not affected and this method is also used in the literature.[113] Each concentration of CCL2 was used in duplicate wells, this was then averaged and each conjugate experiment was repeated to N = 3. The conjugates were compared to commercially available recombinant human CCL2 (Peprotech), this protein exhibited a maximal migrationary response at 3 nM which agreed well with a range of 1-10 nM as quoted by Peprotech,

this suggested the THP-1 cells were migrating towards a known chemokine and the assay was functioning correctly. Another experimental consideration was that if less than 20×10^3 cells migrated at the maximum response of recombinant CCL2, the experiment was deemed unsuccessful and discarded.

The CCL2 conjugates are clearly chemotactic and have a varied chemotactic response which correlates well with the reported maxima for unmodified sequences described in the literature. CCL2 Ala^{-1}-alk-H exhibited a maxima at 200 nM which corresponds with the literature reported reduction in affinity of 1-200 fold relative to WT CCL2.[224] P8A-alk-H, on the other hand, exhibited a greater affinity for the receptor with maximal induction of chemotaxis at

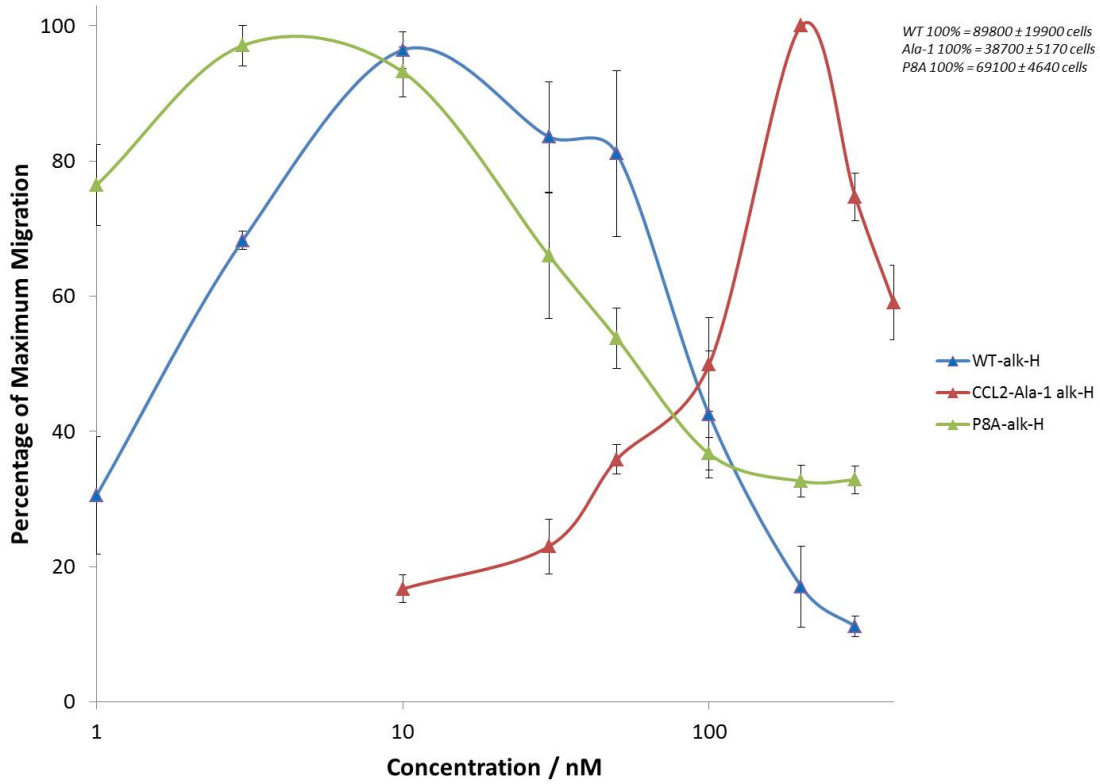

Figure 5.3: The chemotactic migrational repsonses of THP-1 cells to alkyl-linked fluorescent chemokines WT-alk-H, P8A-alk-H and CCL2 Ala^{-1}-alk-H. The number of migrated cells has been normalised to the percentage of the maximal migration and the x-axis is on a log scale. The Boyden transwell chemotaxis assay was devised as described in the previous section and each concentration was carried out in duplicate and averaged. The three conjugates were chemotactic and each exhibited different chemotactic maxima which correlated strongly with literature reports suggesting both the amino acid additions at the C-terminus and the conjugates were not affecting chemotaxis.[224,225] Error bars correspond to standard error where N = 3. Negative controls relevant to each CCL2 conjugate: WT-alk-H = 11.4% ± 3.68%, P8A-alk-H = 30.3% ± 1.87% and CCL2 Ala^{-1}-alk-H = 10.2% ± 2.68%.

3 nM which also agrees with literature reports of the unmodified P8A sequence.[225] Finally, the wild-type sequence WT-alk-H exhibited a slightly reduced maxima at 10 nM, however, this falls within the 1-10 nM range for recombinant CCL2. One reason for this reduction in migrational maxima is the lower purity of the WT sequence relative to P8A-CCL2 which was also an issue in the CuAAC conjugations. For each conjugate, the migratory response gradually reduces above and below the maximal concentration, this behaviour provides more evidence the conjugates are recruiting the cells *via* chemotactic signaling. Clearly, at concentrations less than the maxima, fewer cells will migrate towards the chemokine, however, at higher concentrations fewer cells are recruited as the concentration of chemokine surrounding the cell is so high that the direction of concentration gradient cannot be detected easily. This behaviour is indicative of the action of chemokines and can be rationalised through a switch in mechanism from chemotaxis to chemokinesis, whereby the cells are moving in a random motion, not a chemotactic motion.[11]

The graph displayed in Figure 5.4 highlights the difference between unlabelled and labelled CCL2 variants for WT and P8A sequences. In the case of WT-CCL2 and WT-alk-H, the migratory maxima is the same at 10 nM suggesting the presence of the fluorophore at the C-terminus has little effect on chemotactic signalling. It could be argued that the curve is slightly shifted to higher concentration in WT-alk-H relative to WT-CCL2, however, this shift is minor and would have little effect on subsequent experiments. Interestingly, P8A-alk-H and P8A-CCL2 had the same maximal chemotactic concentrations but there was more peak broadening in P8A-alk-H. The reasons for this broadening were unclear as only one species was present in the MALDI-MS spectrum (Figure 4.9a) and so this effect was not due to a mixture of P8A-alk-H and P8A-CCL2. The chemotactic response of recombinant CCL2 was used as a positive control (5.4b) which shows the assay is operating correctly. Finally, the lower affinity CCL2 Ala^{-1} chemokine displayed a migratory peak shifted to higher concentrations relative to recombinant CCL2 (Figure 5.5). The unlabelled CCL2 Ala^{-1} protein exhibited a chemotactic maxima of around 300 nM whereas the CCL2 Ala^{-1}-alk-H exhibited a maxima at 200 nM. However, close inspection of the unlabelled peak suggests this maxima

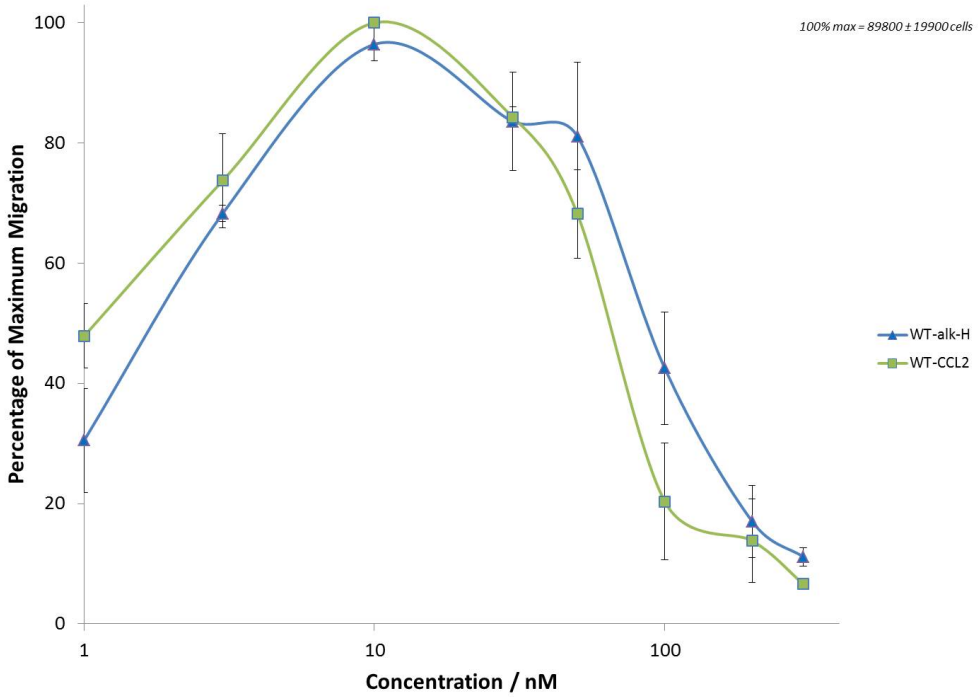

(a) Migration data for labelled and unlabelled WT-CCL2

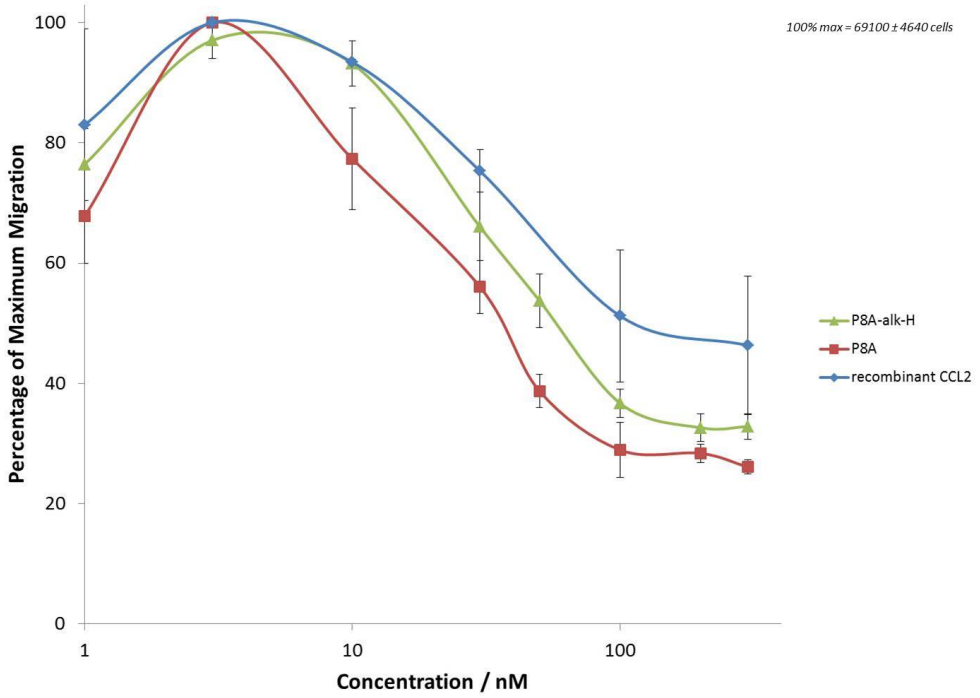

(b) Migration data for recombinant CCL2 and labelled and unlabelled P8A-CCL2

Figure 5.4: Transwell chemotaxis assay showing the migratory responses for both unlabelled and labelled CCL2 variants. Generally, the presence of the fluorophore had little effect on the chemotactic potency of the chemokines, however, some peak broadening was observed in P8A-alk-H. Recombinant CCL2 (Peprotech) exhibited a maxima at 3 nM with a slightly broader peak than P8A-CCL2. Negative control for WT-CCL2 = 11.4% ± 3.68 and for P8A-CCL2 = 30.3% ±1.87. Error bars refer to standard error for N = 3.

may not be accurate due to the error at 400 and 200 nM, this suggests the maxima may lie between 200 and 300 nM. For the purposes of this project, this was deemed acceptable as calculating the chemotactic maxima to high accuracy would involve radioligand labelling which is beyond the scope of this project.

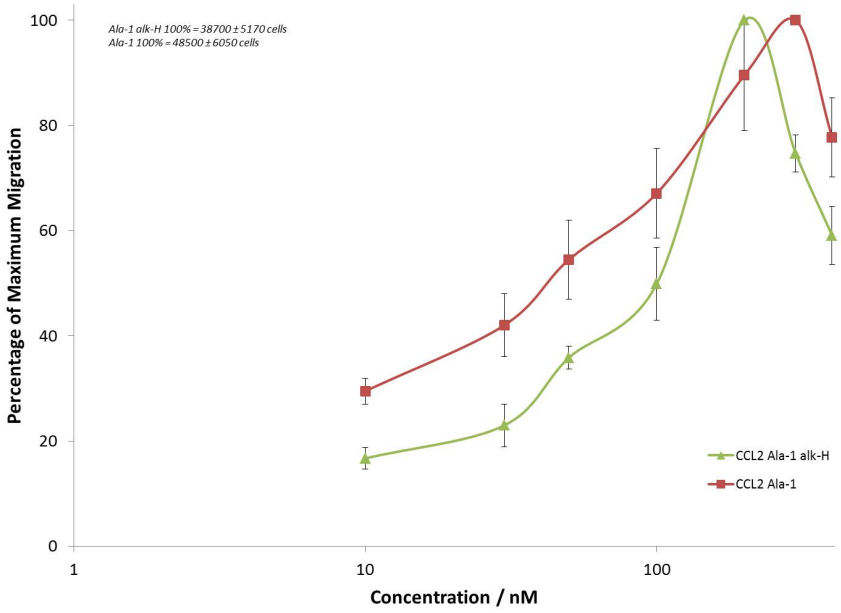

Figure 5.5: Boyden transwell chemotaxis assay displaying migration data for unlabelled CCL2 Ala^{-1} and CCL2 Ala^{-1}-alk-H. The chemokines have less affinity for CCR2 and therefore exhibit maxima at 300 and 200 nM, respectively. However, the error around the maxima for unlabelled CCL2 Ala^{-1} suggests the true maxima may be between 200 and 300 nM. Negative control = 10.2% ± 2.68%. Error bars refer to standard error and N = 3.

The median fluorescence across the THP-1 cells was also utilised in these experiments to determine internalisation dynamics of the fluorescent chemokines. Figure 5.6 highlights the fluorescence of the cells with respect to the chemokine concentration and this data is co-plotted alongside the migration data for comparison with chemotaxis. The fluorescence of P8A-alk-H and WT-alk-H rapidly increase with higher concentration until a pseudo-steady state is reached at around 30 nM. An important point to note is that the cells migrate in the receiver well and are then in a high CCL2 concentration medium for the remainder of the experiment and so should continue to internalise the ligand. In terms of P8A-alk-H, a steady state was observed at approximately ten-fold higher concentration than the chemotactic maxima and for WT-alk-H the steady state began around 3-5 fold above the chemotactic

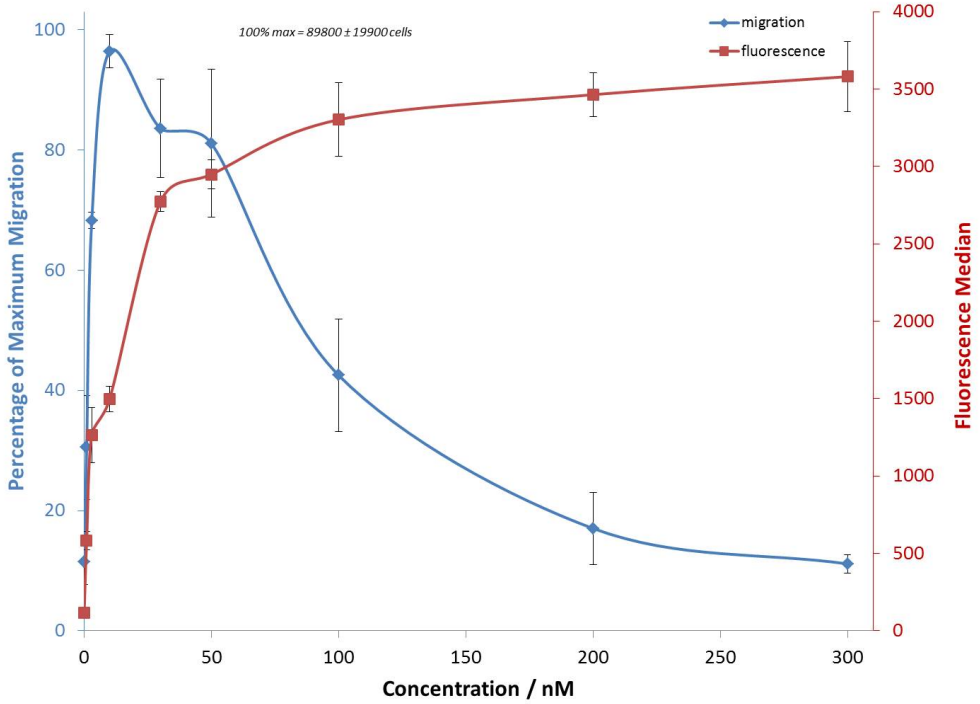

(a) Comparison of fluorescence and chemotaxis for WT-alk-H.

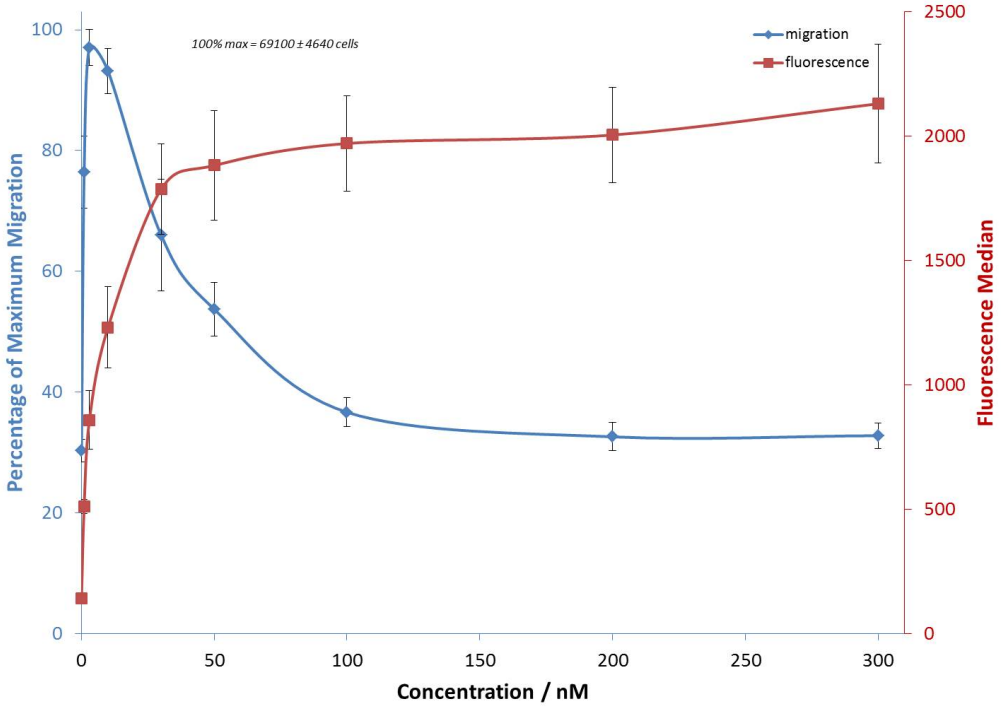

(b) Comparison of fluorescence and chemotaxis for P8A-alk-H.

Figure 5.6: Graphs showing the migration of THP-1 cells in a transwell Boyden chemotaxis assay as a bar graph and the median fluorescence of migrated cells as a scatter graph. Steady states of fluorescence are observed for both WT-alk-H and P8A-alk-H above the chemotactic maxima suggesting depletion of surface CCR2 limits internalisation of the chemokine. The steady state could also be caused by equilibria between internalisation and lysosomal degradation of the fluorophore under acidic conditions. Error bars refer to standard error at N = 3.

maxima. A steady state in fluorescence above the chemotactic maxima was not observed for CCL2 Ala^{-1}-alk-H, however, in comparison to P8A-alk-H and WT-alk-H, the concentrations measured were perhaps not high enough to attain a steady state (Figure 5.7). Attempts were therefore made to find a steady state between internalisation and degradation of the fluorophore in CCL2 Ala^{-1} by measuring the migration and fluorescence at 200, 600, 800 and 1000 nM in a Boyden transwell chemotaxis assay. Figure 5.8 displays two attempts at evaluating these higher concentrations, however, some inconsistent results were encountered which made drawing any conclusions difficult. In Figure 5.8a, the migration above the chemotactic maxima appeared to give a second peak in comparison to the data presented in Figure 5.7, however, the fluorescence increased from around 2500 A.U. to 5000 A.U. from 200 nM to 600 nM and then modestly increased to around 6000 A.U. at 800 nM which was then maintained to 1000 nM. This suggested some steady state in fluorescence but the ambiguous chemotactic data meant that this was not conclusive. At this stage, no further experiments wer performed due to the inconsistency of the results requiring more repeats which were very costly in terms of the amount of CCL2 Ala^{-1}-alk-H required to produce the high concentrations. The inconsistent results could have been due to occasional formation of high order oligomers (known to occur in chemokines[254]) which may then internalise through a non-endocytic mechanism such as macro-pinocytosis or phagocytosis. The steady states observed in WT-alk-H and P8A-alk-H are interesting because if the chemokines are being continuously internalised, this fluorescence should steadily increase with higher concentrations. The steady states suggest that the levels of surface receptor CCR2 are being depleted at high concentrations which limits the entry of the fluorescent chemokines. Another explanation is that the ligand-receptor complex is being processed by the endocytic machinery and the fluorophore is being localised in lysosomes, this could then lead to degradation of the fluorophore and loss of fluorescence (the acid-sensitivity of the boron centre of BODIPY would suggest this is possible). An equilibrium would then be achieved between uptake of the chemokine and degradation of the fluorophore, leading to the steady state.

In terms of the absolute fluorescence of the chemokines, CCL2 Ala^{-1}-alk-H exhibited the

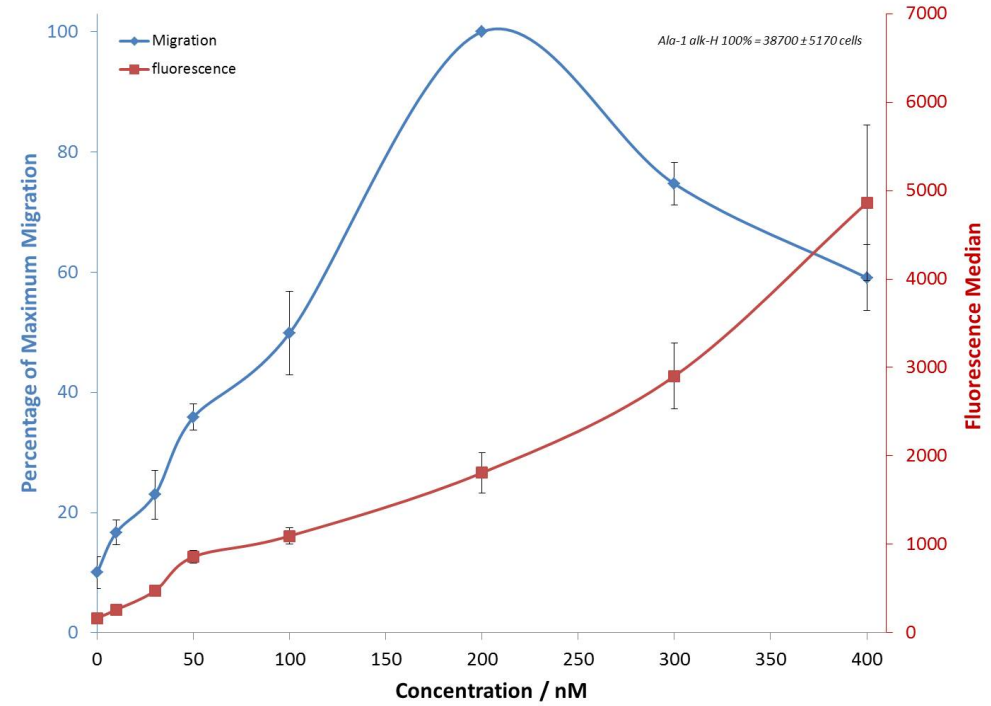

(a) Comparison of fluorescence and chemotaxis for CCL2 Ala^{-1}-alk-H.

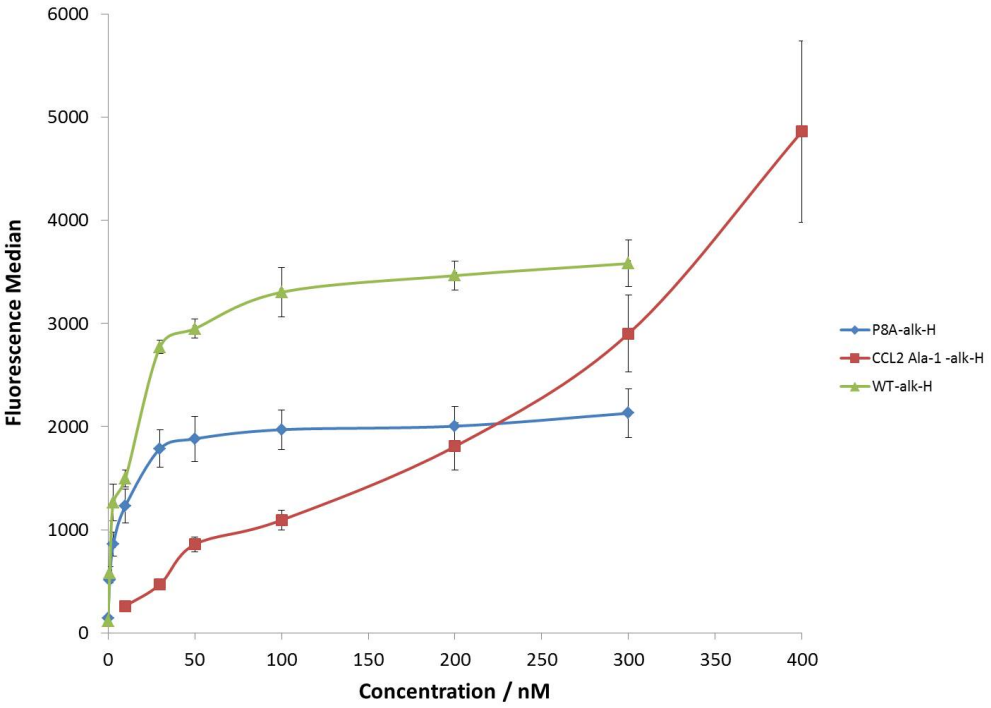

(b) Median fluorescence of the three CCL2-alk-H conjugates.

Figure 5.7: The CCL2 Ala^{-1}-alk-H conjugate did not exhibit a steady state suggesting the equilibrium found with P8A and WT-CCL2 was not reproduced (5.7a). A graph showing concentration of chemokine conjugate against median fluorescence, highlighting the difference in progression of chemokine internalisation and the absolute fluorescence achieved (5.7b). The steady state achieved by WT-alk-H is at a higher level than P8A-alk-H, however, these are both surpassed by CCL2 Ala^{-1}-alk-H which does not reach a steady state at the concentrations examined. Error bars refer to standard error at N=3.

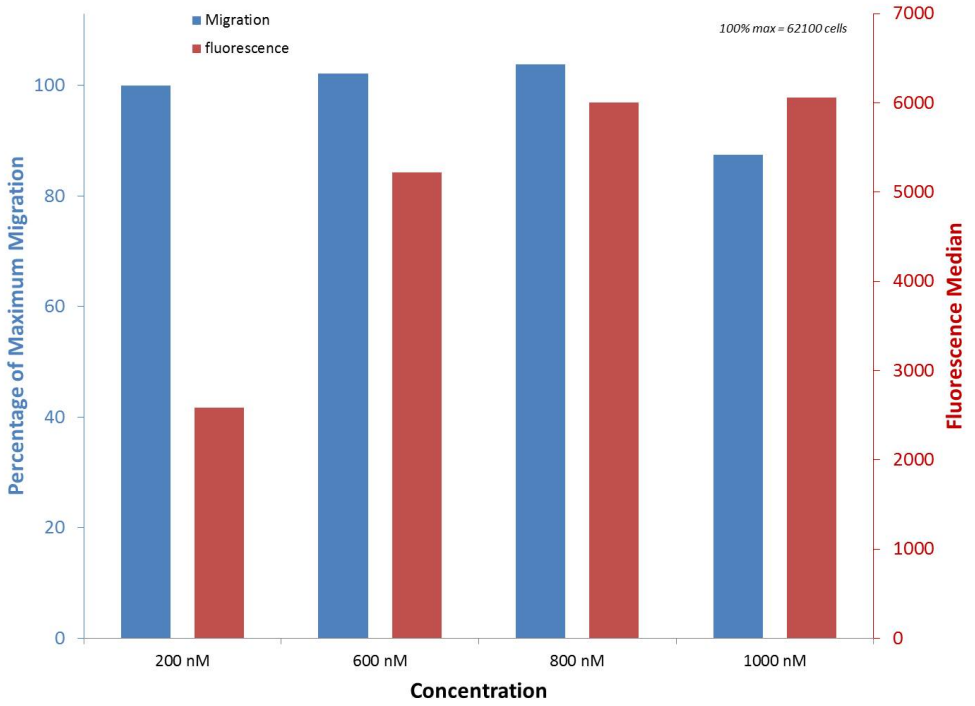

(a) First attempt at comparison of fluorescence and chemotaxis for high concentrations of CCL2 Ala^{-1}-alk-H.

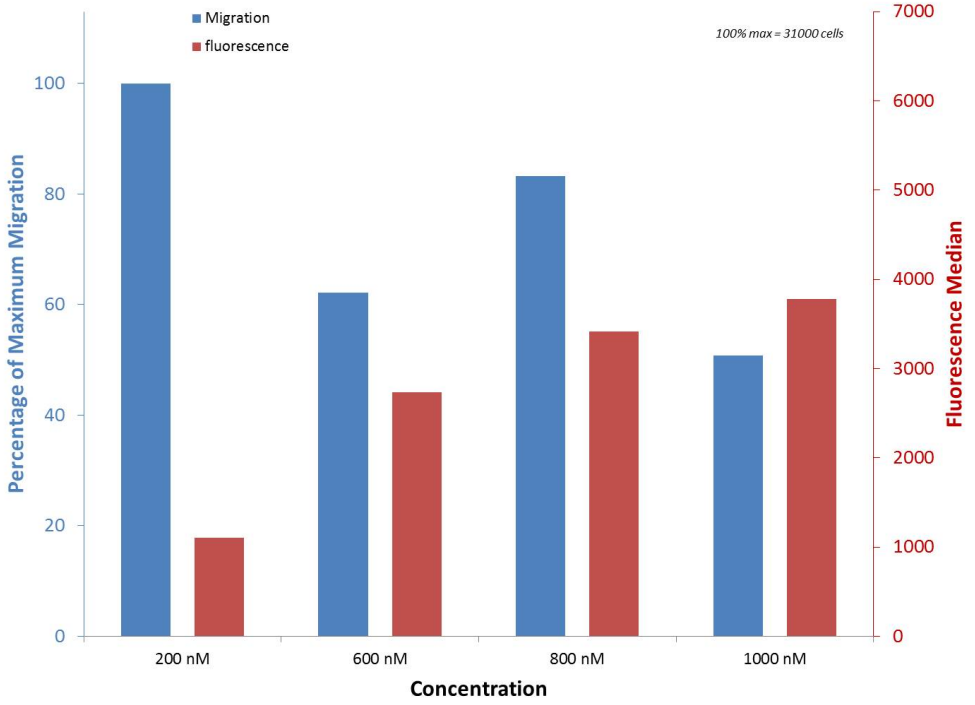

(b) Second attempt at comparison of fluorescence and chemotaxis for high concentrations of CCL2 Ala^{-1}-alk-H.

Figure 5.8: Boyden transwell chemotaxis assay comparing the fluorescence and migration of THP-1 cells towards high concentrations of CCL2 Ala^{-1}-alk-H, in order to discover a steady state between internalisation and fluorophore degradation. Some indications of a steady state were observed but the ambiguity of the migratory response of the cells rendered these results unclear.

highest fluorescence median at 400 nM, this could therefore be an attractive prospect for future therapeutic applications as the lack of a steady state does not limit the internalisation of the conjugate (Figure 5.7). However, if the CCL2 Ala^{-1}-alk-H conjugate is forming oligomers at high concentrations leading to non-specific internalisation pathways this limits therapeutic applications. The differences in internalisation of the chemokine variants appear to correlate with the relative chemotactic affinities of the CCL2 variants and so there is limited evidence of separation of internalisation and chemotaxis in these models. Compared to the results reported by Handel *et al.*, the behaviour of P8A-alk-H appears to replicate the *in vitro* behaviour of P8A-CCL2 leading to induction of chemotaxis and internalisation.[225]

5.2.2.1 CCL2/CCR2 Inhibition Studies

The transwell Boyden chemotaxis assay allowed the confirmation that the CCL2 conjugates were behaving as chemokines and that the sequence alterations were having a pronounced effect on both the chemotactic signalling and internalisation of the THP-1 cells. The next aim was to then demonstrate that this chemotaxis and internalisation was the result of CCR2-mediated endocytosis and not some other unknown mechanism. This was pursued through the use of a small molecule CCR2 antagonist developed by Incyte, this compound should prevent chemotaxis and internalisation of the CCL2 conjugates if they are CCR2 specific.[172] This compound has an $IC_{50} = 4.7$ nM for chemotaxis inhibition and 3.7 nM for internalisation of CCL2, it was therefore decided to work from 4.7 nM to prevent both chemotaxis and internalisation. Inhibition studies were performed in the transwell chemotaxis assay with an additional incubation step with INCB 3284. The concentrations of INCB 3284 used for inhibition were 4.7, 47 and 470 nM which represents a theoretical inhibitory dose of 50, 90 and 95%, respectively. This experiment was initially performed on recombinant CCL2 showing that the INCB 3284 does inhibit the action of CCL2 (Appendix, Figure 8.21). A dose dependent inhibitory response was observed against WT-alk-H and WT-CCL2 (Figure 5.9). At 4.7 nM of INCB 3284, migration was inhibited to around 60% of the maximum response, this was accompanied by a reduction in fluorescence of around 20%. This suggests that the

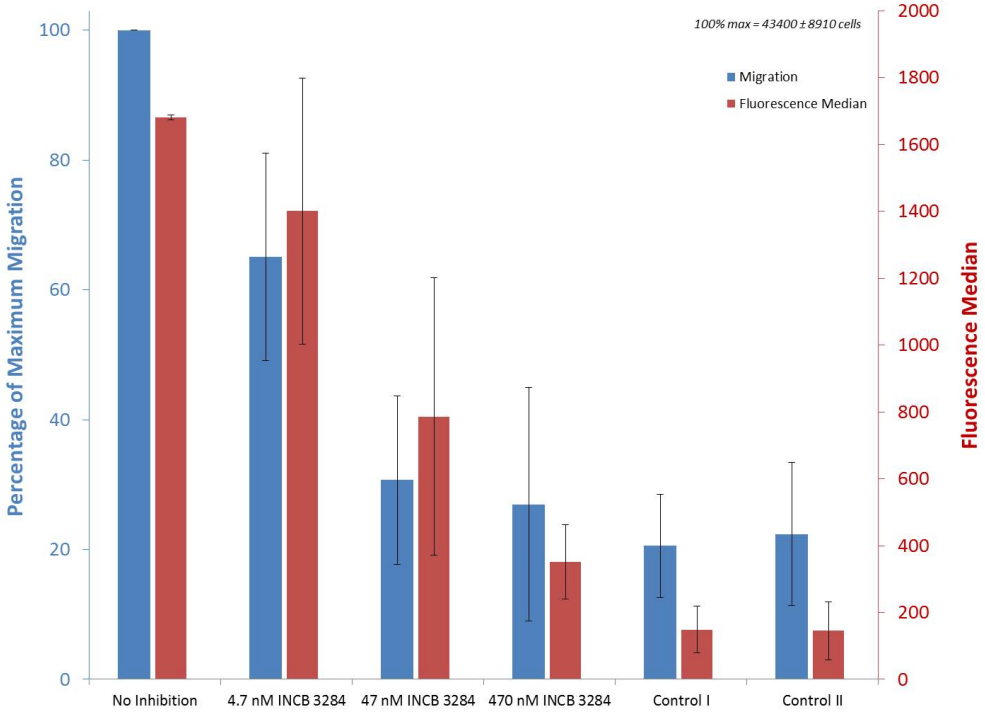

(a) Comparison of fluorescence and chemotaxis for WT-alk-H (10 nM) after CCR2 inhibition.

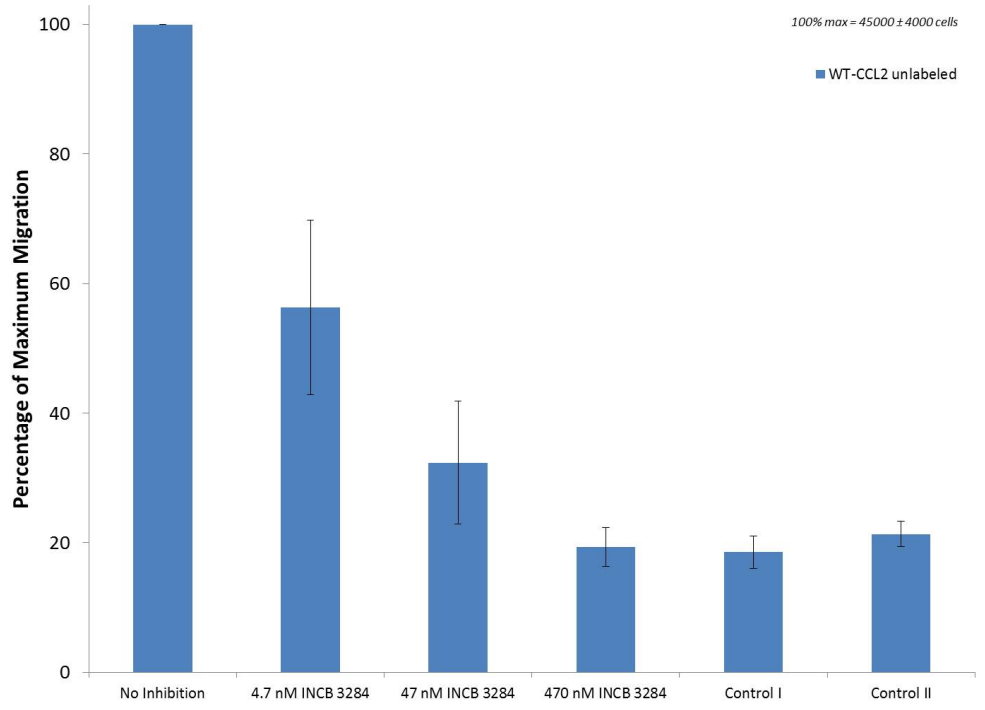

(b) Chemotactic response of unlabelled WT-CCL2 (10 nM) after CCR2 inhibition.

Figure 5.9: Boyden chemotaxis transwell assay with CCR2 inhibition using INCB 3284 at 4.7, 47 and 470 nM representing 50, 90 and 95% inhibition, respectively. The chemokines were used at their respective chemotactic maxima (WT-alk-H = 10 nM, WT-CCL2 unlabelled = 10 nM). Control I: no chemokine or antagonist, control II: no chemokine, 470 nM INCB 3284. A clear trend can be observed whereby both migration and fluorescence decrease with increasing doses of the CCR2 antagonist. Error bars refer to standard error at N=2.

chemotaxis is CCR2-dependent and similarly, the internalisation of the fluorescent chemokine is also CCR2-dependent. This inhibition then continues in a dose-dependent manner in terms of the antagonist; chemotaxis is inhibited by 470 nM INCB 3284 to around 30% of the untreated cells. This amount of migration is slightly greater than both controls, firstly this indicates that CCR2 blockade almost completely inhibits chemotaxis, and secondly, this slight increase over the controls likely indicates the 5% of the population which are not inhibited and thus respond to the chemokine ligand. The fluorescence of cells inhibited with 470 nM INCB 3284 was greatly reduced relative to the maximum response and followed the dose-dependent trend observed with chemotaxis inhibition. The level of fluorescence observed with 470 nM INCB 3284 is around double that of both controls (which represent autofluorescence levels), this provides further evidence for the hypothesis that an equilibrium is reached between uptake of chemokine and degradation of the fluorophore. At this concentration of antagonist, 95% of CCR2 is inhibited and the remaining receptors can bind the ligand, if an equilibrium was not achieved the remaining 5% of receptors would gradually internalise the fluorescent chemokine over the duration of the experiment to a level resembling non-inhibition. This is not observed, suggesting an equilibrium of reduced magnitude is reached in the 5% of receptors not blocked by the antagonist. The chemotactic function of the unlabelled WT-CCL2 was also inhibited by INCB 3284 in a dose dependent manner, with 4.7 nM INCB 3284 reaching approximately 60% maximum migration, followed by 30% and 20% for 47 and 470 nM INCB 3284 respectively. This level of inhibition closely matches the inhibition observed in WT-alk-H providing further evidence that the conjugation does not affect function.

Antagonism of CCR2 in the same experimental system also resulted in inhibition of both P8A-alk-H and unlabelled P8A-CCL2 (Figure 5.10). A dose dependent reduction in migration was observed for P8A-alk-H (Figure 5.10a), however, this trend was increasingly step-wise from 4.7 - 470 nM INCB 3284 relative to WT-alk-H which rapidly reduced from 4.7 - 47 nM INCB 3284. The migration at 4.7 nM reduced to 70% of the maximum migration, which represents a lower amount of inhibition compared to WT-alk-H. This is likely a result of the 35% migrational response of the negative controls meaning the dose response may be contracted.

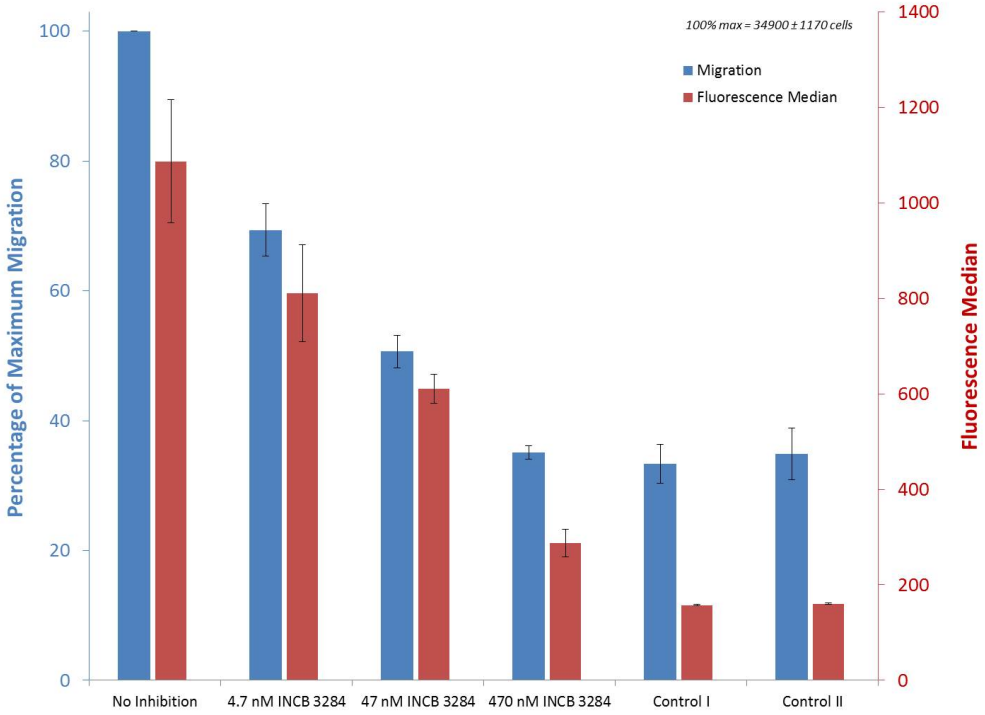

(a) Comparison of fluorescence and chemotaxis for P8A-alk-H (3 nM) after CCR2 inhibition.

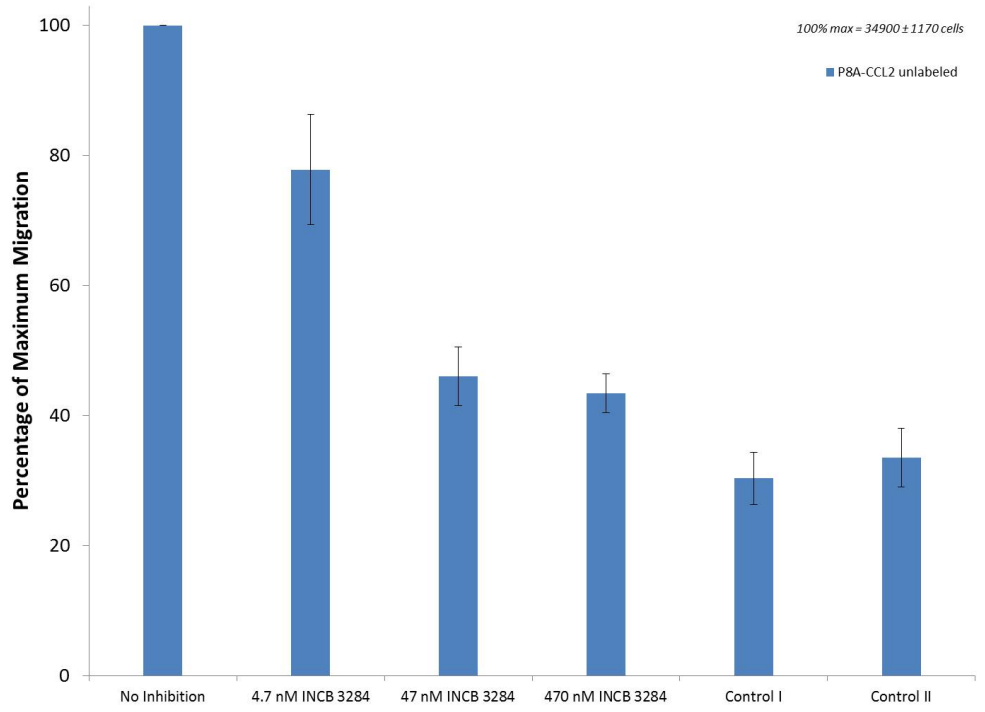

(b) Comparison of fluorescence and chemotaxis for unlabelled P8A-CCL2 (3 nM) after CCR2 inhibition.

Figure 5.10: Chemotaxis assay with CCR2 inhibition using INCB 3284 at 4.7, 47 and 470 nM. The chemokines were used at their respective chemotactic maxima (P8A-alk-H = 3 nM, P8A-CCL2 unlabelled = 3 nM). Control I: no chemokine or antagonist, control II: no chemokine, 470 nM INCB 3284. P8A-alk-H elicited a similar effect to WT-alk-H whereby both migration and fluorescence decrease with increasing doses of INCB 3284, however, higher concentrations of antagonist are needed to completely inhibit P8A-alk-H relative to WT-alk-H. Error bars refer to standard error at N=2.

This 70% migration for 4.7 nM INCB 3284 represents a midway point between the control and the maximum migration, which for 4.7 nM INCB 3284 would represent half-maximal inhibition. At 47 nM, the approximately 50% of maximum migration does not represent the expected 90% inhibition but is still a dose-dependent decrease in migration. The near total inhibition at 470 nM towards control I and II, in terms of migration, suggests the action of this conjugate is similarly due to CCR2 and not another mechanism. The fluorescence also decreases in a dose-dependent manner suggesting that P8A-alk-H internalisation is also inhibited. Again, this response is initially incremental but after 470 nM the fluorescence median has significantly decreased to similar levels found with WT-alk-H. The 470 nM INCB 3284 is then at a concentration high enough to effectively inhibit P8A-alk-H to approach control levels of migration. This conjugate also exhibits the residual fluorescence at 470 nM INCB 3284 suggesting the presence of an equilibrium between internalisation and fluorophore degradation, this suggests both peptides are operating through a similar mechanism which is likely to be *via* CCR2. The unlabelled P8A-CCL2 (Figure 5.10b) is similar to the conjugated peptide at 4.7 nM but exhibits the expected 90 - 95% inhibition level, relative to control, at 47 and 470 nM INCB 3284.

The final CCL2 variant, CCL2 Ala^{-1}-alk-H, was also inhibited in a dose-dependent manner, however, this effect was different to the previous two CCL2 variants (Figure 5.11). A slight decrease in migration at 4.7 nM INCB 3284 occurred, followed by a large decrease at 47 nM to around 30% of maximum migration, and again the 470 nM INCB 3284 was sufficient to render migration to background levels. The inhibition of fluorescence did not follow the same trend which gave a gradual decrease in fluorescence with increasing inhibitor concentration. At 470 nM INCB 3284 the fluorescence median was still significantly higher than autofluorescence (at around 40% of the fluorescence median when not inhibited). Whilst CCL2 Ala^{-1}-alk-H did possess a higher level of fluorescence at the migrational maxima than the other CCL2 variants, effective inhibition of CCL2 Ala^{-1}-alk-H with 470 nM INCB 3284 should result in a fluorescence median closer to autofluorescence levels. This suggests that either CCL2 Ala^{-1}-alk-H does not reach an equilibrium between internalisation and fluorophore degradation

(which is possible and was suggested by the lack of a steady state in the chemotaxis assays, Figure 5.7) resulting in the fluorescence gradually increasing inside the cell as chemokine is internalised through the reduced number of available CCR2 receptors. An alternative explanation is that there is a disconnect between signalling and internalisation in CCL2 Ala^{-1} resulting in a larger difference between IC_{50} for chemotaxis and CCR2 binding, suggesting CCL2 Ala^{-1} mediated chemotaxis is more readily inhibited than internalisation.

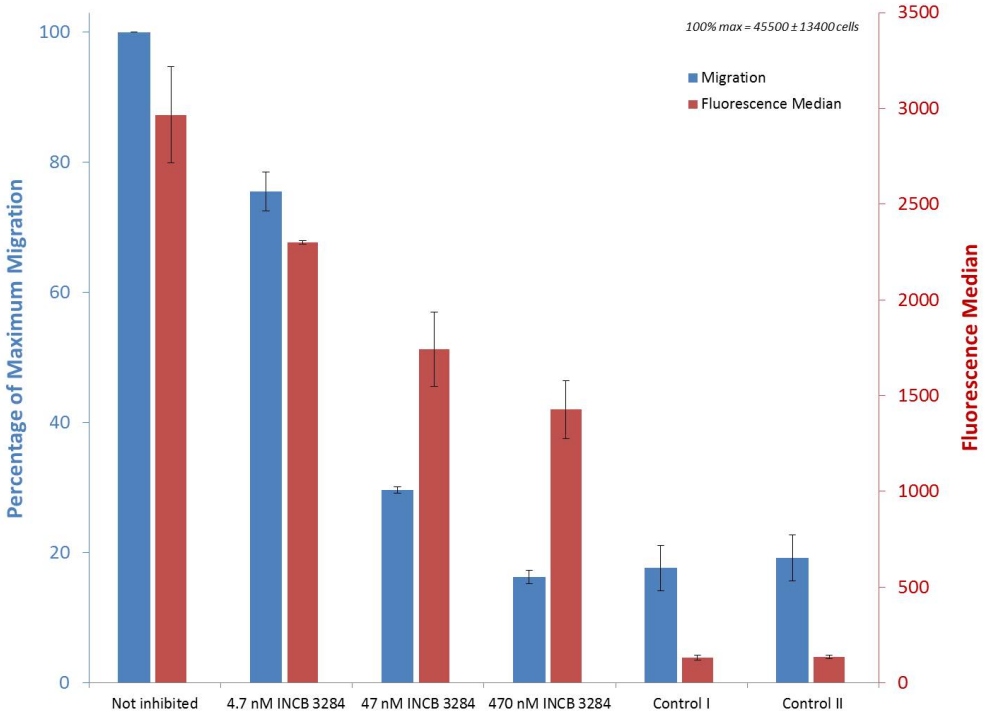

Figure 5.11: Boyden chemotaxis transwell assay with CCR2 inhibition using the CCR2 antagonist INCB 3284. The chemokine was used at the chemotactic maxima (CCL2 Ala^{-1}-alk-H = 200 nM). Control I: no chemokine or antagonist, control II: no chemokine, 470 nM INCB 3284. The difference between migration and internalisation inhibition suggests these pathways may be more independent with respect to CCL2 Ala^{-1}-alk-H. Error bars refer to standard error at N=2.

Further evidence for CCR2-mediated chemotaxis was attained following inspiration from Graham *et al.*, in this study it was found that pre-incubation of murine monocytes with 250 nM recombinant CCL2 resulted in surface CCR2 depletion to levels resembling $CCR2^{-/-}$ knockout mice.[184] We therefore treated THP-1 cells with 250 nM CCL2 prior to the chemotaxis assay as a second method to determine CCR2 selectivity of the chemokine conjugates. Figure 5.12 displays both the migration and fluorescence data resulting from this experiment, the method described by Graham *et al.* was slightly modified to include a pre-incubation

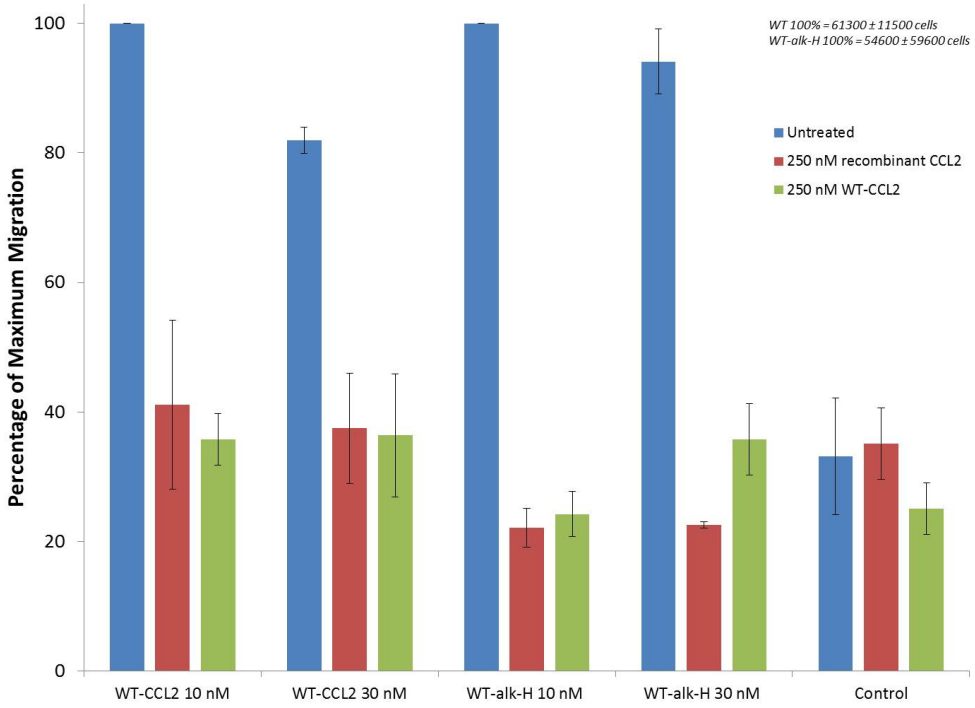

(a) Response of cell migration to pre-incubation of 250 nM CCL2 using WT-CCL2 and WT-alk-H.

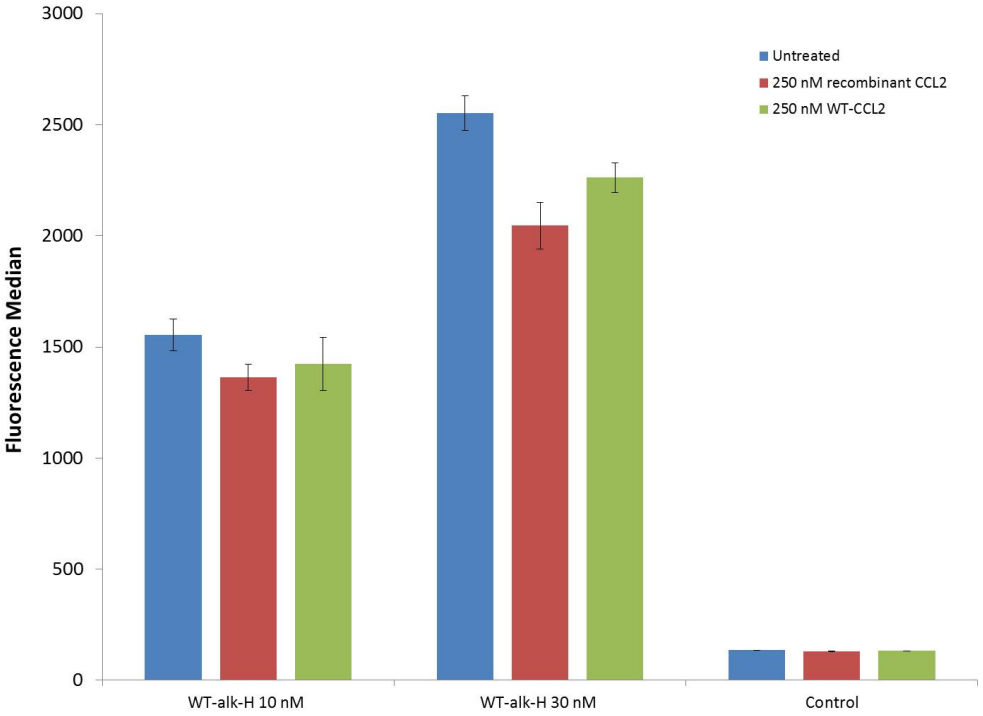

(b) Effect of pre-incubation with 250 nM CCL2 on fluorescent CCL2 uptake.

Figure 5.12: Boyden chemotaxis transwell assay with initial 250 nM CCL2 pre-incubation to reduce surface levels of CCR2, evaulating WT-CCL2 and WT-alk-H.[184] The migration of THP-1 cells towards the unlabelled and fluorescent WT-CCL2 is reduced when pre-incubated with either recombinant CCL2 or unlabelled WT-CCL2 (5.12a). The fluorescence is not greatly affected by pre-incubation which is most likely due to the pre-incubation creating a heterogeneous population of CCR2 levels giving a positive selection process in the transwell assay (5.12b). Error bars correspond to N = 2. Untreated - no pre-incubation. 250 nM recombinant CCL2 - pre-incubation with this dose.

using either recombinant human CCL2 or the unlabelled synthetic CCL2 variant of interest. For example, in the case of Figure 5.12, this included recombinant human CCL2 and a separate incubation of unlabelled WT-CCL2, these cells were then exposed to either 10 or 30 nM WT-alk-H or WT-CCL2, measuring both migration and, where appropriate, fluorescence. The concentrations of 10 nM and 30 nM were selected such that the chemotactic maxima was used which would give the strongest chemotactic response, and a second concentration was selected to show any results were consistent in terms of migration and fluorescence. Figure 5.12a highlights that inhibition of chemotaxis is achieved using this method, suggesting the chemokines are signalling through CCR2. With WT-CCL2 10 nM, the recombinant CCL2 reduced migration to around 40% of the maximum response suggesting that the action of the recombinant CCL2 reduces surface levels of CCR2 such that the synthetic WT-CCL2 was not able to recruit the cells. A similar effect was observed with pre-incubation using WT-CCL2, this evidence is two-fold in that it shows incubation with 250 nM WT-CCL2 reduces levels of surface CCR2 (through binding and internalisation of the ligand-receptor complex) such that a dose of 10 nM WT-CCL2 is not able to recruit cells chemotactically. Similar results were observed with 30 nM WT-CCL2. This effect is also seen on the fluorescent WT-alk-H for both 10 and 30 nM, particularly for WT-alk-H at 10 nM with reduction in migration to around 20%. Again, a similar result was found with WT-alk-H at 30 nM, indicating that for both fluorescent and non-fluorescent WT-CCL2, the ability to recruit cells is reduced by recombinant and synthetic WT-CCL2 incubations.

The fluorescence medians for this experiment are displayed in Figure 5.12b and present an interesting effect. For both 10 and 30 nM WT-alk-H, the fluorescence medians only slightly decrease when pre-treated with recombinant CCL2 and unlabelled WT-CCL2. This effect is very different to the studies using the CCR2 antagonist INCB 3284 where a dose-dependent reduction in fluorescence was observed with increasing concentrations of inhibitor. This effect could be due to the cells which are able to migrate into the receiver well having only slightly reduced levels of surface CCR2 and so continue to internalise fluorescent chemokine when in the receiver well. This is because the pre-incubation of CCL2 likely produces a

heterogeneous population of THP-1 cells with respect to surface CCR2 expression and so the cells measured in the receiver well have undergone a positive selection process by the nature of the experiment. In the INCB 3284 experiments, all cells possess INCB 3284 bound to 50, 90 or 95% of the CCR2 receptors, leading to the steady state between internalisation and degradation maintaining a reduced fluorescence level.

The CCL2-mediated CCR2 depletion studies were then performed on P8A-alk-H and P8A-CCL2 at 3 nM and 10 nM which represents the chmotactic maxima and a second concentration for comparison. Both the unlabelled P8A-CCL2 and P8A-alk-H exhibited a reduced ability to recruit THP-1 cells after pre-incubation with both recombinant and P8A-CCL2 (Figure 5.13a). This suggests the fluorescent and non-fluorescent proteins are operating through the same mechanisms. This CCL2 variant was more consistent than WT-alk-H in terms of the level of migration across the treatments and concentrations being reduced to a similar level, which was coincident with the three control conditions. The fluorescence medians with P8A-alk-H were again only slightly lower in the CCL2 pre-incubated cells than the untreated cells (Figure 5.13b). The study into P8A antagonism concluded the mode of action was an inability to dimerise on GAGs and so CCL2-P8A heterodimers would not then bind GAGs leading to chemotaxis inhibition *in vivo*. The results displayed in Figure 5.13b therefore provide indirect evidence that P8A-CCL2 does not directly antagonise CCR2.

Finally, the CCL2 Ala^{-1} variant was tested in a similar manner (Figure 5.14), however, unlabelled CCL2 Ala^{-1} was not used in pre-incubation as very high concentrations would be required. For example, recombinant CCL2 (potency 1-10 nM) requires a dose of 250 nM; this represents a 25-250 fold increase over the chemotactic maxima which for CCL2 Ala^{-1}, which has a maxima around 200 nM, would be over 5 µM which would represent a significant proportion of material. Furthermore, the inconsistent results obtained with high concentrations of CCL2 Ala^{-1}-alk-H in the previous migration experiments suggest this pre-incubation may not work due to possible oligomerisation of the chemokine at high concentrations. Pre-incubation using 250 nM recombinant CCL2 resulted in a reduction from 70% to around 20% of the maximum for 100 nM CCL2 Ala^{-1}-alk-H. Pre-incubation for 200 nM CCL2 Ala^{-1}-alk-

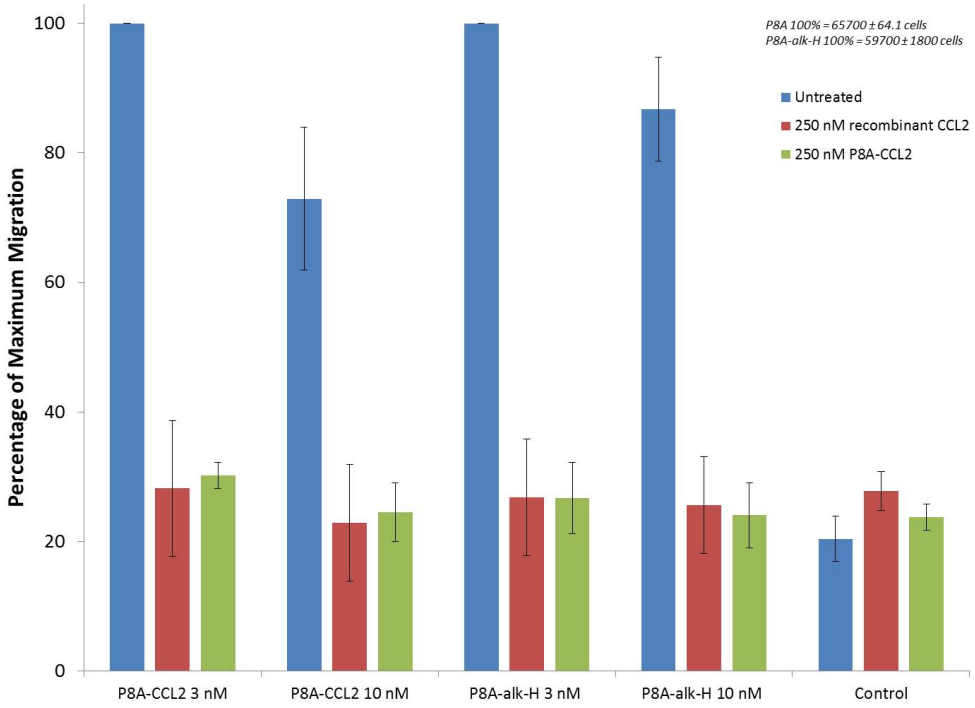

(a) Response of cell migration to pre-incubation of 250 nM CCL2, using P8A-CCL2 and P8A-alk-H.

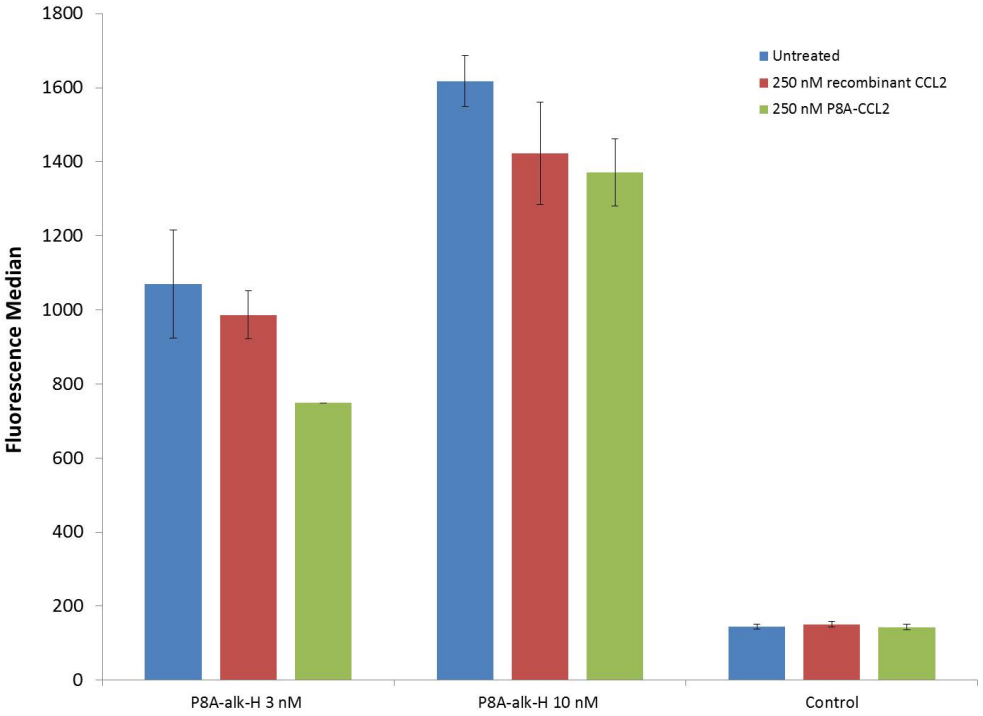

(b) Effect of pre-incubation with 250 nM CCL2 on fluorescent CCL2 uptake.

Figure 5.13: Boyden chemotaxis transwell assay with initial 250 nM CCL2 pre-incubation to reduce surface levels of CCR2, evaluating P8A-CCL2 and P8A-alk-H. Pre-treatment with recombinant CCL2 or unlabelled P8A-CCL2 results in reduced migration towards both unlabelled P8A-CCL2 and P8A-alk-H indicating these initiate chemotaxis through the CCR2 receptor. This also shows P8A-CCL2 is able to reduce surface CCR2 similarly to recombinant CCL2. The fluorescence does not greatly decrease with CCL2 pre-incubation due to formation of a CCR2 heterogeneous population. Error bars correspond to N = 2. Untreated - no pre-incubation. 250 nM recombinant CCL2 - pre-incubation with this dose.

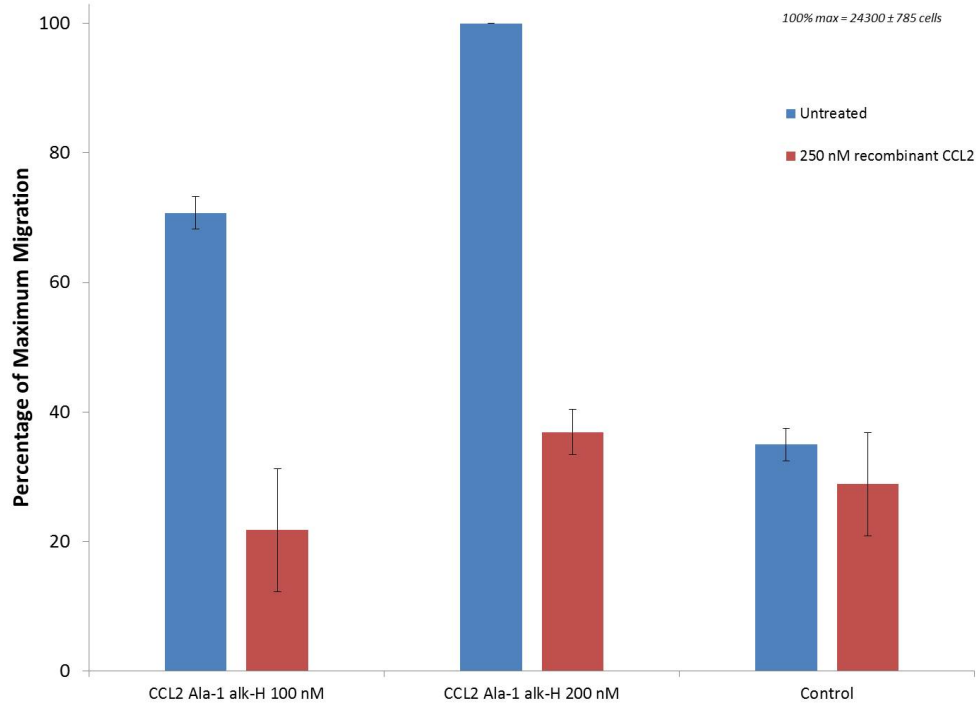

(a) Response of cell migration to pre-incubation of 250 nM recombinant CCL2, using CCL2 Ala^{-1}-alk-H.

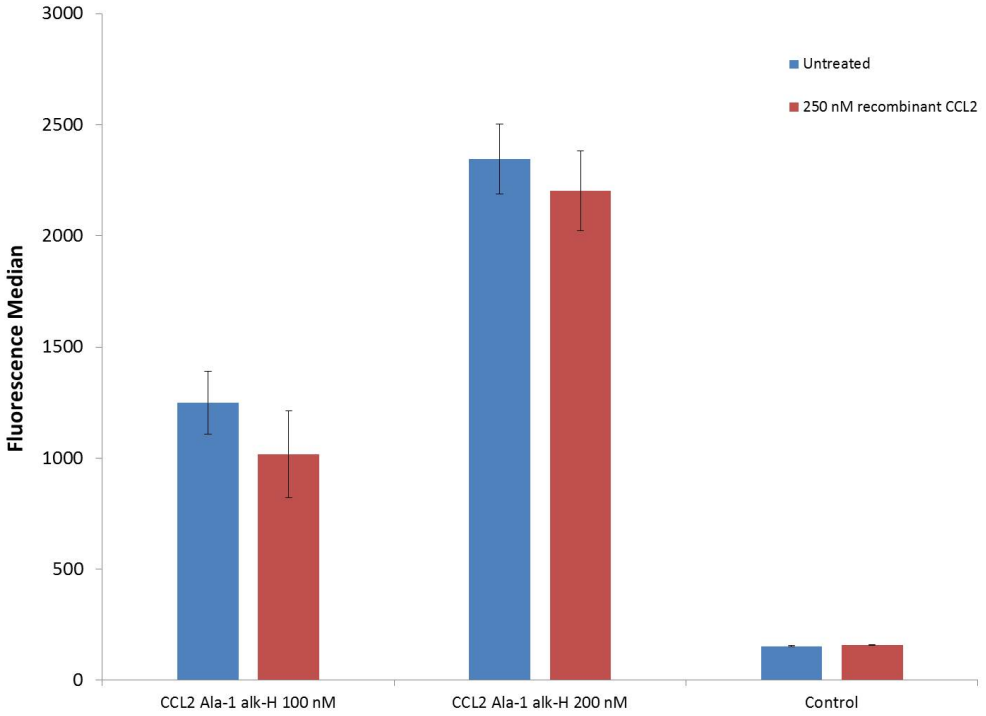

(b) Effect of pre-incubation with 250 nM CCL2 on fluorescent CCL2 Ala^{-1} uptake.

Figure 5.14: Boyden chemotaxis transwell assay with initial 250 nM CCL2 pre-incubation to reduce surface levels of CCR2, evaluating CCL2 Ala^{-1}-alk-H. Pre-treatment with recombinant CCL2 results in reduced migration towards CCL2 Ala^{-1}-alk-H, indicating this initiates chemotaxis through the CCR2 receptor. A similar effect was observed with the possible formation of a heterogeneous population leading to minimal differences in fluorescence for CCL2 Ala^{-1}-alk-H. Error bars correspond to standard error N = 2. Untreated - no pre-incubation. 250 nM recombinant CCL2 - pre-incubation with this dose.

H led to a reduction from 100% to around 35%, this reduction in the amount of migrated cells is of a level close to the control cells. This result is similar to both P8A-CCL2 and WT-CCL2 suggesting that CCL2 Ala^{-1} is inducing chemotaxis *via* CCR2 and the reduction in chemotactic potency is due to a reduced affinity for CCR2 due to the N-terminal alanine addition. The fluorescence median behaved in much the same manner as found with the previous two CCL2 variants whereby a slight reduction in fluorescence median was observed, suggesting a heterogeneous population of CCR2-bearing cells is being produced. This represents consistent fluorescence data for three separate fluorescent CCL2 variants when cells are treated with recombinant or synthetic CCL2, suggesting these conjugates are operating as chemokines and the effect of pre-incubation of the cells with recombinant or synthetic CCL2 is to produce a heterogeneous population of CCR2-bearing cells. Finally, similar chemotactic inhibition was found when the experiments were performed on recombinant CCL2 demonstrating these experiments consistently work on known systems (see Appendix, Figure 8.22).

5.2.2.2 CCL2 Conjugate Timecourse Experiments

The CCL2 variants have been extensively characterised in the transwell Boyden chemotaxis assay and strong evidence for CCR2-mediated chemotaxis and internalisation has been presented. The steady-state between internalisation and fluorophore degradation seen in the transwell experiments suggests this internalisation is a receptor-mediated endocytosis event whereby the cell processes the incoming material through lysosomes which prevents further increase of fluorescence. The next series of experiments involve incubation of the THP-1 cells in the fluorescent chemokines over a timecourse in order to determine if a similar steady-state is observed over time, without the involvement of a migration step. Figure 5.15a shows the fluorescence medians resulting from incubation of THP-1 cells in media containing WT-alk-H over 4 hours which reflects the time period of the transwell experiments. At 0 h, the fluorescence median begins at around 150 A.U. due to autofluorescence, this gradually increases to around 650 A.U. after 2 h with 10 nM WT-alk-H, demonstrating that internalisation is occurring at a higher rate than any degradation. However, after 2 h the fluorescence only

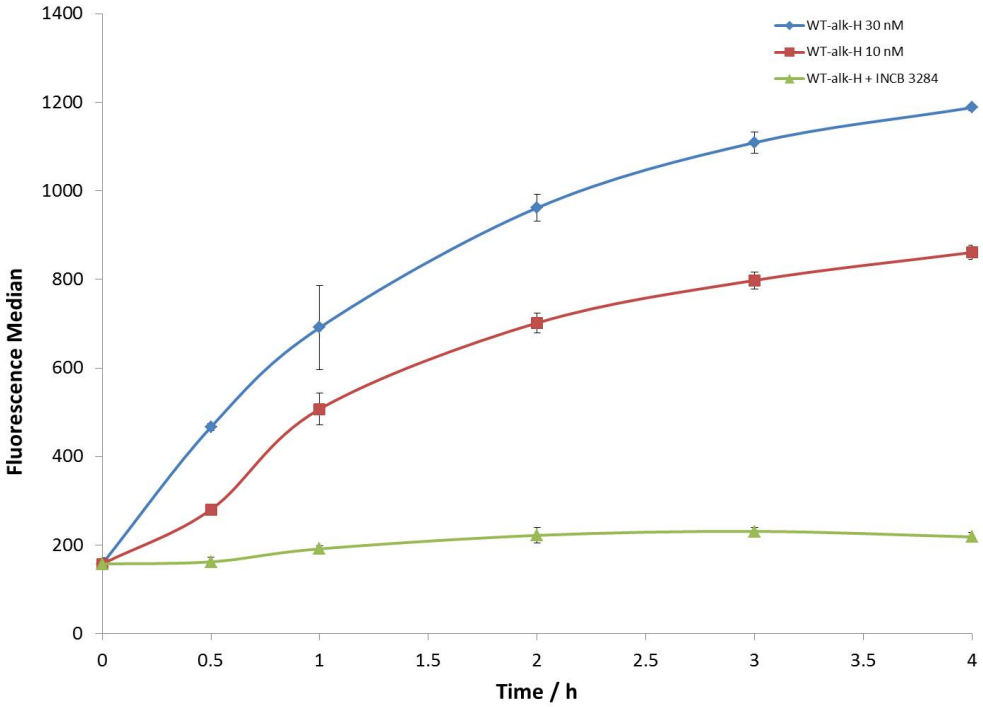

(a) Fluorescence timecourse of WT-alk-H.

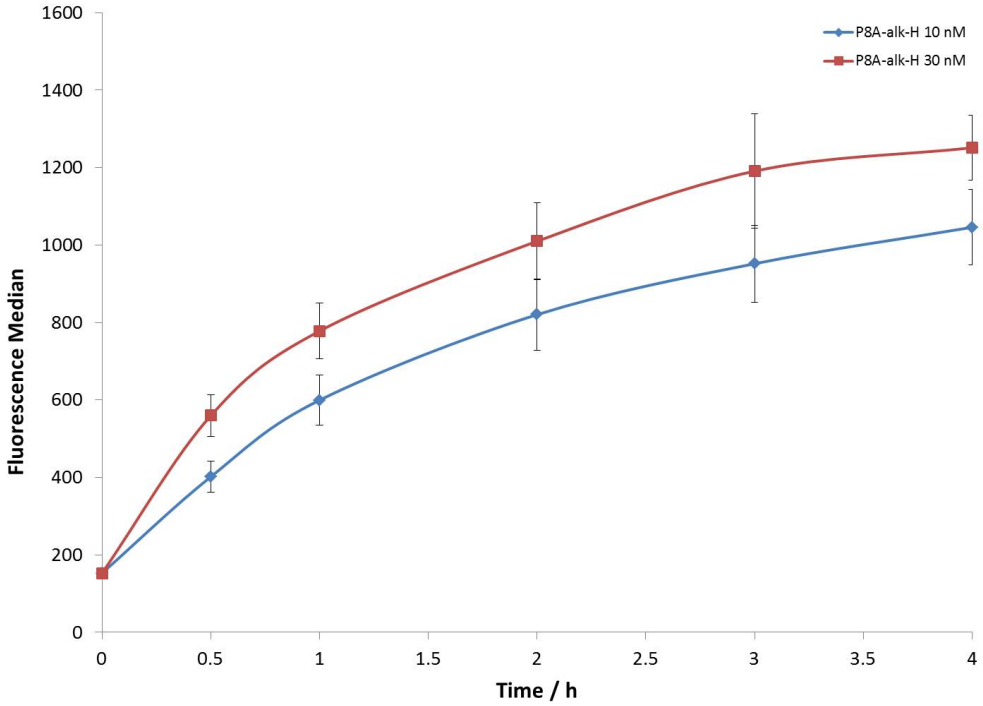

(b) Fluorescence timecourse of P8A-alk-H.

Figure 5.15: Timecourse experiment monitoring the fluorescence median of THP-1 cells incubated in WT-alk-H (5.15a) or P8A-alk-H (5.15b). For each CCL2 variant, the fluorescence increases from 0 - 2 h, a steady state is then reached whereby fluorescence only modestly increases from 2 - 4 h. Concentrations of 10 and 30 nM only affect the magnitude of the curve, not the shape, suggesting an equilibrium between internalisation of the ligand and lysosomal degradation of the fluorophore. 100 x 10^3 cells seeded and error bars represent standard error at N = 2.

increases to around 800 A.U. suggesting a steady state has been reached between these times. The higher concentration of 30 nM WT-alk-H exhibited a similar response but at an increased overall magnitude. This higher magnitude steady state demonstrates that this behaviour is not just due to depletion of surface CCR2 receptors which prevent further internalisation of fluorescent chemokine at the same rate. If this was the case, the 10 and 30 nM chemokines would reach the same fluorescence median but the 30 nM WT-alk-H would approach this maxima faster than the 10 nM, as the magnitude of the steady state is dictated by the cell-surface receptor not the ligand. This is clearly not the case as both concentrations approach the steady state after 2 h and the magnitudes of these states are different. Instead, this provides further evidence of a steady state between internalisation and lysosomal degradation of the fluorophore which is independent of the amount of CCR2 available on the surface of the cells. This is further supported by the inclusion of 470 nM INCB 3284, firstly this largely diminished fluorescence profile demonstrates that the fluorescence is due to selective CCR2-mediated uptake. Secondly, a contracted increase in fluorescence can be observed from 0 - 2 h which then equalises to form a steady state, it could be argued that after 4 h the fluorescence then decreases but this is a very small reduction in fluorescence and is likely within biological variation.

The P8A-alk-H variant also displayed similar behaviour (Figure 5.15b) to WT-alk-H, beginning at around 150 A.U. at 0 h, this then increased to around 400 A.U. after 0.5 h for 10 nM P8A-alk-H. This continues to increase to around 750 A.U. at 2 h and only reaches around 950 A.U. by the end of the experiment. The shape of the curve is almost identical with 30 nM P8A-alk-H, just at a higher magnitude mirroring the behaviour of WT-alk-H. This identifies another steady state which presents around 2 h after first stimulation with the fluorescent chemokine suggesting that P8A-CCL2 is operating through the same underlying molecular mechanisms as WT-CCL2. This behaviour was also observed with CCL2 Ala^{-1}-alk-H (Figure 5.16a), after 0.5 h the fluorescence rapidly increased to around 500 A.U. which then increased to 750 A.U. at 1 h. The increase began to slow whereby at 2 h the median reached around 1050 A.U., this represented the beginning of a steady state. By 4 h the fluorescence

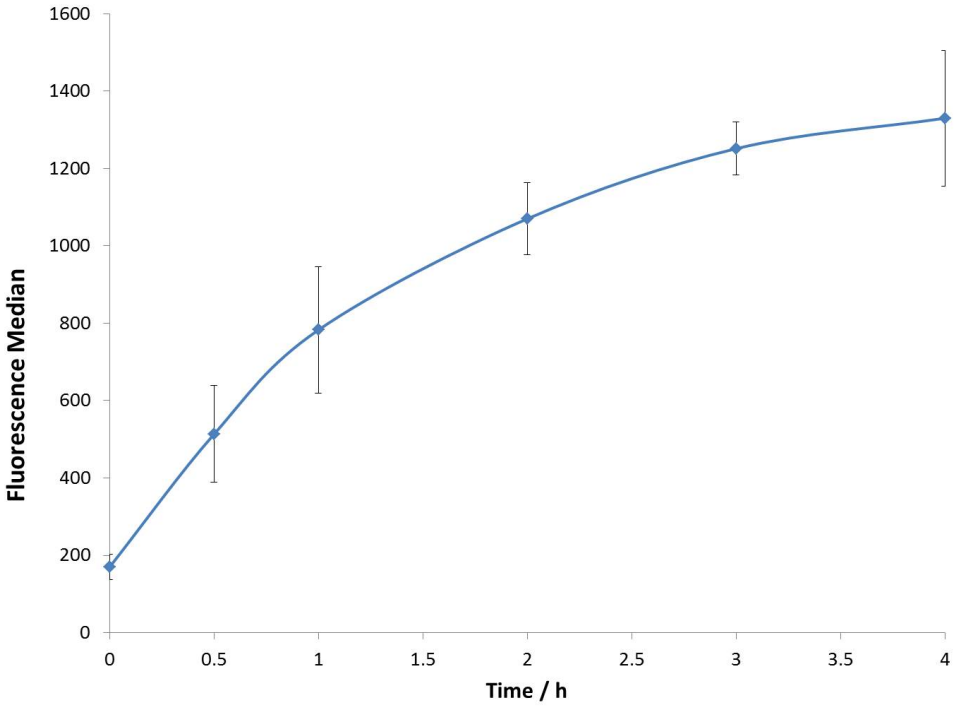

(a) Fluorescence timecourse of CCL2 Ala^{-1}-alk-H.

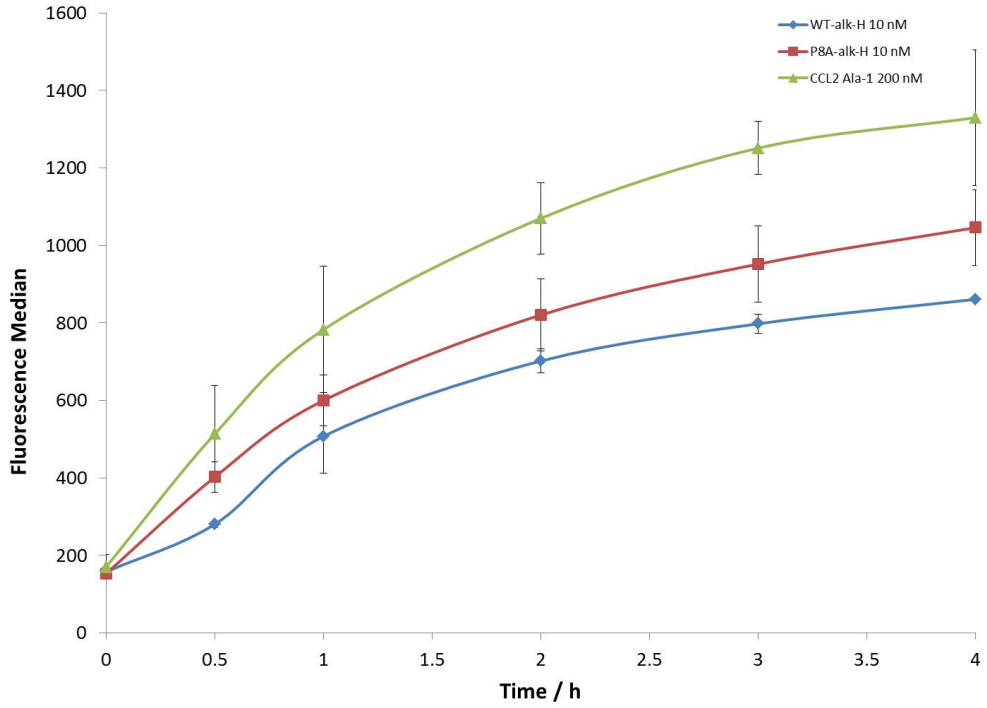

(b) Comparison of the fluorescence timecourse for WT-alk-H, P8A-alk-H and CCL2 Ala^{-1}-alk-H.

Figure 5.16: Timecourse experiment monitoring the fluorescence median of THP-1 cells incubated in 200 nM CCL2 Ala^{-1}-alk-H (5.16a). The fluorescence increases from 0 - 2 h before a steady state is reached. 100 x10^3 cells seeded and error bars refer to standard error for N = 2. Timecourse data overlaid for WT-alk-H, P8A-alk-H and CCL2 Ala^{-1}-alk-H which shows that the curves are very similar in shape and differ slightly in magnitude (5.16b). This suggests each conjugate is internalising through the same mechanism and the fluorophores are being degraded by the cell.

was only modestly increased to around 1250 A.U., suggesting that CCL2 Ala^{-1} also exhibits a steady state between internalisation and lysosomal degradation. This is interesting as this was not conclusively observed in the transwell data at the concentrations tested. The three CCL2 variants are overlaid in Figure 5.16b for direct comparison in the timecourse experiments. The similarity in the shape of the curves is evident, the only difference being the magnitude of the curves, suggesting all chemokines are behaving similarly and each reaches a steady state between internalisation and lysosomal degradation. The magnitude of the CCL2 Ala^{-1} is perhaps unexpectedly high relative to the other sequences as 200 nM is still at the chemotactic maxima of the compound and so should be closer to the other chemokines in terms of fluorescence.

The next set of experiments involved further testing of the selectivity of the chemokine conjugates towards monocytes. The previous experiments have all been performed on the monocytic cell line THP-1 and while there is very strong evidence for CCR2-selective uptake and migration, this could be due to some irregularity of the cell line rather than a true result. We therefore decided to test the response of the jurkat cell line which is a lymphoycte cell line that does not express CCR2 but will respond to other chemokines. As can be seen from Figure 5.17, the jurkat cells do not migrate towards WT-alk-H at either 30 or 10 nM and the background level of migrated cells do not internalise the fluorescent chemokine. The jurkat cells migrated towards CXCL12 in a dose-dependent manner which demonstrates that the cells are able to respond chemotactically given the correct stimulus. This gives further evidence that chemotaxis resulting from the CCL2 conjugates in the THP-1 cells is CCR2 specific. An incubation experiment was also performed with the jurkat cells in case the transwell experiment resulted in some unfavourable selection process through the membrane which rendered migrated jurkat unable to internalise the fluorescent chemokine by another CCR2 independent process. WT-alk-H, P8A-alk-H and CCL2 Ala^{-1}-alk-H all behaved similarly and produced fluorescence medians which coincided with the negative control cells demonstrating that jurkat cells were unable to internalise any chemokines.

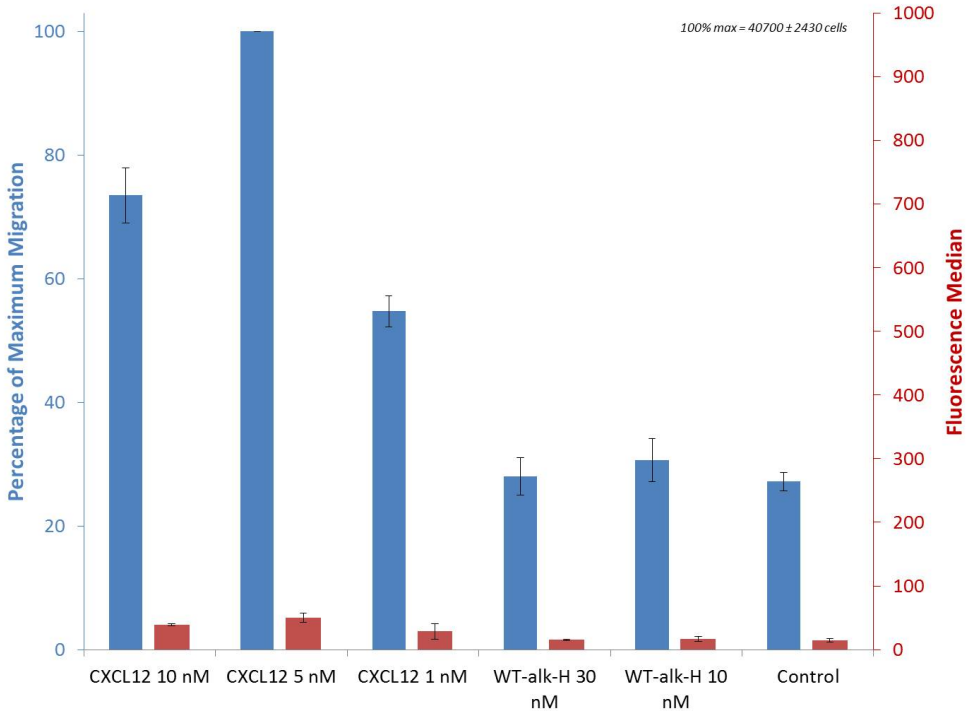

(a) Migration of jurkat cells towards CXCL12 and WT-alk-H.

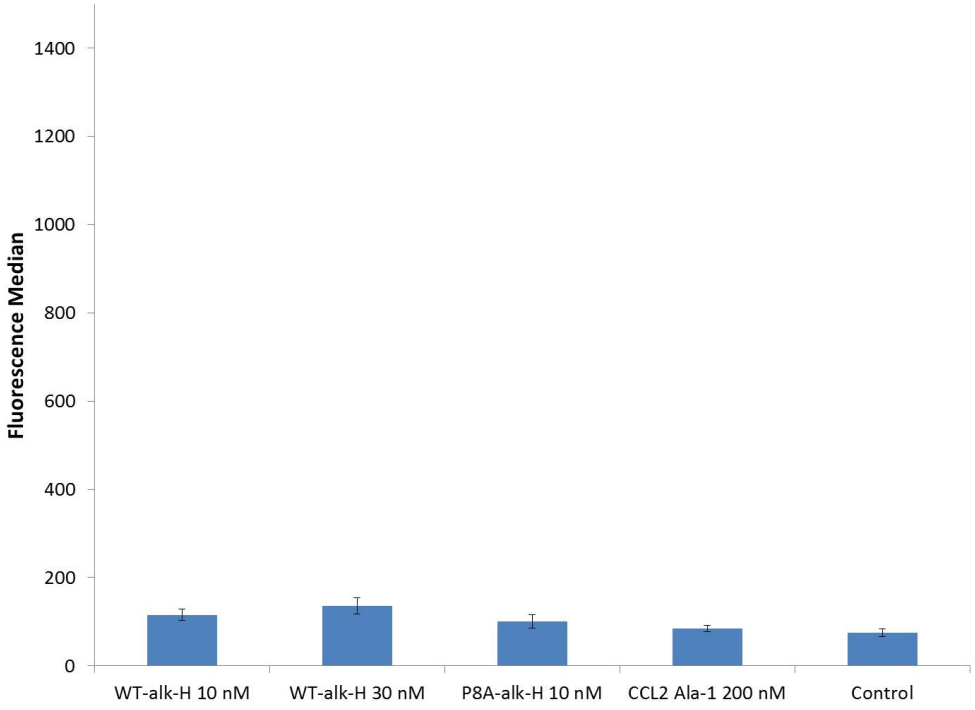

(b) Incubation of jurkat cells in the fluorescent CCL2 conjugates.

Figure 5.17: Boyden transwell chemotaxis assay using the lymphocyte cell line, jurkat, showing positive chemotactic migration towards CXCL12 in a dose dependent manner (5.17a). Migration is then not observed with the CCL2 conjugate WT-alk-H, demonstrating the selectivity of the CCL2 conjugates for CCR2-expressing cells. Incubation of the CCL2 conjugates also does not result in internalisation of the fluorescent chemokines, presumably due to the lack of CCR2 (5.17b). Error bars refer to standard error for N = 2.

5.2.3 Comparison of the Properties of CCL2 Conjugates

The previous section characterised the three CCL2 constructs which resulted in determination of chemotactic maxima both pre- and post-labelling, and also demonstrated the chemotaxis and fluorophore internalisation was CCR2-dependent. The next stage of the project was to determine whether the nature of the fluorophore core and the accompanying linker had any effect on the properties described in the previous section. High concentrations of DMSO were needed in the preparation of the remaining CCL2 conjugates and so it was important to determine if this had a deleterious effect on the function of the chemokine. The CCL2 conjugates used are listed in Table 5.1, this summarises the reaction conditions used to form the conjugates, this will become important in interpreting results obtained in the subsequent experiments. Unfortunately, the difficulties encountered in these CuAAC reactions meant that only small amounts of the CCL2 conjugates were prepared, thus a only a reduced dose response could be measured in the Boyden chemotaxis assays.

The Boyden transwell chemotaxis assay was first used on the CCL2 Ala^{-1} conjugates, these were normalised against P8A-alk-H at 3 nM which was used as a reference point and as a positive control (Figure 5.18a). The -alk-L and -SS-L conjugates were measured at 50, 100 and 200 nM in order to generate a maximal response and to limit the amount of material used in a larger dose response. The CCL2 Ala^{-1}-alk-L conjugate resulted in around 40% of maximal migration for 50 and 100 nM, the expected chemotactic maximal concentration of 200 nM actually resulted in a decrease to around 20% of the maximum migration. When these data points are compared to the negative control (at 38% of the maximum) and accounting for error, this suggests the CCL2 Ala^{-1}-alk-L conjugate was not initiating much chemotaxis of THP-1 cells in this assay. The CCL2 Ala^{-1}-SS-L was slightly more encouraging, 50 nM resulted in 41% of maximal migration which again could be attributed to background levels of migrations, however slight increases for 100 and 200 nM to 52 and 56% respectively, were observed which, even accounting for error, resembles limited chemotactic activity. The best performing conjugate was CCL2 Ala^{-1}-SS-H which resulted in 51% migration at 100 nM and

Table 5.1: Summary of conditions used to form the CCL2 conjugates taken forward into biological characterisation experiments.

Conjugate	**Conditions**	**Reaction Completion**
CCL2 Ala^{-1}-alk-L	$CuSO_4$, Na ascorbate, DMSO	Yes
CCL2 Ala^{-1}-SS-L	$CuSO_4$, Na ascorbate, DMSO	Product and reduced disulfide
CCL2 Ala^{-1}-SS-H	CuBr, DMSO (under N_2)	Yes
P8A-alk-L	$CuSO_4$,Na ascorbate, DMSO	>80% product
P8A-SS-L	CuBr, DMSO (under N_2)	Product and reduced disulfide
P8A-SS-H	CuBr, DMSO (under N_2)	Yes

a strong increase to 86% of the maximal migration at the expected maxima of 200 nM. This behaviour indicates the THP-1 cells are migrating to a concentration gradient of CCL2 Ala^{-1}-SS-H. The median fluorescence intensity for the CCL2 Ala^{-1} conjugates is displayed in Figure 5.18b, these results were unexpected and help elucidate the behaviour observed in Figure 5.18a. The most striking result was the greatly increased intensities observed for CCL2 Ala^{-1}-alk-L which reach around 68000 A.U. at 200 nM, the corresponding concentration for CCL2 Ala^{-1}-alk-H was less than 2000 A.U. in the transwell assay. Whilst these are different fluorophores with different properties (see Table 3.4), the higher quantum yield of 0.63 for -alk-L and similar extinction coefficient could not explain this large increase in fluorescence between the two conjugates. Furthermore, the concentrations of 50, 100 and 200 nM are doubling and a similar trend is observed in the respective fluorescence intensities of CCL2 Ala^{-1}-alk-L from 19000 to 35000 to 68000 A.U. which was not observed for the -alk-H conjugate. This could be attributed to endosomal escape, however, the alkyl linker and triazole ring would tether the compound to the C-terminus of CCL2 which would reduce endosomal escape even if the peptide chain was hydrolysed by lysosomes. Therefore, the lack of chemotactic migration of CCL2 Ala^{-1}-alk-L and the doubling effect of the median fluorescence intensity suggest that the chemokine is not being internalised through CCR2 and the protein is entering the cell *via* another process, such as pinocytosis.

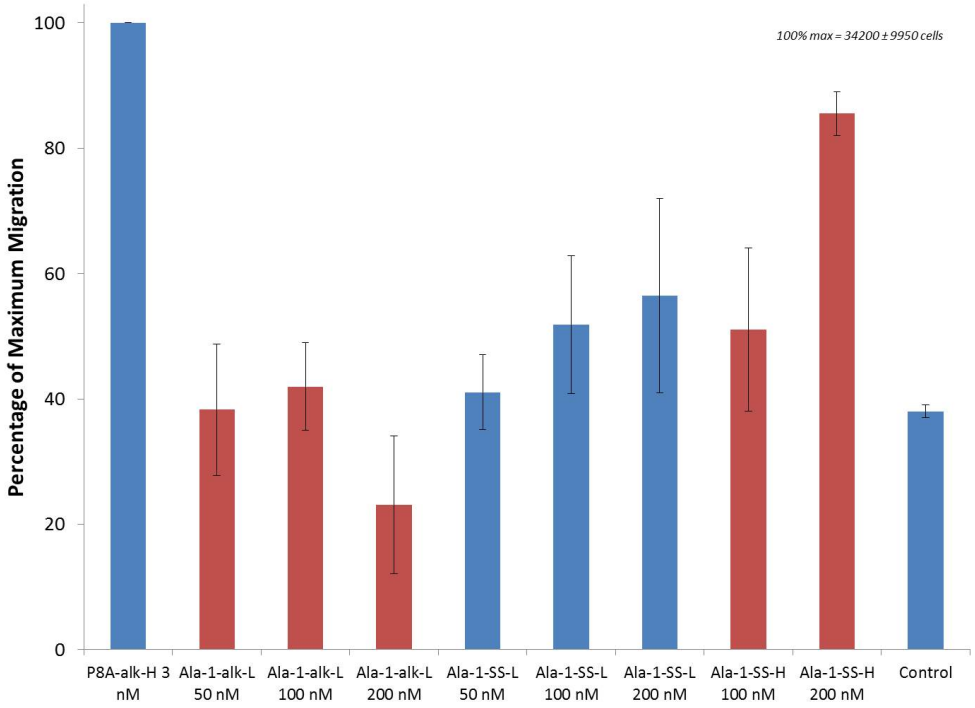

(a) Migratory responses for CCL2 Ala^{-1} fluorescent conjugates.

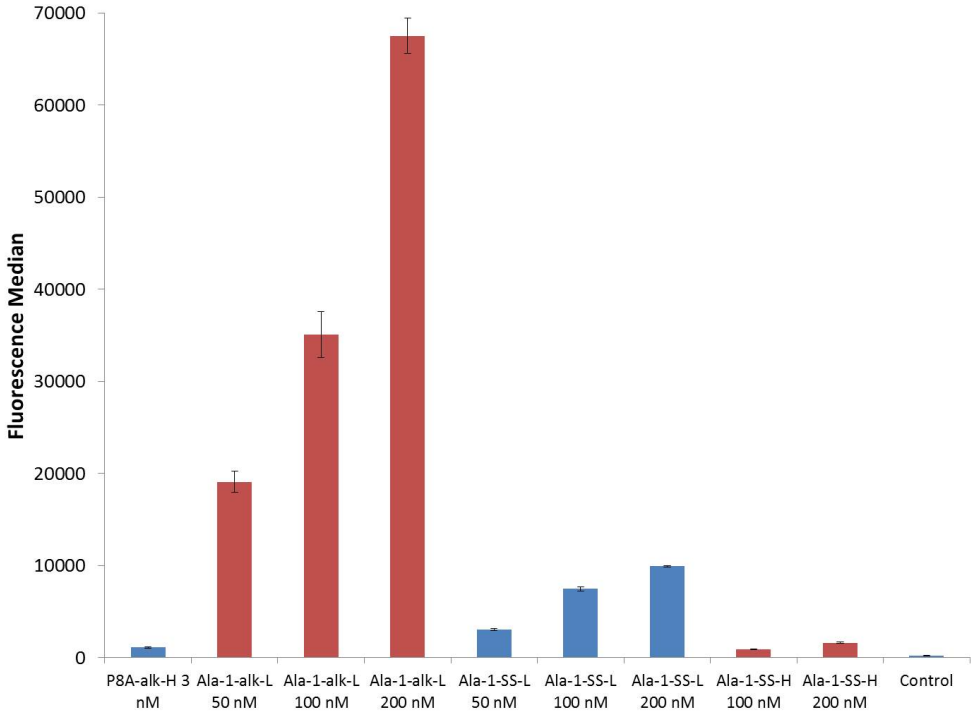

(b) Fluorescence medians of the CCL2 Ala^{-1} conjugates.

Figure 5.18: Migration and fluorescence responses for THP-1 cells towards CCL2 Ala^{-1} conjugates in the Boyden transwell chemotaxis assay. Migration responses were normalised against P8A-alk-H (3 nM, 100%), CCL2 Ala^{-1}-alk-L did not appear to be chemotactic, whereas CCL2 Ala^{-1}-SS-L appeared to have a slight response with a stunted maxima at 200 nM. A strong response was observed with CCL2 Ala^{-1}-SS-H with a maxima at 200 nM. The fluorescence medians (5.18b) were highly varied with high ranges for -alk-L and -SS-L suggesting non-specific uptake, the -SS-H conjugate exhibited medians around 2000 A.U. which correlated with CCL2 Ala^{-1}-alk-H. Error bars refer to standard error of N = 2.

CCL2 Ala^{-1}-SS-L did not exhibit median fluorescence intensities as high as CCL2 Ala^{-1}-alk-L, with 3000, 7500 and 10000 A.U. for 50, 100 and 200 nM, respectively. The fluorescence intensities are not always doubling in proportion to the doubling of concentration of the chemokine suggesting the cell has some control over the fluorescence intensity, unlike the observations found with CCL2 Ala^{-1}-alk-L. It is possible that the -SS-L fluorophore is able to avoid lysosomal degradation *via* endosomal escape due to reduction of the disulfide linker which liberates the lipophilic fluorophore from the protein leading to increased fluorescence. The final conjugate, CCL2 Ala^{-1}-SS-H exhibited median fluorescence intensities which resembled CCL2 Ala^{-1}-alk-H in terms of magnitude and also the trend from 100 to 200 nM. The similarity in fluorescence intensity and the chemotactic migration suggest this conjugate is functioning as a chemokine and is highly similar to CCL2 Ala^{-1}-alk-H. Interestingly, despite the disulfide bond in CCL2 Ala^{-1}-SS-H, the median fluorescence intensity at 100 and 200 nM still closely matches CCL2 Ala^{-1}-alk-H, this suggests that the fluorophore cannot escape the endosome after the disulfide bond is reduced due to the hydrophilicity of the fluorophore. This means that the BODIPY undergoes lysosomal degradation, preventing the fluorescence intensity from increasing in proportion to concentration of the chemokine in the same manner as CCL2 Ala^{-1}-alk-H.

Chemotactic responses for P8A-CCL2 conjugates are displayed in Figure 5.19a, generally these conjugates performed better than the CCL2 Ala^{-1} conjugates. The P8A-alk-L conjugate exhibited a maximal response at 3 nM at 69% which decreased to 51% at 10 nM. This did not reach the same amount of migrated cells as P8A-alk-H but was dose-dependent indicating a level of chemotaxis that may be weaker than P8A-alk-H. The P8A-SS-H conjugate exhibited a clear chemotactic dose-dependent response; the maxima of 98% at 3 nM matches the P8A-alk-H maxima and this gradually decreases to 65% at 10 nM and 38% at 30 nM. The P8A-SS-L conjugate attained 111% of maximal migration at 3 nM which then rapidly decreased to 52% and 45% at 10 and 30 nM respectively, demonstrating the dose-dependent chemotactic response.

The median fluorescence intensity is displayed in Figure 5.19b, P8A-alk-L fluorescence is at

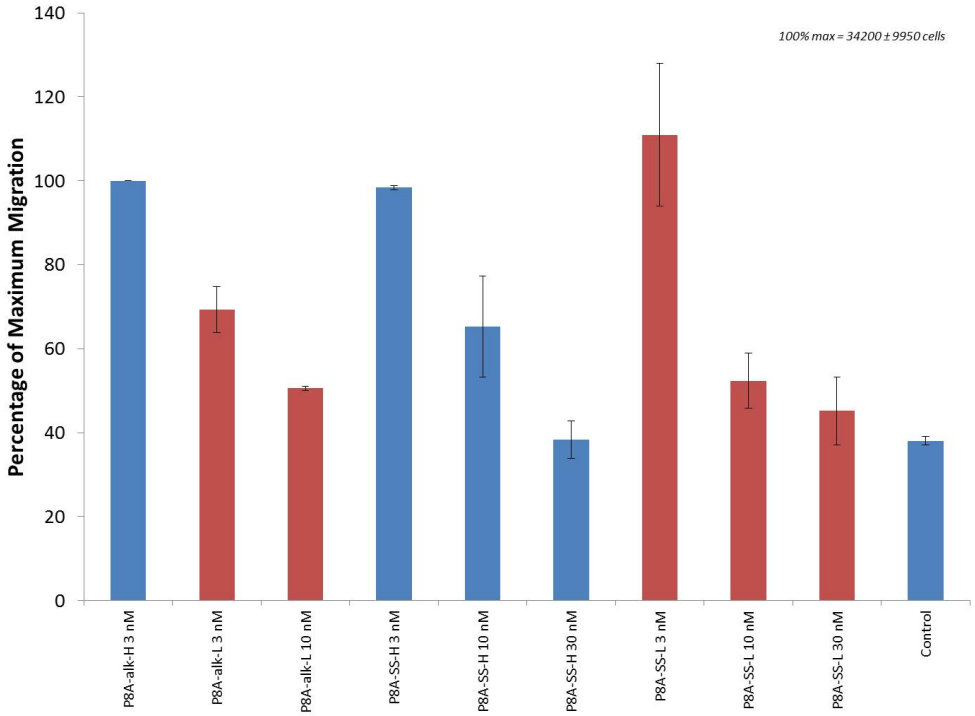

(a) Migratory responses for P8A-CCL2 fluorescent conjugates.

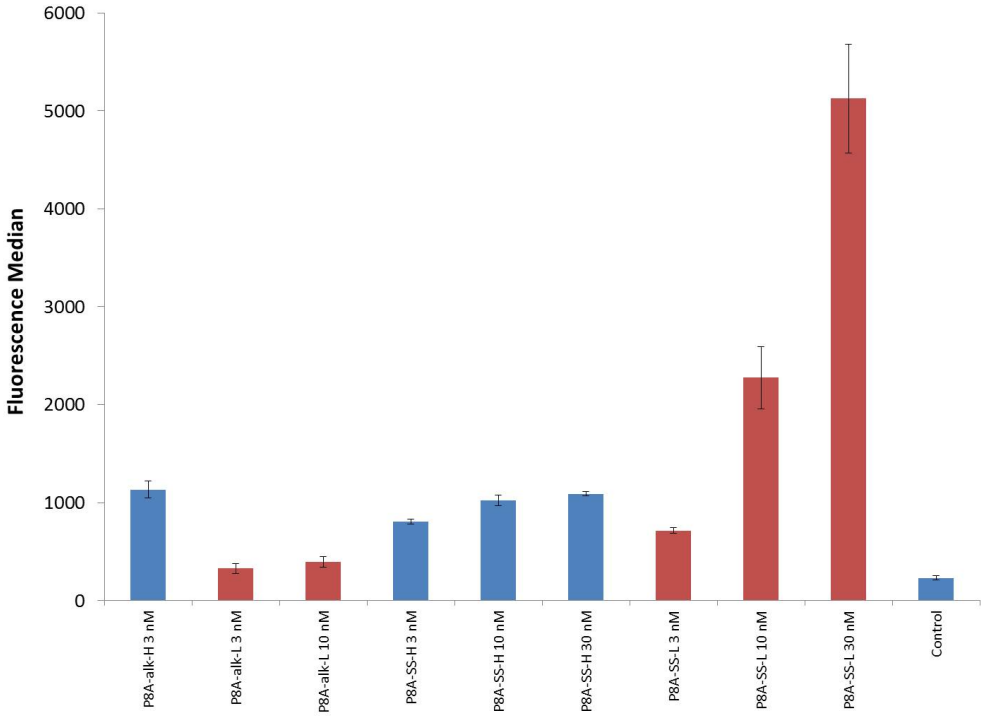

(b) Fluorescence medians of the P8A-CCL2 conjugates.

Figure 5.19: Migration and fluorescence responses for THP-1 cells towards P8A-CCL2 conjugates in the Boyden transwell chemotaxis assay. Migration responses were normalised against P8A-alk-H (3 nM), All conjugates appeared to be chemotactic, however P8A-alk-L only reached around 70% of the maximum response. The fluorescence medians (5.19b) were generally of similar ranges to P8A-alk-H apart from P8A-SS-L which continued to increase. Error bars refer to N = 2.

328 and 397 A.U. for 3 and 10 nM respectively, this is minimally greater than autofluorescence (232 A.U.). This suggests P8A-alk-L is weakly chemotactic and internalisation is also only minimal. The P8A-SS-H conjugate exhibited fluorescence of a similar magnitude to P8A-alk-H, this in combination with the migration data, suggests this conjugate is functioning as a chemokine in a similar manner to P8A-alk-H. Interestingly, the intensity at 3 nM is lower than P8A-alk-H and this only modestly increases from 10 to 30 nM to a level commensurate with P8A-alk-H at 3 nM. The fluorescence is reaching a steady state suggesting the fluorophore is degraded and is not able to escape endosomes which was also observed with CCL2 Ala^{-1}-SS-H. The free fluorophore is then degraded more rapidly by lysosomes than the P8A-alk-H fluorophore which is still bonded to CCL2 and is potentially sterically protected from degradation. The clear outlier in median fluorescence intensity is P8A-SS-L, at 3 nM the fluorescence is 715 A.U., this then rapidly increases to 2275 A.U. and 5126 A.U. at 10 and 30 nM, respectively. This trend suggests the disulfide is being reduced enabling endosomal escape of the lipophilic fluorophore and so lysosomal degradation is avoided resulting in the concentration of fluorescent BODIPY increasing over time as further chemokines are internalised.

These results suggested that the following conjugates were functioning correctly: CCL2 Ala^{-1}-SS-H, P8A-SS-H and P8A-SS-L. The CCL2 Ala^{-1}-alk-L and P8A-alk-L are probably not functioning correctly and CCL2 Ala^{-1}-SS-L was weakly chemotactic but not to the extent of the clearly successful conjugates. Correlating these results with the data presented in Table 5.1 presents a common theme between these less-effective conjugates, all were prepared using DMSO in combination with sodium ascorbate. Chapter 4 indicated that sodium ascorbate is capable of reducing disulfide bonds, this was particularly observed with the disulfide bonds in the fluorophores but it is possible that the sodium ascorbate could also reduce the internal disulfide bonds of CCL2. All the CCL2-alk-H variants contained sodium ascorbate in the reaction, however, these conjugates functioned correctly in terms of chemotaxis and CCR2-dependence. It is therefore possible that the combination of DMSO and sodium ascorbate results in permanent denaturation of CCL2 to an inactive form. In the absence of

DMSO, the sodium ascorbate either is unable to reduce the disulfide bonds of CCL2 due to the folding of the protein or does reduce the bonds momentarily but the conserved tertiary structure of CCL2 holds the cysteines in place such that they oxidise correctly and the correct folding of the protein is maintained. In the presence of DMSO, CCL2 unfolds and if the disulfides are intact, CCL2 can refold correctly after dialysis (which is likely the case with the successful conjugates). The combination of DMSO and sodium ascorbate on the other hand leads to unfolding of the protein and reduction of the disulfides, the linear peptide may then re-oxidise with the disulfides in the incorrect orientation leading to misfolding to an inactive CCL2 species. This scenario would explain the results observed in the chemotaxis assay. One explanation for CCL2 Ala^{-1}-SS-L being partially chemotactic is that the large excess of BODIPY-disulfide relative to CCL2 protects the internal disulfides of CCL2 from reduction as the majority of sodium ascorbate reduces the fluorophore and Cu(II), leaving a percentage of CCL2 folded correctly and another folded incorrectly.

At this stage the activity of the CCL2 Ala^{-1}-FRET conjugate was also measured, unfortunately this conjugate yielded many inconsistent results. The fluorescence spectra was promising in that the conjugate appeared to be acting as a FRET pair (see Appendix Figure 8.23), however, when this conjugate was used in a confocal microscopy system designed to detect FRET signals no FRET signal was observed (data not shown) and some false-positive signals were also detected. Furthermore, the transwell migration data for this compound was poor. It was clear that this research path required extensive optimisation and based on the positive findings from the other CCL2 conjugates it was decided not to pursue this route further.

The single fluorophore conjugates were then further characterised using the CCR2 antagonist INCB 3284, this would determine whether the chemotaxis was CCR2 dependent and could aid in explaining some of the ambiguous results encountered in the chemotaxis assays. Furthermore, with the disulfide-linked conjugates, it is possible that the median fluorescence intensity may not decrease in the presence of inhibitor to the same magnitude encountered with the alkyl-linked conjugates. Figure 5.20 shows migration and fluorescence data for the CCL2 Ala^{-1} conjugates, normalisation to the non-inhibited cells was not used in these ex-

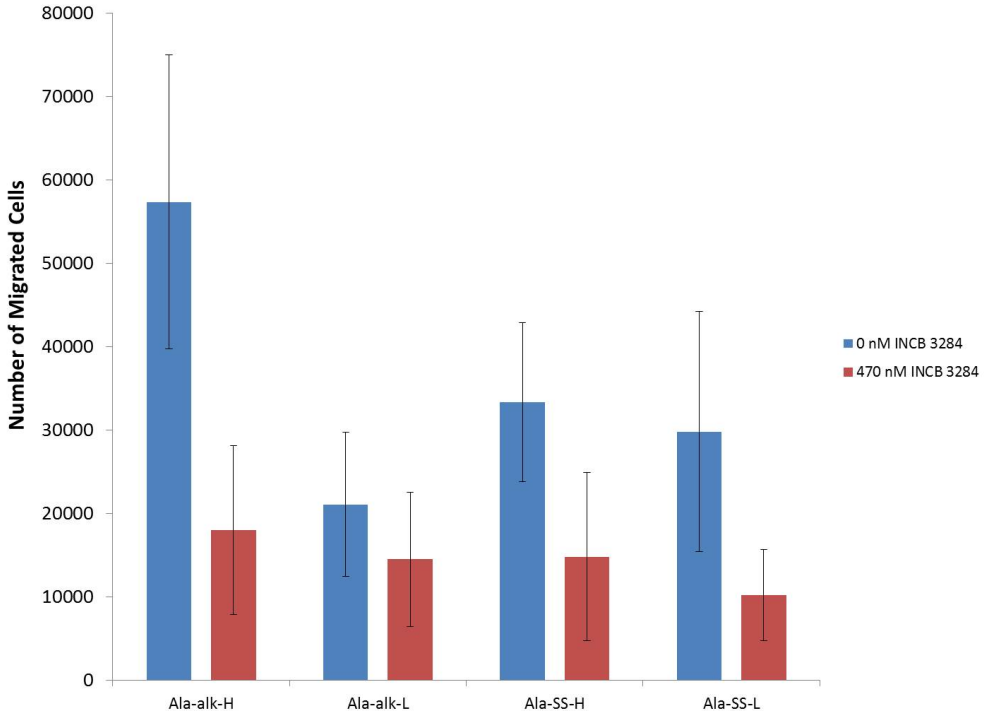

(a) Migratory responses for CCL2 Ala^{-1} fluorescent conjugates post-INCB 3284 treatment.

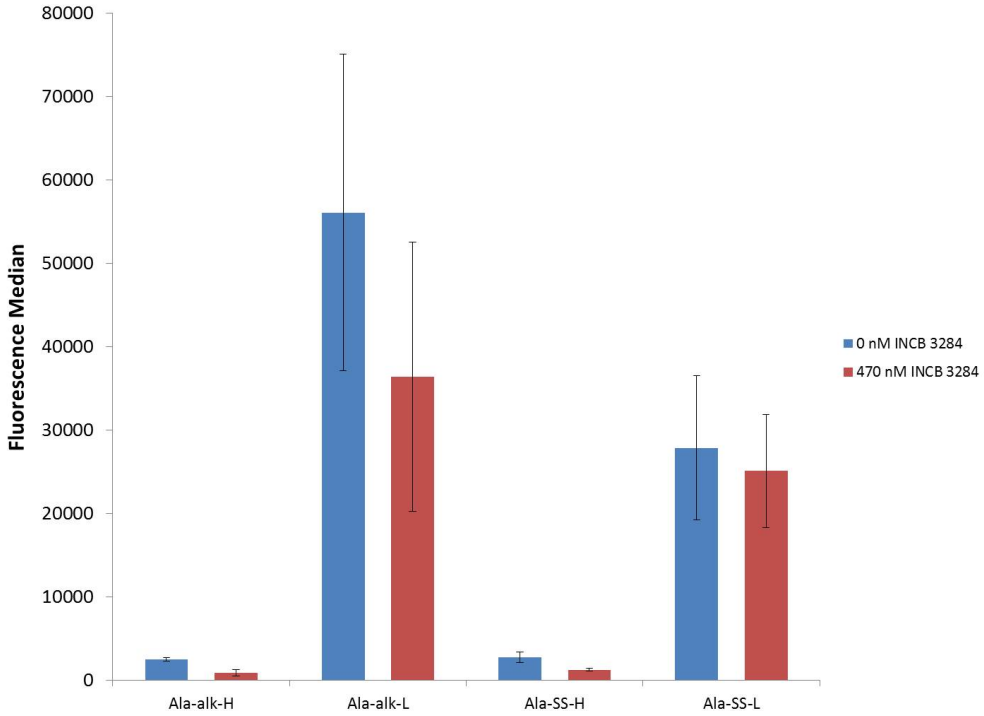

(b) Fluorescence medians of the CCL2 Ala^{-1} conjugates post-INCB 3284 treatment.

Figure 5.20: Migration and fluorescence responses for THP-1 cells towards CCL2 Ala^{-1} conjugates in the Boyden transwell chemotaxis assay when inhibited with INCB 3284. Migration responses were inhibited in the presence of the INCB 3284, except with -alk-L, suggesting the migration observed previously was due to CCR2. The fluorescence medians (5.20b) were similarly inhibited except for CCL2 Ala^{-1}-SS-L which did not alter in the presence of INCB 3284 and also CCL2 Ala^{-1}-alk-L. Negative control uninhibited: migration = 8944 $\pm$2533, fluorescence = 154 $\pm$3. Inhibited: migration = 9722 $\pm$2108, fluorescence = 151 $\pm$2. Error bars refer to N = 2.

periments due to the weak migratory responses for some conjugates which were not clear post-normalisation. The positive control, CCL2 Ala^{-1}-alk-H, functioned correctly resulting in 57000 migrated cells which was then inhibited by 470 nM INCB 3284 to 18000. The level of migration observed with the CCL2 Ala^{-1}-alk-L conjugate had little difference between inhibition and no inhibition. Only 21000 cells were recruited when no INCB 3284 was present and when accounting for error, INCB 3284 appeared to have little effect. Furthermore, the migration to this conjugate was not particularly higher than the negative controls, these results suggest that CCL2 Ala^{-1}-alk-L is not functioning as a chemokine and the CCR2 antagonist has little effect on the conjugate's function. The CCL2 Ala^{-1}-SS-H conjugate was more promising, 33000 cells migrated when uninhibited before decreasing to 15000 cells upon treatment with 470 nM INCB 3284 suggesting CCL2 Ala^{-1}-SS-H initiates chemotaxis in a CCR2-dependent manner. In the previous chemotaxis assay, CCL2 Ala^{-1}-SS-L was weakly chemotactic and it was not clear whether this due to this conjugate operating in a conventional chemotactic manner. Treatment with 470 nM INCB 3284 led to a reduction in the number of migrated cells from 30000 to 10000 cells, indicating that chemotaxis was affected by INCB 3284. The median fluorescence intensities highlighted clear differences in how the conjugates responded to inhibition, for example, CCL2 Ala^{-1}-alk-H was inhibited to the same extent determined previously. CCL2 Ala^{-1}-SS-H was almost identical in that CCR2 antagonism resulted in a decrease in intensity of over 50%. This provided more evidence to suggest that disulfide linkers aid endosomal escape but this can be limited by the hydrophilicity of the compound. The CCL2 Ala^{-1}-alk-L conjugate exhibited extremely high median fluorescence intensities, as found in the previous experiments, and the small reduction in intensity is likely within error. When compared with the poor migration data, the logical conclusion follows that this CuAAC reaction has been unsuccessful in producing functional CCL2. The CCL2 Ala^{-1}-SS-L conjugate is interesting because there is minimal difference in fluorescence intensity whether CCR2 is inhibited or not. The migration of THP-1 cells towards this conjugate was inhibited with INCB 3284, the lack of effect on fluorescence is therefore due to disulfide linker reduction and cytoplasmic distribution of the fluorophore.

Whilst the rate of internalisation has been reduced as fewer CCR2 receptors are available, any fluorophore that is internalised can avoid lysosomal degradation through endosomal escape. This causes the concentration of intact BODIPY to gradually increase over time and reach levels of fluorescence approaching the uninhibited cells.

The responses of the P8A-CCL2 conjugates to INCB 3284 were then measured and these results were generally more consistent and more clearly indicated CCR2-dependency than the CCL2 Ala^{-1} conjugates. Figure 5.21 shows the strong chemotactic response of P8A-alk-H when not inhibited, this is greatly reduced when treated with increasing concentrations of INCB 3284. As expected from the previous chemotaxis assays on these conjugates, P8A-alk-L elicited a weak chemotactic response when not inhibited. CCR2 inhibition actually increased the level of migration with this conjugate, although the large amount of error found with P8A-alk-L suggests this is within error and CCR2 inhibition has little effect on THP-1 migration towards P8A-alk-L. Similarly, the low median fluorescence intensities for this conjugate only slightly reduced in response to CCR2 antagonism, suggesting P8A-alk-L is not fully functional as a chemokine and the CuAAC reaction was unsuccessful. P8A-SS-H was strongly chemotactic when not inhibited and this was greatly reduced in a dose-dependent manner in response to INCB 3284, indicating the chemotaxis was CCR2-dependent. The median fluorescence intensity for this conjugate was relatively low (possibly due to the aforementioned instability of the free fluorophore), however, relatively large reductions in fluorescence intensity can be seen with increasing CCR2 inhibition. This migration and fluorescence data provides evidence that this conjugation was successful and P8A-SS-H is initiating chemotaxis and internalisation *via* CCR2. Migration in response to P8A-SS-L was inhibited by INCB 3284 in a dose dependent manner in proportion to P8A-SS-H. The fluorescence intensities were similar to the behaviour observed with CCL2 Ala^{-1}-SS-L, whereby CCR2 antagonism did not greatly reduce fluorescence intensity. This provides another example where disulfide-linked lipophilic fluorophores do not lead to decreased fluorescence in response to CCR2 antagonism. As before, this is likely due to the remaining CCR2 receptors internalising the conjugate, the fluorophore can then localise outside of endosomes and the fluorescence

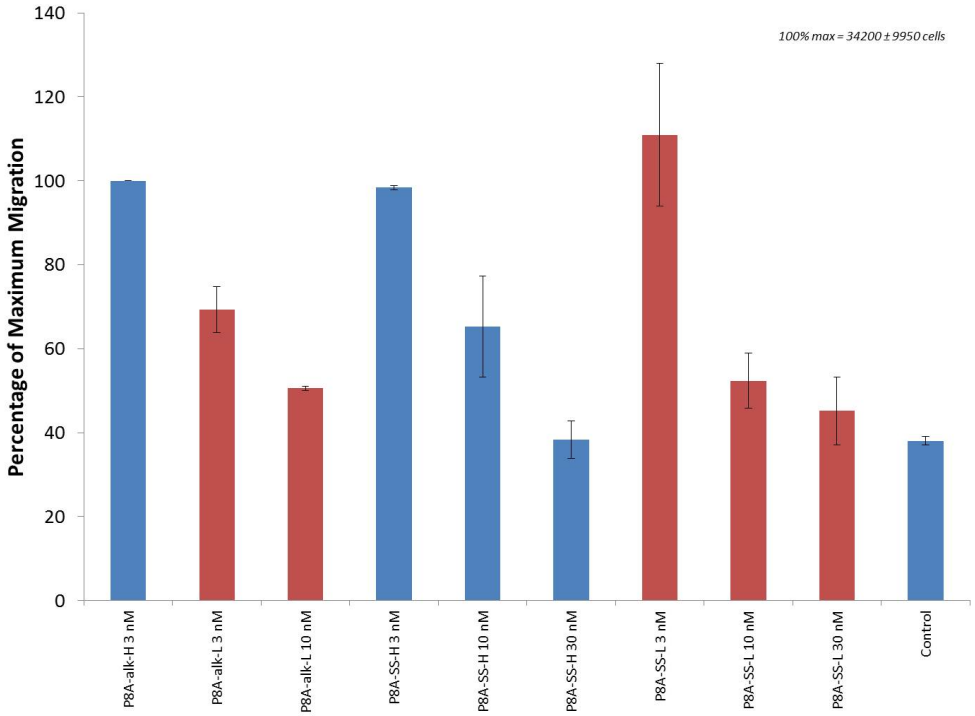

(a) Migratory responses for P8A-CCL2 fluorescent conjugates post-INCB 3284 treatment.

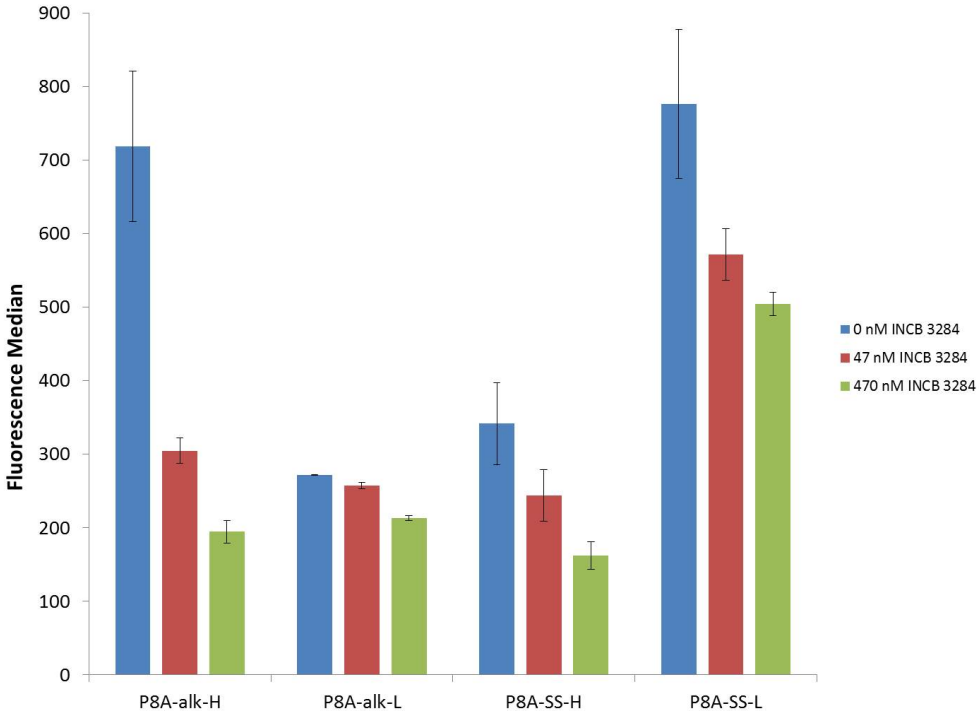

(b) Fluorescence medians of the P8A-CCL2 conjugates post-INCB 3284 treatment.

Figure 5.21: Migration and fluorescence responses for THP-1 cells towards P8A-CCL2 conjugates in the transwell chemotaxis assay with INCB 3284 treatment. Migration responses were all inhibited in the presence of the INCB 3284 except for P8A-alk-L. The fluorescence medians (5.20b) were similarly inhibited except for CCL2 Ala^{-1}-SS-L which did not alter in the presence of INCB 3284. Negative control uninhibited: migration = 17976 ±1054, fluorescence = 149 ±3. 470 nM INCB: migration = 18523 ±1120, fluorescence = 145 ±2. Error bars refer to N = 2.

gradually increases to approach non-inhibited levels.

5.2.4 Uptake of CCL2 Conjugates in White Blood Cells

The previous experiments highlighted P8A-SS-H and P8A-SS-L as successful CCL2 conjugates which can effectively accompany the other alkyl-linked conjugates discussed in 5.2.2 in further experiments. These conjugates were therefore taken forward with CCL2 Ala^{-1}-alk-H, WT-alk-H and P8A-alk-H into flow cytometric experiments with primary human white blood cells. The purpose of using flow cytometry was to determine the selectivity of the CCL2 conjugates towards monocytes and whether any labelling is correlated with CCR2 expression. Furthermore, the use of human primary cells allows more reliable conclusions to be drawn as the *ex vivo* cells are more representative of the *in vivo* environment than the immortalised secondary cell lines. Firstly, blood from healthy donors was taken, PBMCs were isolated as well as neutrophils, these populations were mixed and treated with 30 nM WT-alk-H for 1 h. The cells were then labelled with monoclonal antibodies including anti-CD3, anti-CD14 and anti-CD15 to identify lymphocyte, monocyte and neutrophil populations respectively. Figure 5.22 shows the gating strategy to identify uptake of WT-alk-H in neutrophils; firstly neutrophils were gated based on physical characteristics and the BODIPY fluorescence is then plotted against fluorescence of the aforementioned antibodies to identify which populations are internalising the chemokine. The fluorescence minus one (FMO) plots show that the population cloud consists of CD15-positive neutrophils which should not respond to CCL2 and thus not internalise WT-alk-H. This effect can be seen in the WT-alk-H plot whereby no increase in green fluorescence was observed in any gated population. The FSC/SSC gate was then moved to the lymphocyte/monocyte cloud and the same gating strategy was used to assess uptake of WT-alk-H across these cells (Figure 5.23). As expected, CD14-positive monocytes clearly internalised the WT-alk-H conjugate resulting in the shift of the CD14-positive population to the BODIPY/CD14 double positive quadrant. Interestingly, uptake of WT-alk-H was observed in CD3-positive lymphocyte population, it was not clear which lymphocyte subset was causing this behaviour and so further experiments were devised to

explore this phenomenon.

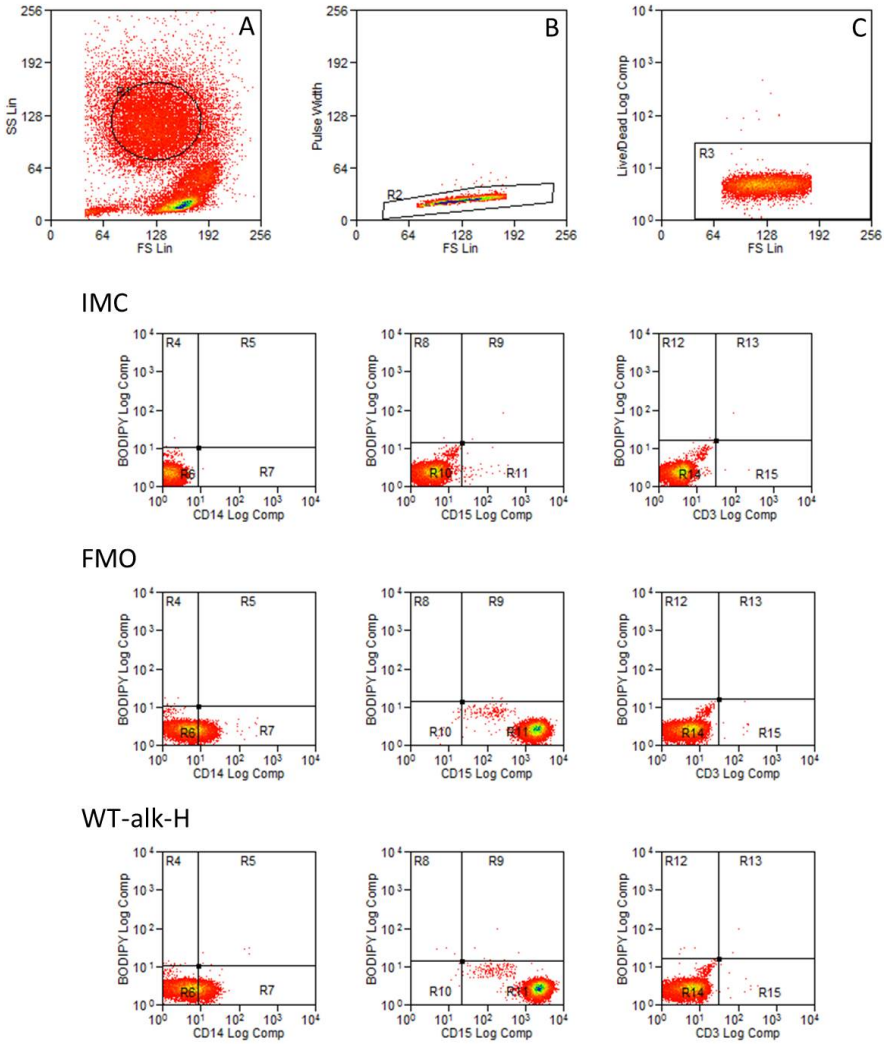

Figure 5.22: Neutrophils are first gated based on physical characteristics such as increased granularity (A), singlet events are selected (B) and dead cells are excluded (C). Matched isotype controls for CD3, CD14 and CD15 directed placement of quadrants for cells untreated with WT-alk-H (IMC). FMO techniques highlight the population consists of CD15-positive neutrophils (FMO). Cells treated with the chemokine show no increase in green fluorescence in any of the gated populations (WT-alk-H).

To further characterise the uptake of CCL2 conjugates across monocyte and lymphocyte populations, experiments were designed to gate populations of classical, intermediate and non-classical monocytes, as well as lymphocyte populations of T cells, NK cells and NKT cells. The gating strategy to assess CCL2 conjugate labelling of monocyte subsets was devised according to the work of Abeles *et al.*, using CD14, CD16 and HLA-DR expression to positively include the monocyte subsets.[255] This gating strategy is displayed in Figure 5.24, firstly the monocyte cloud is gated on physical characteristics using FSC against SSC (A).

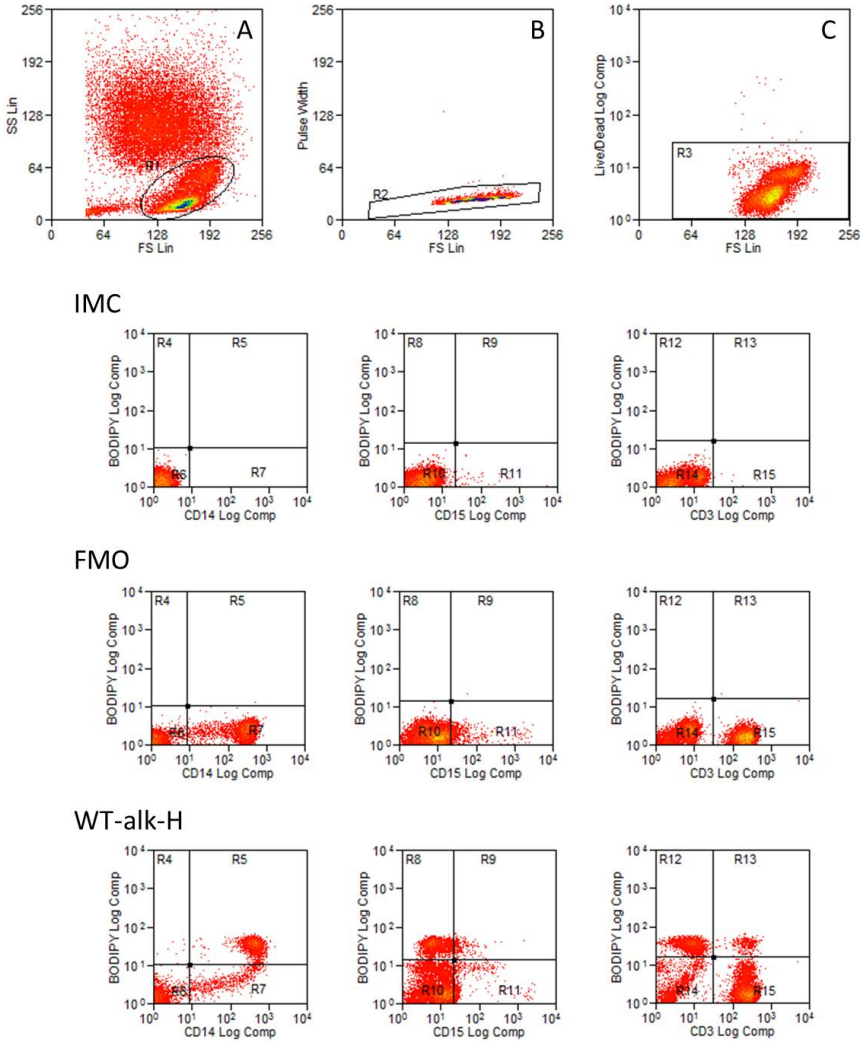

Figure 5.23: The monocyte/lymphocyte population was gated based on physical characteristics (A), singlet events were selected (B) and dead cells are excluded (C). The same antibody labelling strategy as Figure 5.22 was used to identify monocytes, lymphocytes and neutrophils. The majority of the monocyte population were positive for WT-alk-H and a small subset of lymphocytes were also positive.

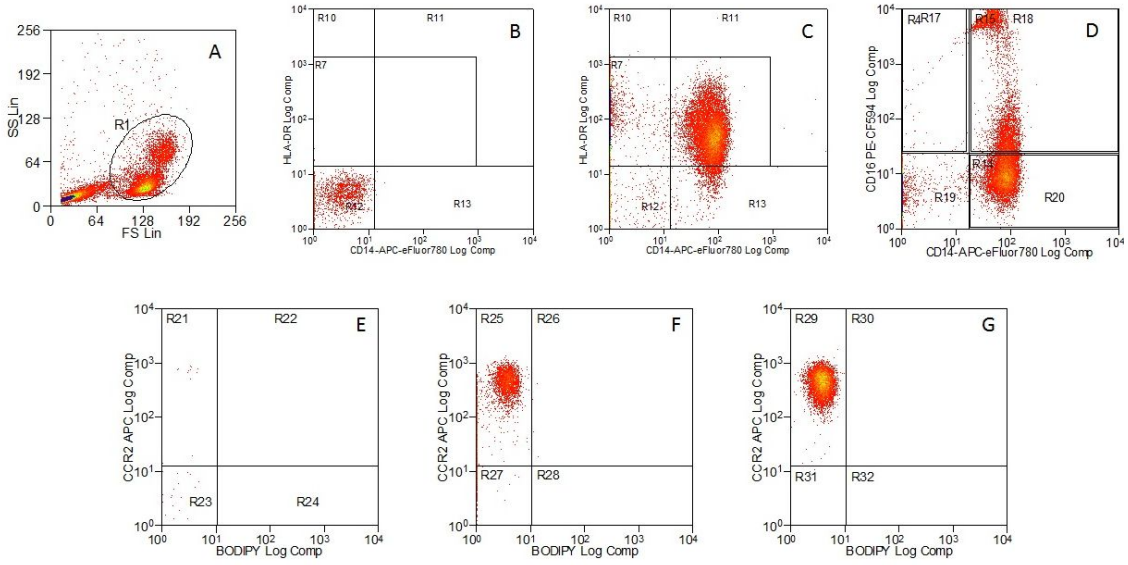

Figure 5.24: Flow cytometry gating strategy for monocyte subsets using CD14, CD16 and HLA-DR. Monocytes were selected based on physical characteristics (A). 'True' monocytes are positively gated using HLA-DR against CD14 (B) using matched isotype controls to direct placement of gates. Monocytes were positively selected with fluorescence minus one (FMO) techniques utilised to minimise bleedthrough issues with CCL2-BODIPY (C). Surface markers CD14 and CD16 labelling allowed classical, intermediate and non-classical monocytes to be gated (D). These individual populations were then assessed in terms of CCR2 expression and CCL2-BODIPY labelling as follows: non-classical (E), intermediate (F) and classical (G).

Monoclonal antibody labelling of the surface markers CD14 and HLA-DR were then used to gate for 'true' monocytes, this was performed with reference to a matched isotype control (B). The gated population then positively selected the monocytes (C) using FMO techniques, this refers to inclusion of all monoclonal antibodies but not fluorescent CCL2 meaning any fluorescence from CCL2 conjugates is due to the BODIPY fluorophore, not a bleedthrough artifact. Finally, CD14 and CD16 were used to identify monocyte subsets (D), showing the three subsets: $CD14^{+}CD16^{-}$ (Classical), $CD14^{+}CD16^{+}$ (Intermediate) and $CD14^{-}CD16^{+}$ (Non-classical). The three subsets were individually interrogated in terms of CCR2 expression and CCL2-BODIPY labelling (E, F and G), here the CCR2 expression is shown to be distinct between subsets, for example, classical and intermediate monocytes express high levels of CCR2 and non-classical are generally low in CCR2. The different densities of the plots can be attributed to the relative numbers of the populations, for example, classical monocytes are the most-prevalent monocytes in peripheral blood and this is illustrated in the high density of cells in these plots.

Figure 5.25 shows the extent of CCL2 conjugate labelling of the three monocyte subsets, the double positive gates were selected on the basis of FMO. In this experiment, CCL2 Ala^{-1}-alk-H was used at 200 nM and all other conjugates were used at 30 nM, this was based on the lower affinity of CCL2 Ala^{-1} for CCR2. Using 30 nM for the other conjugates was due to this lower concentration being near the chemotactic maxima for these sequences, however, the maxima at 3 and 10 nM for WT-alk-H and P8A-alk-H were difficult to detect in these experiments and so the higher concentration of 30 nM was selected. CCL2 Ala^{-1}-alk-H did not greatly affect surface CCR2 levels on the classical monocytes, however a clear increase in green fluorescence can be seen for CCR2 positive cells. This was also observed in the intermediate monocytes although to a lesser extent. Heterogeneity was observed in this population where cells with lower CCR2 expression exhibited diminished CCL2 labelling. The non-classical monocytes were also heterogeneous whereby cells with higher CCR2 expression exhibited higher CCL2 labelling and cells negative in CCR2 giving no CCL2 Ala^{-1}-alk-H labelling. This data suggests that this conjugate is uptaken only by CCR2-positive monocytes, with a preference for classical and intermediate monocytes. The WT-alk-H conjugate had a stronger effect on surface CCR2 levels relative to FMO, suggesting the chemokine was binding CCR2 and reducing surface levels of the receptor. Similar population heterogeneities were observed in intermediate monocytes with WT-alk-H whereby a proportion of the population exhibited lower CCR2 expression and concurrently no WT-alk-H labelling. Interestingly, the population of non-classical monocytes high in CCR2 were labelled with WT-alk-H and the level of surface CCR2 was reduced relative to cells treated with CCL2 Ala^{-1}-alk-H, suggesting WT-alk-H had a greater effect on CCR2 than CCL2 Ala^{-1}-alk-H. The effect on CCR2 with P8A-alk-H treated cells appeared to be greater still, for example, the classical monocytes were clearly labelled with P8A-alk-H to a greater extent than WT-alk-H and similarly the CCR2 surface levels were also diminished. This trend of increasing fluorescence from CCL2 Ala^{-1} to WT-CCL2 to P8A-CCL2 is consistent with the THP-1 chemotaxis assays as this trend reflects the relative affinities of the chemokines.

A noteworthy observation is that CCL2 Ala^{-1}-alk-H, despite the concentration being almost

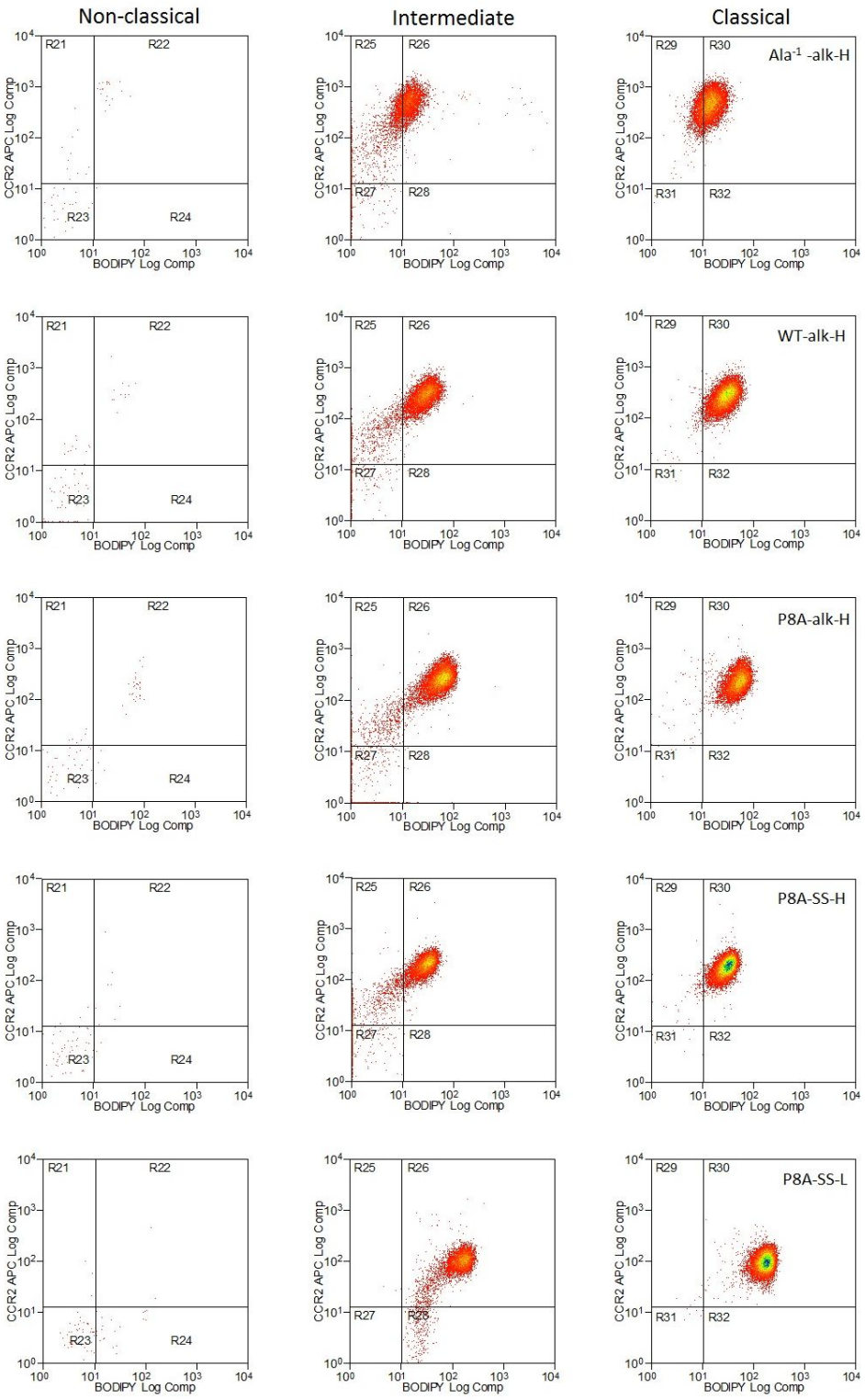

Figure 5.25: Density plots of cells treated with CCL2 conjugates in positively gated classical, intermediate and non-classical monocytes based the strategy presented in Figure 5.24. P8A-alk-H exhibited the strongest BODIPY labelling of the three alkyl-linked conjugates and the largest effect on CCR2-surface expression, followed by WT-alk-H and CCL2 Ala^{-1}-alk-H. A clear preference for classical monocytes was observed, followed closely by intermediate, with non-classical monocytes having the lowest amount of CCL2-labelling. The disulfide linked conjugates behaved similarly with the exception of P8A-SS-L labelling CCR2-negative cells, likely as a result of leaching.

ten-fold higher than the other variants, still exhibited a reduction in fluorescence. This difference in CCR2 binding affinity is also indicated by the effects on surface CCR2 across the three chemokines in all three subsets, this provides more evidence that the chemokine conjugates operate through CCR2-binding and the extent of labelling of these cells is due to relative affinities for the CCR2 receptor. The relative behaviour of the P8A-CCL2 conjugates was similar in terms of selectivity towards classical and intermediate monocytes over non-classical monocytes, and also the relationship between BODIPY labelling and surface levels of CCR2 pre- and post-CCL2 labelling. Some contrasting behaviour was apparent in the disfulfide-linked conjugates, however, P8A-SS-H exhibited a lower level of BODIPY labelling relative to P8A-alk-H despite a similar level of CCR2-levels on the surface of the classical and intermediate monocytes. This suggests the chemokine is being uptaken by CCR2 to a similar extent but the properties of the conjugate are altering the level of fluorescence inside the cell. This is consistent with data presented in Figure 5.19, where P8A-SS-H did not exhibit as high median fluorescence intensity as P8A-alk-H and that fluorescence intensity did not increase with concentration relative to P8A-alk-H, possibly due to fluorophore stability post-disulfide reduction. The P8A-SS-L conjugate on the other hand was very different, this compound exhibited a greater level of fluorescence in the classical monocytes and an even greater effect on CCR2 surface levels. The high level of BODIPY labelling in P8A-SS-L was likely due to endosomal escape due to the lipophilicity of the fluorophore, evidence for this behaviour was observed in Figure 5.19 whereby median fluorescence intensity greatly increased with concentration and did not reach a steady state as was found in the other conjugates. The intermediate monocytes exhibited further differences and a large amount of heterogeneity both in terms of BODIPY labelling and CCR2 levels. The major population behaved identically to classical monocytes with a population of cells with decreasing CCR2 and BODIPY labelling which was also observed in the other conjugates. However, a handful of events can be observed in the CCR2-negative/BODIPY-positive quadrant suggesting a small amount of uptake by CCR2-negative intermediate monocytes. This could be due to complete depletion of surface CCR2 to IMC levels or leaching of the lipophilic fluorophore

out of the initial cell and into nearby cells, resulting in labelling of CCR2-negative cells. The classical monocytes do not appear to be affected as this population are homogeneous in terms of CCR2 and so any free fluorophore which leaches into these cells is not easily detected. The intermediate monocytes and non-classical monocytes, however, are heterogeneous in CCR2 and so CCR2-negative cells which absorb leached fluorophore are more clearly observed.

Figure 5.26 quantitatively describes the preferential uptake of the CCL2 conjugates towards classical monocytes, with intermediate monocytes closely behind. All conjugates except CCL2 Ala^{-1}-alk-H effectively labelled all classical monocytes, with CCL2 Ala^{-1}-alk-H reaching 77% of the population likely as a result of the reduced affinity of this peptide for CCR2. Intermediate monocytes were labelled to around 70% of the population with P8A-alk-H being the highest at 77% followed by WT-alk-H, P8A-SS-H and P8A-SS-L; again, CCL2 Ala^{-1}-alk-H labelled around 50% of the intermediate population. The reason for the intermediate monocytes being labelled to a lesser extent is clear from the heterogeneity of CCR2 expression (Figure 5.25), this suggests CCL2 uptake is mitigated by CCR2. Finally, non-classical monocytes were poorly labelled by all conjugates indicating a selectivity of the CCL2 conjugates for classical and intermediate monocytes. Figure 5.26b highlights a negative correlation between CCR2 surface levels and BODIPY fluorescence. As CCR2 is high, the level of CCL2-BODIPY uptake is low and as the CCL2-BODIPY uptake increases (to P8A-SS-L intensities) the CCR2 MFI decreases suggesting the CCR2 receptor is being depleted by the chemokine conjugates. The fitted line has a reasonable R^2 which is only adversely affected by the reduced MFI of P8A-SS-H. The intermediate population exhibited a similar negative correlation between CCR2 MFI and BODIPY MFI (Figure 5.27a) with a similar R^2 fitted line. The gradient of this line was slightly reduced relative to the classical population suggesting the BODIPY fluorescence does not increase as rapidly as the CCR2 receptor is depleted. The non-classical monocyte population was quite different to the preceding populations; the negative correlation was still present but the gradient was reduced (Figure 5.27b). Furthermore the line of best fit was relatively poor as a result of the P8A-SS-H outlier which has been observed throughout these data. The plot indicates that surface CCR2 is being depleted more

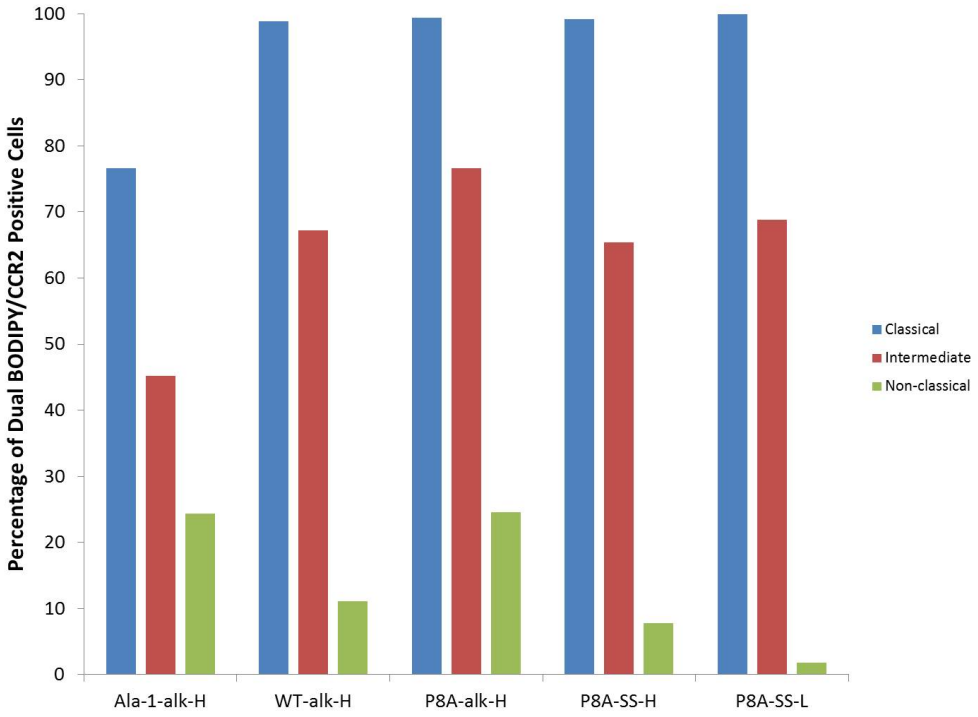

(a) Dual CCR2/BODIPY percentage for CCL2 conjugates across monocyte subsets

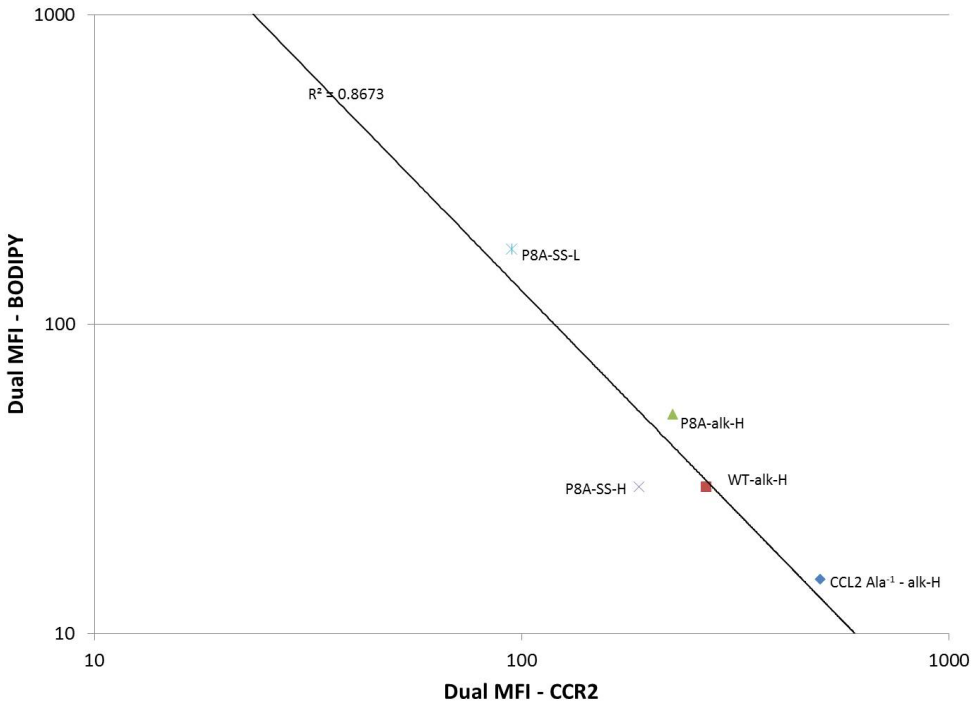

(b) MFI of CCR2 against BODIPY in classical monocytes

Figure 5.26: Comparison of classical, intermediate and non-classical monocytes in the BODIPY/CCR2 dual positive quadrant, showing clear preferential uptake in classical and intermediate monocytes (5.26a). FMO CCR2 expression level: 99.98, 70.90 and 19.67% for classical, intermediate and non-classical monocytes respectively. 5.26b shows MFI for CCR2 against BODIPY for classical monocytes, indicating a negative correlation between CCR2 and BODIPY, as a result of ligand depletion of the CCR2 receptor. Data is representative of N=1.

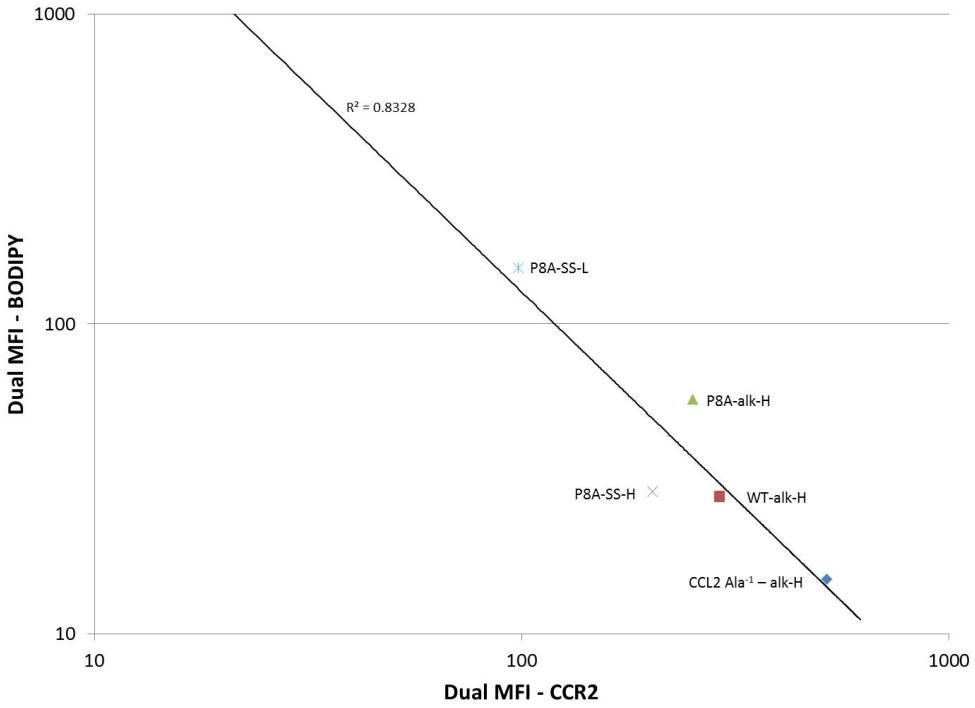

(a) MFI of CCR2 against BODIPY in intermediate monocytes

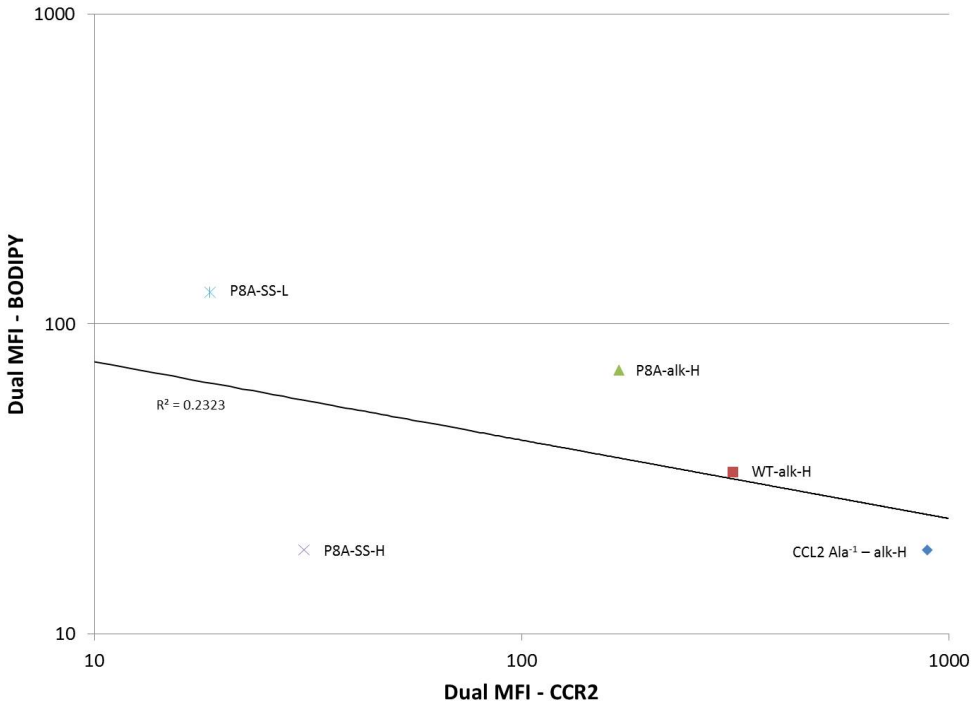

(b) MFI of CCR2 against BODIPY in non-classical monocytes

Figure 5.27: 5.27a shows MFI for CCR2 against BODIPY for intermediate monocytes, indicating a negative correlation between CCR2 and BODIPY (which was also found in classical monocyte populations) suggesting increased uptake of CCL2 conjugates depletes CCR2. 5.27b exhibited a weaker negative correlation with poor R^2, mostly due to the P8A-SS-H outlier. Data is representative of N=1.

strongly by the P8A conjugates but only a modest increase in BODIPY MFI is occurring as a result.

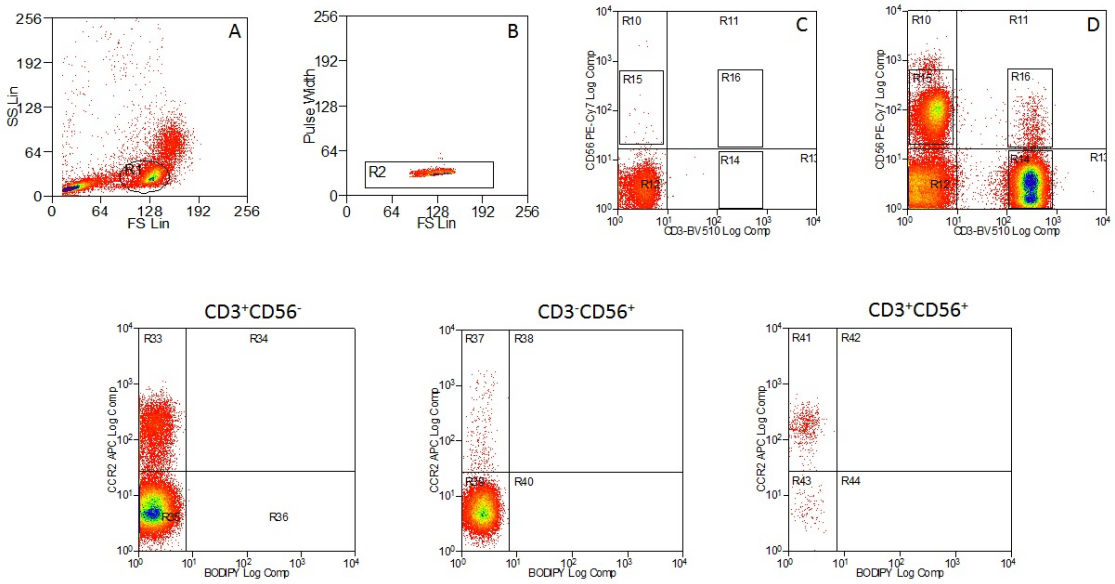

Figure 5.28: Gating strategy to define T cells, NK cells and NKT cells. Lymphocyte populations defined physically (A) and singlet events were positively gated (B). Matched isotype controls directed gate placement for CD3 and CD56 expression (C). FMO techniques presented positive lymphocyte sub-populations which were further gated (D). The defined populations were then characterised in terms of CCR2 expression relative to BODIPY (Bottom, FMO).

Initial flow cytometry experiments using PBMCs revealed labelling of the CCL2-BODIPY conjugates in some $CD3^+$ lymphocyte populations, further experiments were therefore designed to probe the nature of this sub-population. Interestingly, a number of CCR2-positive lymphocyte sub-populations have been identified in the literature including effector memory $CD4^+$ T cells, NK subsets and NKT cell sub-populations.[256–258] In consideration of these studies, it was decided to segregate the lymphocyte population into T cell, NK cell and NKT cell using $CD3^+CD56^-$, $CD3^-CD56^+$ and $CD3^+CD56^+$ antibody labelling respectively. Figure 5.28 highlights the gating strategy used to define these populations, firstly, the lymphocyte cloud was selected based on physical characteristics (A) and the pulse width ensured events were singlets (B). Lymphocyte subsets were then defined through differential CD3 and CD56 expression, gates were aligned using matched isotype controls (C) and positive populations were selected using FMO techniques (D). The FMO density plots then display the surface CCR2 level for each population, this highlighted that each population contained

$CCR2^+$ subsets to varying extents, with the NKT cells containing the highest proportion of $CCR2^+$ cells.

Figure 5.29 shows the extent of labelling of the T cell, NK cell and NKT cell populations and the effect on surface CCR2 post-labelling. CCL2 Ala^{-1}-alk-H caused a slight increase in BODIPY fluorescence intensity in only the CCR2-positive cells showing that uptake of this chemokine in lymphocytes was CCR2-dependent and all three subsets displayed a modest increase in BODIPY intensity. The WT-alk-H conjugate gave a greater increase in BODIPY fluorescence intensity in the same $CCR2^+$ populations which highlighted the difference in affinity for CCR2 between these peptides which provided further evidence this CCL2 uptake was due to CCR2. Similarly, P8A-alk-H also increased the BODIPY intensity and this was accompanied by a notable reduction in surface CCR2 in NKT cells, NK and T cells. The P8A conjugates were again interesting in that the P8A-SS-H conjugate greatly reduced surface CCR2 but was accompanied by only a modest increase in BODIPY intensity which varied across the lymphocyte populations. For example, the NKT cells and the T cells yielded a similar level of BODIPY intensity and surface CCR2, however, the NK cells exhibited a much greater level of both BODIPY intensity and surface CCR2. Further evidence for leaching of the P8A-SS-L fluorophore out of the initial cell and into neighbouring cells was observed in lymphocytes. In the NKT cell population, the CCR2-negative BODIPY-positive population could just be a result of very effective depletion of surface CCR2 to CCR2-negative intensities, and a similar phenomena could be observed in the other subsets. However, in the NK cells, for example, the large CCR2-negative population (pre-chemokine treatment) is clearly shifted to increased BODIPY intensity. Similar arguments can be made for the T cell and NKT cell $CCR2^-$ subset, this suggests that the P8A-SS-L fluorophore is indeed being liberated from endosomes and subsequently leaching into $CCR2^-$ cells.

The percentage of CCR2/BODIPY dual positive events (Figure 5.30) is more difficult to interpret correctly with the lymphocytes than the monocyte populations described previously due to the CCR2-expression heterogeneity. For example, a clear preference can be seen for NKT cells where high proportions of the NKT subset were labelled by BODIPY in the

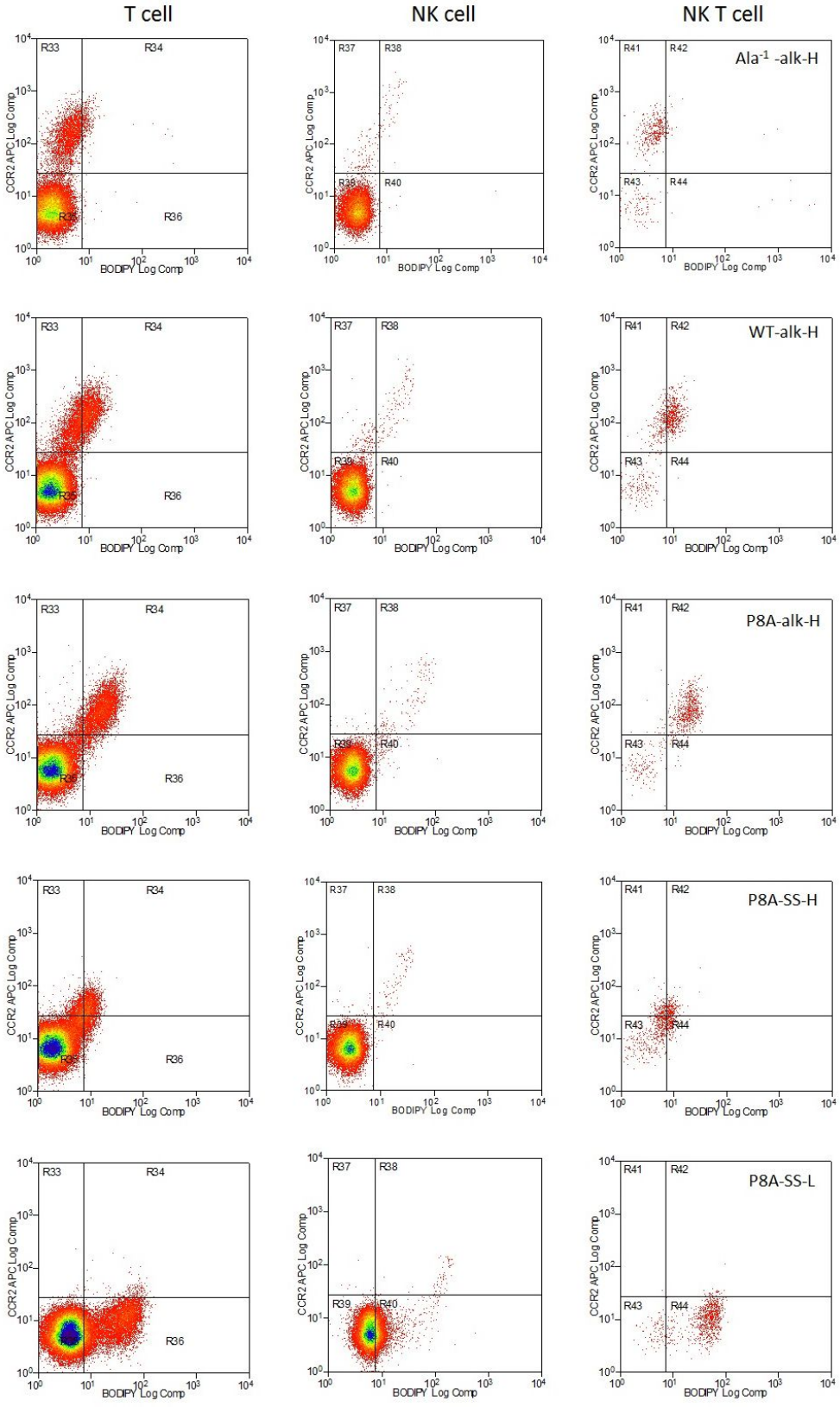

Figure 5.29: Density plots of lymphocyte populations gated into T cell, NK cell and NKT cells with surface CCR2 labelling against CCL2-BODIPY labelling for CCL2 conjugates. All lymphocyte subsets displayed heterogeneity in terms of CCR2 expression and this CCR2-positive population was labelled by all CCL2 conjugates. Some CCR2 negative populations were BODIPY-positive, however, this was likely due to ligand-mediated depletion of the receptor and in the case of P8A-SS-L the labelling of $CCR2^{-}$ cells was likely due to fluorophore leaching.

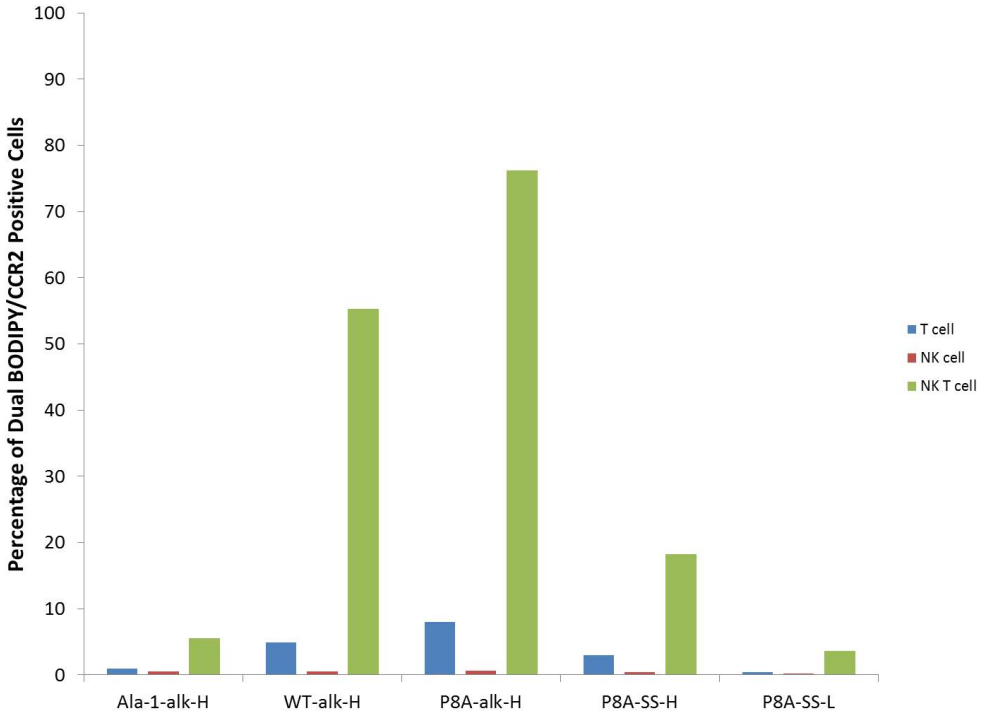

(a) Dual CCR2/BODIPY percentage for CCL2 conjugates across lymphocyte subsets.

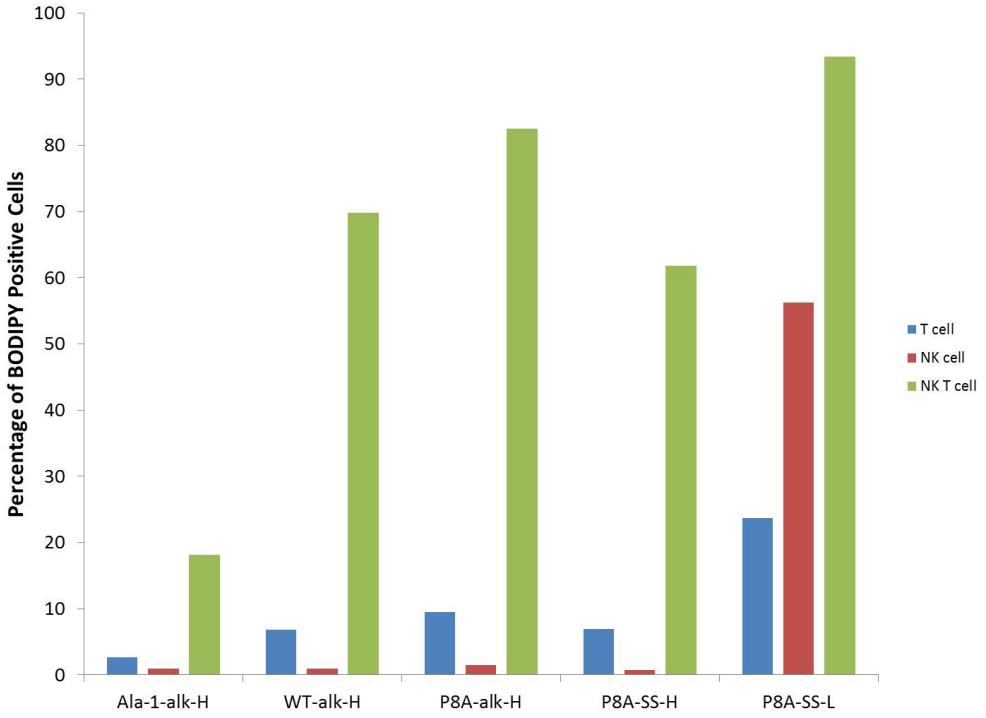

(b) Percentage of BODIPY-positive cells in each gated sub-population.

Figure 5.30: Comparison of T cell, NK cells and NKT cells in the BODIPY/CCR2 dual positive quadrant, showing clear preferential uptake in NKT cells (Figure 5.31). FMO CCR2 expression level: 10.11 , 1.42 and 83.47% for T cells, NK cells and NKT cells respectively. 5.30b displays the global percentage of BODIPY across the T cell, NK cell and NKT cell populations which exhibit a clear preference for NKT cells in all CCL2 conjugates. P8A-SS-L exhibits uptake in the NK cells and T cells as a result of fluorophore lipophilicity and leaching. Data is representative of N=1.

majority of CCL2 conjugates, however, this is as a result of the CCR2-positive NKT subset being the largest subset of the NKT cells. On the other hand, the NK population is mostly CCR2-negative and so the CCR2/BODIPY dual positive population is relatively small but the BODIPY MFI is in fact higher than the NKT subset. The correct interpretation of these results would be that the CCL2 conjugates are generally selective for NKT cells due to the large proportion of $CCR2^+$ cells in this subset and the overwhelming majority of T cells and NK cells do not possess surface CCR2 and are therefore not labelled by the CCL2 conjugates. The small proportion of T cells and NK cells which are $CCR2^+$ are labelled by the CCL2 conjugates to a similar extent as the $CCR2^+$ NKT cells. The exception to this trend is P8A-SS-L which was only 3.6% CCR2/BODIPY dual positive, this can be explained by the comparison with Figure 5.29 where the NKT cells are clearly being depleted of surface CCR2 by a large amount relative to FMO, moving these cells to a BODIPY positive/$CCR2^-$ population. Another factor is P8A-SS-L labelling of formally $CCR2^-$ cells most likely as a result of leaching into these cells due to the physicochemical properties of the linker-fluorophore system. This behaviour is effectively illustrated in Figure 5.30b whereby preference for NKT cells is clear in all conjugates but P8A-SS-L was more promiscuous across cell types, again, most likely due to extracellular leaching.

Analysis of the relationship between surface CCR2 and BODIPY fluorescence intensity is displayed in Figure 5.31, a negative correlation was present between surface CCR2 and uptake of CCL2 conjugates in lymphocyte populations. The MFI of BODIPY was generally higher in the NK cells than T or NKT cells suggesting the conjugates were more effectively internalised in NK cells. Interestingly, the surface CCR2 rapidly decreases across the conjugates in both T and NKT cells, however, the BODIPY fluorescence does not increase at the same rate. This suggests CCR2 is being depleted but the fluorescent chemokines are either not being internalised or any internalised fluorophores are rapidly degraded.

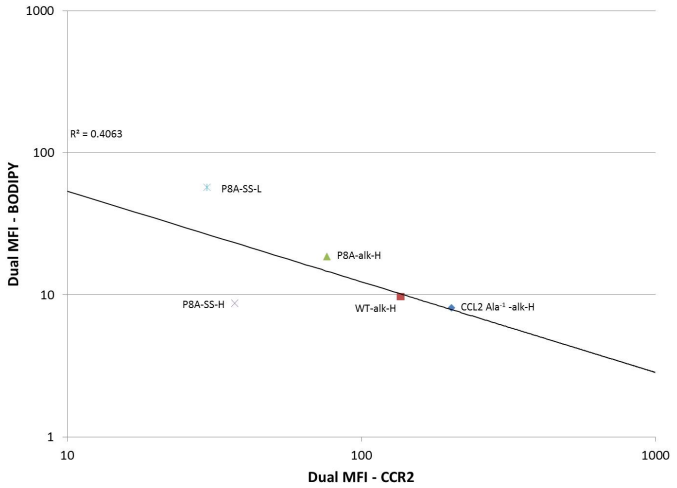

(a) Dual MFI CCR2/BODIPY of the T cell sub-population.

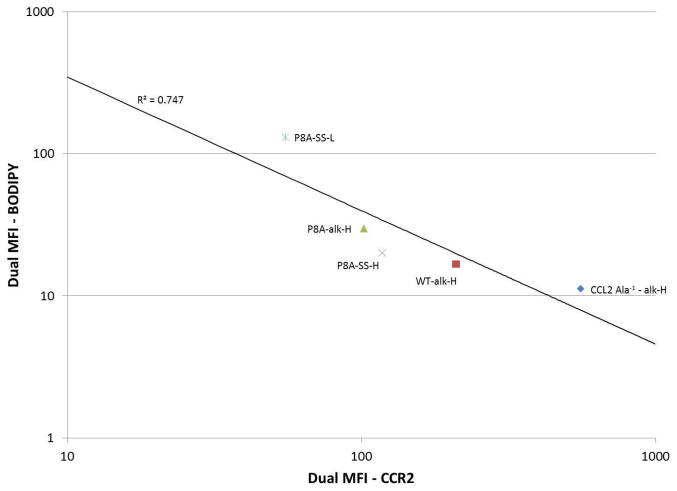

(b) Dual MFI CCR2/BODIPY of the NK cells.

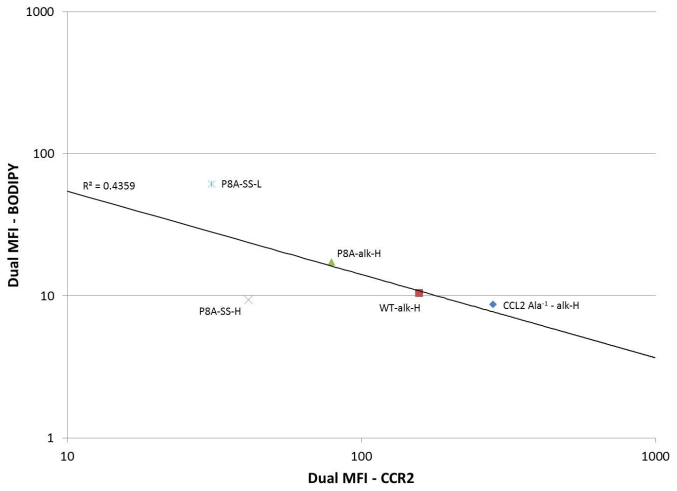

(c) Dual MFI CCR2/BODIPY of the NKT cells.

Figure 5.31: Relationship between CCR2 and CCL2-BODIPY uptake in T cell, NK cell and NKT cell populations. Dual MFI of CCR2 against BODIPY reveals a negative correlation between surface CCR2 and CCL2-BODIPY fluorescence intensity, akin to the behaviour in monocytes but the correlation is weaker. NK cells had the strongest correlation and best R^2 for the fitted line, clearly demonstrating the CCL2 conjugates deplete the surface receptor. Data is representative of N=1.

5.2.5 Fluorescence Microscopy with CCL2 conjugates

The fluorescent CCL2 conjugates have been extensively characterised in both primary human PBMCs and the secondary THP-1 cell line, both in terms of chemotaxis and the CCR2-selective internalisation pathway. The behaviour of these fluorescent systems inside cells was then determined using fluorescence microscopy to investigate whether the nature of fluorophore or linker system had any effect on sub-cellular localisation in both THP-1 cells and PBMCs. Initially, THP-1 cells were incubated in media containing either of the five CCL2 conjugates for 2 h before the cells were mounted onto glass coverslips *via* cytospin and fixed in para-formaldehyde (pFA). The 2 h incubation time was selected on the basis of timecourse experiments which showed fluorescence generally did not greatly increase after this time. The nuclei were stained with 4',6-diamidino-2-phenylindole (DAPI) to ascertain that BODIPY fluorescence is excluded from the nucleus. Images were captured on a Zeiss Axio Observer, this microscope simulates confocal microscopy through utilising diffraction grating to distort a grid over topological abberations, these deformations allow for optical sectioning of the cells, any fluorescence was therefore originating from inside the cell. The images were captured as follows: five slices were captured through the cell and maximum intensity projections averaged the distribution of fluorescence intensity throughout the slices into a single 2d image.

Figure 5.32 shows fluorescence microscopy images from THP-1 cells treated with the alkyl-linked CCL2 conjugates CCL2 Ala^{-1}-alk-H, WT-alk-H and P8A-alk-H. The low level of autofluorescence originating from the negative control suggests that increases in fluorescence originating from cells treated with CCL2-conjugates is resulting from the conjugated fluorophore not any endogenous fluorescent species. In CCL2 Ala^{-1}-alk-H, the green channel exhibited mainly circular regions of fluorescence that resemble vesicle structures and the previous chemotaxis assays suggested a steady state between internalisation and lysosomal degradation of the BODIPY fluorophore meaning the vesicles are likely to be endosomes or lysosomes. The majority of the fluorescence is outside the nucleus in all conjugates, however,

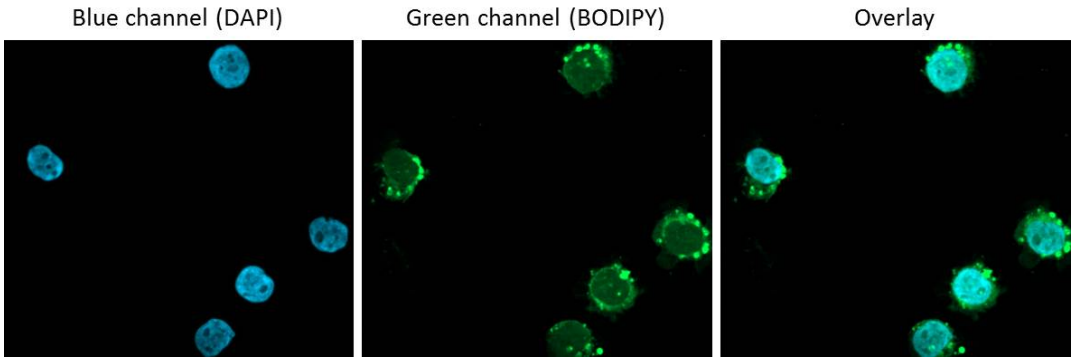

(a) THP-1 cells treated with CCL2 Ala^{-1}-alk-H.

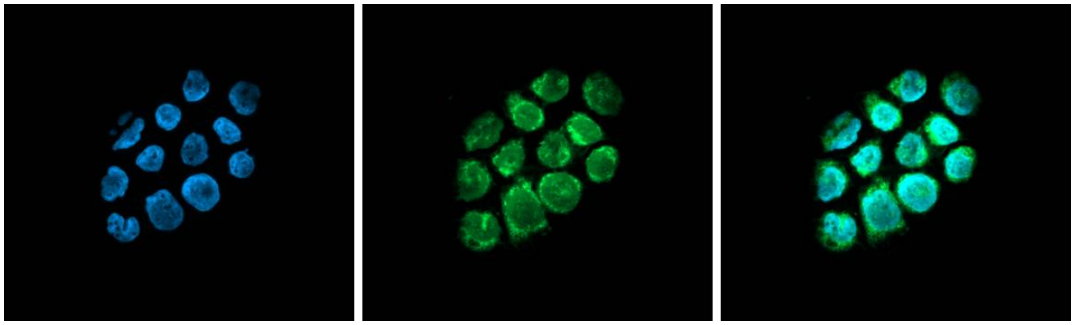

(b) THP-1 cells treated with WT-alk-H.

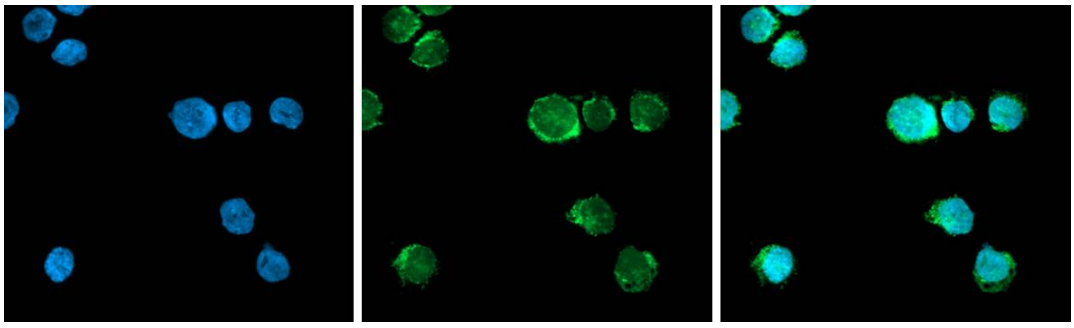

(c) THP-1 cells treated with P8A-alk-H.

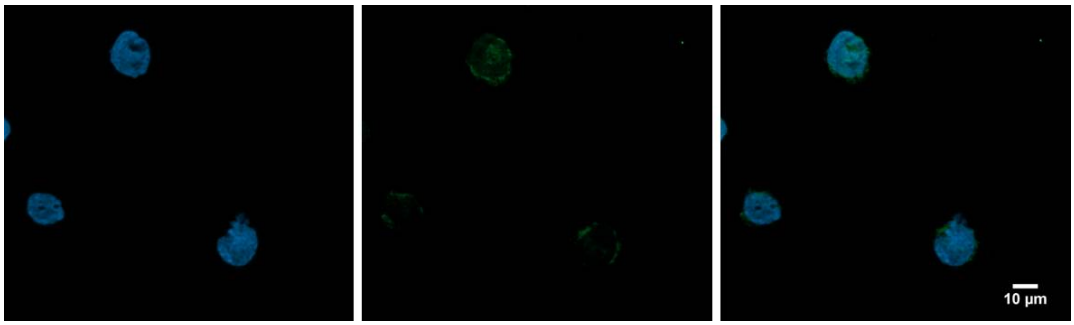

(d) Unlabelled THP-1 cells.

Figure 5.32: Fluorescence images of fixed THP-1 cells treated with alkyl-linked CCL2 conjugates for 2 h. The cells treated with fluorescent conjugates exhibited localised fluorescence in vesicle-like structures which are most likely endosomes or lysosomes, suggesting the chemokine is located intracellularly and the hydrophilic fluorophores cannot escape vesicular environments. A small amount of autofluorescence was observed in the untreated cells which was used as a control. DAPI: blue, CCL2-BODIPY: green. Green channel exposure time: 1000 ms, blue channel exposure time: 120 ms. CCL2 conjugates used at 200 nM.

some indications can be observed inside the nucleus, this is likely due to the maximum intensity projection calculation resulting in green fluorescence above or below the nucleus which is then projected through the cell. In some cases, CCL2 Ala^{-1}-alk-H appeared to be polarised towards one side of the cell, this effect has been observed previously in the literature where fluorescently labelled CCR2 was internalised and the receptor was transported to the rear of the cell.[5] Relative to the maximal migration concentration, both P8A-alk-H and WT-alk-H were used at a higher concentration of 200 nM, this was due to initial experiments with lower concentrations giving weak fluorescence intensities and so the higher concentration was selected. Again, the fluorescence is mostly outside the nucleus of the edge of the cell and appears to be localised in vesicles. Interestingly, the morphology of the vesicles observed with both WT-alk-H and P8A-alk-H are quite different from that of CCL2 Ala^{-1}-alk-H. The vesicles from P8A-alk-H and WT-alk-H are more numerous and are also much smaller in size than the vesicles observed in CCL2 Ala^{-1}-alk-H. This suggests that the THP-1 cells may be processing the chemokine ligands differently, however, the nature of any differential mechanism was unclear. In both WT-alk-H and P8A-alk-H, there appeared to be some polarisation of fluorescence towards one side of the cell, however, it was not as distinct as the polarisation found in CCL2 Ala^{-1}-alk-H.

The fluorescence microscopy images from disulfide-linked CCL2 conjugates are displayed in Figure 5.33. The P8A-SS-H conjugate was consistently of lower fluorescence intensity than the other conjugates in both the Boyden chemotaxis transwell assays and the PBMC flow cytometry experiments potentially due to instability of the fluorophore post-disulfide reduction. This conjugate was localised in vesicles in these images which suggests the compound cannot escape endosomes, however there is little direct evidence to prove the disulfide is being reduced. Combining these observations with the behaviour of P8A-SS-L in previous experiments provides a reasonable argument that the disulfide is being reduced and the hydrophilic fluorophore is more prone to degradation than conjugated fluorophore. The P8A-SS-L image was very different to all previous images for example, very few vesicle-like objects could be identified and a diffuse morphological profile of fluorescence was observed. This is likely due

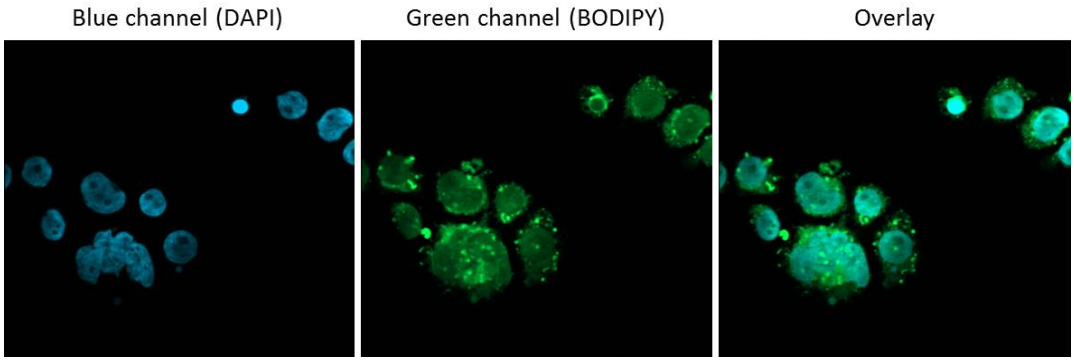

(a) THP-1 cells treated with P8A-SS-H.

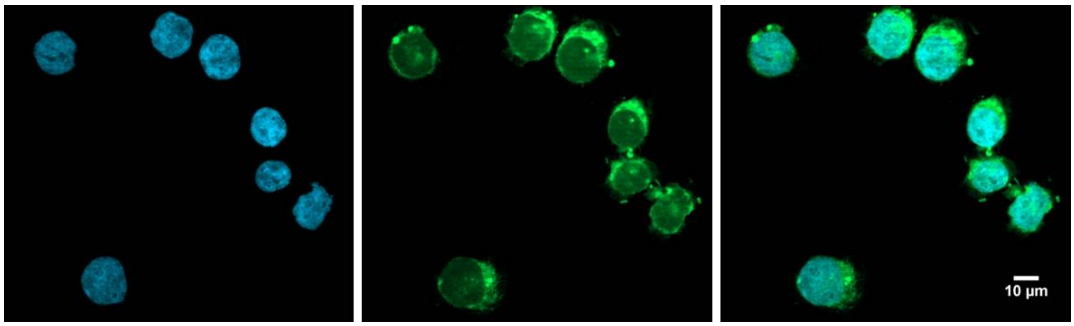

(b) THP-1 cells treated with P8A-SS-L.

Figure 5.33: Fluorescence images of fixed THP-1 cells treated with disulfide-linked CCL2 conjugates for 2 h. Differences in subcellular localisation between P8A-SS-H and P8A-SS-L suggest that the lipophilic fluorophore is able to escape endosomes leading to a diffuse morphological profile. DAPI: blue, CCL2-BODIPY: green. Green channel exposure time: 1000 ms, blue channel exposure time: 120 ms. CCL2 conjugates used at 200 nM.

to disulfide reduction liberating the lipophilic fluorophore which can then escape endosomes and localise in lipophilic environments throughout the cell. This effect corroborates with the results observed with chemotaxis assays and PBMC flow cytometry. Furthermore, the diffuse nature of the fluorescence has not resulted in reduced fluorescence intensity but rather the whole diffuse fluorescence profile is of high intensity. This suggests that the THP-1 cells are capable of continuously internalising the ligand and the fluorophore avoids degradation in lysosomes and the intensity of fluorescence is retained throughout the cell. Interestingly, the fluorescence is still polarised to one side of the cell, this could just be a result of the THP-1 cell being dominated by a large nucleus and so there is little cytoplasm around the opposite sides of the cell. Another explanation is that the early endosomes are transported to the polarised side and the BODIPY then escapes from the polarised endosomes and just resides in nearby lipophilic compartments of the cell. Many cells have a ring of fluorescence outside of the main polarised side of the cell, this is likely the lipophilic BODIPY residing in the cell membrane, these molecules may have originated from the polarised side and diffused along the membrane to encapsulate the cell. In any case, these images are clear evidence of a distinct labelling profile to the other conjugates which correlates with previous experiments.

The imaging experiments were repeated on PBMCs, however, it is important to note that many of the cells are CCR2-negative lymphocytes or granulocytes and therefore some of the cells in the images may not be labelled by the fluorescent chemokines. Figure 5.34 displays fluorescence images of PBMCs treated with the alykl-linked conjugates CCL2 Ala^{-1}-alk-H, WT-alk-H and P8A-alk-H. A large proportion of the cells in the CCL2 Ala^{-1}-alk-H treated PBMCs exhibited fluorescence, interestingly, these fluorophores were localised in small vesicles. This is different to the localisation of this chemokine in the THP-1 cells which were in much larger vesicles, suggesting the behaviour in THP-1 cells could just be a result of the secondary cell line rather than a cross cell-type effect. The large number of vesicles in the PBMCs labelled with CCL2 Ala^{-1}-alk-H suggests the BODIPY was localised in endosomes which correlates with the previous results found in migration experiments and flow cytometry. In WT-alk-H treated PBMCs, a handful of vesicles are present in this image, again, showing

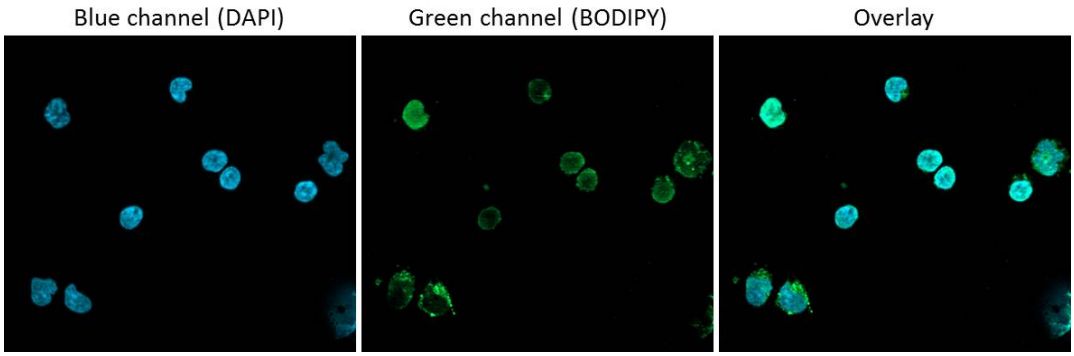

(a) PBMCs treated with CCL2 Ala^{-1}-alk-H.

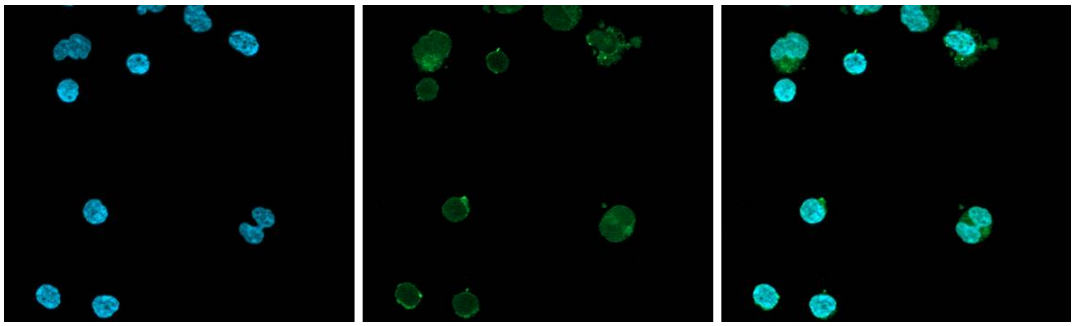

(b) PBMCs treated with WT-alk-H.

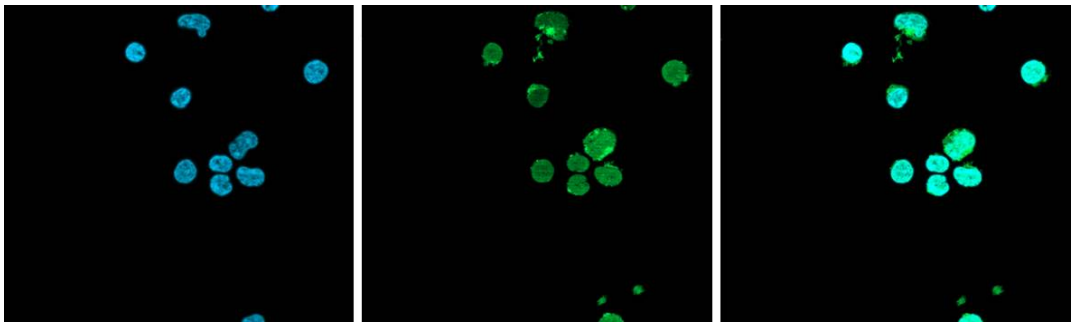

(c) PBMCs treated with P8A-alk-H.

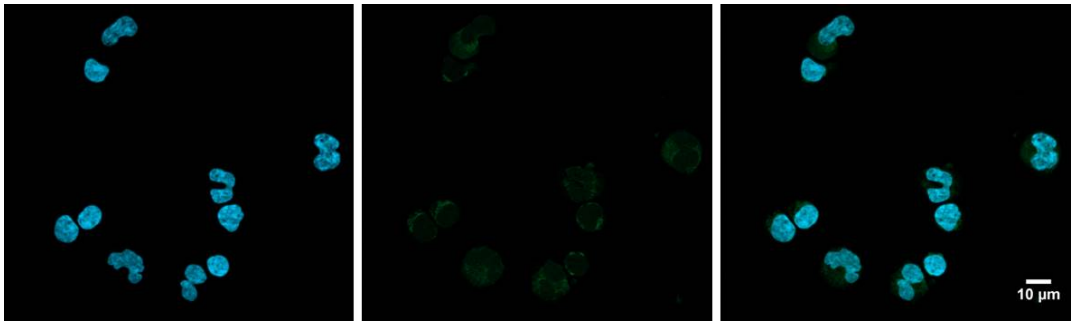

(d) Unlabelled PBMCs.

Figure 5.34: Fluorescence images of fixed PBMCs treated with alkyl-linked CCL2 conjugates for 2 h. The majority of PBMCs internalised the conjugates and the alkyl-linked conjugates appeared to localise within vesicles, similar to the behaviour observed in THP-1 cells. DAPI: blue, CCL2-BODIPY: green. Green channel exposure time: 1000 ms, blue channel exposure time: 120 ms. CCL2 conjugates used at 200 nM.

the conjugate is internalised by the cell and the fluorophore remains in the endosome or lysosome. P8A-alk-H exhibited a wider extent of labelling compared to WT-alk-H, with many vesicles containing the fluorophore present in the cytoplasm.

The disulfide-linked CCL2 conjugates exhibited the greatest extent of labelling (Figure 5.35) of the PBMCs. Interestingly, P8A-SS-H was not particularly effective at labelling THP-1 cells as determined by fluorescence microscopy but this conjugate was more easily visualised in PBMCs. Once again, the hydrophilic fluorophore labelled vesicles indicating the reduced conjugate could not escape endosomes and in some cases a degree of polarisation can be observed in the cells (Larger images for P8A-SS-H and P8A-SS-L are shown in Figure 5.36). The action of P8A-SS-L on the PBMCs was similar to that of the THP-1 cells: a diffuse distribution of fluorescence can be observed indicating the reduced lipophilic fluorophore can escape endosomes. Some of the PBMCs are more polarised than others suggesting a bias exists for how the lipophilic fluorophore distributes across the cell and the fluorescence intensity is still qualitatively high despite the diluting effect of diffusion of the fluorophore. This diluting effect suggests that the fluorophore concentration is being maintained in the cytoplasm by further internalisation of P8A-SS-L and subsequent endosomal escape.

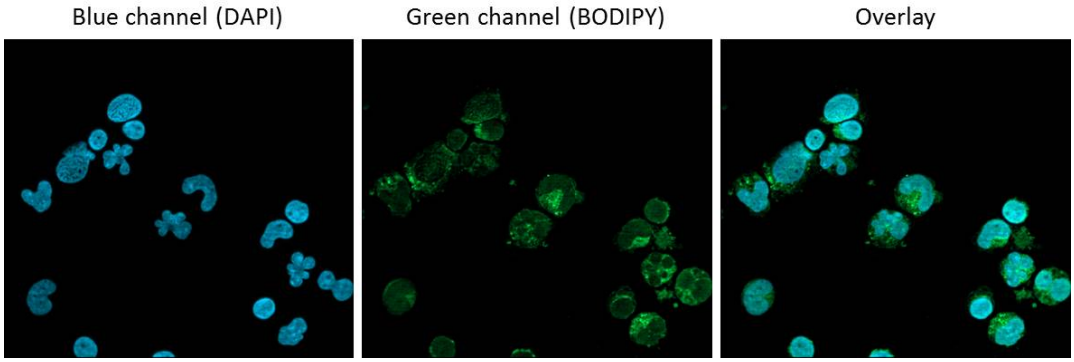

(a) PBMCs treated with P8A-SS-H.

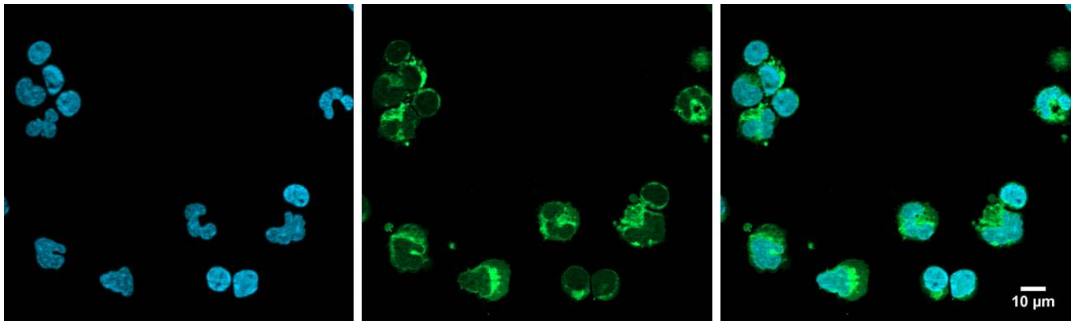

(b) PBMCs treated with P8A-SS-L.

Figure 5.35: Fluorescence images of fixed PBMCs treated with disulfide-linked CCL2 conjugates for 2 h. The lipophilic fluorophore is thoroughly diffused across the cell, again suggesting endosomal escape into the cytoplasm. This behaviour supports evidence for extracellular leaching into $CCR2^{-}$ cells in the flow cytometry experiments. DAPI: blue, CCL2-BODIPY: green. Green channel exposure time: 1000 ms, blue channel exposure time: 120 ms. CCL2 conjugates used at 200 nM.

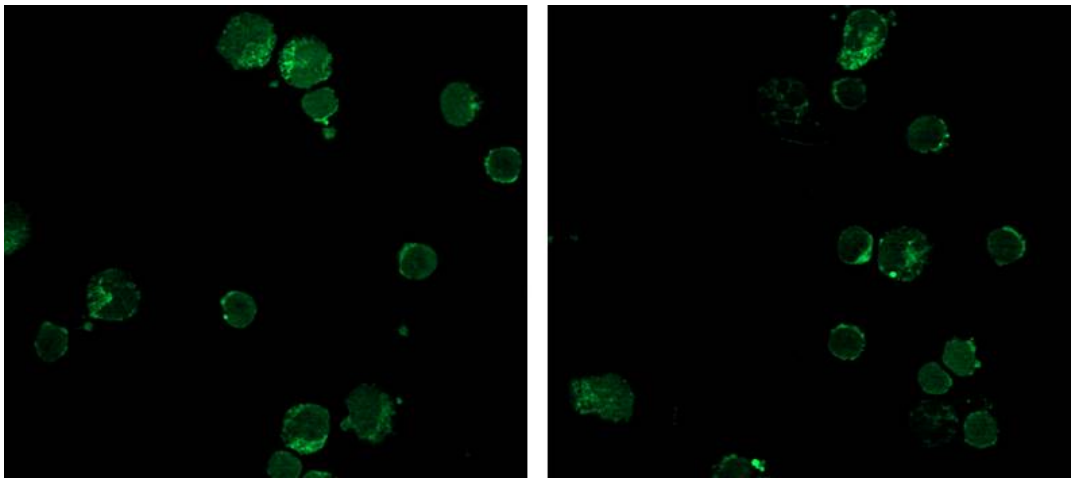

(a) BODIPY channel of PBMCs treated with P8A-SS-H.

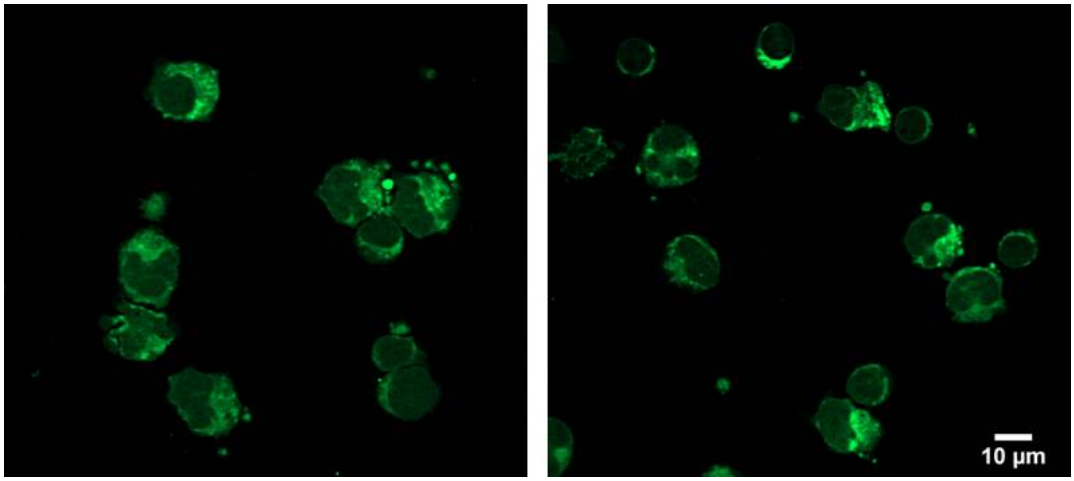

(b) BODIPY channel of PBMCs treated with P8A-SS-L.

Figure 5.36: Comparison of fluorescence images of fixed PBMCs treated with disulfide-linked CCL2 conjugates for 2 h. The P8A-SS-L fluorophore appears to have a more diffuse distribution across the cells than the P8A-SS-H fluorophore. Exposure time: 1000 ms. CCL2 conjugates used at 200 nM.

5.3 Conclusion

This chapter successfully characterised the CCL2 conjugates across a range of experiments and through the use of both THP-1 cell lines and PBMCs. Initial assay development of the Boyden transwell chemotaxis assay allowed experiments to be performed in a high-throughput manner which was essential to gain the results obtained. The use of fixed volume flow cytometry on the BD Biosystems Attune resulted in attainment of a broader range of data from a single chemotaxis assay which decreased experiment time and also increased the consistency of the number of migrated cells. The migration data could be determined simultaneously to the fluorescence intensity of cells which allowed chemotactic function and chemokine internalisation to be coincidentally measured. The three CCL2 variants, CCL2 Ala^{-1}-alk-H, WT-alk-H and P8A-alk-H, exhibited chemotactic maxima which correlated with literature precedent. P8A-alk-H was slightly more potent than WT-alk-H, however, this could have been due to purity of the starting protein rather than as a result of the amino acid substitution. Interestingly, measurement of the fluorescence intensity of migrated cells revealed a state of equilibria at concentrations above the chemotactic maxima in both P8A-alk-H and WT-alk-H. This equilibria demonstrated that the fluorescence did not increase with concentration above the chemotactic maxima, suggesting that the fluorophore was being degraded by lysosomes at the same rate as internalisation of new chemokine. The lower affinity CCL2 Ala^{-1}-alk-H conjugate did not exhibit this same fluorescence steady state, however, some evidence for this was inconsistently observed at higher concentrations. The chemotaxis and internalisation of all the CCL2 conjugates was shown to be CCR2-dependent *via* two distinct inhibitory mechanisms. The small molecule CCR2 antagonist INCB 3284 exhibited a clear dose-dependent inhibitory effect on all CCL2 conjugates, both in terms of chemotaxis and fluorescence internalisation. Similarly, a high dose incubation of recombinant human CCL2 also resulted in inhibition of chemotaxis towards the CCL2 conjugates as a result of surface CCR2 depletion. Interestingly, the fluorescence intensities of cells were not affected by the high dose CCL2 pre-incubation most likely due to the heterogeneous population of

cells created followed by a positive selection of cells still high in surface CCR2 during the chemotaxis assay. This CCR2 dependency was also exemplified in chemotaxis assays with the lymphocytic cell line, jurkats, whereby cessation of chemotaxis was observed. Further evidence for the fluorescence steady state was produced in timecourse incubation experiments highlighting a steady state after 2 hours. The fluorescence properties in the transwell assay and in response to inhibitors could be modulated with differing physicochemical properties of the conjugate. For example, P8A-SS-L did not exhibit a steady state in fluorescence and was also not affected by INCB 3284 inhibition, most likely as a result of the disulfide reduction followed by endosomal escape of the very lipophilic fluorophore.

The selectivity for CCR2 by the CCL2 conjugates was also demonstrated in primary human PBMCs, both in monocyte and lymphocyte sub-populations. The only outlier was again P8A-SS-L which exhibited uptake in CCR2-negative cells, however, as directed by earlier chemotaxis experiments this was probably due to leaching of the reduced fluorophore into neighbouring cells by passive diffusion. The other CCL2 conjugates were selective for CCR2-positive cells resulting in labelling of disease-associated monocyte subsets such as classical and intermediate but very little uptake in non-classical monocytes. In the lymphocytes, the majority of lymphocytes were not labelled (due to no CCR2 expression) and so labelled cells included: NKT cells and subsets of NK cells and T cells (presumably memory effector T cells) which correlated with CCR2 expression. Finally, fluorescence microscopy in both THP-1 cells and PBMCs revealed the fluorescent chemokines localised inside the cell, outside the nucleus and generally within vesicles. Again, the P8A-SS-L conjugate was distinct from the other conjugates, the fluorescence was much more diffuse across the cell suggesting the fluorophore was localising in lipophilic microenvironments in the cytoplasm or membrane structures.

Chapter 6

Conclusion

This project aimed to investigate the potential for using CCL2 as a method for targeting monocytes and whether any monocyte subset preference could be achieved. The strategy to answer this question was to utilise fluorescent conjugates of CCL2 in an effort to characterise the system, with a longer term goal to translate these finding towards novel therapeutics. Chapter 3 detailed the synthesis of novel BODIPY azide conjugates whereby the lipophilicity of the fluorescent core was modified to give distinct preferences for microenvironments within the cell. This was combined with varying the linker in the form of a cleavable disulfide bond or a non-cleavable alkyl linker between the fluorophore and the azide group. The project then progressed onto synthesis of a novel FRET pair separated by a disulfide bond which after optimisation was synthesised with the lipophilic BODIPY included as the liberating fluorophore. Synthetic constraints prevented a hydrophilic BODIPY from being installed on the FRET pair due to difficulty in forming the disulfonate in combination with a thiol. The successfully synthesised FRET pair gave a clear FRET signal from the BODIPY donor to the rhodamine acceptor, treatment with TCEP led to cessation of the energy transfer confirming the on/off behaviour of the system in response to reducing agents. At this stage, a potential issue was observed in the photophysical behaviour of the FRET pair involving fluorescence quenching in aqueous media. Further experiments confirmed this behaviour was due to aggregation of the FRET pair leading to auto-quenching and loss of fluorescence.

Chapter 4 then aimed to conjugate the five compounds synthesised in the previous chapter to three CCL2 variants: WT-CCL2, P8A-CCL2 and CCL2 Ala^{-1}. The 'alk-H' fluorophore was the most successful in terms of ability to conjugate, resulting in facile CuAAC conjugations with all three CCL2 variants. The reaction conditions were modified for the 'alk-L' fluorophore to include DMSO as a co-solvent which was necessary to facilitate solubility. Unfortunately, issues with WT-CCL2 were present resulting in only the WT-alk-H conjugate being successfully formed and failure to form any of the other fluorophore conjugates. This could have been due to the lower purity of WT-CCL2 preventing reaction completion in the more complex reactions involving DMSO and the disulfide-linked fluorophores. With both P8A-CCL2 and CCL2 Ala^{-1}, the reaction conditions were modified to include DMSO as a co-solvent which successfully allowed the other fluorophores to be conjugated to these variants. This is a good example of a reaction involving very lipophilic compounds and a protein without losing biological function which highlights the versatility of CCL2. However, it was later revealed that inclusion of sodium ascorbate in reactions containing DMSO led to loss of CCL2 function, likely due to native disulfide reduction followed by denaturation. The internal disulfides of CCL2 appear to anchor the tertiary structure such that it can re-fold correctly after DMSO denaturation, it is therefore very important to maintain these bonds. Sodium ascorbate mitigated disulfide reduction was therefore avoided through the use of copper (I) salts and the exclusion of oxygen *via* an Atmosbag, this was performed on P8A-CCL2 resulting in successful formation of P8A-SS-L and P8A-SS-H and also the FRET pair formation on CCL2 Ala^{-1}. This issue of sodium ascorbate reducing disulfides is a neglected area in the literature and highlights an issue with using these conditions in protein CuAAC conjugations. For example, it is possible this phenomenon is occurring in other conjugates in the literature but investigators may be unaware, leading to reaction failure due to the conditions rather than some intrinsic reaction difficulty.

In relation to the literature, CCL2-mCherry and CCL2-SA1 were successful bis-functional proteins however the protein fusion limits the scope of these systems to proteins. The inclusion of an extra conjugation step in this project broadens the scope of potential conjugates

which could be explored and the nature of CuAAC conjugations means that only minimal alterations to molecules are needed. For example, in the case of the PPTase system, it is unclear whether larger conjugates (such as oligonucleotides, nanoparticles or sugars) could interfere with the enzymatic reaction or whether the inclusion of coenzyme A is feasible.[7] The use of CuAAC requires only an azide to be installed on the conjugate and the azide can be alkyl or aryl in nature which broadens the scope of the reaction to oligonucleotides, nanoparticles, sugars, lipids or virtually any conceivable molecule. Clearly, as this project demonstrates, the reaction is not perfect and care must be taken when designing these systems but the problems encountered in this project could be optimised.

The CCL2 conjugates were thoroughly characterised in Chapter 5 which identified P8A-CCL2 as the most active chemokine, followed by WT-CCL2 and finally CCL2 Ala^{-1}. This behaviour validated reports of these systems in the literature and also gave evidence that the chemokines were functioning correctly. The combination of the chemotaxis experiment with flow cytometry enabled both migration and fluorescence internalisation to be assessed in the same experiment which was not done in the CCL2-mCherry or the chemokine PPTase projects.[5,7] This allowed the chemotactic responses of the cells to be correlated with fluorescence internalisation which resulted in the detection of a fluorescence steady state at concentrations higher than the chemotactic maxima. The CCR2-dependency of this behaviour was also determined across all three CCL2 variants using two distinct inhibitory mechanisms which presented some interesting results. When CCR2 was antagonised using INCB 3284, both the migration and fluorescence internalisation were inhibited in all variants, however, when surface CCR2 was depleted using both recombinant human CCL2 and the unlabelled synthetic variants, only migration was inhibited. This was most likely due to production of a heterogeneous CCR2-presenting population of THP-1 cells and a positive selection of cells high in surface CCR2 through the transwell membrane. The CCR2 antagonist, on the other hand, likely resulted in a homogeneous population of CCR2-inhibitor complexes and so any migrated cells were still inhibited by bound INCB 3284 thus the fluorescence remained low. Jurkat cells lacking in CCR2 were also refractory to WT-alk-H recruitment but were

chemotactic towards CXCL12, suggesting that CCR2 was necessary for migration in these assays.

Similar experiments with the other P8A-CCL2 and CCL2 Ala^{-1} conjugates highlighted the issue with using sodium ascorbate in combination with DMSO in the CuAAC conjugations as these compounds all performed poorly in these experiments. This meant that only the P8A-SS-L and P8A-SS-H had conjugated successfully to produce functional CCL2, however, this was only due to reaction conditions and not an intrinsic property of CCL2 Ala^{-1} or the lipophilic BODIPY azide **8**. It was at this point that the effects of the disulfide linker in combination with a lipophilic leaving group were apparent as the P8A-SS-L conjugate exhibited a greatly increasing MFI at increasing concentrations relative to other conjugates which all attained a maximum. This suggestion of endosomal escape was further evidenced by the MFI of P8A-SS-L being of a similar magnitude whether inhibited by INCB 3284 or not. More evidence of P8A-SS-L endosomal escape was provided in fluorescence microscopy experiments in both THP-1 cells and PBMCs.

The final aims of the project were then achieved *via* monoclonal antibody labelling in flow cytometry. PBMCs were obtained from human donors and four of these conjugates demonstrated selectivity for CCR2-positive cells, with the exception of P8A-SS-L, however, considering the suggestion for endosomal escape from the cell line experiments this was likely due to secondary-leaching. Monocyte subsets were separated and a preference for classical monocytes was observed, followed by intermediate monocytes and only some uptake by the non-classical monocytes. This also correlated closely with CCR2 expression and a relationship between increased MFI and decreased surface CCR2 was also observed in these experiments suggesting the conjugates were depleting the receptor from the surface of the cells. Similar behaviour in lymphocytes was observed whereby conjugates were CCR2 selective and labelled subsets of T cells, NK cells and NKT cells. In terms of percentage of each population, the NKT cells were preferentially selected by the CCL2 conjugates due to high CCR2 expression. However, uptake was observed in all three populations due to CCR2 expressing subsets of both NK cells and T cells, though this was in a very small minority

of these populations. In terms of the suitability of CCL2 variants as a monocyte-specific delivery vehicle, the consensus of data suggests a strong preference for the classical and intermediate monocytes which are the intentional targets of this project. Whilst some uptake occurs in cells outside this target (for example, lymphocyte subsets), this is a minority of cells and it is also an expected effect of using the CCL2-CCR2 pathway which can be predicted. This means that uptake of the CCL2 conjugates will likely occur in all cells which express functional CCR2 (and potentially related chemokine scavengers such as D6/DARC).

6.1 Future Work

This project was able to achieve the majority of the goals which were established in the aims section and promising results were obtained for this initial proof of concept to identify the potential for CCL2 conjugates to be a monocyte-subset specific delivery vehicle. This section will now detail potential routes to progress the project further towards the longer term goals of monocyte specific therapeutics. Some evidence for endosomal escape of P8A-SS-L was observed, to confirm this behaviour, endosomal or lysosomal markers (such as EEA-1 or LAMP-1) could be used in fluorescence microscopy to colocalise these signals with the hydrophilic fluorophores and a lower colocalisation should be apparent with P8A-SS-L. Another option would be to inhibit the action of dynamin through the use of the well known endocytosis inhibitor dynasore. Re-development of the CCL2 FRET system would be complementary to these experiments as loss of FRET due to disulfide reduction provides more evidence that the fluorophores are separated from the parent protein conjugate. These imaging experiments could be further progressed through incorporating this into a live imaging system to remove any effects of fixation and also monitor uptake of the chemokines in real time. An interesting imaging experiment would utilise the 3D chemotaxis assays available from IBIDI, these involve formation of a collagen matrix which hosts the cells and a chemotactic gradient can be applied across the gel. This then allows imaging of the cells which would internalise the fluorescent chemokine and also allow observation of chemotactic migration through a medium which better simulates the *in vivo* environment.

To ascertain whether the uptake of P8A-SS-L was in CCR2-negative cells due to leaching, the INCB 3284 antagonist could be used to prevent primary uptake and therefore reduce leaching effects. Further characterisation of cell-type uptake would also be beneficial, for example, identification of the CCR2-positive populations in the lymphocyte subsets. Gating of the PBMC population to MDSCs would offer further clinical relevance to this project, broadening the scope of the CCL2 conjugates to cancer.

Finally, the characterisation of the chemokines would translate into the development of monocyte targeted therapeutics in an effort to address the issues with treatment of diseases in this area. The variable phenotypes of monocytes mean that systemic inhibition or killing of these cells has not generally been effective. Using the CCL2 conjugates to select the monocyte subsets closely related to a disease would be the optimal route, therefore conjugating small molecule therapeutics to CCL2 is a clear pathway for development. This would be guided by the findings generated in this project in terms of the need for both a disulfide linker and that the therapeutic would need to be sufficiently lipophillic in order to reach the cytoplasm where the majority of therapeutics operate. The lipophilicity would need to be carefully modulated depending on the disease due to the leaching effect observed with P8A-SS-L, this would be problematic in treatment of delocalised monocytes in fibrosis for example, however, this effect could be useful when targeting monocytes or macrophages in the treatment of solid tumours. Evidently, the scope for future work is varied and the research would benefit from performing the experiments outlined at the beginning of this section first before moving onto the applications of the CCL2 conjugates towards therapeutic delivery.

Chapter 7

References

Bibliography

[1] Pease, J. and Horuk, R. Chemokine receptor antagonists. *J. Med. Chem.*, **55** (22):9363–9392, 2012.

[2] Gordon, S. and Taylor, P. R. Monocyte and macrophage heterogeneity. *Nat. Rev. Immunol.*, **5** (12):953–64, 2005.

[3] Friedman, S. L. Mechanisms of hepatic fibrogenesis. *Gastroenterology*, **134** (6):1655–69, 2008.

[4] Schuppan, D. and Kim, Y. O. Evolving therapies for liver fibrosis. *J. Clin. Invest.*, **123** (5):1887–1901, 2013.

[5] Volpe, S., Cameroni, E., Moepps, B., Thelen, S., Apuzzo, T. *et al.* CCR2 Acts as Scavenger for CCL2 during Monocyte Chemotaxis. *PLoS One*, **7** (5):1–10, 2012.

[6] McIntosh, L. M., Barnes, J. L., Barnes, V. L., and McDonald, J. R. Selective CCR2-targeted macrophage depletion ameliorates experimental mesangioproliferative glomerulonephritis. *Clin. Exp. Immunol.*, **155** (2):295–303, 2009.

[7] Kawamura, T., Stephens, B., Qin, L., Yin, X., Dores, M. R. *et al.* A general method for site specific fluorescent labeling of recombinant chemokines. *PLoS One*, **9** (1):1–10, 2014.

[8] Ziegler-heitbrock, L., Ancuta, P., Crowe, S., Dalod, M., Grau, V. *et al.* Nomenclature of monocytes and dendritic cells in blood. *Blood*, **116** (16):5–7, 2016.

[9] Appleby, L. J., Nausch, N., Midzi, N., Mduluza, T., Allen, J. E. *et al.* Sources of heterogeneity in human monocyte subsets. *Immunol. Lett.*, **152** (1):32–41, 2013.

[10] Yang, J., Zhang, L., Yu, C., Yang, X.-F., and Wang, H. Monocyte and macrophage differentiation: circulation inflammatory monocyte as biomarker for inflammatory diseases. *Biomark. Res.*, **2** (1):1–9, 2014.

[11] Shi, C. and Pamer, E. G. Monocyte recruitment during infection and inflammation. *Nat. Rev. Immunol.*, **11** (11):762–774, 2011.

[12] Nathan, C. Neutrophils and immunity: challenges and opportunities. *Nat. Rev. Immunol.*, **6** (3):173–182, 2006.

[13] Auffray, C., Sieweke, M. H., and Geissmann, F. Blood monocytes: development, heterogeneity, and relationship with dendritic cells. *Annu. Rev. Immunol.*, **27**:669–92, 2009.

[14] Dai, X., Ryan, G. R., Hapel, a. J., Dominguez, M. G., Russell, R. G. *et al.* Targeted disruption of the mouse CSF-1 receptor gene results in osteopetrosis, mononuclear phagocyte deficiency, increased primititive progenitor cell frequencies and reproductive defects. *Blood*, **99** (1):111–120, 2002.

[15] Cecchini, M. G., Dominguez, M. G., Mocci, S., Wetterwald, A., Felix, R. *et al.* Role of colony stimulating factor-1 in the establishment and regulation of tissue macrophages during postnatal development of the mouse. *Development*, **120** (6):1357–72, 1994.

[16] Fogg D, Sibon C, Miled C, Jung S, Aucouturier, Dan R. Littman, Ana Cumano, F. G. A clonogenic bone marrow progenitor specific for macrophages and dendritic cells. *Science (80-.).*, **311** (March):83–88, 2006.

[17] Klappacher, G. W., Lunyak, V. V., Sykes, D. B., Sawka-Verhelle, D., Sage, J. *et al.* An induced Ets repressor complex regulates growth arrest during terminal macrophage differentiation. *Cell*, **109** (2):169–180, 2002.

[18] Pixley, F. J., Stanley, E. R., Stanley, E., Bartelmez, S., et Al. *et al.* CSF-1 regulation of the wandering macrophage: complexity in action. *Trends Cell Biol.*, **14** (11):628–38, 2004.

[19] Yona, S., Kim, K. W., Wolf, Y., Mildner, A., Varol, D. *et al.* Fate Mapping Reveals Origins and Dynamics of Monocytes and Tissue Macrophages under Homeostasis. *Immunity*, **38** (1):79–91, 2013.

[20] Hashimoto, D., Chow, A., Noizat, C., Teo, P., Beasley, M. B. *et al.* Tissue-resident macrophages self-maintain locally throughout adult life with minimal contribution from circulating monocytes. *Immunity*, **38** (4):792–804, 2013.

[21] Ginhoux, F. and Jung, S. Monocytes and macrophages: developmental pathways and tissue homeostasis TL - 14. *Nat. Rev. Immunol.*, **14 VN - r** (6):392–404, 2014.

[22] Nguyen, K. D., Fentress, Sarah J. Qiu, Y., Yun, K., Cox, J. S., and Chawla, A. Circadian gene Bmal1 regulates diurnal oscillations of Ly6Chi inflammatory monocytes. *Science (80-.).*, **341**:6153 – 6168, 2013.

[23] Serbina, N. V. and Pamer, E. G. Monocyte emigration from bone marrow during bacterial infection requires signals mediated by chemokine receptor CCR2. *Nat. Immunol.*, **7** (3):311–7, 2006.

[24] Jakubzick, C., Gautier, E. L., Gibbings, S. L., Sojka, D. K., Schlitzer, A. *et al.* Minimal differentiation of classical monocytes as they survey steady-state tissues and transport antigen to lymph nodes. *Immunity*, **39** (3):599–610, 2013.

[25] Varol, C., Vallon-Eberhard, A., Elinav, E., Aychek, T., Shapira, Y. *et al.* Intestinal Lamina Propria Dendritic Cell Subsets Have Different Origin and Functions. *Immunity*, **31** (3):502–512, 2009.

[26] Bogunovic, M., Ginhoux, F., Helft, J., Shang, L., Hashimoto, D. *et al.* Origin of the Lamina Propria Dendritic Cell Network. *Immunity*, **31** (3):513–525, 2009.

[27] Tamoutounour, S., Henri, S., Lelouard, H., de Bovis, B., de Haar, C. *et al.* CD64 distinguishes macrophages from dendritic cells in the gut and reveals the Th1-inducing role of mesenteric lymph node macrophages during colitis. *Eur. J. Immunol.*, **42** (12):3150–3166, 2012.

[28] Ludovic Arnold,1 Adeline Henry,2 Françoise Poron,1 Yasmine Baba-Amer, ., Nico van Rooijen,3 Anne Plonquet,4 Romain K. Gherardi, ., and Bénédicte Chazaud1, Arnold, L., Henry, A. *et al.* Inflammatory monocytes recruited after skeletal muscle injury switch into antiinflammatory macrophages to support myogenesis. *J Exp Med*, **204** (5):1057–1069, 2007.

[29] Lessner, S. M., Prado, H. L., Waller, E. K., and Galis, Z. S. Atherosclerotic lesions grow through recruitment and proliferation of circulating monocytes in a murine model. *Am. J. Pathol.*, **160** (6):2145–55, 2002.

[30] Swirski, F. K., Pittet, M. J., Kircher, M. F., Aikawa, E., Jaffer, F. A. *et al.* Monocyte accumulation in mouse atherogenesis is progressive and proportional to extent of disease. *Proc. Natl. Acad. Sci. U. S. A.*, **103** (27):10340–5, 2006.

[31] Landsman, L., Liat, B. O., Zernecke, A., Kim, K. W., Krauthgamer, R. *et al.* CX3CR1 is required for monocyte homeostasis and atherogenesis by promoting cell survival. *Blood*, **113** (4):963–972, 2009.

[32] Hoeffel, G., Wang, Y., Greter, M., See, P., Teo, P. *et al.* Adult Langerhans cells derive predominantly from embryonic fetal liver monocytes with a minor contribution of yolk sac-derived macrophages. *J. Exp. Med.*, **209** (6):1167–81, 2012.

[33] Schulz, C., Gomez Perdiguero, E., Chorro, L., Szabo-Rogers, H., Cagnard, N. *et al.* A lineage of myeloid cells independent of Myb and hematopoietic stem cells. *Science*, **336** (6077):86–90, 2012.

[34] Mills, C. D. and Ley, K. M1 and M2 macrophages: The chicken and the egg of immunity. *J. Innate Immun.*, **6** (6):716–726, 2014.

[35] Mills, C. D., Kincaid, K., Alt, J. M., Heilman, M. J., and Hill, A. M. M-1/M-2 macrophages and the Th1/Th2 paradigm. *J. Immunol.*, **164** (12):6166–73, 2000.

[36] Mantovani, A., Sica, A., Sozzani, S., Allavena, P., Vecchi, A. *et al.* The chemokine system in diverse forms of macrophage activation and polarization. *Trends Immunol.*, **25** (12):677–686, 2004.

[37] Geissmann, F., Gordon, S., Hume, D. A., Mowat, A. M., and Randolph, G. J. Unravelling mononuclear phagocyte heterogeneity. *Nat Rev Immunol*, **10** (6):453–460, 2010.

[38] Martinez, F. O. and Gordon, S. The M1 and M2 paradigm of macrophage activation: time for reassessment. *F1000Prime Rep.*, **6**:13, 2014.

[39] Murray, P. J., Allen, J. E., Biswas, S. K., Fisher, E. A., Gilroy, D. W. *et al.* Macrophage Activation and Polarization: Nomenclature and Experimental Guidelines. *Immunity*, **41** (1):14–20, 2014.

[40] Mantovani, A., Biswas, S. K., Galdiero, M. R., Sica, A., and Locati, M. Macrophage plasticity and polarization in tissue repair and remodelling. *J. Pathol.*, **229** (2):176–185, 2013.

[41] Wynn, T. A. FIBROTIC DISEASE AND THE TH 1/TH 2 PARADIGM. *Nat Rev Immunol*, **4** (8):583–594, 2009.

[42] Biswas, S. K. and Mantovani, A. Macrophage plasticity and interaction with lymphocyte subsets : cancer as a paradigm. *Nat. Immunol.*, **11** (10):889–896, 2010.

[43] Roca, H., Varcos, Z. S., Sud, S., Craig, M. J., and Pienta, K. J. CCL2 and interleukin-6 promote survival of human CD11b+ peripheral blood mononuclear cells and induce M2-type macrophage polarization. *J. Biol. Chem.*, **284** (49):34342–34354, 2009.

[44] Nizet, V. and Johnson, R. S. Interdependence of hypoxic and innate immune responses. *Nat. Rev. Immunol.*, **9** (9):609–17, 2009.

[45] Corna, G., Campana, L., Pignatti, E., Castiglioni, A., Tagliafico, E. *et al.* Polarization dictates iron handling by inflammatory and alternatively activated macrophages. *Haematologica*, **95** (11):1814–1822, 2010.

[46] Gustafsson, C., Mjösberg, J., Matussek, A., Geffers, R., Matthiesen, L. *et al.* Gene expression profiling of human decidual macrophages: Evidence for immunosuppressive phenotype. *PLoS One*, **3** (4):1–9, 2008.

[47] Bellora, F., Castriconi, R., Dondero, A., Reggiardo, G., Moretta, L. *et al.* The interaction of human natural killer cells with either unpolarized or polarized macrophages results in different functional outcomes. *Proc. Natl. Acad. Sci. U. S. A.*, **107** (50):21659–21664, 2010.

[48] Friedman, S. Liver fibrosis – from bench to bedside. *J. Hepatol.*, **38**:38–53, 2003.

[49] Matsuoka, M. and Tsukamoto, H. Stimulation of hepatic lipocyter collagen production by Kupffer cell-derived Transforming Growth factor b: implication for a pathogenetic role in alcoholic liver fibrogenesis. *Hepatology*, **11** (4):599–605, 1989.

[50] Karlmark, K. R., Zimmermann, H. W., Roderburg, C., Gassler, N., Wasmuth, H. E. *et al.* The fractalkine receptor CX3CR1 protects against liver fibrosis by controlling differentiation and survival of infiltrating hepatic monocytes. *Hepatology*, **52** (5):1769–1782, 2010.

[51] Olefsky, J. M. and Glass, C. K. *Macrophages, inflammation, and insulin resistance.*, volume 72. 2010.

[52] Sica, A., Schioppa, T., Mantovani, A., and Allavena, P. Tumour-associated macrophages are a distinct M2 polarised population promoting tumour progression: Potential targets of anti-cancer therapy. *Eur. J. Cancer*, **42** (6):717–727, 2006.

[53] Balkwill, F., Charles, K. A., and Mantovani, A. Smoldering and polarized inflammation in the initiation and promotion of malignant disease. *Cancer Cell*, **7** (3):211–217, 2005.

[54] Balkwill, F. Cancer and the chemokine network. *Nat. Rev. Cancer*, **4** (7):540–550, 2004.

[55] Dong, Z., Yoneda, J., Kumar, R., and Fidler, I. J. Angiostatin-mediated suppression of cancer metastases by primary neoplasms engineered to produce granulocyte/macrophage colony-stimulating factor. *J. Exp. Med.*, **188** (4):755–63, 1998.

[56] Coussens, L. M., Tinkle, C. L., Hanahan, D., and Werb, Z. MMP-9 supplied by bone marrow-derived cells contributes to skin carcinogenesis. *Cell*, **103** (3):481–490, 2000.

[57] Lin, E. Y., Li, J. F., Gnatovskiy, L., Deng, Y., Zhu, L. *et al.* Macrophages regulate the angiogenic switch in a mouse model of breast cancer. *Cancer Res.*, **66** (23):11238–11246, 2006.

[58] Sica, A., Erreni, M., Allavena, P., and Porta, C. Macrophage polarization in pathology. *Cell. Mol. Life Sci.*, **72** (21):4111–4126, 2015.

[59] Coussens, L. M., Zitvogel, L., and Palucka, A. K. Neutralizing tumor-promoting chronic inflammation: a magic bullet? *Science*, **339** (6117):286–91, 2013.

[60] Gabrilovich, D. and Nagaraj, S. Myeloid-derived suppressor cells as regulators of the immune system. *Nat. Rev. Immunol.*, **9** (March):162–174, 2009.

[61] Youn, J.-I., Nagaraj, S., Collazo, M., and Gabrilovich, D. I. Subsets of Myeloid-Derived Suppressor Cells in Tumor-Bearing Mice. *J. Immunol.*, **181** (8):5791–5802, 2008.

[62] Ochoa, A. C., Zea, A. H., Hernandez, C., and Rodriguez, P. C. Arginase, prostaglandins, and myeloid-derived suppressor cells in renal cell carcinoma. *Clin. Cancer Res.*, **13** (2 II):721–726, 2007.

[63] Almand, B., Clark, J. I., Nikitina, E., van Beynen, J., English, N. R. *et al.* Increased production of immature myeloid cells in cancer patients: a mechanism of immunosuppression in cancer. *J. Immunol.*, **166** (1):678–89, 2001.

[64] Lesokhin, A. M., Hohl, T. M., Kitano, S., Cortez, C., Hirschhorn-cymerman, D. *et al.* Monocytic CCR2+ Myeloid-Derived Suppressor Cells Promote Immune Escape by Limiting Activated CD8 T-cell In fi ltration into the Tumor Microenvironment. *Cancer Res.*, **72** (4):876–886, 2012.

[65] Goni, O., Alcaide, P., and Fresno, M. Immunosuppression during acute Trypanosoma cruzi infection: involvement of Ly6G (Gr1(+))CD11b(+) immature myeloid suppressor cells. *Int. Immunol.*, **14** (10):1125–1134, 2002.

[66] Delano, M. J., Scumpia, P. O., Weinstein, J. S., Coco, D., Nagaraj, S. *et al.* MyD88-dependent expansion of an immature GR-1(+)CD11b(+) population induces T cell suppression and Th2 polarization in sepsis. *J. Exp. Med.*, **204** (6):1463–1474, 2007.

[67] Diaz-Montero, C. M., Salem, M. L., Nishimura, M. I., Garrett-Mayer, E., Cole, D. J. *et al.* Increased circulating myeloid-derived suppressor cells correlate with clinical cancer stage, metastatic tumor burden, and doxorubicin-cyclophosphamide chemotherapy. *Cancer Immunol. Immunother.*, **58** (1):49–59, 2009.

[68] Bronte, V. and Zanovello, P. Regulation of immune responses by L-arginine metabolism. *Nat. Rev. Immunol.*, **5** (8):641–654, 2005.

[69] Rodriguez, P. C., Quiceno, D. G., and Ochoa, A. C. L-arginine availability regulates T-lymphocyte cell-cycle progression. *Blood*, **109** (4):1568–1574, 2007.

[70] Rivoltini, L., Carrabba, M., Huber, V., Castelli, C., Novellino, L. *et al.* Immunity to cancer: attack and escape in T lymphocyte-tumor cell interaction. *Immunol. Rev.*, **188** (1):97–113, 2002.

[71] Talmadge, J. E., Hood, K. C., Zobel, L. C., Shafer, L. R., Coles, M. *et al.* Chemoprevention by cyclooxygenase-2 inhibition reduces immature myeloid suppressor cell expansion. *Int. Immunopharmacol.*, **7** (2):140–151, 2007.

[72] Serafini, P., Meckel, K., Kelso, M., Noonan, K., Califano, J. *et al.* Phosphodiesterase-5 inhibition augments endogenous antitumor immunity by reducing myeloid-derived suppressor cell function. *J. Exp. Med.*, **203** (12):2691–702, 2006.

[73] Suzuki, E., Kapoor, V., Jassar, A. S., Kaiser, L. R., and Albelda, S. M. Gemcitabine selectively eliminates splenic Gr-1+/CD11b + myeloid suppressor cells in tumor-bearing animals and enhances antitumor immune activity. *Clin. Cancer Res.*, **11** (18):6713–6721, 2005.

[74] Stansfield, B. K. and Ingram, D. A. Clinical significance of monocyte heterogeneity. *Clin. Transl. Med.*, **4** (1):5, 2015.

[75] Passlick, B., Flieger, D., and Ziegler-Heitbrock, H. W. Identification and characterization of a novel monocyte subpopulation in human peripheral blood. *Blood*, **74** (7):2527–34, 1989.

[76] Grage-Griebenow, E., Flad, H., and Ernst, M. Heterogeneity of human peripheral blood monocyte subsets. *J. Leukoc. Biol.*, **69** (1):11–20, 2001.

[77] Ziegler-Heitbrock, H. Heterogeneity of human blood monocytes: the CD14+CD16+ subpopulation. *Immunol. Today*, **17** (9):424–428, 1996.

[78] Weiner, L. M., Li, W., Holmes, M., Catalano, R. B., Dovnarsky, M. *et al.* Phase I trial of recombinant macrophage colony-stimulating factor and recombinant γ-interferon: Toxicity, monocytosis, and clinical effects. *Cancer Res.*, **54** (15):4084–4090, 1994.

[79] Ancuta, P., Liu, K.-Y., Misra, V., Wacleche, V. S., Gosselin, A. *et al.* Transcriptional profiling reveals developmental relationship and distinct biological functions of CD16+ and CD16- monocyte subsets. *BMC Genomics*, **10**:403, 2009.

[80] Ancuta, P., Rao, R., Moses, A., Mehle, A., Shaw, S. K. *et al.* Fractalkine preferentially mediates arrest and migration of CD16+ monocytes. *J. Exp. Med.*, **197** (12):1701–7, 2003.

[81] Wong, K. L., Tai, J. J.-Y., Wong, W.-C., Han, H., Sem, X. *et al.* Gene expression profiling reveals the defining features of the classical, intermediate, and nonclassical human monocyte subsets. *Blood*, **118** (5):e16–31, 2011.

[82] Cros, J., Cagnard, N., Woollard, K., Patey, N., Zhang, S. Y. *et al.* Human CD14dim Monocytes Patrol and Sense Nucleic Acids and Viruses via TLR7 and TLR8 Receptors. *Immunity*, **33** (3):375–386, 2010.

[83] Zawada, A. M., Rogacev, K. S., Schirmer, S. H., Sester, M., Böhm, M. *et al.* Monocyte heterogeneity in human cardiovascular disease. *Immunobiology*, **217** (12):1273–1284, 2012.

[84] Wong, K. L., Yeap, W. H., Tai, J. J. Y., Ong, S. M., Dang, T. M. *et al.* The three human monocyte subsets: Implications for health and disease. *Immunol. Res.*, **53** (1-3):41–57, 2012.

[85] Skrzeczyñska, J., Kobylarz, K., Hartwich, Z., Zembala, M., and Pryjma, J. CD14 +CD16 + monocytes in the course of sepsis in neonates and small children: Monitoring and functional studies. *Scand. J. Immunol.*, **55** (6):629–638, 2002.

[86] Castaño, D., García, L. F., and Rojas, M. Increased frequency and cell death of CD16+ monocytes with Mycobacterium tuberculosis infection. *Tuberculosis*, **91** (5):348–360, 2011.

[87] Zhang, J. Y., Zou, Z. S., Huang, A., Zhang, Z., Fu, J. L. *et al.* Hyper-activated pro-inflammatory CD16+ monocytes correlate with the severity of liver injury and fibrosis in patients with chronic hepatitis B. *PLoS One*, **6** (3), 2011.

[88] Rodríguez-Muñoz, Y., Martín-Vílchez, S., López-Rodríguez, R., Hernández-Bartolomé, a., Trapero-Marugán, M. *et al.* Peripheral blood monocyte subsets predict antiviral response in chronic hepatitis C. *Aliment. Pharmacol. Ther.*, **34** (8):960–71, 2011.

[89] Grip, O., Bredberg, A., Lindgren, S., and Henriksson, G. Increased subpopulations of CD16(+) and CD56(+) blood monocytes in patients with active Crohn's disease. *Inflamm. Bowel Dis.*, **13** (5):566–72, 2007.

[90] Rossol, M., Kraus, S., Pierer, M., Baerwald, C., and Wagner, U. The CD14 brightCD16+ monocyte subset is expanded in rheumatoid arthritis and promotes expansion of the Th17 cell population. *Arthritis Rheum.*, **64** (3):671–677, 2012.

[91] Kawanaka, N., Yamamura, M., Aita, T., Morita, Y., Okamoto, A. *et al.* CD14+,CD16+ blood monocytes and joint inflammation in rheumatoid arthritis. *Arthritis Rheum.*, **46** (10):2578–2586, 2002.

[92] Baeten, D., Boots, A. M. H., Steenbakkers, P. G. A., Elewaut, D., Bos, E. *et al.* Human cartilage gp-39+, CD16+monocytes in peripheral blood and synovium - Correlation with joint destruction in rheumatoid arthritis. *Arthritis Rheum.*, **43** (6):1233–1243, 2000.

[93] Dayyani, F., Belge, K.-U., Frankenberger, M., Mack, M., Berki, T. *et al.* Mechanism of glucocorticoid-induced depletion of human CD14+CD16+ monocytes. *J. Leukoc. Biol.*, **74** (1):33–9, 2003.

[94] Fingerle-Rowson, G., Angstwurm, M., Andreesen, R., and Ziegler-Heitbrock, H. W. Selective depletion of CD14+CD16+ monocytes by glucocorticoid therapy. *Clin. Exp. Immunol.*, **112**:501–506, 1998.

[95] Wahl, S. M., Allen, J. B., Welch, G. R., and Wong, H. L. Transforming growth factor-beta in synovial fluids modulates Fc gamma RII (CD16) expression on mononuclear phagocytes. *J. Immunol.*, **148** (2):485–90, 1992.

[96] Ziegler-Heitbrock, L. The CD14+ CD16+ blood monocytes: their role in infection and inflammation. *J. Leukoc. Biol.*, **81** (3):584–92, 2007.

[97] Tacke, F., Alvarez, D., Kaplan, T. J., Jakubzick, C., Spanbroek, R. *et al.* Monocyte subsets differentially employ CCR2, CCR5, and CX3CR1 to accumulate within atherosclerotic plaques. *J Clin Invest.*, **117** (1):185–194, 2007.

[98] Rothe, G., Gabriel, H., Kovacs, E., Klucken, J., Stöhr, J. *et al.* Peripheral Blood Mononuclear Phagocyte Subpopulations as Cellular Markers in Hypercholesterolemia. *Arterioscler. Thromb. Vasc. Biol.*, **16** (12):1437–1447, 1996.

[99] Zimmermann, H. W., Seidler, S., Nattermann, J., Gassler, N., Hellerbrand, C. *et al.* Functional contribution of elevated circulating and hepatic non-classical CD14+CD16+ monocytes to inflammation and human liver fibrosis. *PLoS One*, **5** (6):1–15, 2010.

[100] Klein, I., Klein, I., Cornejo, J. C., Cornejo, J. C., Polakos, N. K. *et al.* Kupffer cell heterogeneity: functional properties of bone marrow–derived and sessile hepatic macrophages. *Cell*, **110** (12):4077–4085, 2007.

[101] Karlmark, K. R., Weiskirchen, R., Zimmermann, H. W., Gassler, N., Ginhoux, F. *et al.* Hepatic recruitment of the inflammatory Gr1+ monocyte subset upon liver injury promotes hepatic fibrosis. *Hepatology*, **50** (1):261–274, 2009.

[102] Ramachandran, P., Pellicoro, A., Vernon, M. a., Boulter, L., Aucott, R. L. *et al.* Differential Ly-6C expression identifies the recruited macrophage phenotype, which orchestrates the regression of murine liver fibrosis. *Proc. Natl. Acad. Sci. U. S. A.*, **109** (46):E3186–95, 2012.

[103] Liaskou, E., Zimmermann, H. W., Li, K. K., Oo, Y. H., Suresh, S. *et al.* Monocyte subsets in human liver disease show distinct phenotypic and functional characteristics. *Hepatology*, **57** (1):385–398, 2013.

[104] Deshmane, S. L., Kremlev, S., Shohreh, A., and Sawaya, B. E. Monocyte Chemoattractant Protein-1 (MCP-1): An Overview. *J. Interf. Cytokine Res.*, **29** (6), 2009.

[105] Wu, V.-Y., Walz, D. A., and McCoy, L. E. Purification and Characterization of Human and Bovine Platelet Factor 4. *Prep. Biochem.*, **7** (6):479–493, 1977.

[106] Rollins, B. J. Chemokines. *Blood*, **90** (3):909–929, 1997.

[107] Baggiolini, M. and Loetscher, P. Chemokines in inflammation and immunity. *Trends Immunol.*, **21** (9):418–420, 2000.

[108] Clore, G. M. and Gronenborn, A. M. Three-dimensional structures of alpha and beta chemokines. *FASEB J.*, **9** (1):57–62, 1995.

[109] Clore, G. M., Appella, E., Yamada, M., Matsushima, K., and Gronenborn, a. M. Three-dimensional structure of interleukin 8 in solution. *Biochemistry*, **29** (7):1689–96, 1990.

[110] Handel, T. M. and Domaille Peter J. Heteronuclear (1H, 13C, 15N) NMR assignments and solution structure of the monocyte chemoattractant protein-1 (MCP-1) dimer. *Biochemistry*, **35** (21):6569–6584, 1996.

[111] Crown, S., Yu, Y., and Sweeney, M. Heterodimerization of CCR2 chemokines and regulation by glycosaminoglycan binding. *J. Biol. Chem.*, **281** (35):25438–25446, 2006.

[112] Proudfoot, A. E., Handel, T. M., Johnson, Z., Lau, E. K., LiWang, P. *et al.* Glycosaminoglycan binding and oligomerization are essential for the in vivo activity of certain chemokines. *Proc Natl Acad Sci U S A*, **100** (4):1885–1890, 2003.

[113] Paavola, C. D., Hemmerich, S., Grunberger, D., Polsky, I., Bloom, A. *et al.* Monomeric monocyte chemoattractant protein-1 (MCP-1) binds and activates the MCP-1 receptor CCR2B. *J. Biol. Chem.*, **273** (50):33157–33165, 1998.

[114] Neel, N. F., Schutyser, E., Sai, J., Fan, G.-H., and Richmond, A. Chemokine receptor internalization and intracellular trafficking. *Cytokine Growth Factor Rev.*, **16** (6):637–58, 2005.

[115] Allen, S. J., Crown, S. E., and Handel, T. M. Chemokine:Receptor Structure, Interactions, and Antagonism. *Annu. Rev. Immunol.*, **25** (1):787–820, 2007.

[116] Pierce, K. L., Premont, R. T., Lefkowitz, R. J., and Hughes, T. H. Seven-transmembrane receptors. *Nat. Rev.*, **3** (September):639–650, 2002.

[117] Reiter, E. and Lefkowitz, R. J. GRKs and β-arrestins: roles in receptor silencing, trafficking and signaling. *Trends Endocrinol. Metab.*, **17** (4):159–165, 2006.

[118] Goodman, O. B., Krupnick, J. G., Santini, F., Gurevich, V. V., Penn, R. B. *et al.* Beta-arrestin acts as a clathrin adaptor in endocytosis of the beta2-adrenergic receptor., 1996.

[119] Berchiche, Y. a., Pelletier, M.-e., and Heveker, N. Different Effects of the Different Natural CC Chemokine Receptor 2b Ligands on Arrestin recruitment, Gai Signaling, and Receptor Internalization. *Mol. Pharmacol.*, **79** (3):488–498, 2011.

[120] Mellado, M., Rodriguez-Frade, J. M., Manes, S., and Martinez-A, C. Chemokine signaling and functional responses: the role of receptor dimerization and TK pathway activation. *Annu. Rev. Immunol.*, **19**:397–421, 2001.

[121] Sharma, D. K., Choudhury, A., Singh, R. D., Wheatley, C. L., Marks, D. L. *et al.* Glycosphingolipids internalized via caveolar-related endocytosis rapidly merge with the clathrin pathway in early endosomes and form microdomains for recycling. *J. Biol. Chem.*, **278** (9):7564–7572, 2003.

[122] Andjelkovic, A. V., Song, L., Dzenko, K. A., Cong, H., and Pachter, J. S. Functional expression of CCR2 by human fetal astrocytes. *J. Neurosci. Res.*, **70** (2):219–231, 2002.

[123] Mellado, M., Rodriguez-Frade, J. M., Viila-Coro, A. J., Fernandez, S., Martin de Ana, A. *et al.* Chemokine receptor homo- or heterodimerization activates distinct signaling pathways. *EMBO J.*, **20** (10):2497–2507, 2001.

[124] Thelen, M. Dancing to the tune of chemokines. *Nat. Immunol.*, **2** (2):129–34, 2001.

[125] Mellado, M., Rodriguez-Frade, J. M., Aragay, A., del Real, G., Martin, A. M. *et al.* The chemokine monocyte chemotactic protein 1 triggers Janus kinase 2 activation and tyrosine phosphorylation of the CCR2B receptor. *J. Immunol.*, **161** (2):805–813, 1998.

[126] Overton, M. C. and Blumer, K. J. G-protein-coupled receptors function as oligomers in vivo. *Curr. Biol.*, **10** (6):341–344, 2000.

[127] Darbonne, W. C., Rice, G. C., Mohler, M. A., Apple, T., Hébert, C. A. *et al.* Red blood cells are a sink for interleukin 8, a leukocyte chemotaxin. *J. Clin. Invest.*, **88** (4):1362–1369, 1991.

[128] Hadley, T. J., Lu, Z. H., Wasniowska, K., Martin, A. W., Peiper, S. C. *et al.* Postcapillary venule endothelial cells in kidney express a multispecific chemokine receptor that is structurally and functionally identical to the erythroid isoform, which is the Duffy blood group antigen. *J. Clin. Invest.*, **94** (3):985–991, 1994.

[129] Hansell, C. A. H., Hurson, C. E., and Nibbs, R. J. B. DARC and D6: silent partners in chemokine regulation? *Immunol. Cell Biol.*, **89** (2):197–206, 2011.

[130] Middleton, J., Neil, S., Wintle, J., Clark-Lewis, I., Moore, H. *et al.* Transcytosis and surface presentation of IL-8 by venular endothelial cells. *Cell*, **91** (3):385–395, 1997.

[131] Zhao, Y., Mangalmurti, N. S., Xiong, Z., Prakash, B., Guo, F. *et al.* Duffy antigen receptor for chemokines mediates chemokine endocytosis through a macropinocytosis-like process in endothelial cells. *PLoS One*, **6** (12):e29624, 2011.

[132] Cabello, C. M., Bair, W. B., Lamore, S. D., Ley, S., Alexandra, S. *et al.* The Duffy antigen receptor for chemokines transports chemokines and supports their promigratory activity. *Nat. Immunol.*, **46** (2):220–231, 2010.

[133] Chaudhuri, a., Nielsen, S., Elkjaer, M. L., Zbrzezna, V., Fang, F. *et al.* Detection of Duffy antigen in the plasma membranes and caveolae of vascular endothelial and epithelial cells of nonerythroid organs. *Blood*, **89** (2):701–712, 1997.

[134] Nibbs, R. J., Wylie, S. M., Yang, J., Landau, N. R., and Graham, G. J. Cloning and characterization of a novel promiscuous human beta-chemokine receptor D6. *J. Biol. Chem.*, **272** (51):32078–32083, 1997.

[135] Fra, A. M., Locati, M., Otero, K., Sironi, M., Signorelli, P. *et al.* Cutting Edge: Scavenging of Inflammatory CC Chemokines by the Promiscuous Putatively Silent Chemokine Receptor D6. *J. Immunol.*, **170** (5):2279–2282, 2003.

[136] Weber, M., Blair, E., Simpson, C. V., O'Hara, M., Blackburn, P. E. *et al.* The Chemokine Receptor D6 Constitutively Traffics to and from the Cell Surface to Internalize and Degrade Chemokines. *Mol. Biol. Cell*, **15**:2492–2508, 2004.

[137] Galliera, E., Jala, V. R., Trent, J. O., Bonecchi, R., Signorelli, P. *et al.* beta-arrestin-dependent constitutive internalization of the human chemokine decoy receptor D6. *J. Biol. Chem.*, **279** (24):25590–25597, 2004.

[138] Chensue, S., Lukacs, N., Lincoln, P., Burdick, M., Strieter, R. *et al.* Monocyte chemotactic protein expression during schistosome egg granuloma formation . *Am. J. Pathol.*, **146** (1):130–138, 1995.

[139] Karpus, W. J., Lukacs, N. W., Kennedy, K. J., Smith, W. S., Hurst, S. D. *et al.* Differential CC chemokine-induced enhancement of T helper cell cytokine production. *J Immunol*, **158** (9):4129–4136, 1997.

[140] Lu, B., Rutledge, B. J., Gu, L., Fiorillo, J., Lukacs, N. W. *et al.* Abnormalities in monocyte recruitment and cytokine expression in monocyte chemoattractant protein 1-deficient mice. *J. Exp. Med.*, **187** (4):601–8, 1998.

[141] Ajuebor, M. N., Flower, R. J., Hannon, R., Christie, M., Bowers, K. *et al.* Endogenous monocyte chemoattractant protein-1 recruits monocytes in the zymosan peritonitis model. *J. Leukoc. Biol.*, **63** (1):108–116, 1998.

[142] Palframan, R. T., Jung, S., Cheng, G., Weninger, W., Luo, Y. *et al.* Inflammatory Chemokine Transport and Presentation in HEV: A Remote Control Mechanism for Monocyte Recruitment to Lymph Nodes in Inflamed Tissues. *J. Exp. Med.*, **194** (9):1361–1374, 2001.

[143] Sato, S., Sakurai, T., Ogasawara, J., Takahashi, M., Izawa, T. *et al.* A circadian clock gene, Rev-erb-a, modulates the inflammatory function of macrophages through the negative regulation of Ccl2 expression. *J. Immunol.*, **192** (1):407–17, 2014.

[144] Kurihara, B. T., Warr, G., Loy, J., and Bravo, R. Defects in Macrophage Recruitment and Host Defense Mice Lacking the CCR2 Chemokine Receptor. *J Exp Med*, **186** (10):1757–1762, 1997.

[145] Jia, T., Serbina, N. V., Brandl, K., Zhong, M. X., Leiner, I. M. *et al.* Additive roles for MCP-1 and MCP-3 in CCR2-mediated recruitment of inflammatory monocytes during Listeria monocytogenes infection. *J. Immunol.*, **180**:6846–6853, 2008.

[146] Aldridge, J. R., Moseley, C. E., Boltz, D. A., Negovetich, N. J., Reynolds, C. *et al.* TNF/iNOS-producing dendritic cells are the necessary evil of lethal influenza virus infection. *Proc. Natl. Acad. Sci.*, **106** (13):5306–5311, 2009.

[147] Peters, W., Dupuis, M., and Charo, I. F. A Mechanism for the Impaired IFN-γ Production in C-C Chemokine Receptor 2 (CCR2) Knockout Mice: Role of CCR2 in Linking the Innate and Adaptive Immune Responses. *J. Immunol.*, **165** (12):7072–7077, 2000.

[148] Shen, J. Z., Morgan, J., Tesch, G. H., Fuller, P. J., and Young, M. J. CCL2-Dependent Macrophage Recruitment Is Critical for Mineralocorticoid Receptor-Mediated Cardiac Fibrosis, Inflammation, and Blood Pressure Responses in Male Mice. *Endocrinology*, **155** (January):1057–1066, 2014.

[149] Namiki, M., Kawashima, S., Yamashita, T., Ozaki, M., Hirase, T. *et al.* Local overexpression of monocyte chemoattractant protein-1 at vessel wall induces infiltration of macrophages and formation of atherosclerotic lesion: Synergism with hypercholesterolemia. *Arterioscler. Thromb. Vasc. Biol.*, **22** (1):115–120, 2002.

[150] Haukeland, J. W., Damås, J. K., Konopski, Z., Løberg, E. M., Haaland, T. *et al.* Systemic inflammation in nonalcoholic fatty liver disease is characterized by elevated levels of CCL2. *J. Hepatol.*, **44** (6):1167–1174, 2006.

[151] Weisberg, S. P., Hunter, D., Huber, R., Lemieux, J., Slaymaker, S. *et al.* CCR2 modulates inflammatory and metabolic effects of high-fat feeding. *J. Clin. Invest.*, **116** (1):115–124, 2006.

[152] Ehling, J., Bartneck, M., Wei, X., Gremse, F., Fech, V. *et al.* CCL2-dependent infiltrating macrophages promote angiogenesis in progressive liver fibrosis. *Gut*, **63** (12):1960–71, 2014.

[153] Wehr, A., Baeck, C., Ulmer, F., Gassler, N., Hittatiya, K. *et al.* Pharmacological inhibition of the chemokine CCL2 (MCP-1) diminishes liver macrophage infiltration and steatohepatitis in chronic hepatic injury. *Gut*, **61**:416–426, 2012.

[154] Baeck, C., Wei, X., Bartneck, M., Fech, V., Heymann, F. *et al.* Pharmacological inhibition of the chemokine C-C motif chemokine ligand 2 (monocyte chemoattractant protein 1) accelerates liver fibrosis regression by suppressing Ly-6C+ macrophage infiltration in mice. *Hepatology*, **59** (3):1060–1072, 2014.

[155] Mitchell, C., Couton, D., and Couty, J. Dual role of CCR2 in the constitution and the resolution of liver fibrosis in mice. *Am. J. Pathol.*, **174** (5):1766–1775, 2009.

[156] Conti, I. and Rollins, B. J. CCL2 (monocyte chemoattractant protein-1) and cancer. *Semin. Cancer Biol.*, **14** (3):149–154, 2004.

[157] Rollins, B. J. and Sunday, M. E. Suppression of tumor formation in vivo by expression of the JE gene in malignant cells. *Mol Cell Biol*, **11** (6):3125–3131, 1991.

[158] Walter, S., Bottazzi, B., Govoni, D., Colotta, F., and Mantovani, A. Macrophage infiltration and growth of sarcoma clones expressing different amounts of monocyte chemotactic protein/JE. *Int. J. Cancer*, **49** (3):431–435, 1991.

[159] Soria, G. and Ben-Baruch, A. The inflammatory chemokines CCL2 and CCL5 in breast cancer. *Cancer Lett.*, **267** (2):271–85, 2008.

[160] Ueno, T., Toi, M., Saji, H., Muta, M., Bando, H. *et al.* Significance of macrophage chemoattractant protein-1 in macrophage recruitment, angiogenesis, and survival in human breast cancer. *Clin. Cancer Res.*, **6** (8):3282–3289, 2000.

[161] Mantovani, A., Bottazzi, B., Colotta, F., Sozzani, S., and Ruco, L. The origin and function of tumor-associated macrophages. *Immunol. Today*, **13** (7):265–270, 1992.

[162] Visscher, D. W., Tabaczka, P., Long, D., and Crissman, J. D. Clinicopathologic analysis of macrophage infiltrates in breast carcinoma. *Pathol. Res. Pract.*, **191** (11):1133–9, 1995.

[163] Kudo-Saito, C. and Shirako, H. CCL2 is critical for immunosuppression to promote cancer metastasis. *Cinical Exp. Metastasis*, **30**:393–405, 2013.

[164] Huang, B., Lei, Z., Zhao, J., Gong, W., Liu, J. *et al.* CCL2/CCR2 pathway mediates recruitment of myeloid suppressor cells to cancers. *Cancer Lett.*, **252** (1):86–92, 2007.

[165] Dwyer, R. M., Potter-Beirne, S. M., Harrington, K. a., Lowery, a. J., Hennessy, E. *et al.* Monocyte Chemotactic Protein-1 Secreted by Primary Breast Tumors Stimulates Migration of Mesenchymal Stem Cells. *Clin Cancer Res*, **13** (17):5020–5027, 2007.

[166] Allavena, P., Sica, A., Solinas, G., Porta, C., and Mantovani, A. The inflammatory micro-environment in tumor progression: The role of tumor-associated macrophages. *Crit. Rev. Oncol. Hematol.*, **66** (1):1–9, 2008.

[167] Bonapace, L., Coissieux, M.-M., Wyckoff, J., Mertz, K. D., Varga, Z. *et al.* Cessation of CCL2 inhibition accelerates breast cancer metastasis by promoting angiogenesis. *Nature*, **515** (7525):130–133, 2014.

[168] Monteclaro, F. S. and Charo, I. F. The amino-terminal extracellular domain of the MCP-1 receptor, but not the RANTES/MIP-1a receptor, confers chemokine selectivity. Evidence for a two-step mechanism for MCP-1 receptor activation. *J. Biol. Chem.*, **271** (32):19084–19092, 1996.

[169] Rosenkilde, M. M., Benned-Jensen, T., Frimurer, T. M., and Schwartz, T. W. The minor binding pocket: a major player in 7TM receptor activation. *Trends Pharmacol. Sci.*, **31** (12):567–574, 2010.

[170] Andrews, G., Jones, C., and Wreggett, K. A. An Intracellular Allosteric Site for a Specific Class of Antagonists of the CC Chemokine G Protein-Coupled Receptors CCR4 and CCR5. *Mol. Pharmacol.*, **73** (3):855–867, 2008.

[171] Yang, L., Jiao, R. X., Moyes, C., Morriello, G., Butora, G. *et al.* The discovery of MK-0812, a potent and selective CCR2 antagonist. In *233rd ACS Natl. Meet.* Chicago, 2007.

[172] Xue, C.-B., Feng, H., Cao, G., Huang, T., Glenn, J. *et al.* Discovery of INCB3284, a Potent, Selective, and Orally Bioavailable hCCR2 Antagonist. *ACS Med. Chem. Lett.*, **2** (6):450–454, 2011.

[173] Hughes, R. O., Rogier, D., Devraj, R., Zheng, C., Cao, G. *et al.* Discovery of ((1S,3R)-1-isopropyl-3-((3S,4S)-3-methoxy-tetrahydro-2H-pyran-4-ylamino)cyclopentyl)(4-(5-(trifluoromethyl)pyridazin-3-yl)piperazin-1-yl)methanone, PF-4254196, a CCR2 antagonist with an improved cardiovascular profile. *Bioorg. Med. Chem. Lett.*, **21** (9):2626–2630, 2011.

[174] Lagu, B., Gerchak, C., Pan, M., Hou, C., Singer, M. *et al.* Potent and selective CC-chemokine receptor-2 (CCR2) antagonists as a potential treatment for asthma, 2007.

[175] Hou, C.; Singer, M.; Matheis, M. JNJ-17166864, a Selective CCR2 Antagonist with Potential Therapeutic Implications for Inflammatory Diseases. In *104th Int. Conf. Am. Thorac. Soc.* 104th International Conference American Thoracic Society, Toronto, 2008.

[176] Balkwill, F. and Mantovani, a. Cancer and inflammation: implications for pharmacology and therapeutics. *Clin. Pharmacol. Ther.*, **87** (4):401–6, 2010.

[177] Loberg, R. D., Ying, C., Craig, M., Day, L. L., Sargent, E. *et al.* Targeting CCL2 with systemic delivery of neutralizing antibodies induces prostate cancer tumor regression in vivo. *Cancer Res.*, **67** (19):9417–9424, 2007.

[178] Loberg, R. D., Day, L. L., Harwood, J., Ying, C., St John, L. N. *et al.* CCL2 is a potent regulator of prostate cancer cell migration and proliferation. *Neoplasia*, **8** (7):578–86, 2006.

[179] Fridlender, Z. G., Buchlis, G., Kapoor, V., Cheng, G., Sun, J. *et al.* CCL2 blockade augments cancer immunotherapy. *Cancer Res.*, **70** (1):109–118, 2010.

[180] Zhu, X., Fujita, M., Snyder, L. A., and Okada, H. Systemic delivery of neutralizing antibody targeting CCL2 for glioma therapy. *J. Neurooncol.*, **104** (1):83–92, 2011.

[181] Haringman, J. J., Gerlag, D. M., Smeets, T. J. M., Baeten, D., Van Den Bosch, F. *et al.* A randomized controlled trial with an anti-CCL2 (anti-monocyte chemotactic protein 1) monoclonal antibody in patients with rheumatoid arthritis. *Arthritis Rheum.*, **54** (8):2387–2392, 2006.

[182] Vergunst, C. E., Gerlag, D. M., Lopatinskaya, L., Klareskog, L., Smith, M. D. *et al.* Modulation of CCR2 in rheumatoid arthritis: A double-blind, randomized, placebo-controlled clinical trial. *Arthritis Rheum.*, **58** (7):1931–1939, 2008.

[183] Lebre, M. C., Vergunst, C. E., Choi, I. Y. K., Aarrass, S., Oliveira, A. S. F. *et al.* Why CCR2 and CCR5 blockade failed and why ccr1 blockade might still be effective in the treatment of rheumatoid arthritis. *PLoS One*, **6** (7):8–13, 2011.

[184] Ford, L. B., Cerovic, V., Milling, S. W. F., Graham, G. J., Hansell, C. a. H. *et al.* Characterization of Conventional and Atypical Receptors for the Chemokine CCL2 on Mouse Leukocytes. *J. Immunol.*, **193** (1):400–411, 2014.

[185] Chen, X., Zaro, J., and Shen, W. Fusion protein linkers: Property, design and functionality. *Adv. Drug Deliv. Rev.*, **65** (10):1357–1369, 2013.

[186] Zhao, H. L., Yao, X. Q., Xue, C., Wang, Y., Xiong, X. H. *et al.* Increasing the homogeneity, stability and activity of human serum albumin and interferon-a-2b fusion protein by linker engineering. *Protein Expr. Purif.*, **61** (1):73–77, 2008.

[187] Arai, R., Ueda, H., Kitayama, a., Kamiya, N., and Nagamune, T. Design of the linkers which effectively separate domains of a bifunctional fusion protein. *Protein Eng.*, **14** (8):529–532, 2001.

[188] Saito, G., Swanson, J. A., and Lee, K. D. Drug delivery strategy utilizing conjugation via reversible disulfide linkages: Role and site of cellular reducing activities. *Adv. Drug Deliv. Rev.*, **55** (2):199–215, 2003.

[189] Chen, X., Bai, Y., Zaro, J. L., and Shen, W.-C. Design of an in vivo cleavable disulfide linker in recombinant fusion proteins. *Biotechniques*, **49** (1):513–8, 2010.

[190] Vessillier, S., Adams, G., and Chernajovsky, Y. Latent cytokines: Development of novel cleavage sites and kinetic analysis of their differential sensitivity to MMP-1 and MMP-3. *Protein Eng. Des. Sel.*, **17** (12):829–835, 2004.

[191] Park, J. H., Yamaguchi, Y., and Inouye, M. Intramolecular regulation of the sequence-specific mrna interferase activity of mazf fused to a maze fragment with a linker cleavable by specific proteases. *Appl. Environ. Microbiol.*, **78** (11):3794–3799, 2012.

[192] Chalker, J. M., Bernardes, G. J. L., Lin, Y. A., and Davis, B. G. Chemical modification of proteins at cysteine: Opportunities in chemistry and biology. *Chem. - An Asian J.*, **4** (5):630–640, 2009.

[193] Lundell, N. and Schreitmüller, T. Sample Preparation for Peptide Mapping - A Pharmaceutical Quality-Control Perspective. *Anal. Biochem.*, **266** (1):31–47, 1999.

[194] Davis, N. J. and Flitsch, S. L. A novel method for the specific glycosylation of proteins. *Tetrahedron Lett.*, **32** (46):6793–6796, 1991.

[195] Swanwick, R. S., Daines, A. M., Tey, L. H., Flitsch, S. L., and Allemann, R. K. Increased thermal stability of site-selectively glycosylated dihydrofolate reductase. *ChemBioChem*, **6** (8):1338–1340, 2005.

[196] Zhang, Y., Bhatt, V. S., Sun, G., Wang, P. G., and Palmer, A. F. Site-selective glycosylation of hemoglobin on Cys beta-93. *Bioconjug. Chem.*, **19** (11):2221–2230, 2008.

[197] Brocchini, S., Balan, S., Godwin, A., Choi, J.-W., Zloh, M. *et al.* PEGylation of native disulfide bonds in proteins. *Nat. Protoc.*, **1** (5):2241–2252, 2006.

[198] Kim, Y., Ho, S. O., Gassman, N. R., Korlann, Y., Landorf, E. V. *et al.* Efficient site-specific labeling of proteins via cysteines. *Bioconjug. Chem.*, **19** (3):786–791, 2008.

[199] Willner, D., Trail, P. A., Hofstead, S. J., King, H. D., Lasch, S. J. *et al.* (6-Maleimidocaproyl) hydrazone of Doxorubicin-A New Derivative for the Preparation of Immunoconjugates of Doxorubicin. *Bioconjugete Chem*, **4**:521–527, 1993.

[200] Woghiren, C., Sharma, B., and Stein, S. Protected thiol-polyethylene glycol: a new activated polymer for reversible protein modification. *Bioconjug. Chem.*, **4** (5):314–318, 1993.

[201] Ellman, G. L. Tissue sulfhydryl groups. *Arch. Biochem. Biophys.*, **82** (1):70–77, 1959.

[202] Gamblin, D. P., Garnier, P., Kasteren, S. V., Oldham, N. J., Fairbanks, A. J. *et al.* Glyco-SeS: Selenenylsulfide-Mediated Protein Glycoconjugation—A New Strategy in Post- Translational Modification. *Angew. Chemie - Int. Ed.*, **43** (7):828–833, 2004.

[203] De Graaf, A. J., Kooijman, M., Hennink, W. E., and Mastrobattista, E. Nonnatural amino acids for site-specific protein conjugation. *Bioconjug. Chem.*, **20** (7):1281–1295, 2009.

[204] Rostovtsev, V. V., Green, L. G., Fokin, V. V., and Sharpless, K. B. A stepwise huisgen cycloaddition process: Copper(I)-catalyzed regioselective "ligation" of azides and terminal alkynes. *Angew. Chemie - Int. Ed.*, **41** (14):2596–2599, 2002.

[205] Hein, J. E. and Fokin, V. V. Copper-catalyzed azide–alkyne cycloaddition (CuAAC) and beyond: new reactivity of copper(i) acetylides. *Chem. Soc. Rev.*, **39** (4):1302, 2010.

[206] Chan, T. R., Hilgraf, R., Sharpless, K. B., and Fokin, V. V. Polytriazoles as copper(I)-stabilizing ligands in catalysis. *Org. Lett.*, **6** (17):2853–2855, 2004.

[207] Presolski, S. I., Hong, V., Cho, S. H., and Finn, M. G. Tailored ligand acceleration of the cu-catalyzed azide-alkyne cycloaddition reaction: Practical and mechanistic implications. *J. Am. Chem. Soc.*, **132** (41):14570–14576, 2010.

[208] Wang, Q., Chan, T. R., Hilgraf, R., Fokin, V. V., Sharpless, K. B. *et al.* Bioconjugation by copper(I)-catalyzed azide-alkyne [3 + 2] cycloaddition. *J. Am. Chem. Soc.*, **125** (11):3192–3193, 2003.

[209] Li, H., Aneja, R., and Chaiken, I. Click chemistry in peptide-based drug design. *Molecules*, **18** (8):9797–9817, 2013.

[210] Tron, G. C., Pirali, T., Billington, R. A., Canonico, P. L., Sorba, G. *et al.* Click Chemistry Reactions in Medicinal Chemistry: Applications of the 1,3-dipolar Cycloaddition Between Azides and Alkynes. *Med. Res. Rev.*, **28** (2):278–308, 2008.

[211] Bock, V. D., Speijer, D., Hiemstra, H., and van Maarseveen, J. H. 1,2,3-Triazoles as peptide bond isosteres: synthesis and biological evaluation of cyclotetrapeptide mimics. *Org. Biomol. Chem.*, **5** (6):971–975, 2007.

[212] Hong, V., Steinmetz, N. F., Manchester, M., and Finn, M. G. Labeling live cells by copper-catalyzed alkyne-azide click chemistry. *Bioconjug. Chem.*, **21** (10):1912–1916, 2010.

[213] Hong, V., Presolski, S. I., Ma, C., and Finn, M. G. Analysis and optimization of copper-catalyzed azide-alkyne cycloaddition for bioconjugation. *Angew. Chemie - Int. Ed.*, **48** (52):9879–9883, 2009.

[214] Leriche, G., Chisholm, L., and Wagner, A. Cleavable linkers in chemical biology. *Bioorg. Med. Chem.*, **20** (2):571–582, 2012.

[215] Chari, R. V. J., Miller, M. L., and Widdison, W. C. Antibody-drug conjugates: An emerging concept in cancer therapy. *Angew. Chemie - Int. Ed.*, **53** (15):3796–3827, 2014.

[216] Olson, E. S., Jiang, T., Aguilera, T. a., Nguyen, Q. T., Ellies, L. G. *et al.* Activatable cell penetrating peptides linked to nanoparticles as dual probes for in vivo fluorescence and MR imaging of proteases. *Proc. Natl. Acad. Sci. U. S. A.*, **107** (9):4311–4316, 2010.

[217] Bildstein, L., Dubernet, C., and Couvreur, P. Prodrug-based intracellular delivery of anticancer agents. *Adv. Drug Deliv. Rev.*, **63** (1):3–23, 2011.

[218] Gao, W., Langer, R., and Farokhzad, O. C. Poly(ethylene glycol) with observable shedding. *Angew. Chemie - Int. Ed.*, **49** (37):6567–6571, 2010.

[219] Henne, W. A., Doorneweerd, D. D., Hilgenbrink, A. R., Kularatne, S. A., and Low, P. S. Synthesis and activity of a folate peptide camptothecin prodrug. *Bioorg. Med. Chem. Lett.*, **16** (20):5350–5355, 2006.

[220] Mahato, R., Tai, W., and Cheng, K. Prodrugs for improving tumor targetability and efficiency. *Adv. Drug Deliv. Rev.*, **63** (8):659–70, 2011.

[221] Lewis Phillips, G. D., Li, G., Dugger, D. L., Crocker, L. M., Parsons, K. L. *et al.* Targeting HER2-positive breast cancer with trastuzumab-DM1, an antibody-cytotoxic drug conjugate. *Cancer Res.*, **68** (22):9280–9290, 2008.

[222] Kellogg, B. A., Garrett, L., Kovtun, Y., Lai, K. C., Leece, B. *et al.* Disulfide-linked antibody-maytansinoid conjugates: Optimization of in vivo activity by varying the steric hindrance at carbon atoms adjacent to the disulfide linkage. *Bioconjug. Chem.*, **22** (4):717–727, 2011.

[223] Lubkowski, J., Bujacz, G., Boqué, L., Peter J., D., Tracy M., H. *et al.* The structure of MCP-1 in two crystal forms provides a rare example of variable quaternary interactions. *Nat. Struct. Mol. Biol.*, **4** (1):64–69, 1997.

[224] Gong, J. H. and Clark-Lewis, I. Antagonists of monocyte chemoattractant protein 1 identified by modification of functionally critical NH2-terminal residues. *J Exp Med*, **181** (2):631–640, 1995.

[225] Handel, T. M., Johnson, Z., Rodrigues, D. H., Dos Santos, A. C., Cirillo, R. *et al.* An engineered monomer of CCL2 has anti-inflammatory properties emphasizing the importance of oligomerization for chemokine activity in vivo. *J. Leukoc. Biol.*, **84** (4):1101–8, 2008.

[226] Williams, A. T. R., Winfield, S. A., and Miller, J. N. Relative fluorescence quantum yields using a computer-controlled luminescence spectrometer. *Analyst*, **108** (1290):1067, 1983.

[227] Kato, T., Kashida, H., Kishida, H., Yada, H., Okamoto, H. *et al.* Development of a robust model system of FRET using base surrogates tethering fluorophores for strict control of their position and orientation within DNA duplex. *J. Am. Chem. Soc.*, **135** (2):741–750, 2013.

[228] Heisig, F., Gollos, S., and Freudenthal, S. Synthesis of BODIPY Derivatives Substituted with Various Bioconjugatable Linker Groups: A Construction Kit for Fluorescent Labeling of Receptor Ligands. *J. Fluoresc.*, **24** (1):213–30, 2013.

[229] Sreenath, K., Yuan, Z., Allen, A., Davidson, M. W., and Zhu, L. A fluorescent indicator for imaging lysosomal zinc(ii) with förster resonance energy transfer (FRET)-enhanced photostability and a narrow band of emission. *Chem. - A Eur. J.*, **21** (2):867–874, 2015.

[230] Pal, M. and Bearne, S. L. Synthesis of coenzyme A thioesters using methyl acyl phosphates in an aqueous medium. *Org. Biomol. Chem.*, **12** (48):9760–9763, 2014.

[231] Bi, L. Novel probes and targeting compounds for mitochondria, 2014.

[232] Nguyen, T. and Francis, M. B. Practical synthetic route to functionalized rhodamine dyes. *Org. Lett.*, **5** (18):3245–8, 2003.

[233] Loudet, A. and Burgess, K. BODIPY dyes and their derivatives: syntheses and spectroscopic properties. *Chem. Rev.*, **107**:4891–4932, 2007.

[234] Kowada, T., Maeda, H., and Kikuchi, K. BODIPY-based probes for the fluorescence imaging of biomolecules in living cells. *Chem. Soc. Rev.*, 2015.

[235] Wagner, R. W. and Lindsey, J. S. Boron-dipyrromethene dyes for incorporation in synthetic multi-pigment light-harvesting arrays. *Pure Appl. Chem*, **68** (7):1373–1380, 1996.

[236] Li, L., Han, J., Nguyen, B., and Burgess, K. Syntheses and spectral properties of functionalized, water-soluble BODIPY derivatives. *J. Org. Chem.*, **73** (15):1963–1970, 2008.

[237] Courtis, A. M., Santos, S. a., Guan, Y., Hendricks, J. A., Ghosh, B. *et al.* Monoalkoxy BODIPYs-A fluorophore class for bioimaging. *Bioconjug. Chem.*, **25** (6):1043–1051, 2014.

[238] Jiao, L., Yu, C., Uppal, T., Liu, M., Li, Y. *et al.* Long wavelength red fluorescent dyes from 3,5-diiodo-BODIPYs. *Org. Biomol. Chem.*, **8** (11):2517–2519, 2010.

[239] Zhang, S., Wu, T., Fan, J., Li, Z., Jiang, N. *et al.* A BODIPY-based fluorescent dye for mitochondria in living cells, with low cytotoxicity and high photostability. *Org. Biomol. Chem.*, **11** (4):555–558, 2013.

[240] Yang, J., Chen, H., Vlahov, I. R., Cheng, J.-X., and Low, P. S. Evaluation of disulfide reduction during receptor-mediated endocytosis by using FRET imaging. *Proc. Natl. Acad. Sci. U. S. A.*, **103** (37):13872–13877, 2006.

[241] Beija, M. and Afonso, C. A. M. Synthesis and applications of Rhodamine derivatives as fluorescent probes. *Chem. Soc. Rev.*, **38**:2410–2433, 2009.

[242] Rumyantsev, E. V., Alyoshin, S. N., and Marfin, Y. S. Kinetic study of Bodipy resistance to acids and alkalis: Stability ranges in aqueous and non-aqueous solutions. *Inorganica Chim. Acta*, **408**:181–185, 2013.

[243] Sauer, R., Turshatov, A., Baluschev, S., and Landfester, K. One-pot production of fluorescent surface-labeled polymeric nanoparticles via miniemulsion polymerization with bodipy surfmers. *Macromolecules*, **45** (9):3787–3796, 2012.

[244] Musiejuk, M. and Witt, D. Recent Developments in the Synthesis of Unsymmetrical Disulfanes (Disulfides). A Review. *Org. Prep. Proced. Int.*, **47** (2):95–131, 2015.

[245] Kruszynski, M., Stowell, N., Das, A., Seideman, J., Tsui, P. *et al.* Synthesis and biological characterization of human monocyte chemoattractant protein 1 (MCP-1) and its analogs. *J. Pept. Sci.*, **12** (1):25–32, 2006.

[246] Grygiel, T. L. R., Teplyakov, A., Obmolova, G., Stowell, N., Holland, R. *et al.* Synthesis by native chemical ligation and crystal structure of human CCL2. *Biopolymers*, **94** (3):350–359, 2010.

[247] Saito, F., Noda, H., and Bode, J. W. Critical Evaluation and Rate Constants of Chemoselective Ligation Reactions for Stoichiometric Conjugations in Water. *ACS Chem. Biol.*, **10** (4):1026–1033, 2015.

[248] Turner, D. M., Tom, C. T. M. B., and Renslo, A. R. Simple Plate-Based, Parallel Synthesis of Disul fi de Fragments using the CuAAC Click Reaction. *ACS Comb. Sci.*, **16**:661–664, 2014.

[249] Giustarini, D., Dalle-Donne, I., Colombo, R., Milzani, A., and Rossi, R. Is ascorbate able to reduce disulfide bridges? A cautionary note. *Nitric Oxide - Biol. Chem.*, **19** (3):252–258, 2008.

[250] Zhang, G., Liu, J., Yang, Q., Zhuo, R., and Jiang, X. Disulfide-containing brushed polyethylenimine derivative synthesized by click chemistry for nonviral gene delivery. *Bioconjug. Chem.*, **23** (6):1290–1299, 2012.

[251] Wang, Y., Du, H., Gao, L., Ni, H., Li, X. *et al.* Reductively and hydrolytically dual degradable nanoparticles by "click" crosslinking of a multifunctional diblock copolymer. *Polym. Chem.*, **4** (5):1657, 2013.

[252] Guan, J.-L. *Cell migration*, volume 294. 2005.

[253] Xue, C. B., Wang, A., Meloni, D., Zhang, K., Kong, L. *et al.* Discovery of INCB3344, a potent, selective and orally bioavailable antagonist of human and murine CCR2. *Bioorganic Med. Chem. Lett.*, **20** (24):7473–7478, 2010.

[254] Kufareva, I., Salanga, C. L., and Handel, T. M. Chemokine and chemokine receptor structure and interactions: implications for therapeutic strategies. *Immunol. Cell Biol.*, **93** (4):372–83, 2015.

[255] Abeles, R. D., McPhail, M. J., Sowter, D., Antoniades, C. G., Vergis, N. *et al.* CD14, CD16 and HLA-DR reliably identifies human monocytes and their subsets in the context of pathologically reduced HLA-DR expression by CD14hi/CD16neg monocytes: Expansion of CD14hi/CD16pos and contraction of CD14lo/CD16pos monocytes in acute liver fail. *Cytom. Part A*, **81 A** (10):823–834, 2012.

[256] van Helden, M. J. G., Zaiss, D. M. W., and Sijts, A. J. A. M. CCR2 Defines a Distinct Population of NK Cells and Mediates Their Migration during Influenza Virus Infection in Mice. *PLoS One*, **7** (12), 2012.

[257] Zhang, H. H., Song, K., Rabin, R. L., Hill, B. J., Perfetto, S. P. *et al.* CCR2 identifies a stable population of human effector memory CD4+ T cells equipped for rapid recall response. *J. Immunol.*, **185** (11):6646–63, 2010.

[258] Metelitsa, L. S., Wu, H.-W., Wang, H., Yang, Y., Warsi, Z. *et al.* Natural killer T cells infiltrate neuroblastomas expressing the chemokine CCL2. *J. Exp. Med.*, **199** (9):1213–1221, 2004.

Chapter 8

Appendix

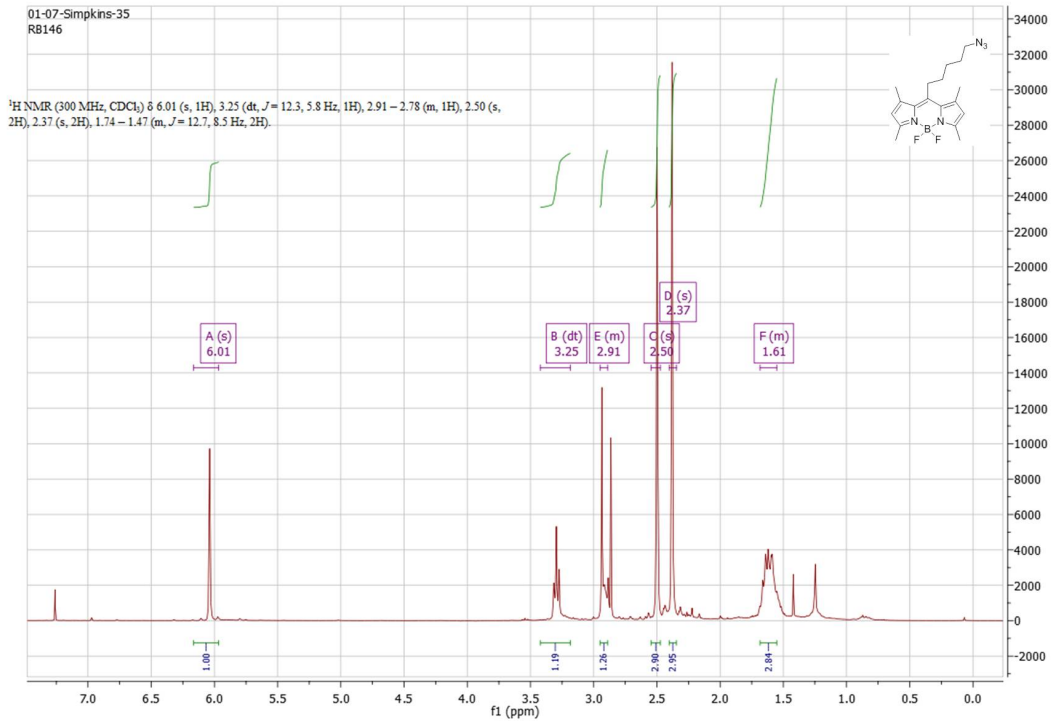

(a) ^{1}H NMR spectrum of BODIPY **8**.

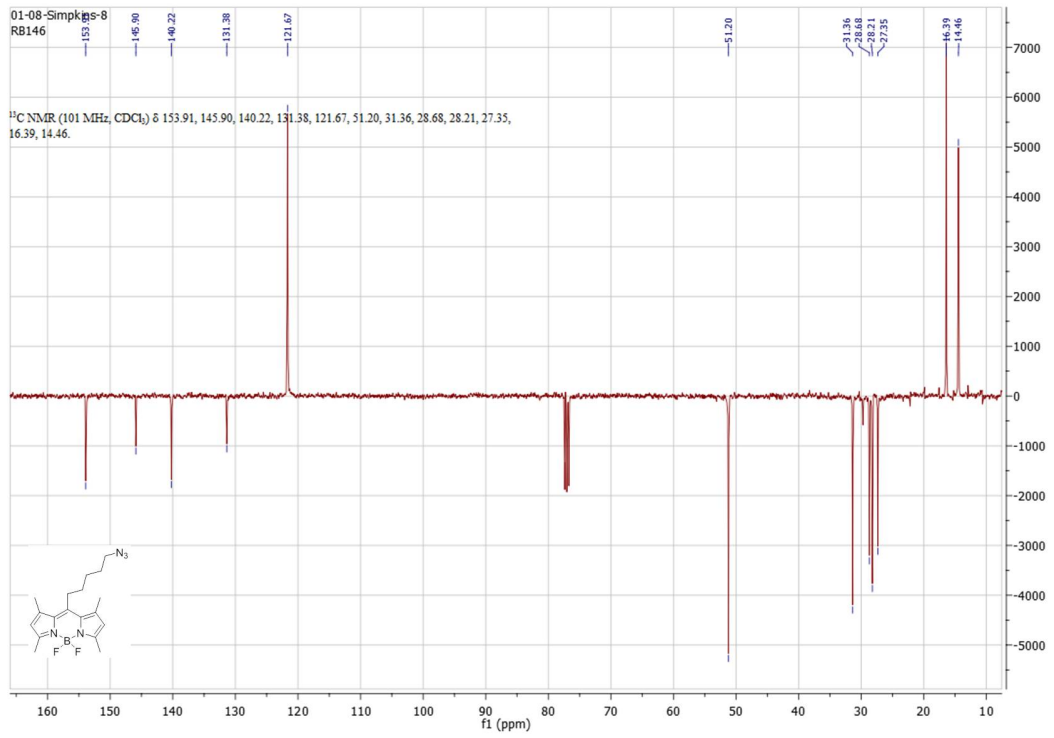

(b) ^{13}C NMR spectrum of BODIPY **8**.

Figure 8.1: 1D NMR spectra of lipophilic BODIPY **8**.

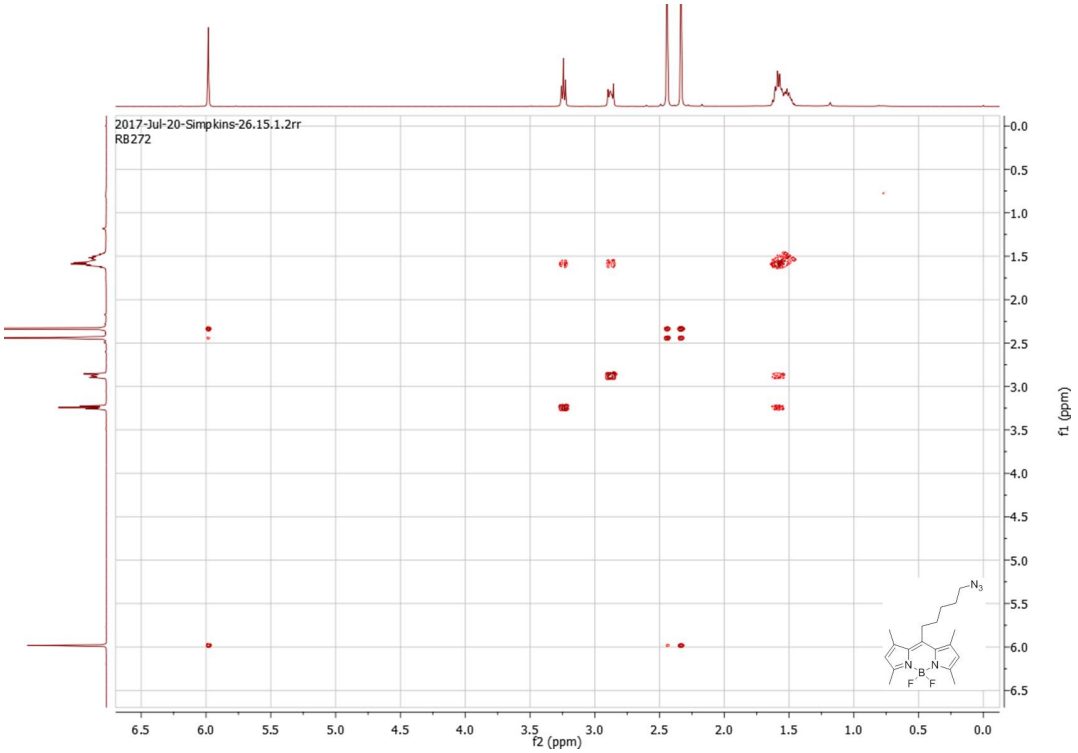

(a) COSY NMR spectrum of BODIPY **8**.

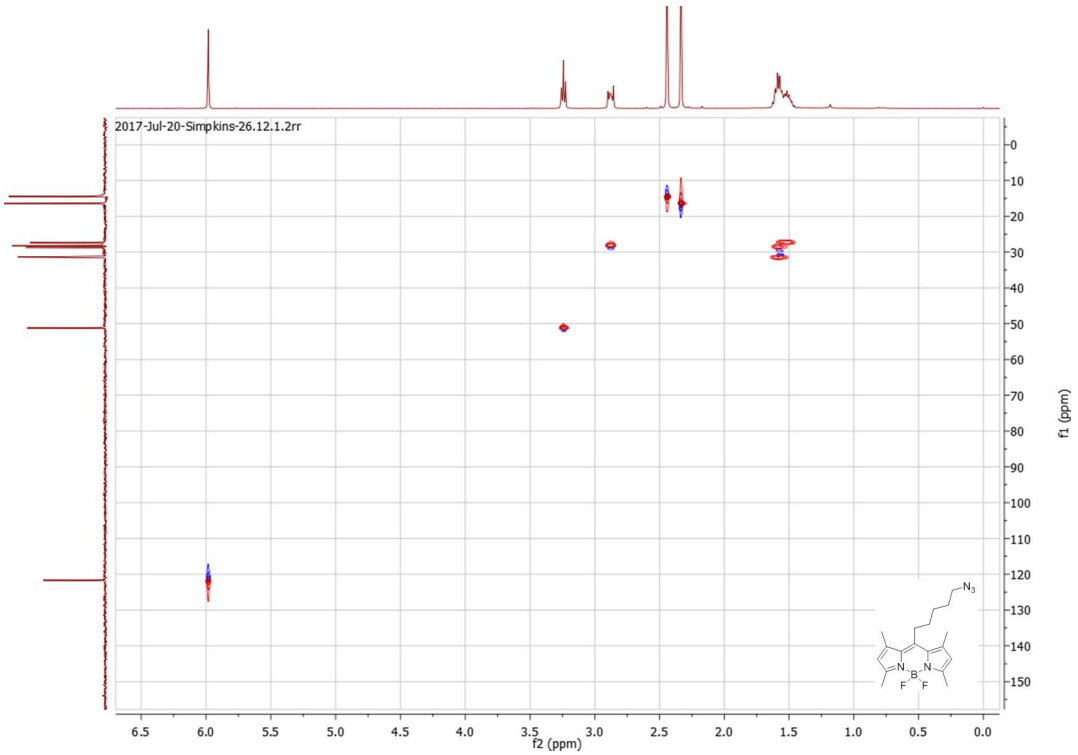

(b) HSQC NMR spectrum of BODIPY **8**.

Figure 8.2: 2D NMR spectra of hydrophilic BODIPY **8**.

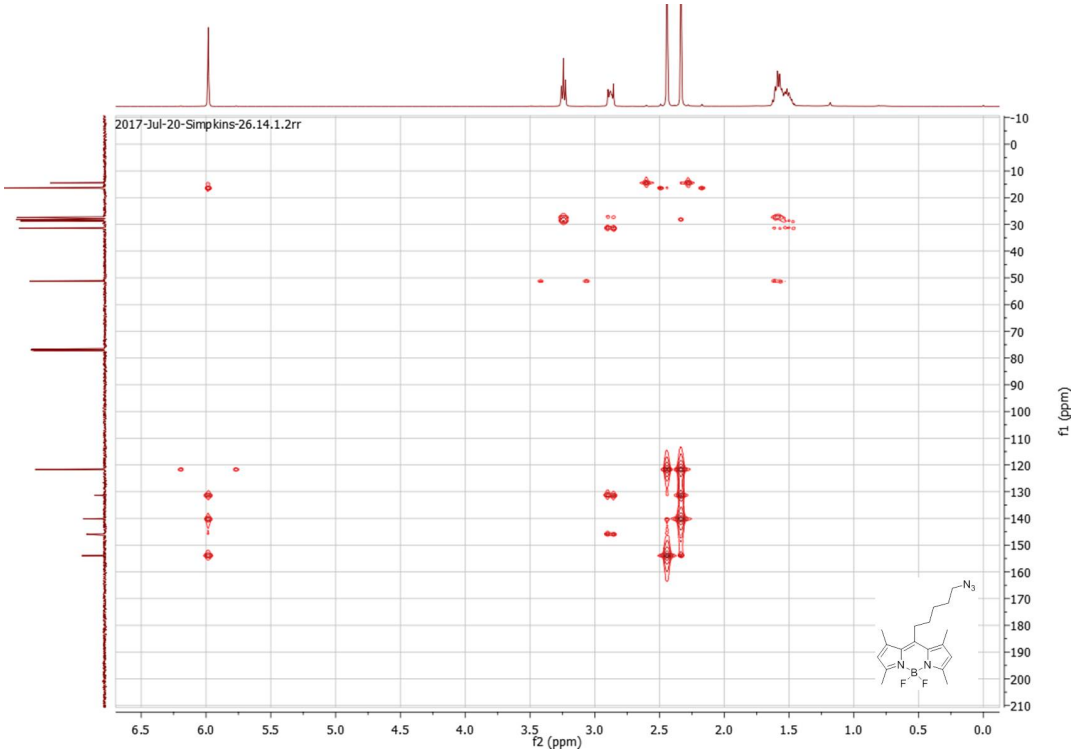

(a) HMBC NMR spectrum of BODIPY **8**.

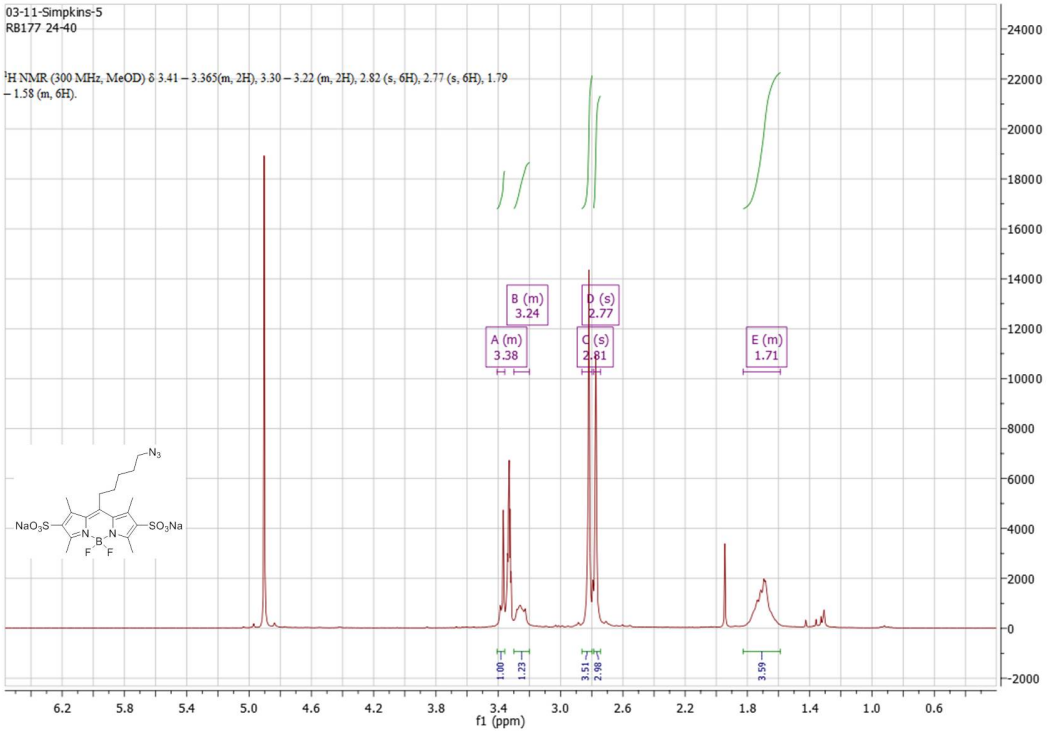

(b) ^{1}H NMR spectrum of BODIPY **10**.

Figure 8.3: HMBC NMR spectra of BODIPY **8** and ^{1}H NMR spectrum of hydrophilic BODIPY **10**.

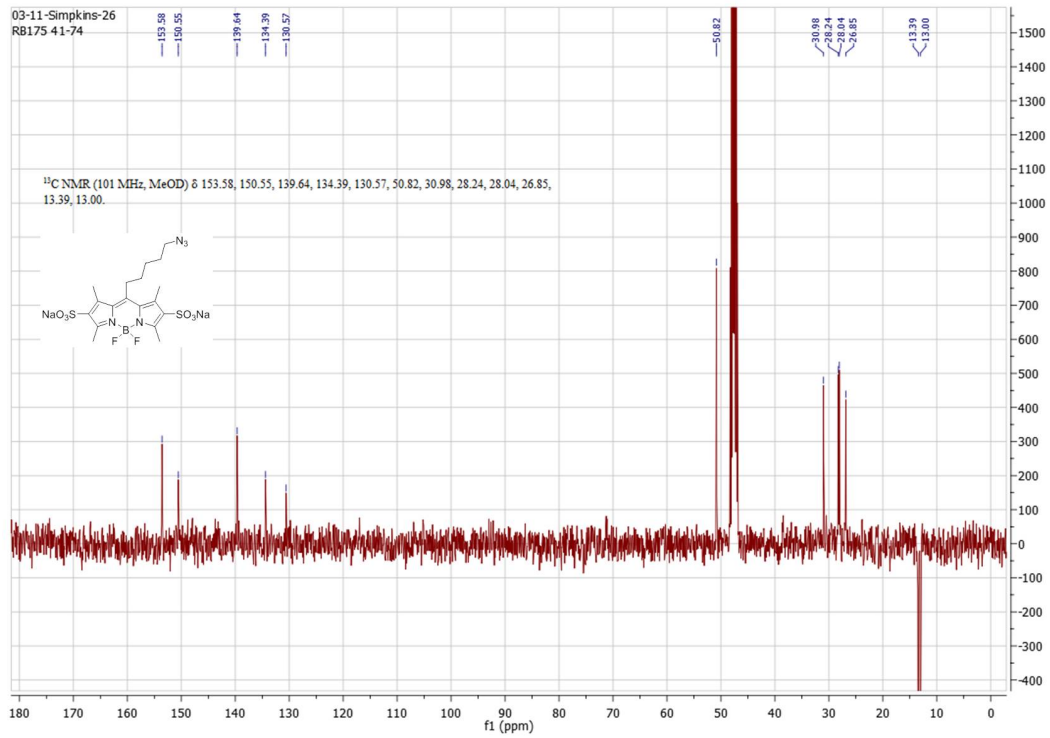

(a) ^{13}C NMR spectrum of BODIPY **10**.

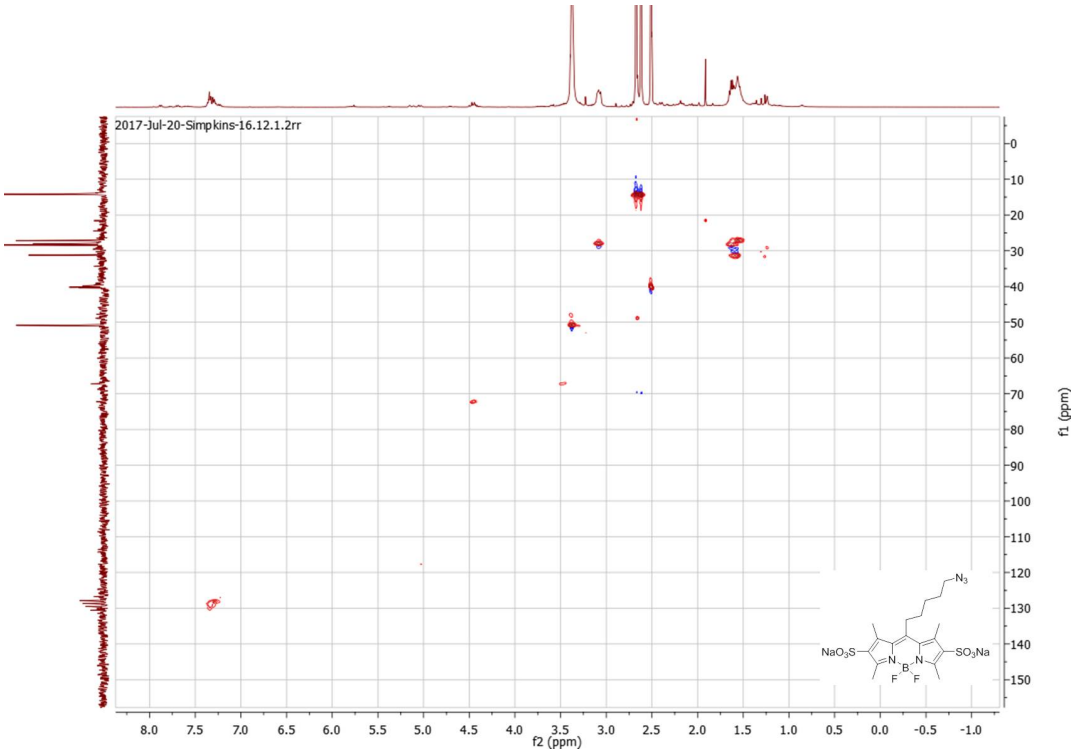

(b) HSQC NMR spectrum of BODIPY **10**.

Figure 8.4: ^{13}C NMR spectrum and HSQC NMR spectra of BODIPY **10**.

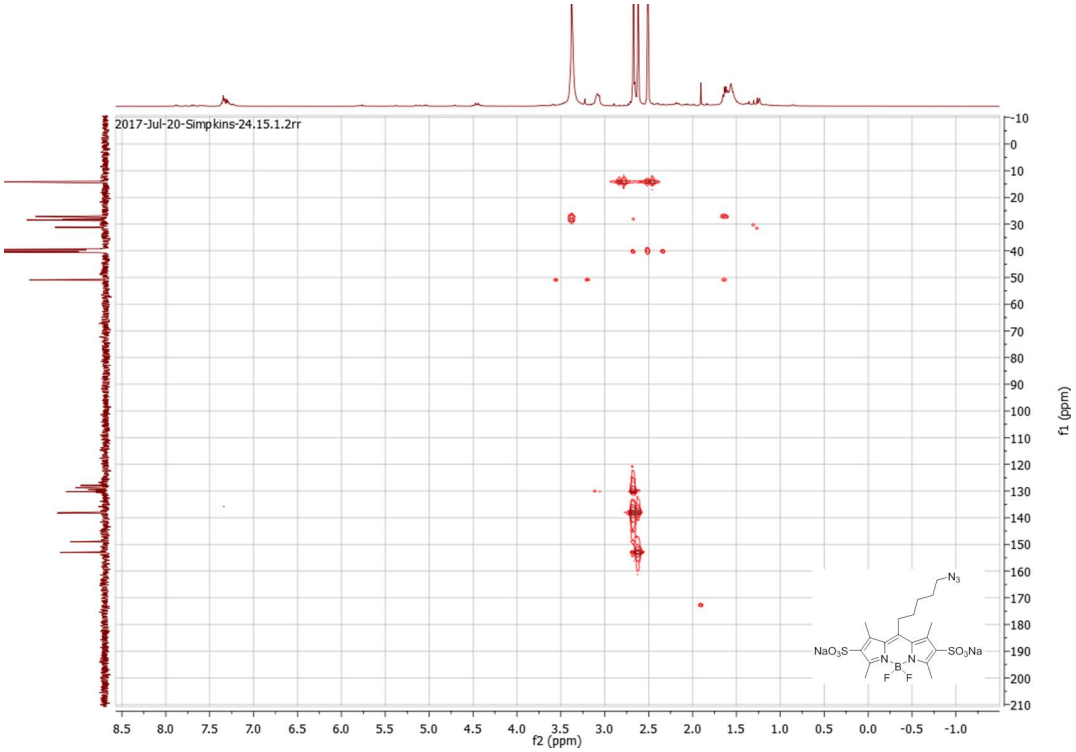

(a) HMBC NMR spectrum of BODIPY **10**.

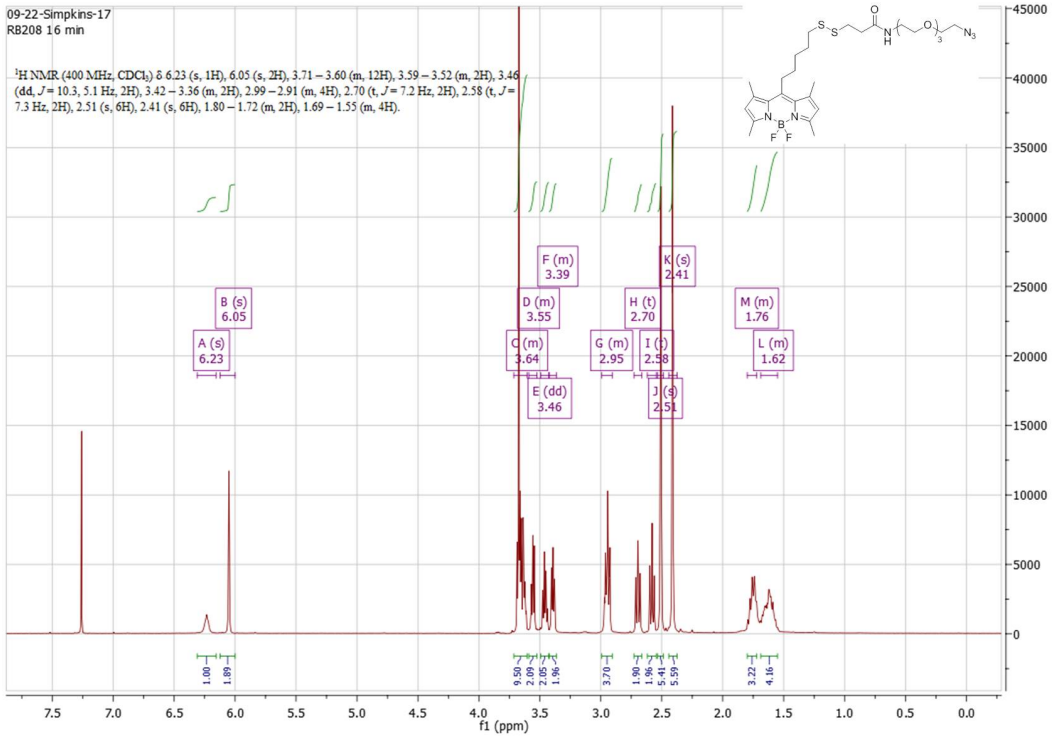

(b) ^{1}H NMR spectrum of BODIPY **24**.

Figure 8.5: HMBC NMR spectrum of BODIPY **10** and ^{1}H NMR spectra of BODIPY **24**.

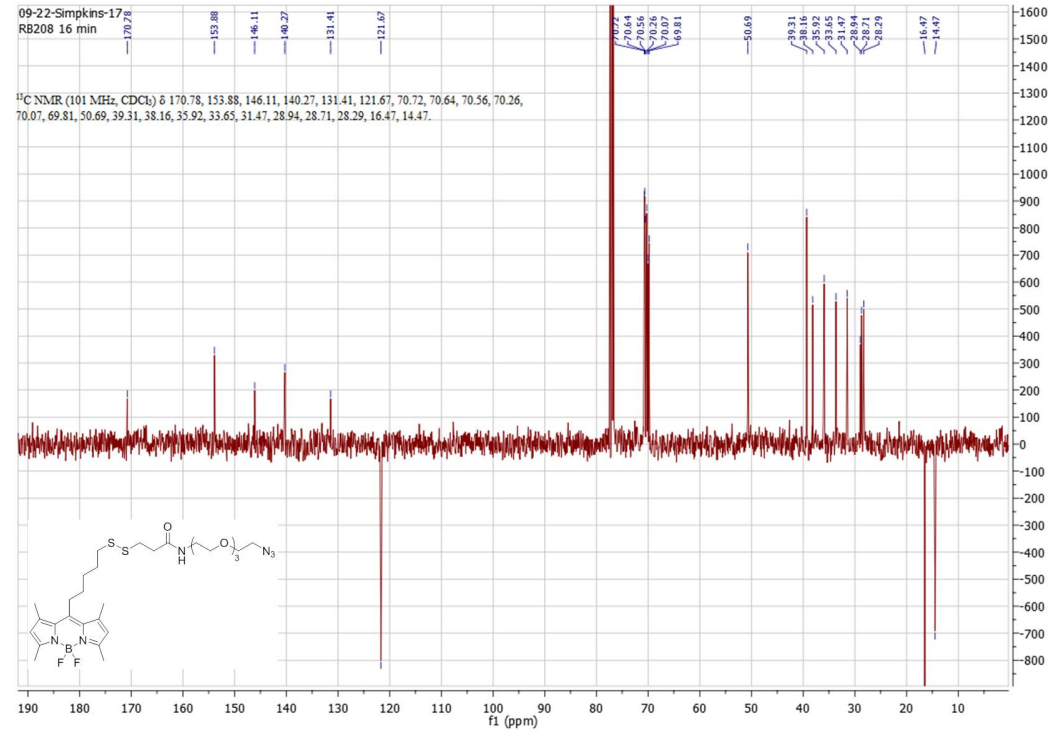

(a) ^{13}C NMR spectrum of BODIPY **24**.

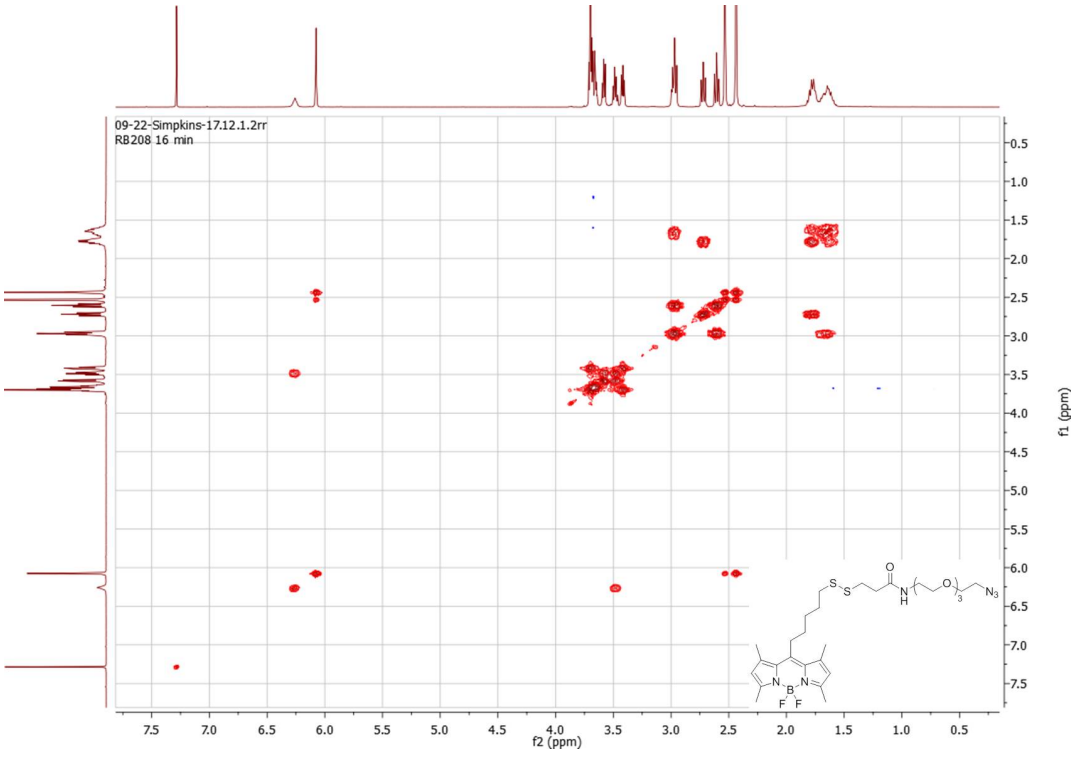

(b) COSY NMR spectrum of BODIPY **24**.

Figure 8.6: ^{13}C NMR and COSY NMR spectra of BODIPY **24**.

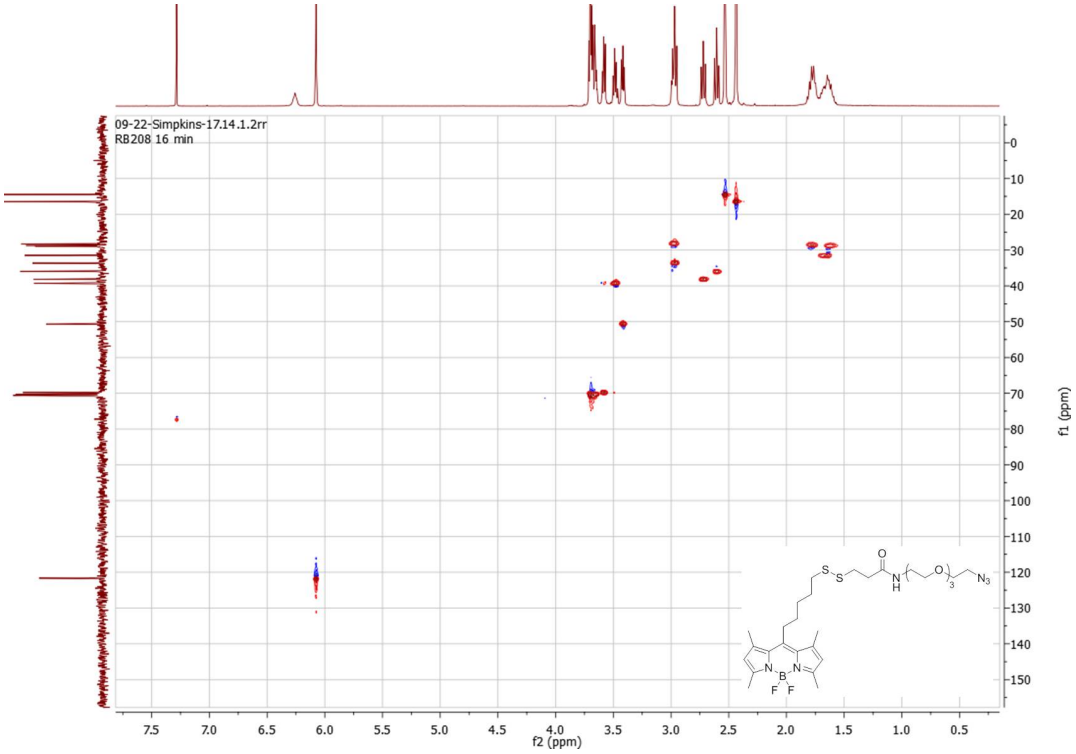

(a) HSQC NMR spectrum of BODIPY **24**.

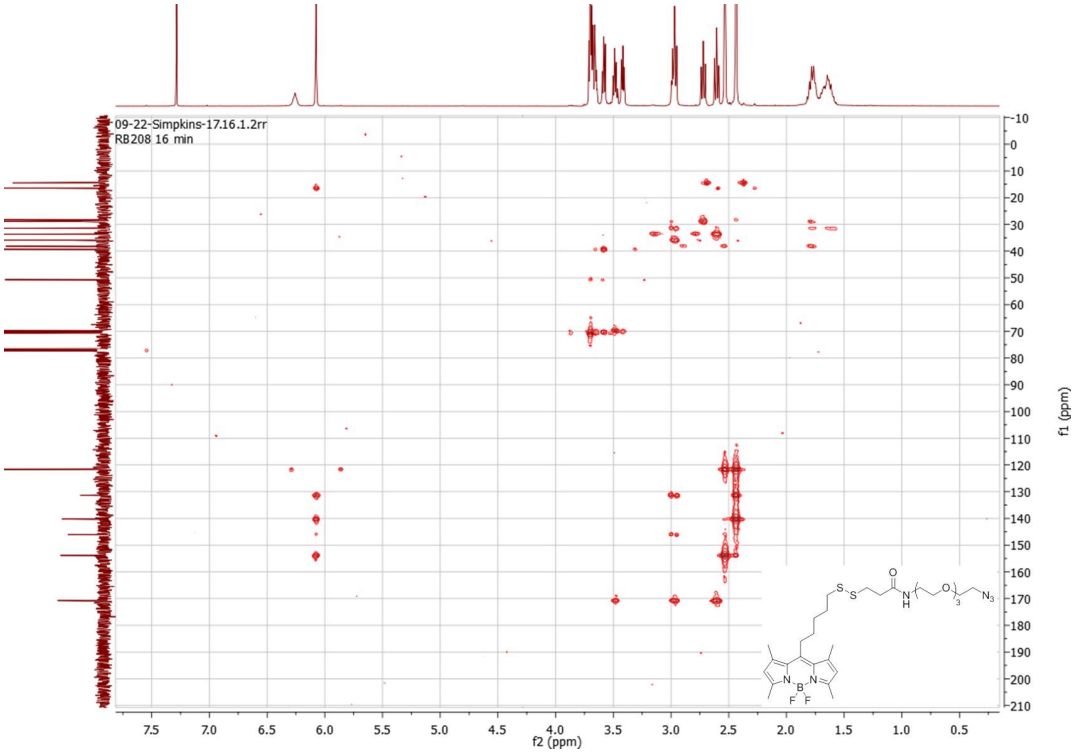

(b) HMBC NMR spectrum of BODIPY **24**.

Figure 8.7: ^{13}C NMR and COSY NMR spectra of BODIPY **24**.

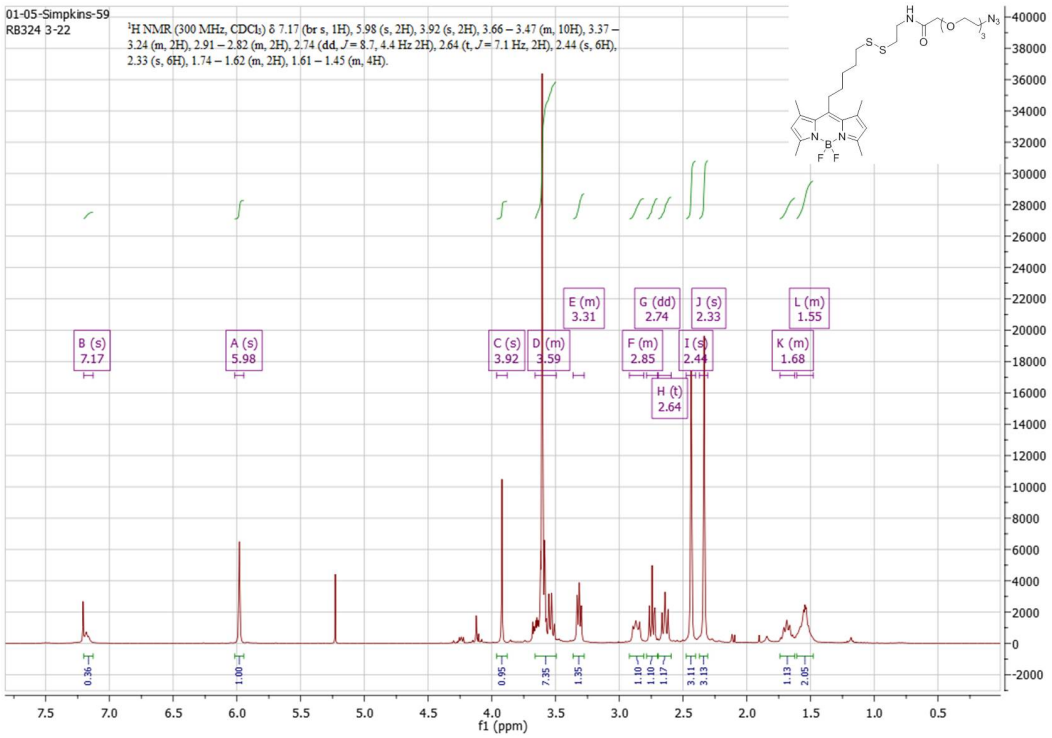

(a) ^{1}H NMR spectrum of BODIPY **32**.

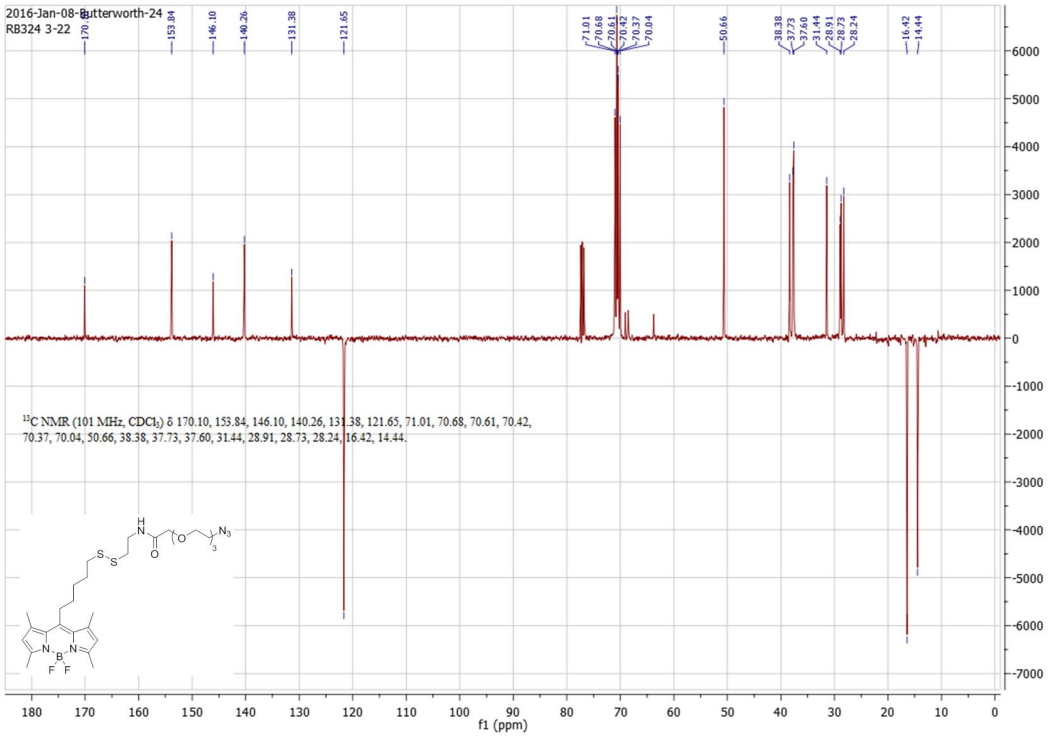

(b) ^{13}C NMR spectrum of BODIPY **32**.

Figure 8.8: ^{1}H and ^{13}C NMR spectra of BODIPY **32**.

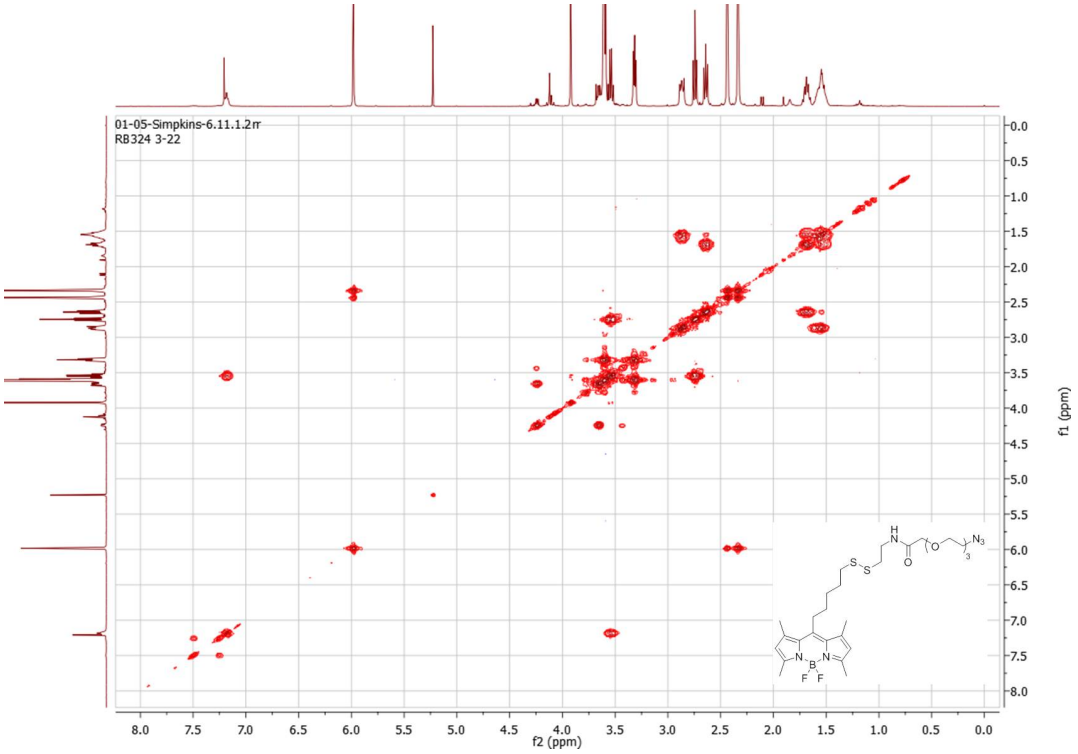

(a) COSY NMR spectrum of BODIPY **32**.

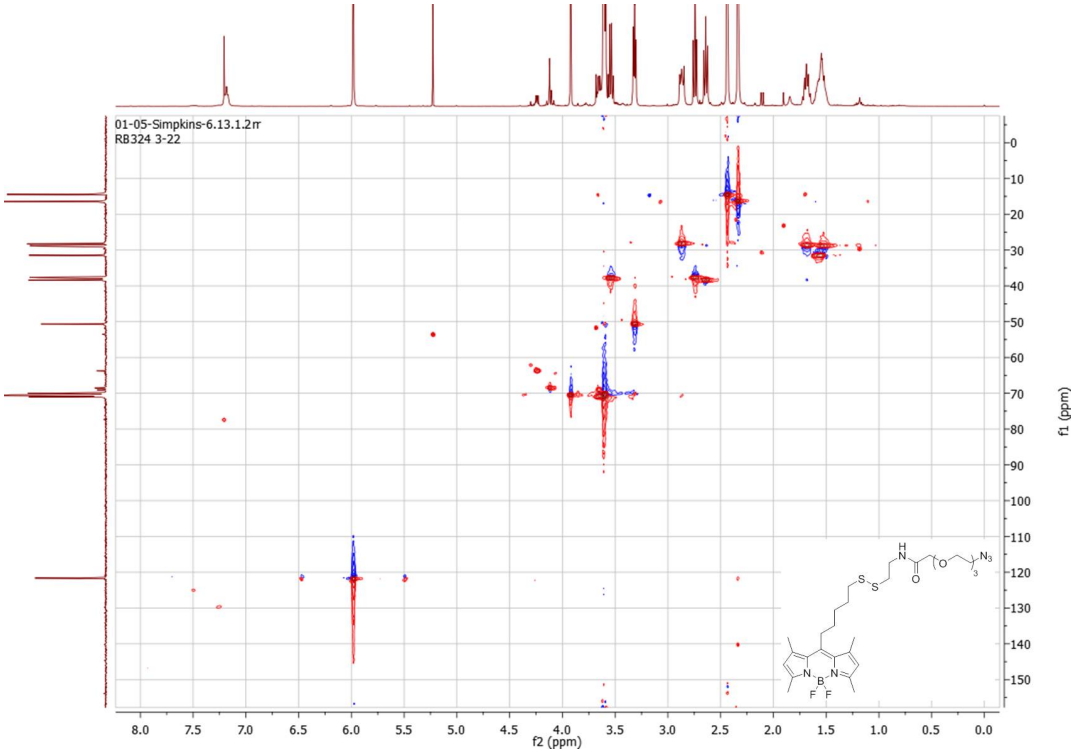

(b) HSQC NMR spectrum of BODIPY **32**.

Figure 8.9: COSY and HSQC NMR spectra of BODIPY **32**.

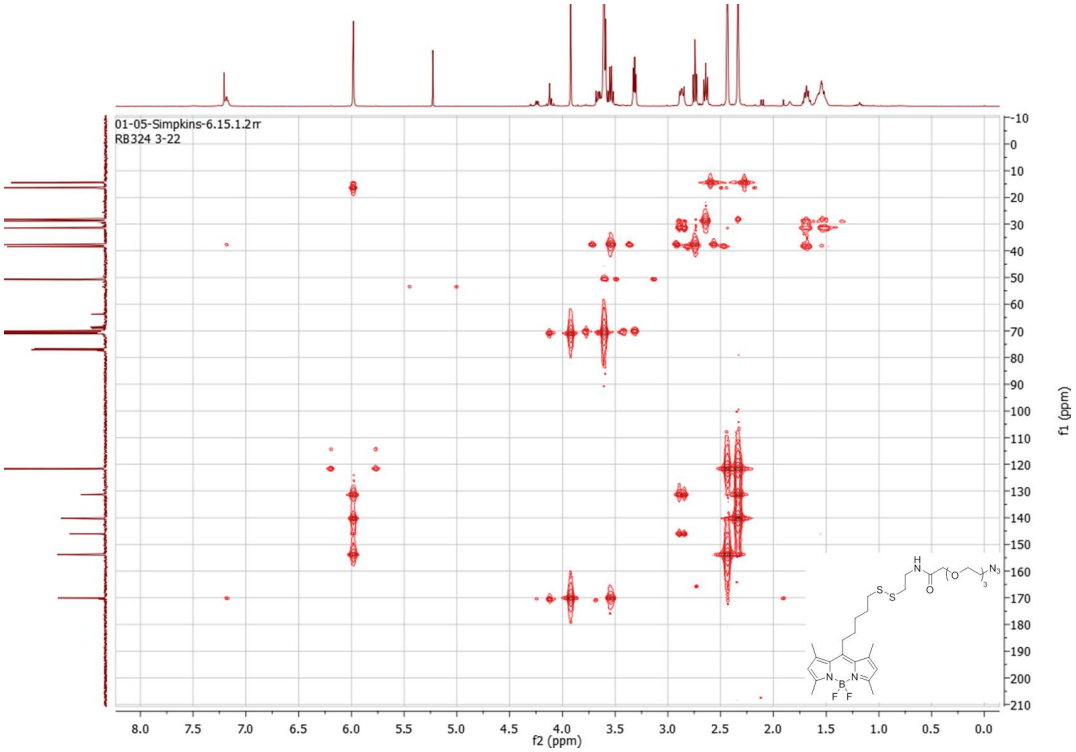

(a) HMBC NMR spectrum of BODIPY **32**.

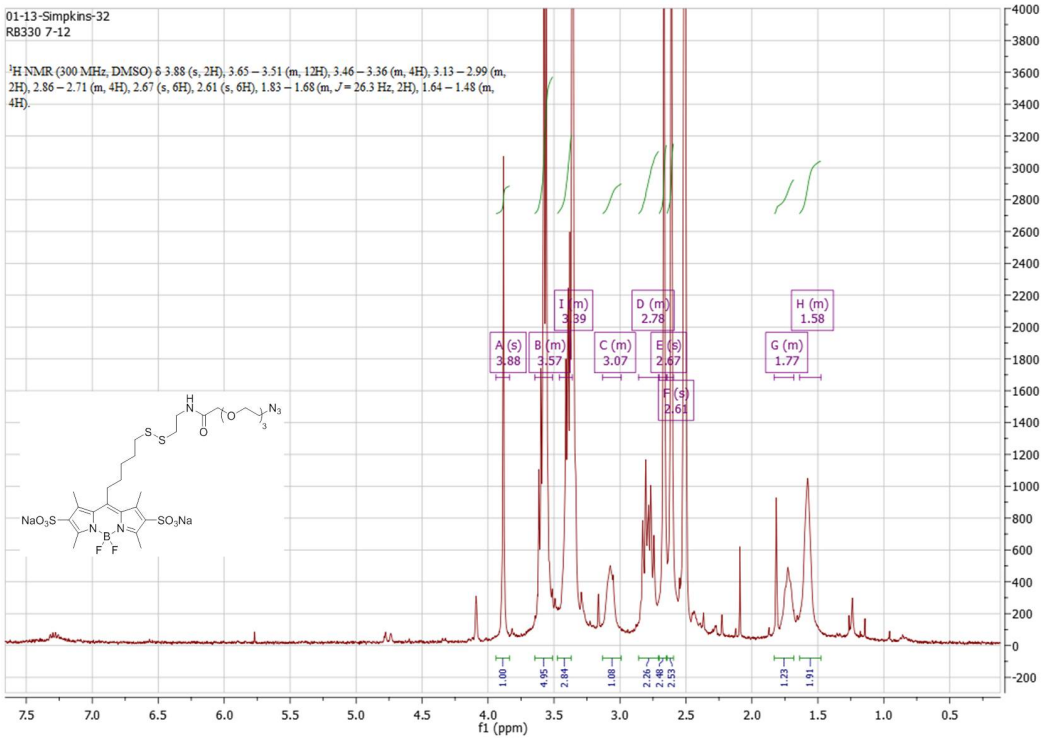

(b) ^{1}H NMR spectrum of BODIPY **33**.

Figure 8.10: HMBC NMR spectra of BODIPY **32** and ^{1}H NMR specra of BODIPY **33**.

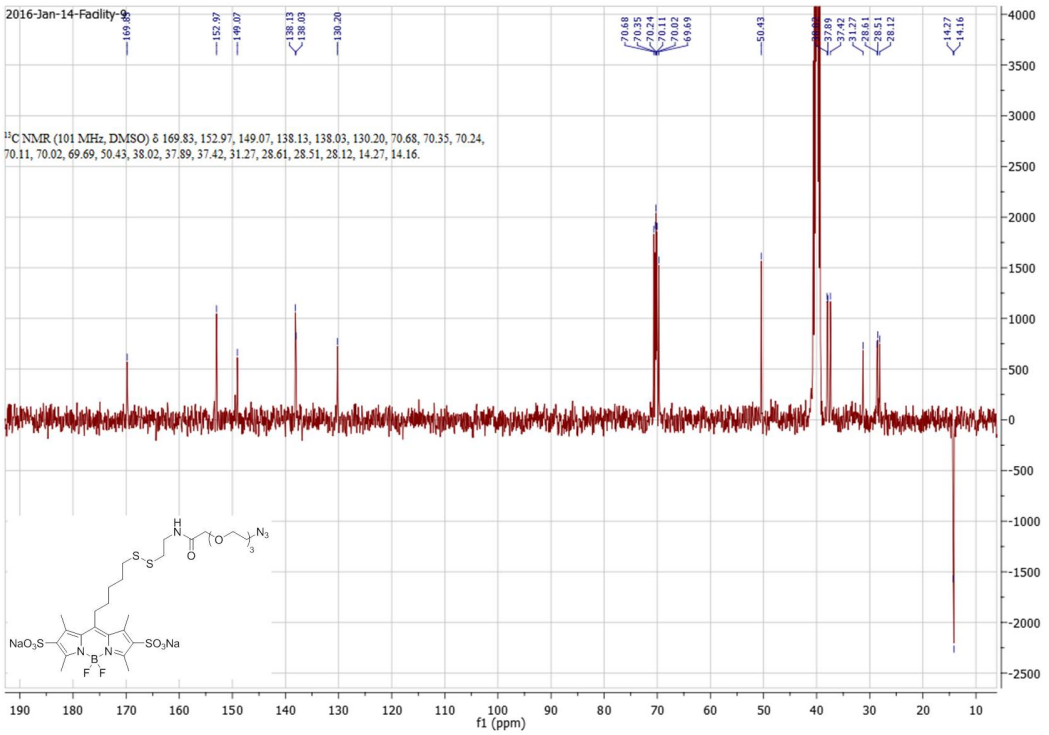

(a) ^{13}C NMR spectrum of BODIPY **33**.

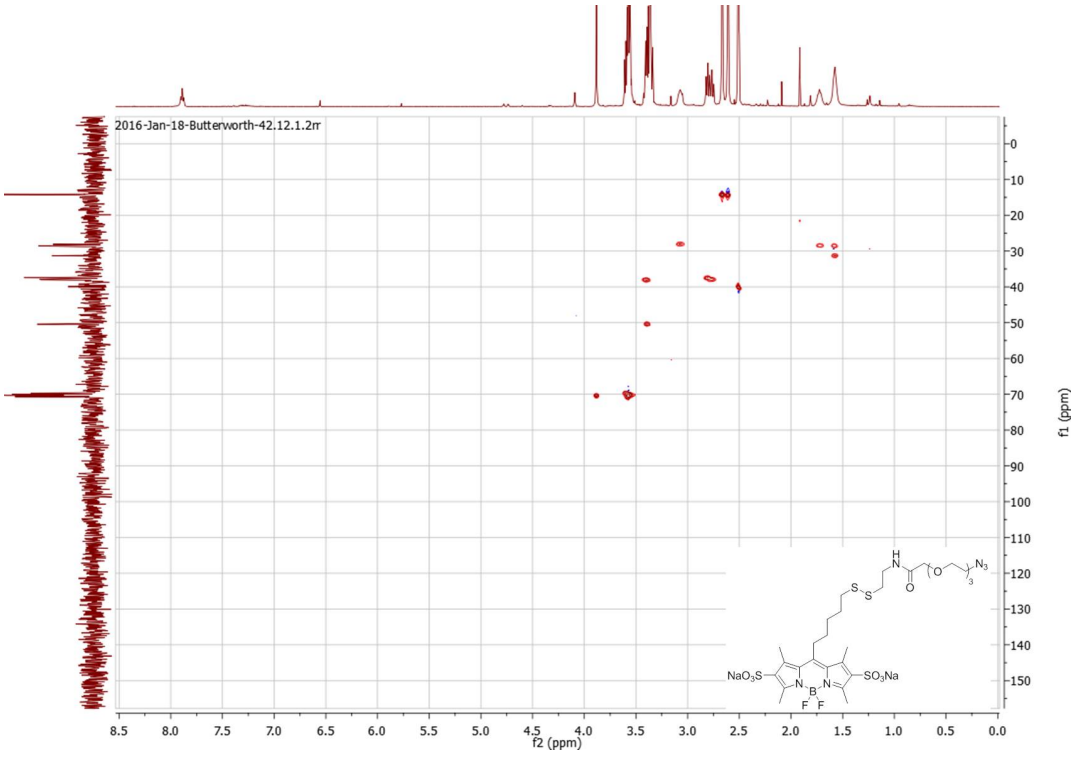

(b) HSQC NMR spectrum of BODIPY **33**.

Figure 8.11: ^{13}C and HSQC NMR spectra of BODIPY **33**.

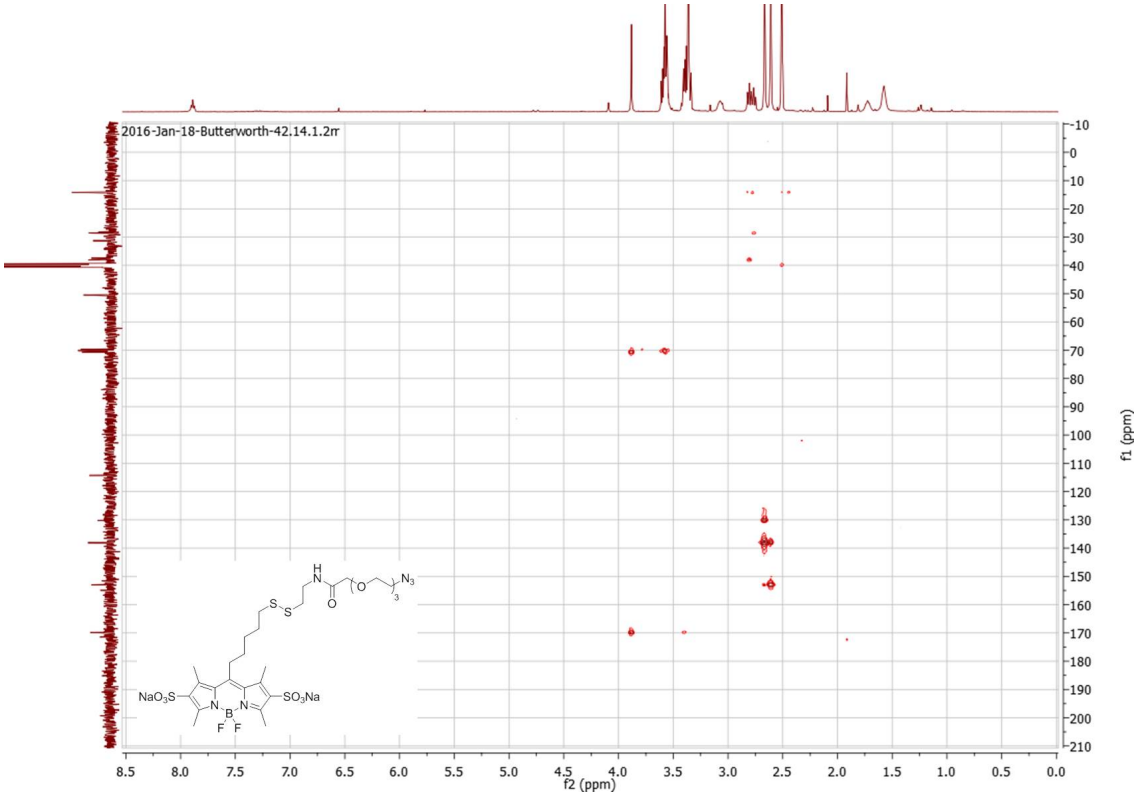

Figure 8.12: HMBC NMR spectrum of BODIPY **33**.

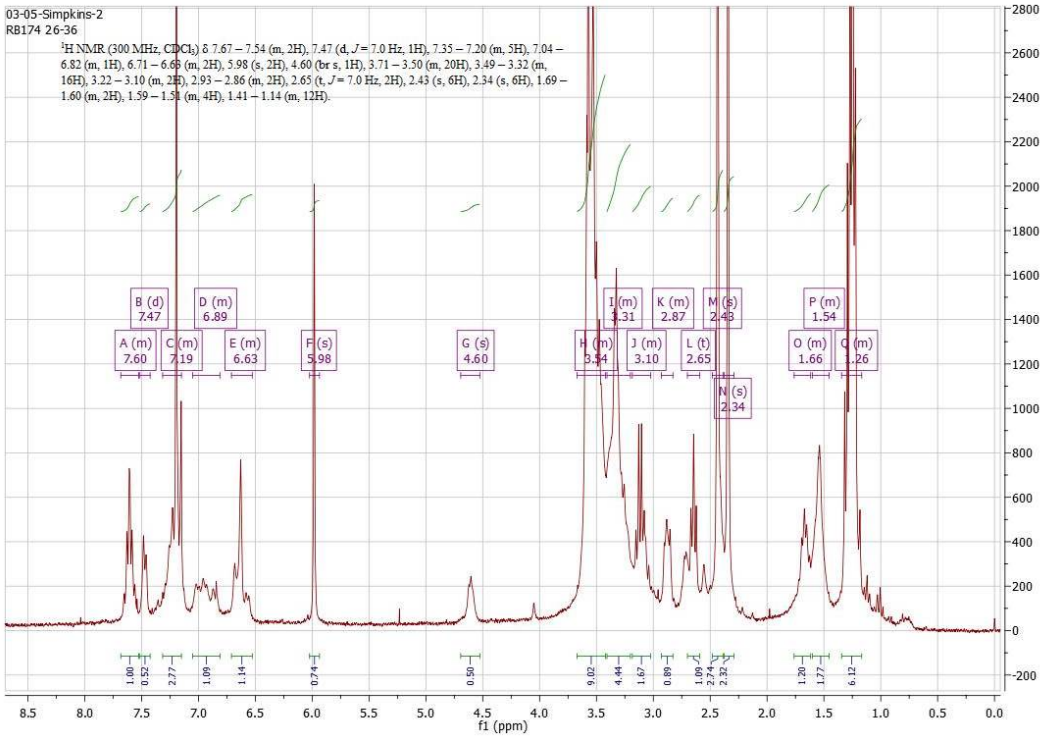

(a) ^{1}H NMR spectrum of FRET pair **45**.

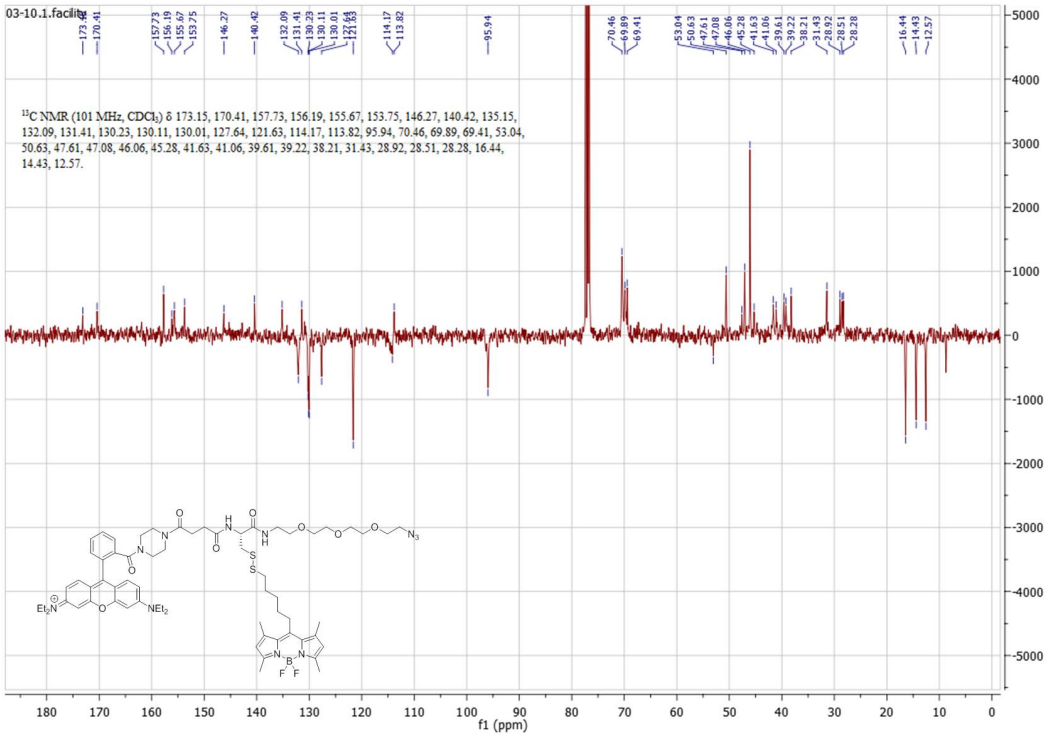

(b) ^{13}C NMR spectrum of FRET pair **45**.

Figure 8.13: ^{13}C and HSQC NMR spectra of BODIPY **33**.

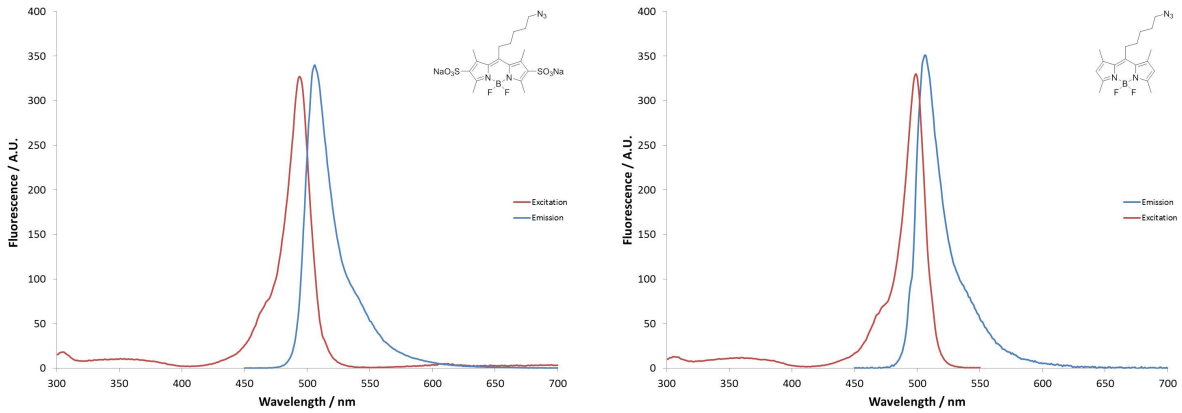

(a) BODIPY 8

(b) BODIPY 10

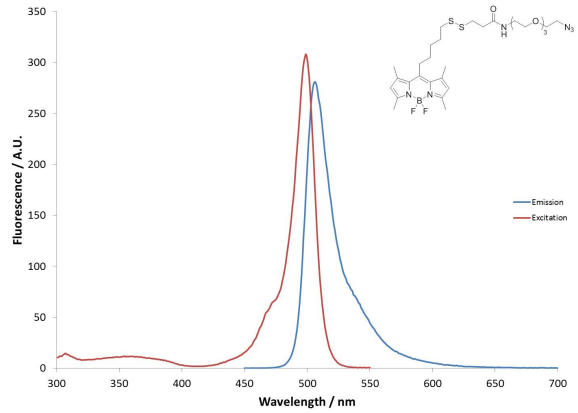

(c) BODIPY 24

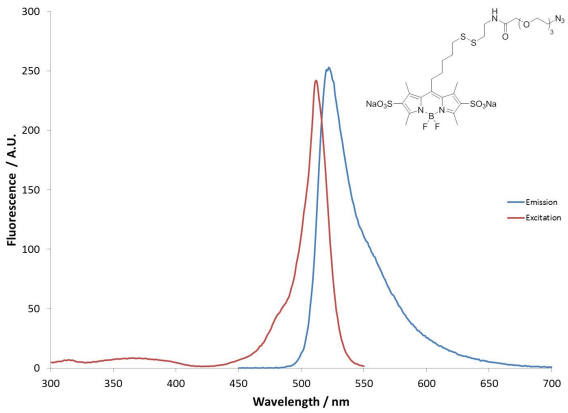

(d) BODIPY 33.

Figure 8.14: Non-normalised fluorescence spectra of fluorophores synthesised in Chapter 3.

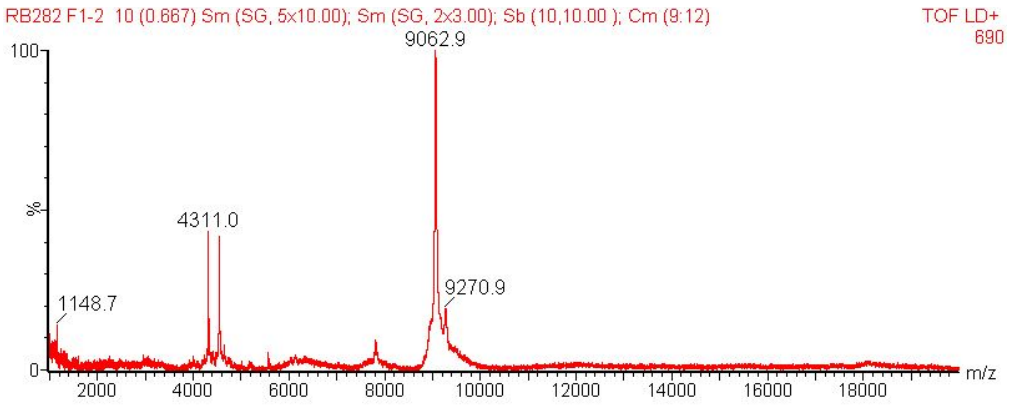

Figure 8.15: MALDI-MS of an unsuccessful attempt to form CCL2 Ala^{-1}-SS-L (corresponding to Scheme 4.4).

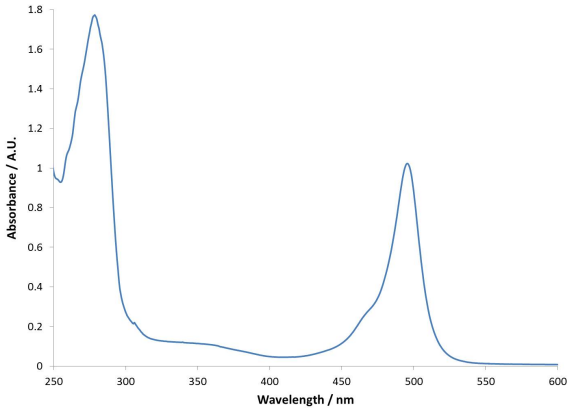

(a) CCL2 Ala^{-1}-alk-H

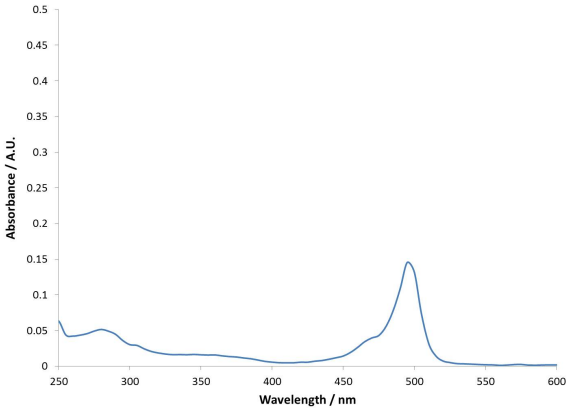

(b) CCL2 Ala^{-1}-alk-L

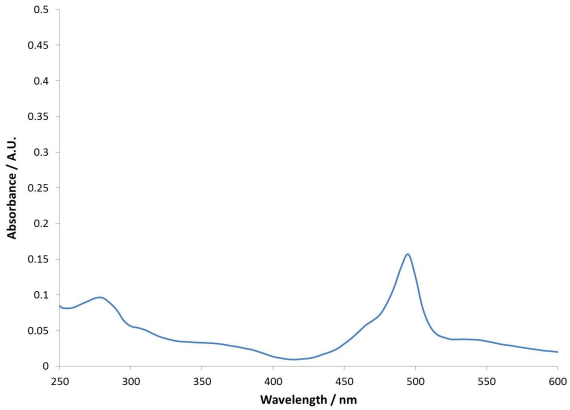

(c) CCL2 Ala^{-1}-SS-L

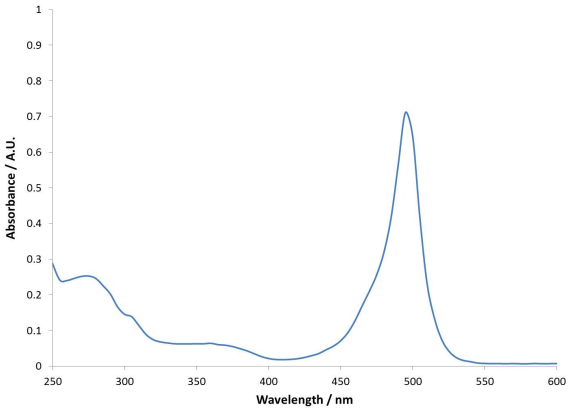

(d) CCL2 Ala^{-1}-SS-H

Figure 8.16: UV-Vis Spectra of CCL2 Ala^{-1} conjugates.

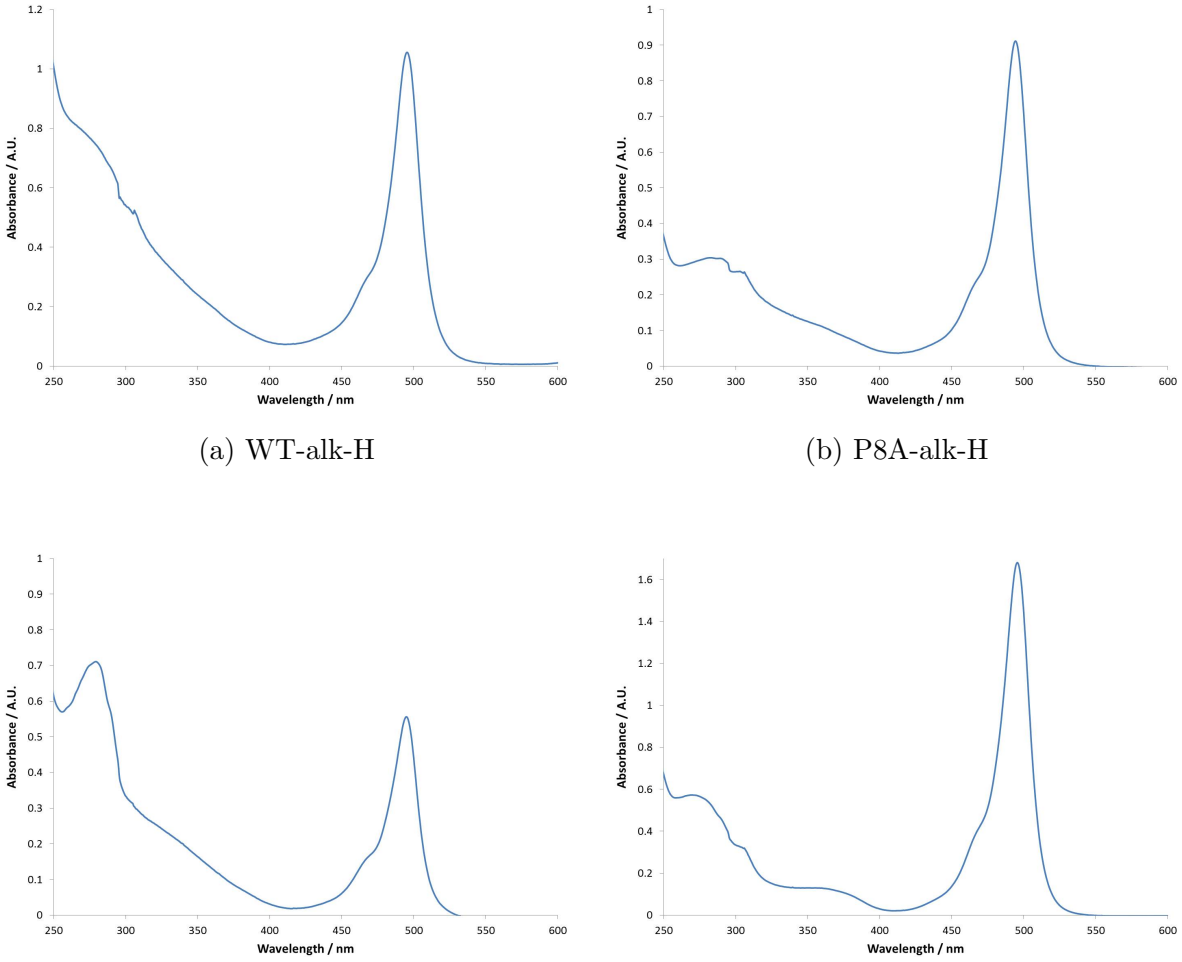

(a) WT-alk-H

(b) P8A-alk-H

(c) P8A-alk-L

(d) P8A-SS-H

Figure 8.17: UV-Vis Spectra of P8A-CCL2 conjugates.

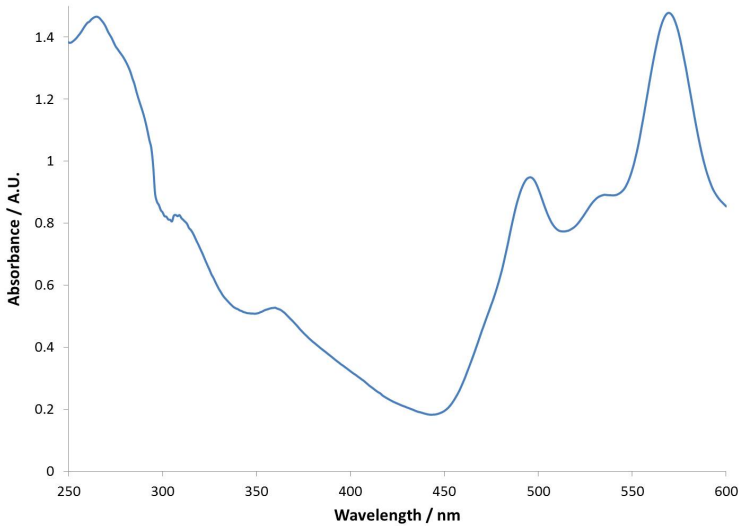

Figure 8.18: UV-Vis Spectra of CCL2 Ala^{-1}-FRET Conjugate.

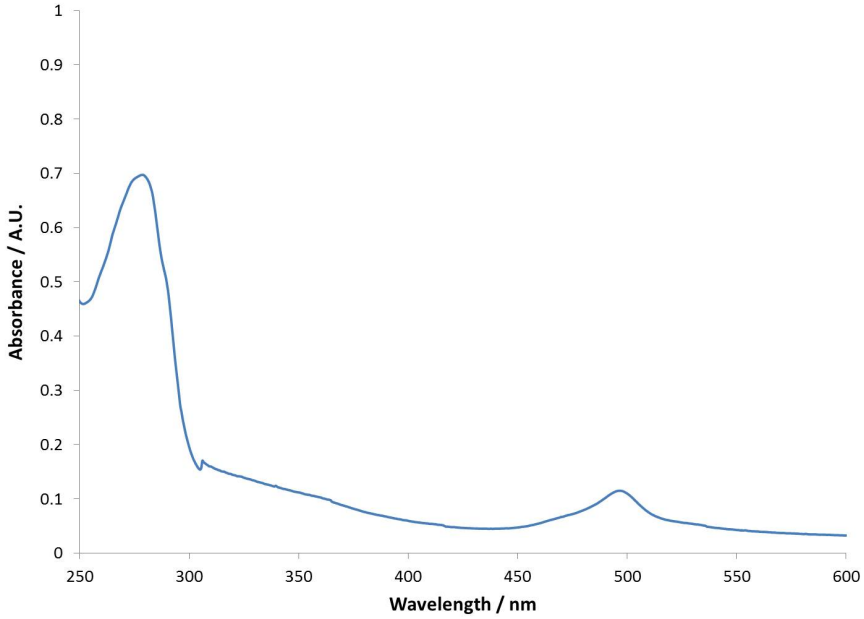

(a) UV-Vis spectra of CuAAC between P8A and **32** (Reaction J).

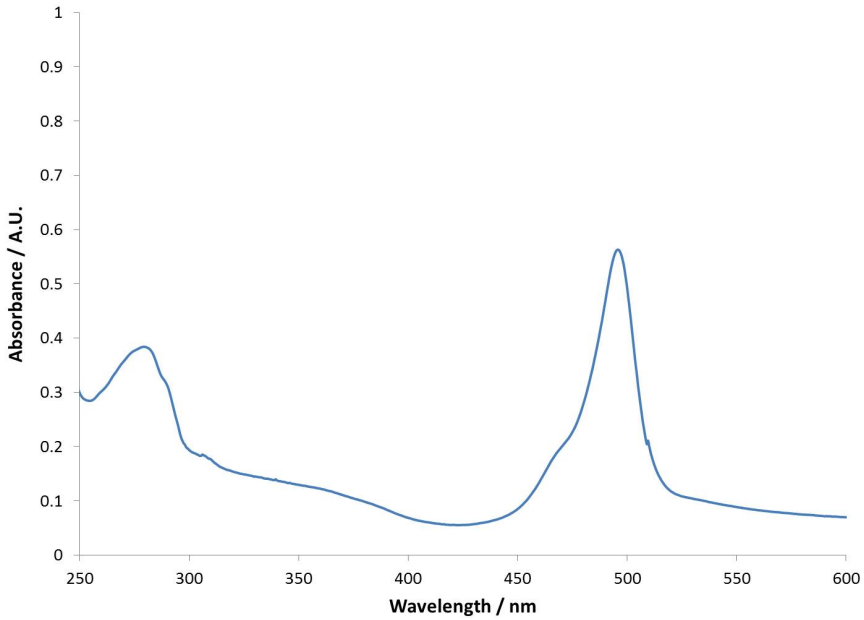

(b) UV-Vis spectra of CuAAC between P8A and **24** (Reaction K).

Figure 8.19: UV-Vis spectra of CuAAC between P8A and lipophilic disulfide-linked BODIPYs **24** and **32**. Whilst the MALDI-MS signal indicated formation of P8A-SS-L from the reaction between P8A-CCL2 and BODIPY compoundRB324, the UV-Vis BODIPY absorption was weak (8.19a) which corresponds to the MALDI-MS displayed in Figure 4.10b. The UV-Vis spectra indicated a greater level of conjugation between P8A-CCL2 and BODIPY **24** (8.19b) which corresponds to the MALDI-MS displayed in Figure 4.10c

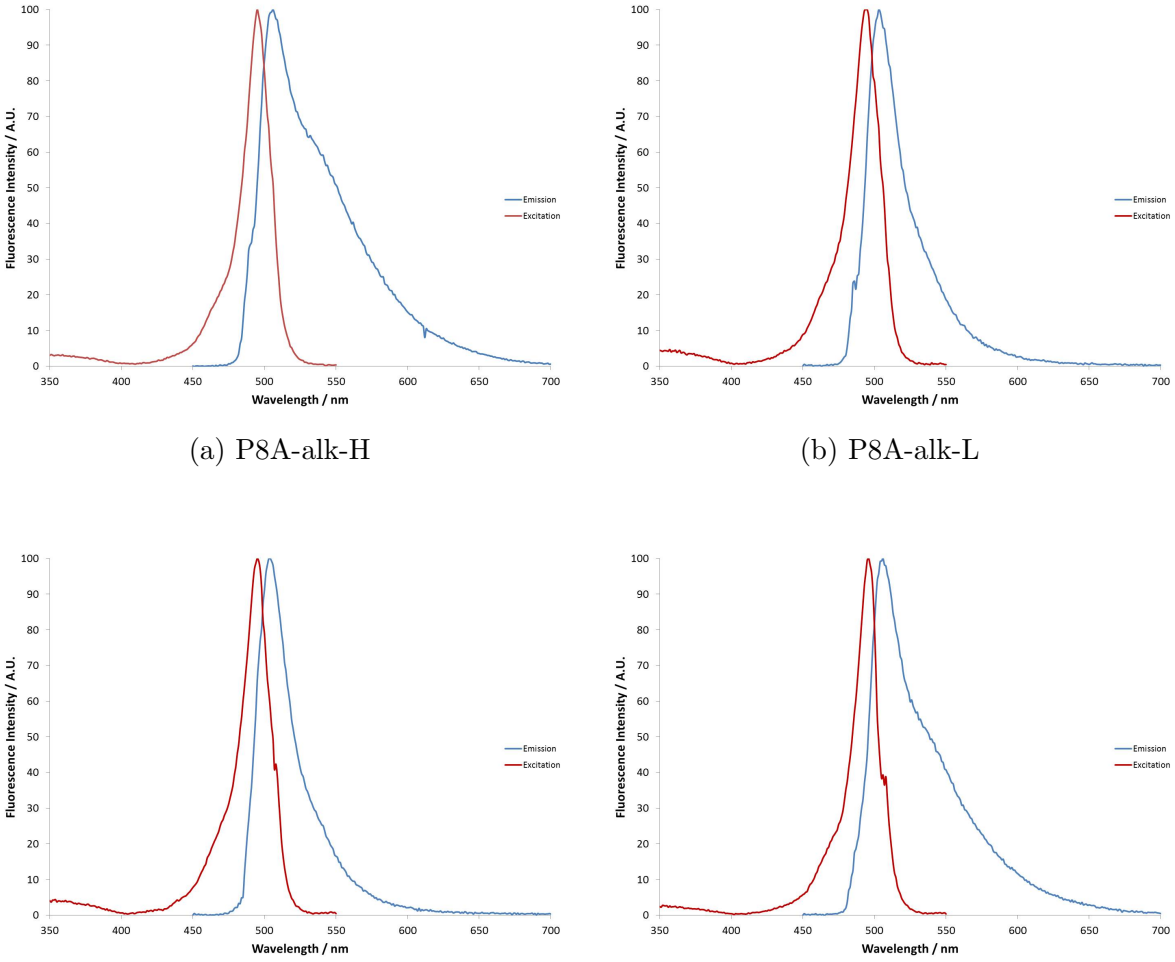

(a) P8A-alk-H

(b) P8A-alk-L

(c) P8A-SS-L

(d) P8A-SS-H

Figure 8.20: Normalised fluorescence spectra of conjugates synthesised on P8A-CCL2, all samples were run in PBS at rt. All CCL2 conjugates were excited at 488 nm as this corresponds to green laser lines which will be used in flow cytometry and microscopy.

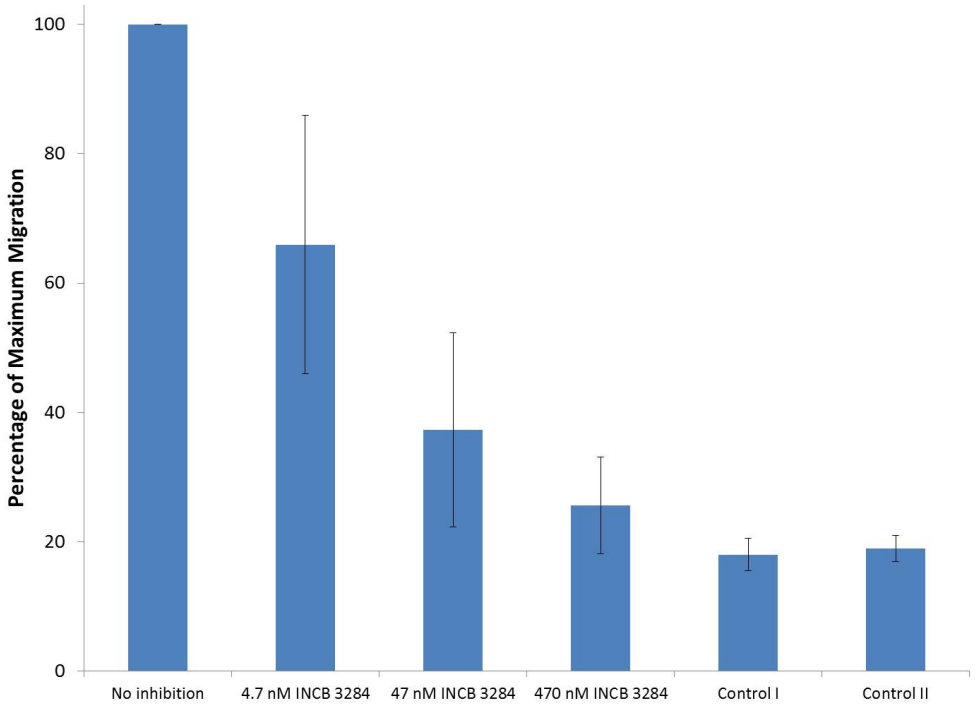

Figure 8.21: Boyden chemotaxis assay of THP-1 cells response to recombinant CCL2 in combination with INCB 3284 inhibition. The CCR2 inhibition is effective at preventing chemotaxis of recombinant CCL2. N = 2.

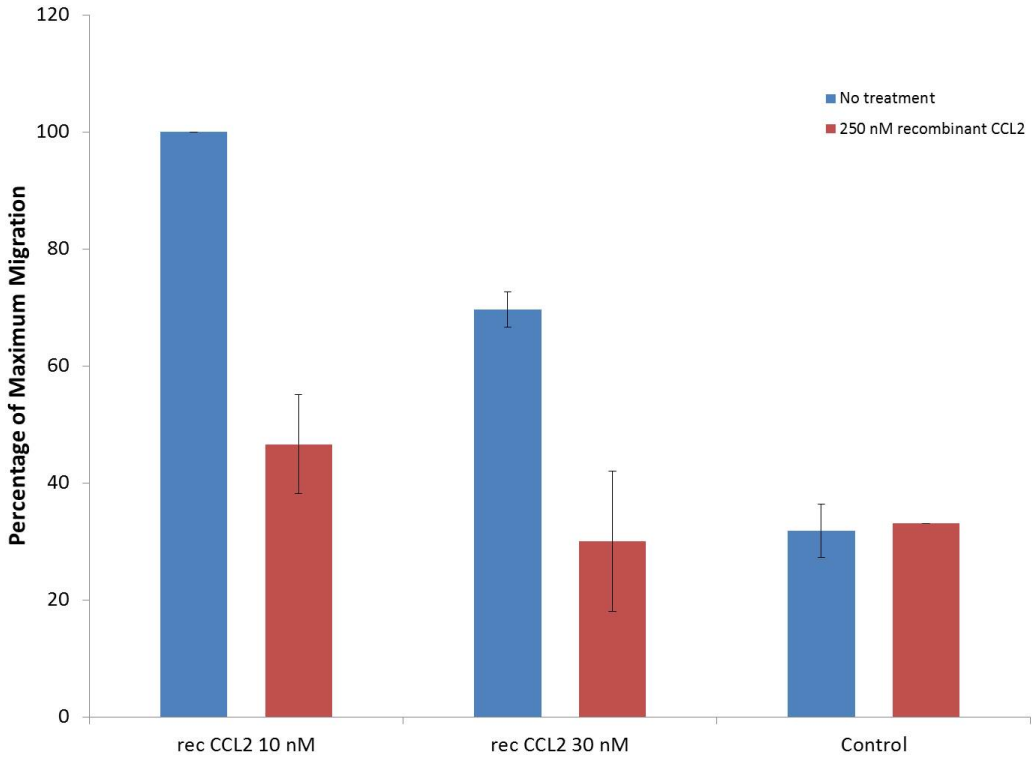

Figure 8.22: Effects of pre-treatment with 250 nM CCL2 on the chemotaxis of recombinant CCL2 in Boyden transwell chemotaxis assays. The high concentration of CCL2 reduces the amount of surface CCR2 on THP-1 cells leading to a reduction in chemotaxis towards CCL2. Error bars refer to standard error at N = 2.

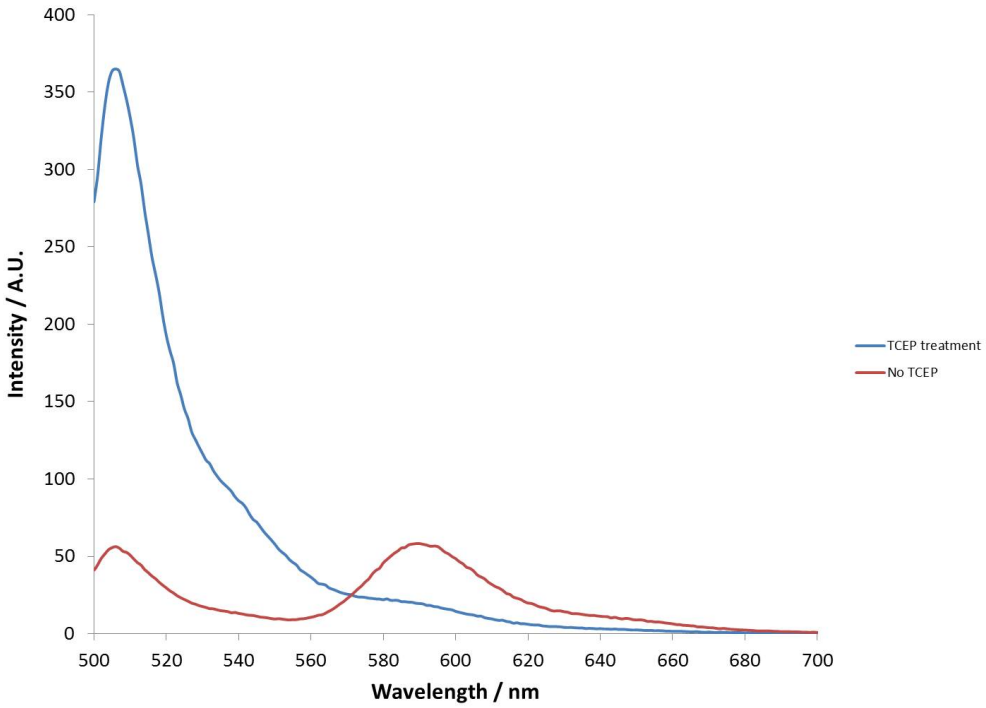

Figure 8.23: Fluorescence spectra of CCL2 Ala^{-1}-FRET before an after TCEP treatment. Some scattering was observed below 500 nm (not shown). The FRET signal was promising but could not be reproduced in a cellular system.

8.1 Publications

Conference abstracts

R. M. Brown, I.B. Styles, R.C. May, S. Butterworth, 'Imaging macrophages and macrophage-resident pathogens', In *M5 Biomedical Imaging Conference*, 9th September 2014, Nottingham, UK.

R. M. Brown, I.B. Styles, R.C May, C.J. Weston, S. Butterworth, 'Selective delivery of biomolecules to monocytes via CCL2-mediated endocytosis', In *ID2Bham*, 24-25th June 2015, Birmingham, UK.

Manuscript in preparation:

Ryan M. Brown, Iain B. Styles, Robin C. May, Christopher J. Weston, Sam Butterworth. Design, synthesis and evaluation of CCL2-derived imaging tools for the assessment of CCL2/CCR2 biology and monocyte function. In preparation (2017).